Measurement of Neutrino Oscillation Parameters with Neutrino-Nucleus Interaction Studies in the K2K Experiment

Masaya Hasegawa

January, 2006

Department of Physics, Graduate School of Science
Kyoto University

Abstract

This thesis describes the final result of neutrino oscillation in the KEK-to-Kamioka (K2K) long baseline neutrino oscillation experiment. The data were taken from June 1999 to November 2004, corresponding to the total number of protons on target of 9.2×10^{19}.

In K2K, the signatures of neutrino oscillation appear as a deficit in the number of neutrino events and a distortion of the neutrino energy spectrum at Super-Kamiokande (SK). The event distributions without oscillation in SK are predicted from the measurements in the near detectors at KEK by using the neutrino interaction models and the detector simulation. In order to improve the reliability of the prediction, the cross section of charged current (CC) coherent pion production ($\nu_\mu + A \to \mu^- + \pi^+ + A$) is measured for the first time in the energy region of a few GeV. No evidence for coherent pion production is observed, and the following upper limit is set at 90% confidence level (CL).

$$\sigma(\text{coherent pion})/\sigma(\nu_\mu CC) < 0.60 \times 10^{-2}$$

This result gives a solution of a long-standing problem on the neutrino-nucleus interaction cross section referred to as "low-q^2 puzzle", which is a significant deficit of the events with a forward going muon. The neutrino interaction models including this result well reproduce all the measurements in the near detectors. By using the refined interaction models, the event distributions in SK are predicted.

One hundred twelve beam neutrino events are observed in the fiducial volume of SK. In the case of no oscillation, the expected number of events is $155.9^{+11.6}_{-10.2}$. This deficit confirms ν_μ disappearance at 99.8 % CL. Among the observed events, fifty eight one-ring muon-like events are used to measure the neutrino energy spectrum. The observed energy spectrum shows a clear distortion compared with the expectation for no oscillation at 99.5% CL. The probability that the observations are due to a statistical fluctuation without oscillation is 0.003% (4.2σ). A two-neutrino oscillation analysis results in the oscillation parameter set of

$$(\Delta m^2, \sin^2 2\theta) = (2.76 \times 10^{-3}[\text{eV}^2],\ 1.0).$$

The 90% confidence level interval for Δm^2 at $\sin^2 2\theta = 1.0$ is

$$1.9 \times 10^{-3} \leq \Delta m^2 \leq 3.5 \times 10^{-3}\ [\text{eV}^2].$$

This constraint is one of the most stringent limits to date. The result of K2K confirms neutrino oscillation discovered in the atmospheric neutrinos by the SK collaboration.

Acknowledgments

First of all, I would like to express my deepest gratitude to my supervisor Prof. Koichiro Nishikawa, for giving me the opportunity of performing this research and for his gentle support. Discussion with him never allows me a compromise, and I was able to promote my study by his supervision. Without his invaluable help, this thesis would not exist.

I would like to thank Prof. Tsuyoshi Nakaya for his genuine support and constant encouragement during my graduate student life. His critical eye and attention to detail is balanced with his willingness to compliment me for a job well done. He has always intrigued and stimulated me through invaluable discussions on various topics.

My warm appreciation goes to Dr. Masashi Yokoyama with whom I worked closely over the years. Discussions with him stimulated me to come up with new ideas, new understandings and new viewpoints, and also made our works highly enjoyable.

I also give another thank to Prof. T. Nakaya and Dr. M. Yokoyama as my English tutor. They patiently proofread and brought my manuscripts into the next level.

I would like to thank T.Nakaya, K.Nishikawa, N.Sasao, K.Imai, and H.Hata, who gave me invaluable advise as members of referees of this thesis. I especially enjoyed discussion with K.Imai at my defense.

I express my heartfelt gratitude and thanks to Dr. A. K. Ichikawa. She has always encouraged me and has always helped me when I didn't understand. I never forget she taught me how to identify nipper from long-nose pliers with some anger.

I also wish to extend my thanks to Prof. Y. Hayato. He has always lent an ear to our voice and took special case of all the students. Personally, I want to take this opportunity to apology for the thing I often woke him in the midnight under the guise of emergency conditions during the run time.

I would like to express my special thanks to Dr. I. Kato. He taught me the basic techniques of physics experiments, analysis and more, which were very helpful for me especially when I knew nothing about K2K.

I am indebted to wonderful fellows at laboratory, Shimpei Yamamoto and Toshi Sumida, for their generous help with my life in the experimental world of high energy physics, without which I could not have survived until now, seriously. I am grateful to all the fellows in the second division of Department of Physics, Kyoto University, for the warm hospitality and the exciting academic environment.

The work presented here is the result from the efforts of many K2K collaborators. I would like to thank those who struggled to design and construct the experiment, to start up it, to take data, to calibrate the detectors.

Prof. Y. Totsuka, Prof. K. Nakamura, Prof. Y. Suzuki, Prof. C. K. Jung, and Prof. R. J. Wilkes have administrated the K2K experiment with best efforts.

The beamline monitors have been supported by Dr. T. Hasegawa, Dr. T. Maruyama and the other beamline group members. Personally, I thank Dr. T. Hasegawa who continued to forward all the e-mails addressed to me without criticism.

The data taking have been performed by the keepers of the K2K DAQ, Prof. Y. Hayato, Prof. T. Kobayashi, Dr. M. Yoshida and the other many people.

I also thank the other sub-detector groups, especially Prof. Y. Itow, Prof. M. Shiozawa, Dr. M. Miura, Dr. J. Kameda Dr. S. Nakayama and Dr. I. Kato from the 1KT group, Prof. M. Sakuda, Dr. T. Ishida, Dr. R. Gran, Dr. T. Iwashita and Dr. H. Yokoyama from the SciFi group, Prof. T. Kobayashi and Dr. M. Yoshida from the LG group, Dr. T. Ishii, Dr. Inagaki and Dr. J. H. Choi from the MRD group, Prof. K. Kaneyuki, Dr. Y. Obayashi and Dr, S. Yamada from the Super-K group.

For the analysis, I am deeply thankful to the members of the K2K-SK oscillation analysis group for their generous help and valuable suggestions. I am specially grateful to Prof. T. Nakaya, Prof. K. Kaneyuki, Prof. C. W. Walter, Dr. Y. Obayashi, Dr. J. Kameda, Dr. S. Nakayama, Mr. R. Terri, Dr. T. Ishida, Dr. R. Gran, and Dr. T. Nakadaira for discussions and advice on the results in the thesis.

I would like to thank to the internal referees, Dr. F. Sanchez, Dr. T. Kutter, Dr. H. Sato, Ms. L. Whitehead and Dr. M. Yokoyama, who helped me to submit the paper on this analysis. They were very quick to understand the essence of my analysis and what is further necessary in the paper. In addition, I am deeply grateful to Prof. C. K. Jung and Dr.K.Scholberg, who carefully proofread the paper draft. I add lastly that Prof. C. K. Jung is the man who first supported non-existence of coherent pion production among the collaborators.

I would like to acknowledge to all the members of SciBar group. Especially, Dr. M. Yoshida, Dr. K. Nitta, Dr. H. Maesaka, Mr. S. Yamamoto, Mr. Y. Takubo, Mr. T. Sasaki and Mr. T. Morita worked together in a busy days of construction, commissioning and operation of the SciBar detector. I never forget hard but exciting days with them.

My thanks extentd to another important person, Mr. M. Taino, who always helped me and exerted energetic efforts to construct the SciBar detector.

I am deeply thankful to the kindness and friendship of all the students who live under the same roof, Dr. I. Kato, Dr. H. Maesaka, Mr. S. Yamamoto, Mr. K. Hayashi, Mr. T.Morita, Mr. T. Sasaki, Mr. S. Ueda, Mr. K. Hiraide and Mr. J. Kubota from Kyoto University, Dr. T. Iwashita and Ms. M. Sekiguchi from Kobe University, Dr. H. Yokoyama from Science University of Tokyo, Dr. M. Yoshida and Mr. Y. Takubo from Osaka University, Mr. S. Nawang from Hiroshima University. Without them, there should not be wonderful five years in KEK.

I am thankful to all the members of High Energy Group of Kyoto University: Prof. N. Sasao,

Prof. H. Sakamoto, Dr. R. Kikuchi, Dr. T. Nomura, Dr. H. Nanjo, Mr. M. Suehiro, Dr. Y. Ushiroda, Dr. H. R. Sakai, Mr. T. Fujiwara, Dr. S. Nishida, Mr. H. Yokoyama, Dr. Y. Honda, Dr. I. Kato, Dr. H. Maesaka, Mr. K. Mizouchi, Ms. K. Uchida, Mr. T. Sumida, Mr. S.Yamamoto, Mr. K. Hayashi, Mr. T. Morita, Mr. T. Sasaki, Mr. S. Ueda, Mr. H. Morii, Mr. K. Hiraide, Mr. J. Kubota, Mr. T. Shirai, Ms. N. Taniguchi, Ms. K. Takezawa, Mr. K. Ezawa, Mr. Y. Kurimoto, Mr. Y. Kurosawa, Mr. Y. Nakajima., Mr. T. Nobuhara, Mr. M. Taguchi and Mr. K. Matsuoka. I would like to address thanks to the secretary Ms. A. Nakao and the other secretaries for taking case of every official/private business.

I have spent four years in Tohoku University as an undergraduate student. Throughout my school life, I have been benefited by wonderful fellows in the the Physics institute. I would like to thank them here.

I wish to make special mention here of the Shimotsuma City where I born and bred. The next thing I should do and I want to do become plainly visible when I stand on the place. Shimotsuma is the center in the entire universe for me.

Finally, I would like to send best thanks to my family for their endless support throughout my life.

Contents

Chapter 1

Introduction

In this chapter, we review the current knowledge of neutrino mass, neutrino oscillation as a probe of finite neutrino mass and the status of neutrino oscillation experiments. We also describe an outline of this thesis in the last section.

1.1 Neutrino and Neutrino Mass

Neutrinos were originally postulated by W. Pauli in 1930 as massless and neutral particles with spin 1/2 in order to explain the continuum electron energy spectrum of the β decay [1]. Pauli's hypothesis was verified by F. Rines and C. Cowan in 1956 [2] through the detection of anti-neutrinos from a nuclear reactor via inverse β decay,

$$\bar{\nu_e} + p \rightarrow e^+ + n, \tag{1.1}$$

The second type of neutrinos, ν_μ was detected in 1962 by Lederman, Schwartz, and Steinberger at Brookhaven [3]. The third type of neutrinos, ν_τ, was observed in 2000 at Fermilab [4] although there was ample indirect evidences of its existence from the weak interactions of τ. The possibility of the fourth light neutrino ($m_\nu < M_Z/2$) is excluded from the measurement of the invisible Z width in LEP experiments [5].

Neutrino mass is searched for in the following three types of experiments: (1) direct kinematic measurements, (2) search for neutrinoless double-β decay and (3) neutrino oscillation experiments. In addition, another bound on neutrino masses comes from cosmology.

Direct mass measurement

The direct mass measurements are performed by measuring the kinematics of a particle decay. The most sensitive measurement of the ν_e mass is performed by using the tritium β decay[1], which gives an upper limit of the ν_e mass 2.3 eV (95% CL) [7]. The best limit of the ν_μ mass of 170 keV (90% CL) has been obtained from the two-body π decay at rest, $\pi \rightarrow \mu + \nu_\mu$, by the PSI group [8]. For ν_τ, the current mass limit was given by the ALEPH collaboration. Results from two kinds of tau decay, $\tau \rightarrow 3\pi\nu_\tau$ and $\tau \rightarrow 5\pi\ (\pi^0)\nu_\tau$, were combined to set the limit at 18.2 MeV at 95% CL [9]. The best upper limit of neutrino masses obtained by the direct mass measurements are summarized in Table 1.1.

Neutrinoless double-β decay

The neutrinoless double β decay ($0\nu\beta\beta$) occurs only if the neutrino is a massive and Majorana particle [10]. The $0\nu\beta\beta$-decay rate is proportional to the square of the effective Majorana neutrino masses, $\langle m_\nu \rangle$. Confident evidence of $0\nu\beta\beta$-decay is not obtained although the

[1] The mass limit of ν_e is also obtained from the spread of the arrival time of neutrinos from Supernova-1987A, to be 5.7 eV [6].

Neutrino	Mass limit	Experiment
ν_e	2.3 eV (95% CL)	^{3}Hβ decay [7]
ν_μ	190 keV (90% CL)	pion decay [8]
ν_τ	18.2 MeV (95% CL)	tau decay [9]

Table 1.1: Present limit of neutrino mass

Heidelberg-moscow group reported a positive signal in 2001 [11]. The upper limit of the mass is set at $\langle m_\nu \rangle < 0.2$ eV [12].

Cosmological constraints

The Wilkinson Microwave Anisotropy Probe (WMAP), together with the Sloan Digital Sky Survey (SDSS), the Lyman alpha forest (Lyα), and other observations, lead to strong constraints on $\sum m_\nu \leq 1$ eV for three degenerate neutrino species [13], in which the most stringent limit is reported as 0.42 eV [14]. However, the upper bound depends strongly on other cosmological parameters, such as the matter density and the Hubble constant.

No evidence for finite neutrino masses is obtained from the direct mass measurements, the $0\nu\beta\beta$ decay search and the cosmological constraints until now.

The smallness of neutrino masses, if they exist, is not explained in the standard model of particle physics (SM) [15–17]. However, some extensions of SM naturally lead to the small nonzero neutrino mass. Among the large number of those models, a theory known as "see-saw mechanism" [18] explains the tiny neutrino mass most naturally. In this theory, the smallness of neutrino masses originates in the new physics of the higher energy scale. Thus, the confirmation of finite neutrino masses is evidence of physics beyond SM.

1.2 Neutrino Oscillation

Neutrino oscillation was first proposed by Pontecorvo as a consequence of finite neutrino masses. This phenomenon is one of the probes to the small neutrino masses of sub-eV order.

If neutrinos have masses, their flavor eigenstates are generally expressed as superpositions of the mass eigenstates,

$$|\nu_\alpha\rangle = \sum_{j=1}^{3} U_{\alpha j} |\nu_j\rangle \qquad (\alpha = \mathrm{e}, \mu, \tau) \tag{1.2}$$

where U is a 3×3 unitary matrix so-called Maki-Nakagawa-Sakata (MNS) matrix.

Time evolution of the states obey the Schrodinger equation as,

$$i\frac{d}{dt}|\nu_j\rangle = E_j |\nu_j\rangle \tag{1.3}$$

where, E_j is the energy of $|\nu_j\rangle$, and the wave function is written as:

$$|\nu_j(t)\rangle = e^{-iE_j t}|\nu_j(0)\rangle \tag{1.4}$$

Using Eq.(1.2)-(1.4), time evolution of the flavor eigenstate is described as:

$$|\nu_\alpha(t)\rangle = \sum_{j=1}^{3} U_{\alpha j} e^{-iE_j t} U^\dagger_{j\alpha} |\nu_\alpha(0)\rangle \tag{1.5}$$

Therefore, the probability that a neutrino produced in weak interaction as ν_α at t=0 is found in ν_α after time t is expressed as

$$P(\nu_\alpha \to \nu_\alpha) = |\langle \nu_\alpha(t)|\nu_\alpha(0)\rangle|^2 \tag{1.6}$$

$$= \sum_{j=1}^{3} |\langle \nu_\alpha(0)|U_{\alpha j} e^{-iE_j t} U^\dagger_{j\alpha}|\nu_\alpha(0)\rangle|^2 \tag{1.7}$$

In order to simplify the treatment, the case of two-flavor neutrino oscillation is considered. The matrix U is simply written as follows

$$U = \begin{pmatrix} \cos\theta & \sin\theta \\ -\sin\theta & \cos\theta \end{pmatrix} \tag{1.8}$$

and the survival probability (1.7) is expressed as

$$P(\nu_\alpha \to \nu_\alpha) = 1 - \sin^2 2\theta \sin^2\left(\frac{(E_i - E_j)t}{2}\right). \tag{1.9}$$

Using an approximation of $E_j \sim (p + m_i^2/2p)$ and neutrino path length L_ν, the survival probability is re-formulated as follows:

$$P(\nu_\alpha \to \nu_\alpha) = 1 - \sin^2 2\theta \sin^2\left(\frac{(1.27\Delta m^2(\mathrm{eV}^2)L_\nu(\mathrm{km})}{E_\nu(\mathrm{GeV})}\right) \tag{1.10}$$

where $\Delta m^2 \equiv m_j^2 - m_i^2$ is the mass-squared difference of the neutrino mass eigenstates. Therefore, if the neutrino mass states mix ($\theta \neq 0$) and possess different masses ($\Delta m^2 > 0$), neutrinos change flavors during flight. This phenomenon is called "neutrino oscillation". The existence of neutrino oscillation is evidence of the finite neutrino mass. The amplitude of oscillation is determined by the mixing angle θ. The L/E dependence of the oscillation probability is characterized by Δm^2. The precision for θ depends on the statistics around the first maximum of the oscillation,

$$\frac{1.27\Delta m^2 L_\nu}{E_\nu} = \frac{\pi}{2}. \tag{1.11}$$

The precision for Δm^2 depends on the resolution of L_ν/E_ν.

1.3 Neutrino Oscillation Experiments

Up to now, a number of experiments have searched for neutrino oscillation. The neutrino oscillation experiments are categorized into the following four types according to their neutrino sources; atmospheric neutrino experiment, solar neutrino experiment, reactor neutrino experiment and accelerator neutrino experiment. We summarize each type of the experiment and the results.

1.3.1 Atmospheric neutrino experiments

When primary cosmic rays interact with air nuclei in the atmosphere of the Earth, secondary particles, mainly pions and some kaons, are produced in hadronic showers. Atmospheric neutrinos are produced from the decay of those particles, mainly through the following reactions of charged pions:

$$\begin{array}{c} \pi^\pm\ (K^\pm) \to \mu^\pm + \overset{(-)}{\nu}_\mu \\ \downarrow \\ \mu^\pm \to e^\pm + \overset{(-)}{\nu}_\mu + \overset{(-)}{\nu}_e \end{array} \tag{1.12}$$

The flight length of atmospheric neutrinos detected in an underground detector ranges from $\sim$ 15 km to $\sim$ 13000 km depending on the zenith angle of the arrival direction. The energy spectrum is widely distributed from $\sim$ 100 MeV to above TeV with a peak energy of $\sim$ 1GeV. Therefore, the L/E of the atmospheric neutrinos stretches from $\mathcal{O}(1) \sim \mathcal{O}(10000)$. The sensitivity for Δm^2 reaches to the $10^{-5}[\mathrm{eV}^2]$ level.

After indications from several experiments [19–23], the first confident evidence for oscillation of atmospheric neutrinos was reported by the Super-Kamiokande (SK) experiment in 1998 [24]. The observed zenith angle distribution of muon neutrinos can not be explained without neutrino oscillation. Subsequently, the SK group directly confirmed neutrino oscillation by observing the first oscillatory signature in the L/E distribution in 2003 [25]. At present, the atmospheric neutrino observations are well explained by the hypothesis of a quasi-two-neutrino oscillation of $\nu_\mu \leftrightarrow \nu_\tau$ with $\Delta m^2_{\mathrm{atm}}$ and a mixing angle θ_{atm} in the ranges:

$$\begin{aligned} 1.9\times10^{-3} < \Delta m^2_{\mathrm{atm}} < 3.1\times10^{-3}\ [\mathrm{eV}^2], \\ \sin^2 2\theta_{\mathrm{atm}} > 0.90 \end{aligned} \tag{1.13}$$

at 90% confidence level (CL).

1.3.2 Solar neutrino experiments

Neutrinos produced in the sun are detected on the earth by several experiments. The nuclear processes that power the sun make only ν_e, not ν_μ or ν_τ. The neutrino energy spectrum of the solar neutrinos ranges from 0 to 15 MeV. The distance between the sun and the earth is $\sim 10^8$ km. The solar neutrino experiments are sensitive down to $\Delta m^2 \sim 10^{-11}\mathrm{eV}^2$, and up to $\Delta m^2 < 10^{-3}\mathrm{eV}^2$ with the MSW effect. Solar neutrino experiments observe lack of the solar ν_e flux arriving at the earth [26–31]. Now, thanks especially to the SK and Sudbury Neutrino Observation (SNO) [32], we have evidence that the missing ν_e changes into neutrinos of other flavors. The combination of the SK results with the SNO results constrain the parameter region as follows.

$$\begin{aligned} 3.2\times10^{-5} < \Delta m^2_{\mathrm{sol}} < 10.4\times10^{-5}\ [\mathrm{eV}^2], \\ 0.37 < \tan^2\theta_{\mathrm{sol}} < 0.54 \end{aligned} \tag{1.14}$$

1.3.3 Reactor neutrino experiments

Long baseline $L \sim \mathcal{O}$ (100km) experiment

The LMA-MSW interpretation of solar neutrino observation implies that a substantial fraction of reactor $\bar{\nu_e}$ oscillate into the other flavors after travelling more than a hundred kilometers. The KamLAND experiment [33] with a typical baseline of $\sim$ 180 km observed both the $\bar{\nu_e}$ flux decrease from the expectation without $\bar{\nu_e}$ oscillation and the spectral distortion as expected from the LMA-MSW solution. A global fit to both the solar and KamLAND data strongly constrains the oscillation parameters;

$$\begin{aligned} 7.4\times10^{-5} < \Delta m^2_{\mathrm{sol}} < 8.5\times10^{-5}\ [\mathrm{eV}^2], \\ 0.33 < \tan^2\theta_{\mathrm{sol}} < 0.50 \end{aligned} \qquad (\mathrm{Solar} + \mathrm{KamLAND}) \tag{1.15}$$

As shown in Equation (1.14) and (1.15), the sensitivity in Δm^2 is dominated by the KamLAND data because the observed L/E distribution of the oscillation probability directly constrains Δm^2, while the solar neutrino data constrains $\sin^2 2\theta$ more thanks to the MSW effect in the sun.

Short baseline $L \sim \mathcal{O}$ (1km) experiments

The atmospheric and solar neutrino results imply another type of oscillation, $\nu_e \to \nu_x$ at the $\Delta m^2_{\rm atm}$ region. Some reactor experiments with the baseline of ~ 1 km search for oscillation. No evidence of oscillation is found. An upper limit on the mixing angle is set at $\sin^2 2\theta < 0.1$ in the region of $\Delta m^2 > 3\times10^{-3}{\rm eV}^2$ at 90% CL [34–36].

1.3.4 Accelerator neutrino experiments

Accelerator-produced neutrinos are also available to explore neutrino oscillation. The energy of the neutrinos ranges from ∼50 MeV to 100 GeV, and the flight length of the neutrinos varies from several tens meters (short-baseline experiments) to several hundred kilo-meters (long-baseline experiments). The short-baseline experiments have sensitivities in the Δm^2 above the ${\rm eV}^2$ scale. The sensitivities of the long-baseline experiments reach down to $\Delta m^2 > 10^{-3}{\rm eV}^2$ region.

Short baseline $L \sim \mathcal{O}$ (1km) experiments

There was no definite theoretical guidance for the neutrino mass and mixing angle, and also no data indicating neutrino oscillation in the past. There was a hint that the dark matter might be neutrinos if neutrinos were massive. Assuming that the dark matter is fully attributed to the massive neutrinos, the heaviest neutrino mass is expected to be greater than several eV. This is a main motivation of the short-baseline experiments.

Among a number of experiments, only LSND reported a positive signal of neutrino oscillation, $\overset{(-)}{\nu}_\mu \to \overset{(-)}{\nu}_e$, with Δm^2 around $\sim {\rm eV}^2$ in 1996 [37,38], although the KARMEN experiment [39,40] with a similar sensitivity did not observe the positive evidence. The MiniBooNE experiment [41], searches for the $\nu_\mu \to \nu_e$ oscillation in order to confirm or reject the LSND result.

Long baseline $L \sim \mathcal{O}$ (100km) experiment

In order to confirm atmospheric neutrino oscillation, an experiment using an accelerator neutrino beam with the baseline more than $\mathcal{O}$ (100km) is conducted. The KEK-to-Kamioka (K2K) long baseline neutrino oscillation experiment (KEK-PS-E362) is the first experiment to search for the $\nu_\mu \to \nu_\tau$ oscillation dominated by the atmospheric mass-squared difference. Thanks to the good L/E resolution of $\sim 10\%$, K2K has an advantage in Δm^2 measurement. In addition, the good L/E resolution is useful to distinguish neutrino oscillation from the other hypothesis which predicts a different transition probability. K2K also searches for the evidence of $\nu_\mu \to \nu_e$ oscillation at the $\Delta m^2_{\rm atm}$. The signal of $\nu_\mu \to \nu_e$ oscillation is not observed so far [42].

1.3.5 Summary of neutrino oscillation experiments

As described above, a number of neutrino oscillation experiments have been performed, and some experiments observe strong evidence for oscillation phenomenon. These experiments provide the results in the form of the allowed or excluded region of oscillation parameters. Figure 1.1 summarizes the allowed or excluded neutrino oscillation parameter regions from various experiments. There are now two confirmed allowed regions, called "solar sector" and "atmospheric sector":

1. Solar sector $(\nu_e \leftrightarrow \nu_\mu/\nu_\tau)$: $\Delta m^2 \sim 8\times10^{-5}{\rm eV}^2$ $\theta \sim 30^\circ$
2. Atmospheric sector $(\nu_\mu \leftrightarrow \nu_\tau)$: $\Delta m^2 \sim 2.5\times10^{-3}{\rm eV}^2$ $\theta \sim 45^\circ$

The K2K experiment, which is the main subject of this thesis, is conducted to test the atmospheric sector by artificially produced neutrino beam.

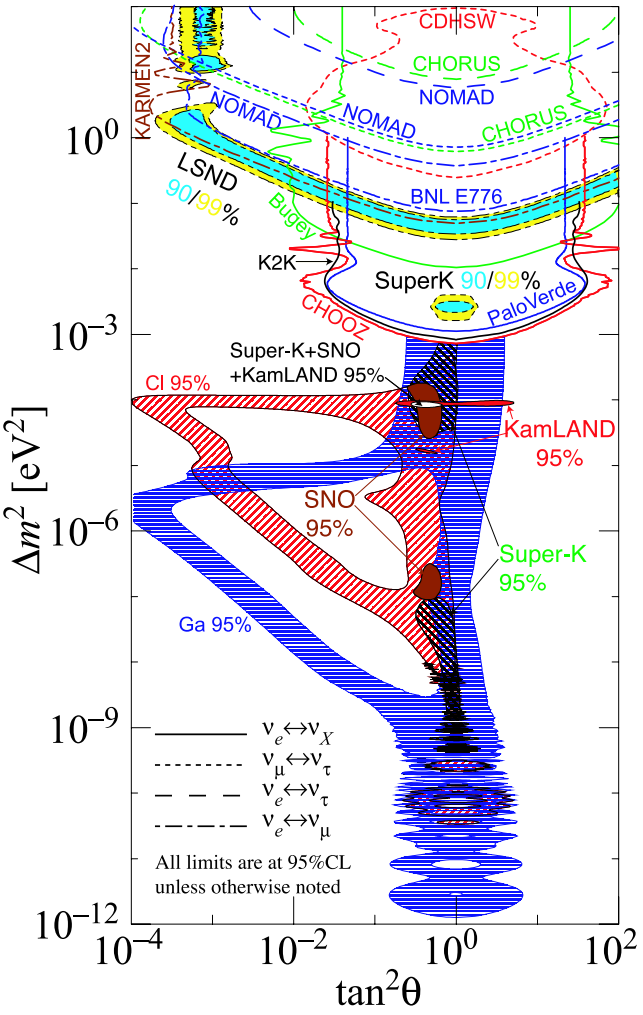

Figure 1.1: The regions of mass-squared difference and mixing angle favored or excluded by various experiments.

1.4 Outline of This Thesis

The purpose of the study presented in this thesis is to determine neutrino oscillation parameters with the whole K2K data set, corresponding to 9.2×10^{19} protons on target. In addition to the increased statistics compared with the previous result [43, 44], the following physics is newly studied.

- **Cross section measurement of charged current coherent pion production**
  We report the first result of the cross section measurement for charged-current (CC) coherent pion production ($\nu_\mu + A \to \mu^- + \pi^+ + A$) in the energy region of a few GeV. This study is performed with a fully active scintillator-bar detector (SciBar). No evidence of this interaction is observed, and the upper limit of the cross section is set. The neutrino interaction models re-tuned by this result well explain the significant deficit of the events with a forward going muon reported by the previous K2K analysis [43, 44]. As a result, the reliability for the neutrino interaction models is improved by this study.

- **Test for non-standard model**
  There are many other models proposed for atmospheric ν_μ disappearance besides mass-induced neutrino oscillation. Especially, the neutrino decay [45] and neutrino decoherence [46] models recently got attention because they can also explain the SK observation [24]. We also test the validity of the alternative models as well as neutrino oscillation.

The dissertation consists of four parts.

Part-I (Chapter 2 - 4): Introduction to K2K Experiment

The K2K experiment is presented in Chapter 2–4. We explain the experimental techniques to study neutrino oscillation, the experimental apparatus, the Monte-Carlo simulation and data set used in this thesis.

Part-II (Chapter 5 - 7): First experimental limit of CC coherent pion production

This part is dedicated to the study of CC coherent pion production with the SciBar detector. First, the design of SciBar detector, the basic performance and the data analysis are presented in Chapter 5 and Chapter 6. Then, the cross section measurement of CC coherent pion production is presented in Chapter 7.

Part-III (Chapter 8 - 11): Neutrino oscillation analysis

Neutrino oscillation analysis is performed. The measurements of neutrino beam properties before neutrinos oscillate are presented in Chapter 8. The detection of the accelerator-produced neutrinos in SK is described in Chapter 9. Neutrino oscillation phenomenon is tested by comparing the SK observation with the expectations without oscillation. After neutrino oscillation is confirmed, the oscillation parameters are determined in a two flavor oscillation scenario in Chapter 10. The non-standard ν_μ disappearance models are also tested here. In Chapter 11, we discuss some possible ideas for improvements of sensitivity for neutrino oscillation in K2K and compare our result with the atmospheric neutrino results.

Part-IV (Chapter 12): Conclusion

The dissertation is concluded in Chapter 12.

Chapter 2

Experimental Technique

We describe experimental techniques to search for neutrino oscillation and to measure the oscillation parameters in the K2K experiment.

2.1 Signatures

In a framework of two-flavor oscillation of $\nu_\mu \leftrightarrow \nu_\tau$ suggested by the SK atmospheric neutrino results, the survival probability of ν_μ is expressed as

$$P(\nu_\mu \rightarrow \nu_\mu) = 1 - \sin^2 2\theta \sin^2 \left(\frac{(1.27\Delta m^2(\mathrm{eV}^2) L_\nu(\mathrm{km})}{E_\nu(\mathrm{GeV})} \right). \tag{2.1}$$

When ν_μs oscillate into ν_τs in flight, the following signatures are observed in K2K.

- **Deficit of the events**
  Because the K2K neutrino energy is below the threshold of ν_τCC interaction, the oscillated ν_τs do not react through CC interaction. Therefore, the deficit of the number of neutrino events is observed.

- **Energy spectrum distortion**
  Since the flight length of ν_μs, L_ν, is fixed at 250 km, the survival probability depends on neutrino energy. The neutrino energy spectrum is distorted according to Equation (2.1) as shown in Fig. 2.1, where we assume the oscillation parameters of $(\sin^2 2\theta, \Delta m^2) = (1.00, 0.0030\ \mathrm{eV}^2)$. In the bottom figure of Fig. 2.1, the depth of the first dip corresponds to $\sin^2 2\theta$ and the energy at the dip position corresponds to Δm^2.

In K2K, the oscillation analysis is performed by using these two signatures.

2.2 Characteristics of the K2K Experiment

We briefly summarize the main characteristics of the K2K experiment.

- **Accelerator-produced neutrinos**
  We monitor and control the neutrino beam by measuring the primary protons, secondary pions and muons, and neutrinos. This leads to a better understanding of the neutrino source compared with atmospheric neutrinos.

- **Sensitivity around $\Delta m^2 \sim 10^{-3} - 10^{-2}\mathrm{eV}^2$**
  As described in the previous chapter, atmospheric neutrino data asserts $\nu_\mu \leftrightarrow \nu_\tau$ oscillation in this Δm^2 region. By using neutrinos with the mean energy of 1.3 GeV and a baseline of 250 km, the sensitivity reaches in the relevant Δm^2 region of $10^{-3} \sim 10^{-2}\mathrm{eV}^2$.

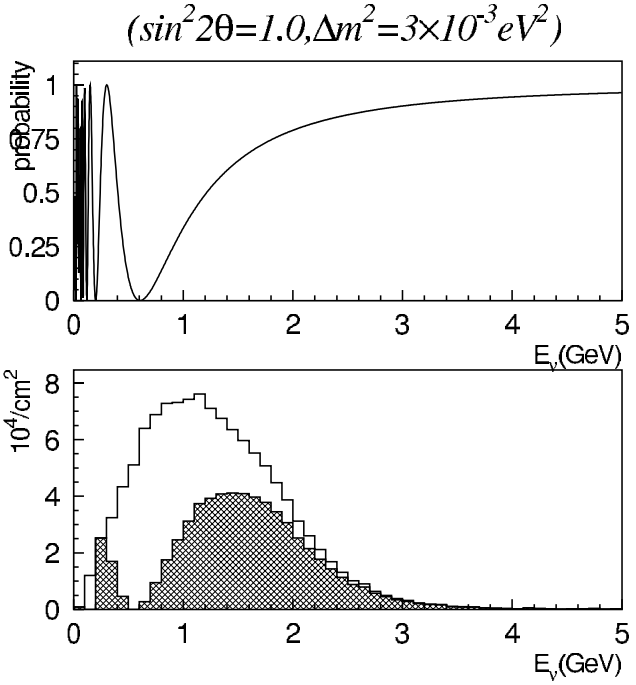

Figure 2.1: Expected distortion of the neutrino energy spectrum at Super-K assuming $(\sin^2 2\theta, \Delta m^2) = (1.00, 0.0030\ \mathrm{eV}^2)$. In the bottom figure, the neutrino energy spectrum distorted by oscillation (hatched histogram) are compared with that for null oscillation case (open histogram). The top figure shows the survival probability as a function of E_ν.

- **Large far detector**
  Thanks to the world's largest water Cherenkov detector, Super-Kamiokande (SK), we typically expect the 0.4 events per day without oscillation.

- **Timing synchronization**
  SK is continuously taking data of atmospheric neutrinos at the rate of ~ 8 events/day. We produce neutrinos only for a 1.1 μsec every 2.2 sec and select the SK events synchronized with the beam timing. The background rate of atmospheric neutrinos is suppressed by the order of 10^{-6}.

- **Simultaneous measurement at the near and the far site**
  We install a set of neutrino detectors at about 300 m downstream from the production target as near detectors (ND). The purpose of ND is to measure the neutrino beam properties, such as neutrino flux and energy spectrum, before neutrinos oscillate. The uncertainties in the flux and spectrum shape of the neutrino beam, and the cross section of neutrino-nucleus interaction are largely canceled out by comparing the observations in SK with the measurements in ND.

2.3 Measurements in the K2K Experiment

We explain how to perform the study of neutrino oscillation in the K2K experiment and importance of understanding of neutrino-nucleus interaction.

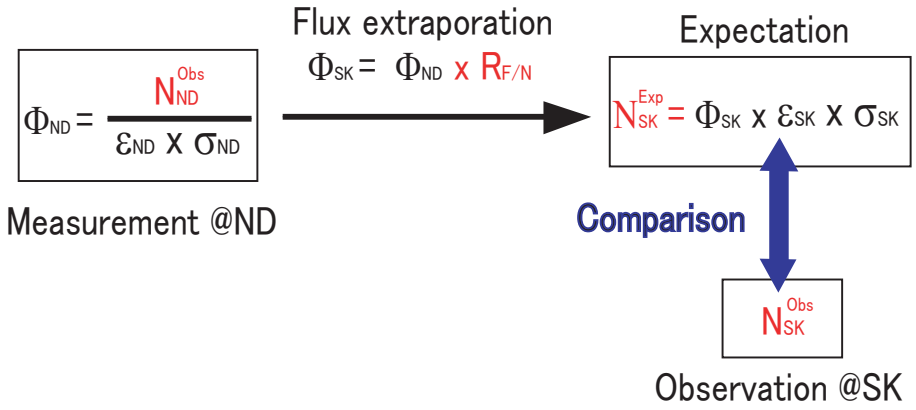

Figure 2.2: A simple flow of number of event analysis.

2.3.1 The number of events (Normalization) analysis

We explain a flow of the analysis using deficit of the number of events in Fig. 2.2. This analysis consists of the following three steps.

1. Measurement of the number of neutrino events at the near site

The number of neutrino events at the near site, $N_{\rm ND}^{\rm Obs}$, is counted to derive the neutrino flux before oscillation, $\Phi_{\rm ND}$. The neutrino interaction cross section, $\sigma_{\rm ND}$, and neutrino detection efficiency, $\epsilon_{\rm ND}$, are evaluated with neutrino-nucleus interaction models and a detector simulation. The measurement is performed with a similar detector to SK, a one-kiloton water Cherenkov detector (1KT), in order to cancel out a large part of the uncertainties on the cross section and the detection efficiency by comparison.

2. Extrapolation of the neutrino flux from the near to far site

The neutrino flux at SK, $\Phi_{\rm SK}$, is extrapolated from that at the near site by multiplying the flux ratio of the far site to the near site, $R_{\rm F/N}(E_\nu)$. The flux ratio is evaluated by a Monte Carlo simulation, and is experimentally confirmed [47].

3. Comparison between the prediction and the observation in the far site

The number of events in SK, $N_{\rm SK}^{\rm Exp}$, is estimated by using the extrapolated flux, selection efficiency ($\epsilon_{\rm SK}$), and neutrino interaction cross section ($\sigma_{\rm SK}$). When the number of observed events, $N_{\rm SK}^{\rm Obs}$, is smaller than the prediction, this means ν_μ disappearance. In addition, the oscillation parameters are determined so that the expectation of oscillation matches with the observation.

2.3.2 Spectrum shape analysis

Figure 2.3 shows a flow of the analysis of spectrum distortion. This analysis consists of the following three steps.

1. Measurement of the E_ν spectrum at the near site

The neutrino energy spectrum is measured with charged current quasi-elastic (QE) interaction ($\nu_\mu + n \to \mu + p$). QE is the dominant process in our neutrino energy region. Assuming QE

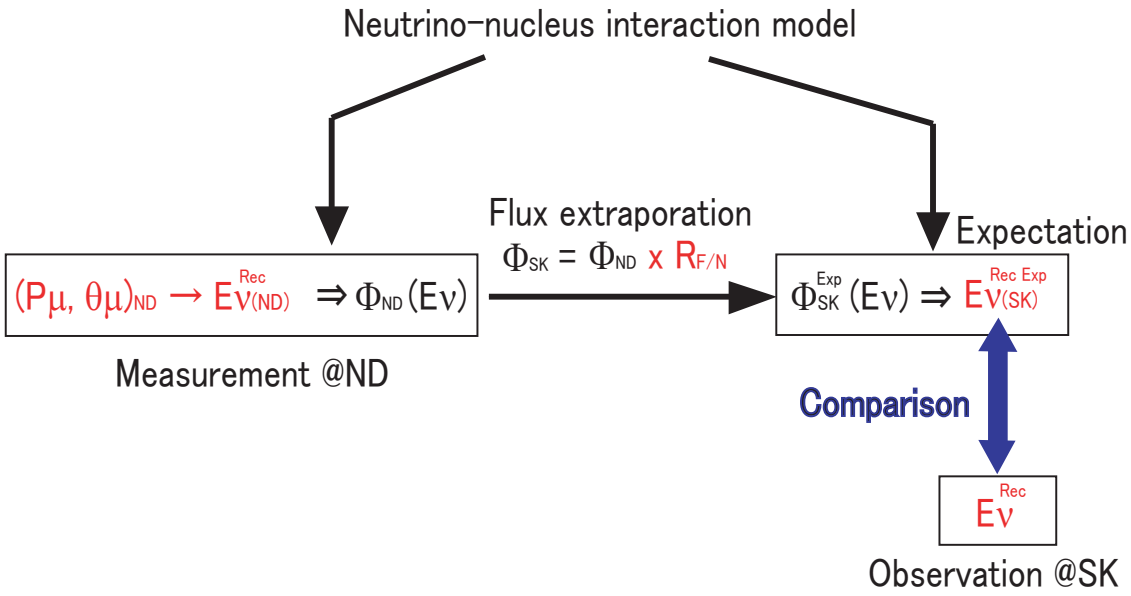

Figure 2.3: A simple flow of spectrum shape analysis.

interaction, the parent neutrino energy is reconstructed from the muon momentum (p_μ) and the angle with respect to the beam direction (θ_μ) as

$$E_\nu^{\rm rec} = \frac{1}{2}\frac{(M_p^2 - m_\mu^2) + 2E_\mu(M_n - V) - (M_n - V)^2}{-E_\mu + (M_n - V) + p_\mu \cos\theta_\mu} \tag{2.2}$$

where M_p, M_n, m_μ, E_μ, V are the proton mass, the neutron mass, the muon mass and muon energy and nuclear potential set at 27 MeV, respectively. In order to derive the true neutrino energy from $E_\nu^{\rm rec}$, the understanding of neutrino nucleus interaction is important. The neutrino energy spectrum at the near site, $\Phi_{\rm ND}(E_\nu)$, is derived from the (p_μ, θ_μ) two-dimensional distribution by using the neutrino-nucleus cross section and a detector simulation.

2. Extrapolation of the neutrino flux from the near to far site.

This step is the same as that explained in 2.3.1.

3. Comparison between the prediction and the observation in the far site

In SK, the QE events are detected as an event with only one muon-like Cherenkov ring (1Rμ) because the proton is typically below Cherenkov threshold. The $E_\nu^{\rm rec}$ distribution is measured using the QE candidate (1Rμ) sample. The observed $E_\nu^{\rm rec}$ is compared with the expectation, $E_{\nu({\rm SK})}^{\rm Rec\ Exp}$. The disagreement of $E_\nu^{\rm rec}$ distribution is evidence of neutrino oscillation. In addition, the oscillation parameters are determined to match the expectation with the observation.

2.3.3 Neutrino-nucleus interaction study

In the oscillation analysis, the neutrino detection efficiency in each detector and the fraction of the non quasi-elastic (nonQE) events in the samples are crucial information. Because they are affected by neutrino-nucleus interaction, such as the interaction cross section and the kinematics of secondary particles, the knowledge of neutrino-nucleus interaction is indispensable.

In the K2K experiment, we construct a fine-grained detector (FGD) system in the near site to better understand neutrino interaction. FGD provides the following two measurements.

1. Measurement of the nonQE to QE cross section ratio.

In the spectrum analysis, the neutrino energy should be reconstructed correctly. However, the $E_\nu^{\rm rec}$ of the nonQE event is lower than true energy because of the missing particles in the reconstruction. The fraction of the nonQE components in the QE candidate sample should be correctly evaluated since the $E_\nu^{\rm rec}$ distribution is affected by the nonQE fraction. The cross section ratio of nonQE to QE interaction is measured using FGD together with 1KT.

2. Cross section measurement of CC coherent pion production.

K2K reports a significant deficit of the events with a forward going muon [43, 44]. The charged current coherent pion production, $\nu_\mu + A \to \mu^- + \pi^+ + A$, is one of the candidate interactions causing the deficit. Consequently, we measure the cross section with a one of the FGD detectors, SciBar. This is the first experimental measurement of this interaction in the neutrino energy region of a few GeV. No evidence for coherent pion production is observed contrary to the theoretical prediction. The neutrino interaction models re-tuned by this result are used for the oscillation analysis. This study is a main topic in this thesis as well as the oscillation analysis.

2.4 Expected Sensitivity of the K2K Experiment

Rejection of null oscillation

We use the Monte Carlo simulation (virtual experiments) to check the rejection power of null oscillation if neutrino oscillation exists. Here, we assume the oscillation parameters of $(\sin^2 2\theta, \Delta m^2) = (1.0, 2.8 \times 10^{-3}{\rm eV}^2)$ and neutrino data corresponding to the total number of protons on target of 9.2×10^{19}. Under this assumption, we can reject the null oscillation hypothesis at 99.994% CL (4.02σ) level.

Sensitive parameter region

Figure 2.4 shows the sensitivity of the K2K experiment calculated by the method in PDG [48]. The sensitivity covers the allowed region reported by the atmospheric neutrinos.

2.5 History of the K2K Experiment

We summarize a history of the K2K experiment in Table 2.1. The K2K experiment was proposed in 1995 to confirm atmospheric neutrino oscillation [49]. The civil construction of the beamline and detectors started in 1996. The construction completed in 1998. The test operations of the beam and horn system were done in early 1999. From June 1999, physics data-taking started with the horn current of 200kA. This period is referred to as 'K2K-Ia'. The first K2K neutrino event was observed at SK on June 19th, 1999. From November 1999 to July 2001, the horn was operated with 250kA. This period is called 'K2K-Ib'. In November 2001, a severe accident happened in Super-Kamiokande, and more than half of PMTs were broken. To resume K2K, we re-built the SK detector quickly with half of PMTs[1]. We restarted the data-taking from January 2003 (K2K-IIa). Before the K2K-IIa period, the lead glass calorimeter was removed. After the K2K-IIa run, in the summer in 2003, a new near detector, SciBar was installed. From October 2003, data-taking was started together with SciBar, and continued until November 2004. The period until February in 2004 is referred to as K2K-IIb and the rest of the period as K2K-IIc,

[1] I took the reconstruction shift only 2 weeks fewer than other collaborators because I was hospitalized for a while. I thank kind persons who took the shift instead of me.

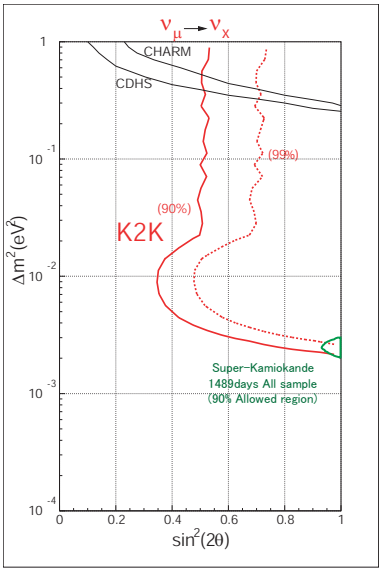

Figure 2.4: Sensitivity to the $\nu_\mu \rightarrow \nu_\tau$ oscillation in the K2K experiment. The vertical and the horizontal axis are $\Delta m^2[\mathrm{eV}]^2$ and $\sin^2 2\theta$, respectively. The red lines show the sensitivity contours of the K2K experiment with the confidence levels of 90% (solid line) and 99% (dotted line).

Table 2.1: History of K2K.

1995	Proposal was approved at KEK.
1996	Civil construction started.
1999 Jun.	Data taking with the horn current of 200kA. (K2K-Ia)
1999 Nov.– 2001 Jul.	Data taking with the horn current of 250kA. (K2K-Ib)
2001 Nov.	SK accident. Removal of LG.
2003 Jan.– 2003 Jun.	Data taking with a half PMT density of SK. (K2K-IIa)
2003 Jul.– 2003 Sep.	Construction of SciBar.
2003 Oct.– 2004 Nov.	Data taking with SciBar (K2K-IIb – K2K-IIc)
2004 Nov.–	1st magnetic horn was broken and K2K was finished

respectively. In November 2004, the first magnetic horn was broken, and the K2K experiment was finished with accumulation of almost all of the planned neutrino data, 10^{20} protons on target.

Chapter 3

Experimental Apparatus and Data Set

The K2K experimental facility consists of the neutrino beam-line, the near detector system, and the far detector, Super-Kamiokande.

3.1 Neutrino Beam Line

We describe each component of the K2K neutrino beam-line. Detailed description is found in [44, 47, 50–52].

3.1.1 Primary proton beam

The primary proton beam is extracted from the 12 GeV Proton Synchrotron (KEK-PS) at KEK (High Energy Accelerator Research Organization). A schematic view of KEK-PS is shown in Fig. 3.1 and its specifications are summarized in Table 3.1. The KEK-PS provides $\sim 6 \times 10^{12}$ protons per spill every 2.2 second in a 1.1 μsec spill width. Protons are bent to the direction of SK, and hit on an aluminum target. The intensity and spatial profile of the proton beam are monitored by using current transformers (CT) and segmented planes ionization chambers (SPIC) installed in the beam line. Figure 3.2 shows the accumulated number of protons on the target (POT) monitored by CT from June 1999 to November 2004. In total, 104.67×10^{18} protons are delivered on the target to generate the neutrino beam.

3.1.2 Target and horn magnets system

The aluminum target of 3 cm in diameter (2 cm in June 1999) and 66 cm in length, is embedded inside of a magnetic horn system. The horn is operated every 2.2 seconds with a 2 msec long 250 kA pulsed current (200kA in June 1999). The positive-charged secondary particles, mainly π^+, are focused to the SK direction. The pions enter a 200 m long decay volume and decay to ν_μ and muon. The produced neutrino beam is 98% pure ν_μ with a mean energy of 1.3 GeV.

3.1.3 Secondary beam monitors

We monitor the energy spectrum, direction and yield of neutrino beam by measuring the pions and, the muons from the pion decay together with ν_μ. The apparatus called pion monitor (PIMON) and muon monitor (MUMON) are described below.

Accelerator components	Pre-injector (750 keV, Cockroft-Walton acc.) LINAC (40 MeV) BOOSTER (500 MeV) Main ring (12 GeV in kinematic energy)
Operation mode for K2K	fast extraction (single turn) to EP1-A
Typical intensity in main ring	7×10^{12} protons per spill
Typical intensity after extraction	6×10^{12} protons per spill
Typical intensity at the target	5.5×10^{12} protons per spill
Number of bunches	9
Bunch spacing	125ns
Total spill length	1.1 μsec
Repetition cycle	2.2 sec

Table 3.1: Specification summary of KEK-PS for K2K experiment.

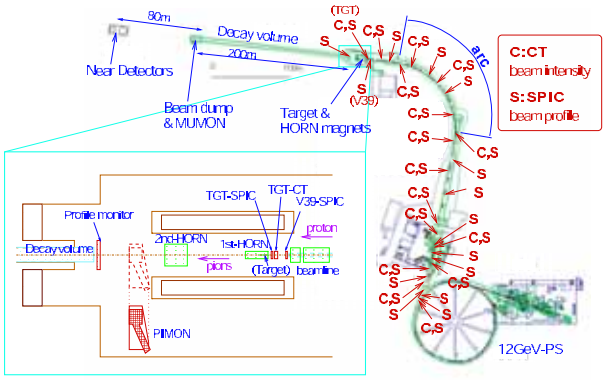

Figure 3.1: A schematic view of KEK-PS and the neutrino beam line. The characters 'C' and 'S' mean the CT and the SPIC, respectively.

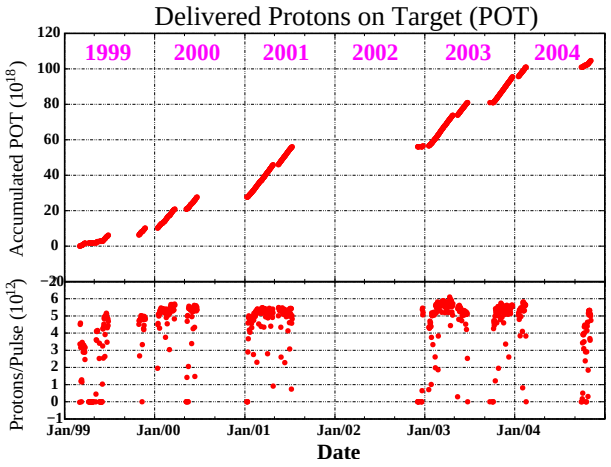

Figure 3.2: Accumulated number of protons on the target, measured by CT in front of the target.

Pion Monitor (PIMON) [47, 52]

PIMON is a gas Cherenkov detector used to measure the pion momentum (p_π) and the pion angle with respect to the beam direction (θ_π) just downstream of the horn system. We can predict the neutrino energy spectrum at any location from the (p_π, θ_π) distribution since the decay kinematics of the two-body pion decay is completely understood. Thus, the ratio of neutrino spectra between KEK and SK called "far/near ratio" is estimated based on the PIMON data. In the analysis, the PIMON measurement is used to validate the far/near ratio calculated by the beam-MC simulation.

Muon Monitor (MUMON) [47, 50, 52]

We measure the yield and profile of muons spill-by-spill with MUMON. MUMON is placed in a pit at the downstream of the beam dump. MUMON consists of two parts; an ionization chamber (ICH) and a silicon pad detector (SPD) array. We control the profile center of muons to the SK direction within 1 mrad during the experiment with ICH. We monitor the muon yield stability with SPD.

Detector	Total mass (ton)	Target	purpose
1KT	$\sim$ 1000	water	Flux, spectrum
SciFi	6.0	water	interaction study and spectrum
Lead Grass (-2001)		—	ν_e flux
SciBar (2003-)	15	CH_n	interaction study and spectrum
MRD	864	Fe	beam direction and rate stability

Table 3.2: The components of the K2K near detectors.

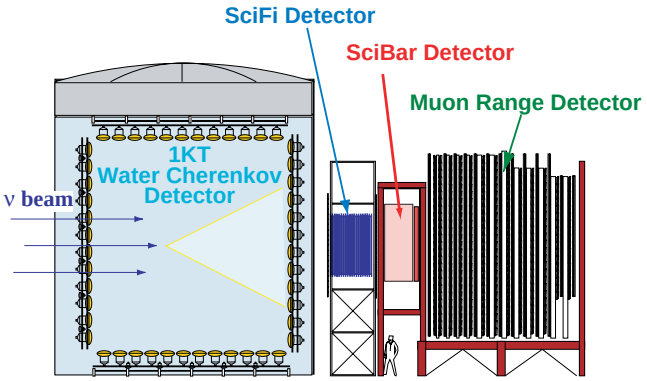

Figure 3.3: A schematic view of the K2K-IIb near detectors. From upstream, 1KT, SciFi, SciBar and MRD are arranged. The lead grass calorimeter was located at the position of SciBar in K2K-I.

3.2 Near Detectors

The near neutrino detectors (ND) are placed about 300 m downstream of the target in the underground cylindrical hall of 24 m in diameter and 16 m in depth. The main purpose of ND is to measure the beam direction, the flux and energy spectrum of neutrino beam before neutrinos oscillate. ND also provides the measurements of neutrino-nucleus interaction, which are necessary inputs for the neutrino oscillation study. The components and schematic view of ND is shown in Table 3.2 and Fig. 3.3.

ND is comprised of two detector systems; a water Cherenkov detector (1KT) and a fine-grained detector (FGD) system. FGD consists of a scintillating-fiber tracker (SciFi), the lead grass calorimeter in K2K-I, a fully-active fine-segmented scintillator-bar tracker (SciBar) since K2K-IIb and a muon range detector (MRD).

The direction of ν_μ beam is measured with MRD by using neutrinos. The flux normalization is measured by 1KT to estimate the expected number of events at the far detector. The energy spectrum is measured by both 1KT and FGD. 1KT has a high efficiency for muons below 1.0 GeV/c, and full 4π coverage in solid angle. However, 1KT has little efficiency for muons above 1.5 GeV/c when we require that the muons stop inside the 1KT detector. On the other hand, FGD has high efficiency for muons above 1 GeV/c. Thus, the two detector systems are complementary to cover the relevant neutrino energy region.

We describe each detector element in the following.

3.2.1 The 1kt ring imaging water cherenkov detector (1KT)

A 1kt ring imaging water cherenkov detector (1KT) is a cylindrical tank, 10.8 m in diameter and 10.8 m in height, holding approximately 1000 tons of pure water. The tank itself is re-used

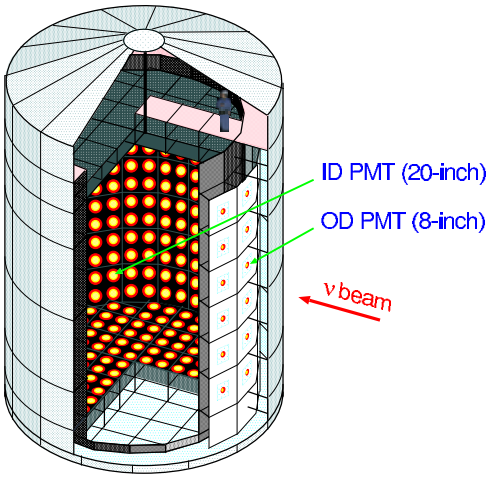

Figure 3.4: A schematic view of the 1kt water cherenkov detector

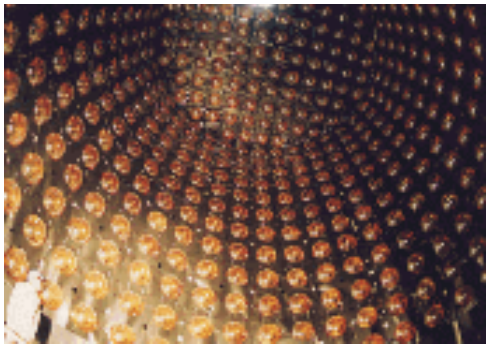

Figure 3.5: A photograph of the inner detector viewed from the bottom.

from the KEK-PS E261A experiment [53]. A schematic drawing of 1KT is shown in Fig. 3.4. The detector is optically separated into two regions, the inner detector (ID) and the outer detector (OD), by black sheets and Tyvek sheets. The ID volume is a cylinder of 8.6 m in diameter and 8.6 m in height and viewed by 680 inward facing 50 cm PMTs, giving a 40% photocathode coverage. The OD has 68 PMTs of a 20 cm diameter to identify the incoming particles. Figure 3.5 shows a photograph of ID.

The electron and muon separation is performed based on the pattern and the opening angle of the ring image. According to the Monte Carlo (MC) simulation, 0.7 % of muon neutrino events with single-ring is mis-identified as electron-like (e-like) events, and 3.7 % of electron neutrino events are mis-identified as muon-like (mu-like) events. The momentum of each particle is reconstructed with the light yield inside the cherenkov ring. The resolution of muon momentum (p_μ) is estimated to be $2.0 \sim 2.5$ %. The momentum scale error is evaluated to be $^{+2.0}_{-3.0}$ %. The stability of the momentum scale is monitored and confirmed that it is better than 1 %. The details of 1KT are described in [52, 54].

3.2.2 Scintillating fiber tracker (SciFi)

A scintillating fiber tracker (SciFi) is located downstream of 1KT. Figure 3.6 shows a schematic view of the SciFi detector. SciFi has 20 scintillating fiber layers perpendicular to the beam direction. Each layer consists of vertical and horizontal scintillating fiber sheets. Each fiber layer is 9 cm apart. Water filled tanks made of 0.18 cm thick aluminum are inserted between the fiber layers. The scintillating fiber used in SciFi is 3.7 m long and 0.692 mm diameter coupled to image-intensifier tubes with a CCD camera.

The position resolution, the hit finding efficiency and the track finding efficiency for the track with hits more than five layers are evaluated to be 0.8 mm, 92 $\pm$ 2 %, and 98 $\pm$ 2 %, respectively. The detailed description for SciFi performances is found in [55–58].

3.2.3 Scintillator-bar tracker (SciBar)

A fully-active scintillator-bar detector (SciBar) is installed in summer 2003 in the place of LG to study neutrino interaction with the better sensitivity. The details are described in the next chapter.

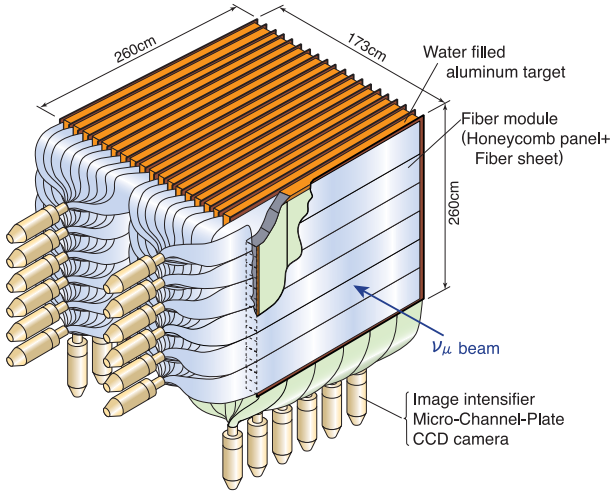

Figure 3.6: Schematic view of SciFi.

3.2.4 Muon range detector (MRD)

A muon range detector (MRD) [59] is located at the most downstream of the near detector system. It consists of vertical and horizontal drift-tube layers interleaved with iron absorber. The size of the layer is approximately 7.5 m × 7.6 m. In order to get a better muon energy resolution, the four iron plates in the upstream side are 10 cm thick, and the other eight planes are 20 cm thick. MRD covers up to 2.8 GeV/c muons, which corresponds to 95% of all the muons in neutrino interaction. The mass of iron is 864 tons and the mass of drift tubes is 51 tons. The basic performance of MRD is summarized in Table 3.3.

Item	Performance
Hit efficiency	97%
Spatial resolution	2 mm
Track finding efficiency	97.5% (>3 planes)
Energy threshold	250 MeV
Energy resolution	150 MeV
Angle resolution	8 degree
Vertex resolution	10 cm

Table 3.3: The detector performance of the muon range detector.

3.3 Far Detector: Super-Kamiokande (SK)

The far detector, Super-Kamiokande (SK), is the world's largest water Cherenkov detector, with a mass of 50,000 tons. SK is located in the Mozumi mine of Kamioka Mining and Smelting Company, near the village of Higashi-Mozumi, Gifu, Japan. It is 250 km far from KEK. The detector cavity lies under the peak of Mt. Ikenoyama, with 1,000 meters of rock, or 2,700 meters-water-equivalent (m.w.e.) to reduce the cosmic ray muon flux. The observed muon flux is $6 \times 10^{-8}\mathrm{cm}^{-2}\mathrm{s}^{-1}\mathrm{sr}^{-1}$. The SK started data taking on April 1, 1996. There was a serious accident in 2001 as described in Section 2.5. The period before (after) the accident is called SK-I (SK-II). There are many detailed description on the particle detection, data acquisition

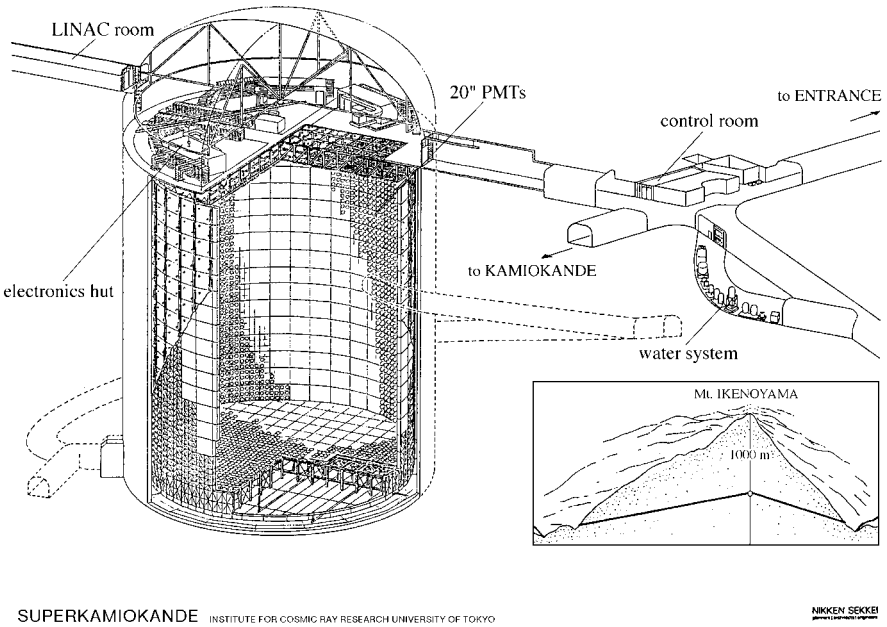

Figure 3.7: Schematic view of Super-Kamiokande.

system, event reconstruction and detector calibration in [60–66]. Here we provide only brief description on the detector configuration and the event reconstruction performance.

A schematic drawing of the SK detector is shown in Fig. 3.7. The detector is optically separated into two parts, the inner detector (ID) and the outer detector (OD), by the stainless steel structure covered by black sheets and Tyvek sheets. The size of ID is 36.2 m in height and 33.8 m in diameter, which contains 32 ktons of water. ID is viewed by 11,146 and 5182 inward-facing 50 cm PMTs, giving the 40% and 20% photo cathode coverage for SK-I and SK-II, respectively. The thickness of OD layer is 2.0 m for the side area and 2.2 m for the top and bottom area. OD volume serves as an active veto counter against incoming particles as well as a passive shield for neutrons and γ rays from the surrounding rocks. OD is instrumented with 1,885 outward-facing 20 cm PMTs, most of which are recycled from the IMB experiment [67].

The physical parameters of an event in SK such as the vertex position, the number of Cherenkov rings, particle types and momenta are reconstructed. First, the vertex position of an event is reconstructed from the PMT timing information. Then, the number of Cherenkov rings and their directions are reconstructed based on the vertex position by a maximum-likelihood procedure. Events with only one ring are called "single-ring" events, and those with greater than one ring are called "multi-ring" events. Each ring is than classified as e-like or μ-like by using its ring pattern. The vertex position of a single-ring event is refined based on the particle type. The momentum of each ring is reconstructed from the Cherenkov light intensity.

The vertex resolution of muons and electrons is evaluated to be better than 30 cm for momentum region above 300 MeV/c with the MC simulation. For the particle identification, a few % mis-ID probability is expected for both $\mu \rightarrow$ e and e $\rightarrow \mu$ with the MC simulation. The resolution of momentum and angle for muons are estimated to be 2.0%–3.0% and 2.0 degree with the MC simulation, respectively. The momentum scale uncertainty is evaluated to be 2.0% (2.1%) for SK-I (SK-II) from the various calibration sources. All the reconstruction performances of SK-I and SK-II are comparable [44].

3.4 Global Positioning System (GPS)

In the K2K experiment, time synchronization between KEK and SK is necessary to select the beam event against continuous background events from atmospheric neutrinos. Clocks at both sites need to be synchronized to within an accuracy of ~ 100 ns. We achieve the resolution of time synchronization better than 40 nsec in average by employing a Global Positioning System (GPS), with a maximum fluctuation of 150 nsec. The detailed description is found in [51, 68].

3.5 Data Set

We use the data taken in the whole K2K period with 104.67×10^{18} protons on the target in this thesis. Among these protons, those with "good beam condition" and SK being alive are selected for oscillation analysis. We also describe the neutrino beam stabilities, such as beam direction, flux and energy spectrum, monitored by MUMON and MRD.

3.5.1 Good beam spill selection

We select the good beam spills by using the beam-line monitor and GPS system. The detailed selection criteria is found in [44]. After applying the good beam spill selection, data of 92.23×10^{18} POT are remained for the analysis.

3.5.2 Beam stability during the data taking

We monitor the stabilities of the neutrino beam flux, direction and energy spectrum with MUMON on spill-by-spill basis and with MRD every a few days. The detail of the measurement is found in Appendix-A. We only present the results here.

The neutrino yield is stable for whole run period at the standard deviation of 2.5%. This is quite small compared with the statistical error in the number of events at SK of $\sim$ 10%. The neutrino beam is pointed to the direction of SK within ± 1 mrad during whole run period. This result guarantees that the flux change during whole run period is less than 1%. MRD also confirm that the muon energy and angle distributions are stable. It guarantees that the neutrino energy spectrum is stable during whole run period. Therefore, we perform the oscillation analysis in the condition that the neutrino beam is stable. Although SciBar is installed in the middle of experimental period, we extend the SciBar measurements results to whole run period because no change of neutrino beam.

Chapter 4

Monte Carlo Simulation

In this chapter, we briefly describe the monte carlo (MC) simulation used in K2K. The MC simulation is made of the following three constituents; neutrino beam simulator (Beam-MC), neutrino interaction simulator (NEUT) and detector response simulator. The detailed description is given in Appendix-A and other references [47, 52, 69].

4.1 Neutrino Beam Simulation (Beam-MC)

Beam-MC simulates the process of neutrino beam generation to provide neutrino flux and energy spectrum shape at the near and far site. The beam line geometry is implemented in GEANT [70], and particles are tracked in materials. For the pion production in the target, we adopt the Cho-CERN model [71], with the Sanford-Wang parameterization [72, 73] determined experimentally.

The result of neutrino flux at the near and far site with the 250 kA horn current and the target of 3 cm in diameter are shown in Fig. 4.1. The ν_e/ν_μ flux ratio is estimated to be 1.3%. $\bar{\nu_\mu}/\nu_\mu$ is 0.5%, and $\bar{\nu_e}/\nu_\mu$ is $\sim 2 \times 10^{-4}$, respectively.

4.2 Neutrino Interaction (NEUT)

The NEUT program library [69] is used to simulate neutrino interactions with the nucleus. The library is first developed to study atmospheric neutrino background for nucleon decay search in the Kamiokande experiment. Then it is inherited to K2K together with Super-Kamiokande with various modifications [51, 63, 64, 74]. In NEUT, the following interactions are considered:

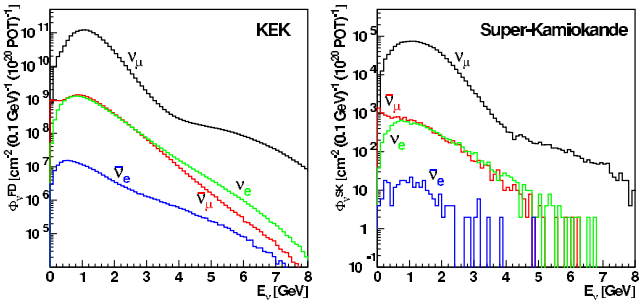

Figure 4.1: The energy spectrum for each type of neutrinos at ND (left) and SK (right) estimated by the beam-MC.

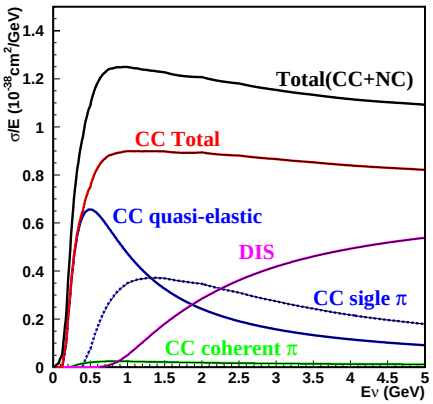

Figure 4.2: The cross section divided by E_ν of each neutrino interaction mode with CH target as a function of E_ν.

CC/NC (quasi-) elastic scattering	$\nu + N \rightarrow l + N'$
CC/NC single meson (1π) production	$\nu + N \rightarrow l + N' + \text{meson}$
CC/NC coherent pion (coherent π) production	$\nu +^{16} O\ (^{12}C) \rightarrow l +^{16} O\ (^{12}C) + \pi$
CC/NC deep inelastic interaction (multi-π)	$\nu + N \rightarrow l + N' + \text{hadrons}$

where N and N' are nucleons (proton or neutron) and l is a lepton, respectively.

The Lewellyn Smith model [75] and the Rein and Sehgal model [76] are employed for (quasi-) elastic scattering (QE) and single pion (1π) production, respectively. The axial vector mass in the dipole formula of the nucleon form factor is set at 1.1 GeV/c^2 for both (quasi-) elastic and single pion production [77]. For coherent pion production, we will describe the models in Chapter 7 because this is one of the main topic in this thesis. For deep inelastic scattering (multi-π), the GRV94 nucleon structure functions [78] with a cross section correction by Bodek and Yang [79] is used. This correction reduces the cross section by 25% on average for the K2K neutrino energy spectrum. The final state hadrons are simulated with a custom-made program [80] and PYTHIA/JetSet package [81] for the hadronic invariant mass, W, 1.3$-$2.0 GeV/c^2 and larger than 2.0 GeV/c^2, respectively.

Hadrons produced in neutrino interaction often rescatter inside the target nucleus. This process changes kinematics of the hadrons and is called "nuclear-effect". Nuclear effects are taken into account in the MC simulation. The absorption, elastic scattering and charge exchange process inside the target nucleus are simulated for the pions originating from neutrino interactions. The pion cross sections are calculated using the model by Salcedo et. al. [82] which is tuned to reproduce the past experimental data [83]. The proton re-scattering inside the target nucleus is also simulated. Here, elastic scattering and one or two pion productions are considered.

Figure 4.2 shows the result of the cross section divided by E_ν of each neutrino interaction mode with CH target as a function of E_ν. NEUT also simulates kinematic information of produced particles.

4.3 Detector Simulation

Once a neutrino event is generated, the detector response to the particles are simulated as the next step. The response of each detector is correctly digitized so that analysis code would work

for both the real data and MC data in the same way. In K2K, GEANT-3.21 package [70] is utilized. It takes the simulated data from NEUT and traces each particle in the detector and simulates the detector response. The simulation of responses in all the K2K detector elements are summarized in Appendix-A.

Chapter 5

SciBar Detector

SciBar is a fully-active scintillator detector installed in the near site in summer 2003. In this chapter, we describe the overview of SciBar, motivation and design, each component and basic performance.

5.1 Overview

The main purposes of SciBar are to improve the measurement of neutrino energy spectrum at the near site and neutrino-nucleus interaction. In order to achieve the goals, we select charged-current quasi-elastic scattering (QE) from non-QE interaction with the high efficiency and high purity. We identify each interaction mode clearly in SciBar. The following features are required to the detector,

- Detect all particles generated from neutrino interaction.
- Identify a muon and measure the momentum
- Identify a proton

The SciBar detector is designed and constructed to satisfy the requirements.

Figure 5.1 shows a schematic drawing of SciBar. The main part of SciBar consists of approximately 15,000 extruded plastic scintillator strips arranged vertically and horizontally. The dimension of each strip is $1.3 \times 2.5 \times 300\text{cm}^3$. As a whole, the detector size is $3.0 \times 3.0 \times 1.7\text{m}^3$, giving a total mass of 15 ton. The scintillation light is collected by wavelength-shifting (WLS) fibers and sent to multi-anode PMT (MAPMT) as shown in Fig. 5.2. The MAPMT signals are processed with the custom-made electronics. The charge information of each channel and the timing information of ORed of 32 channels are recorded. The conceptual drawing of the readout system is shown in Fig. 5.3. The stability of the readout system including the gain of MAPMT is monitored by a custom-made system so-called "HASE-moni". Just behind the main part, an electro-magnetic calorimeter (EC) is installed for measuring the ν_e contamination in the beam and π_0 production in neutrino interaction.

The scintillator also acts as the neutrino interaction target; it is a fully active detector and has high efficiency for a low momentum particle. Due to the fine segmentation, the minimum reconstructable track length is 8 cm, which corresponds to 450 MeV/c for a proton and 100 MeV/c for a muon, respectively. The protons with the momentum less than the tracking threshold are detected as a large energy deposit in the vertex strip or additional hit around the vertex. The particle identification (PID) of proton and pion is performed based on dE/dx information of each strip. We present the performance of tracking and PID in Chapter 6.

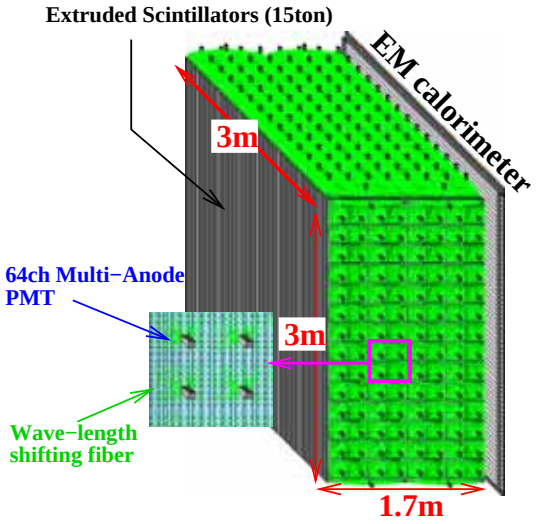

Figure 5.1: A schematic drawing of SciBar. Extruded scintillator strips are arranged vertically and horizontally.

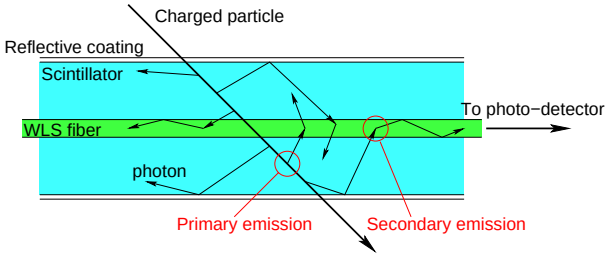

Figure 5.2: Conceptual scheme of the WLS fiber readout of the Scintillation light.

We define the SciBar local coordinate system, which is commonly used in this thesis, as shown in Fig. 5.4. In the Cartesian coordinate system, the z-axis is the beam direction, the y-axis is the vertical upward direction, and the x-axis satisfies the relation of the right-hand system, i.e. $\vec{x} = \vec{y} \times \vec{z}$.

SciBar operates stably since October 2003[1]. We collect data of to 2.1×10^{19} protons on target with SciBar. An event display of a typical CCQE event candidate is shown in Fig. 5.5.

In the following, we give a brief description of the detector components and their basic performance.

5.2 Components

5.2.1 Extruded scintillator

The extruded scintillator used in SciBar is made of Dow STYRON 663 polystyrene pellets with PPO (1% by weight) and POPOP (0.03% by weight). The emission spectrum is shown in Fig. 5.6. The wavelength of the spectrum peak (420 nm) matches with the absorption spectrum of the WLS fiber shown in Fig. 5.7.

The profile of the SciBar scintillator strip is shown in Fig. 5.8. It has a rectangular cross section of 25 mm wide and 13 mm thick. There is a 1.8 mm diameter hole in the center for the WLS fiber. The scintillator is covered with co-extruded reflector material. This coating is 0.25 mm thick and contains 15 % of TiO_2 by weight in polystyrene.

In SciBar, 14,848 strips are used in total. The scintillator strips are arranged in 64 layers. Each layer consists of two planes, with 116 strips to give horizontal and vertical position. We measure the the dimensions and weight of 10% of all the strips before installation. The result is summarized in the Table 5.2.

[1]In December 2002, only four layers with six MAPMTs so-called mini-SciBar were installed and had been operated until June 2003 for engineering study. Then SciBar was completely constructed in only 3 months during summer shutdown.

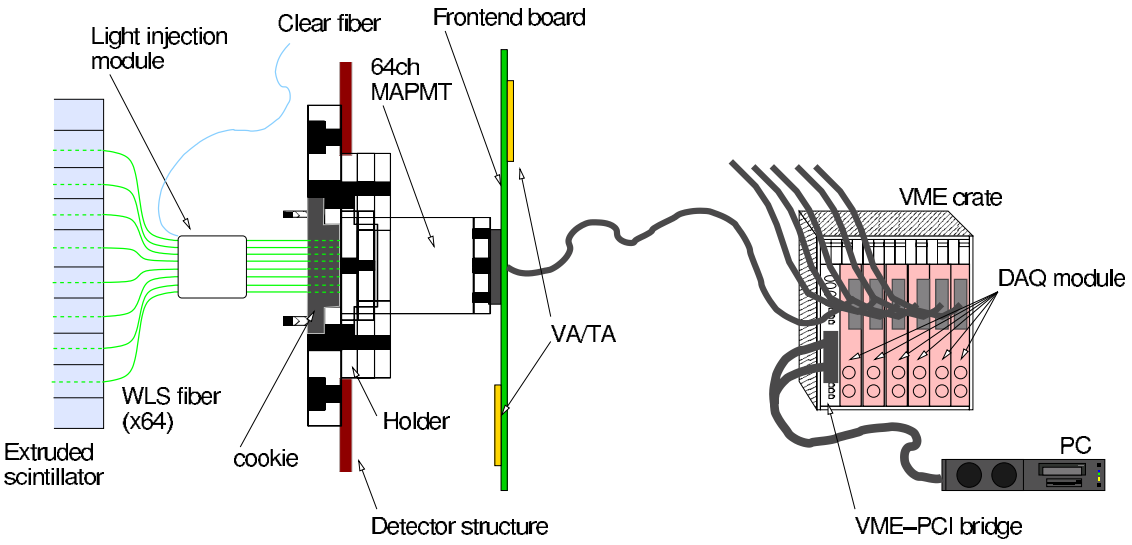

Figure 5.3: Conceptual scheme of the SciBar readout system.

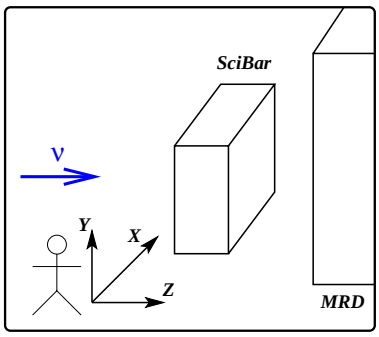

Figure 5.4: The SciBar local coordinate.

Table 5.1: Basic characteristic of Extruded scintillator.

Scintillator material	polystyrene with PPO (1%) and POPOP (0.03%)
Emission wavelength	420 nm (blue)
Dimensions	$2.5 \times 1.3 \times 300$ cm^3
Hole diameter	1.8 mm
Reflector material	TiO_2 (15 %) infused in polystyrene
Number of strips	14,848
Whole size	$3 \times 3 \times 1.7$ m^3
Total weight	15 ton

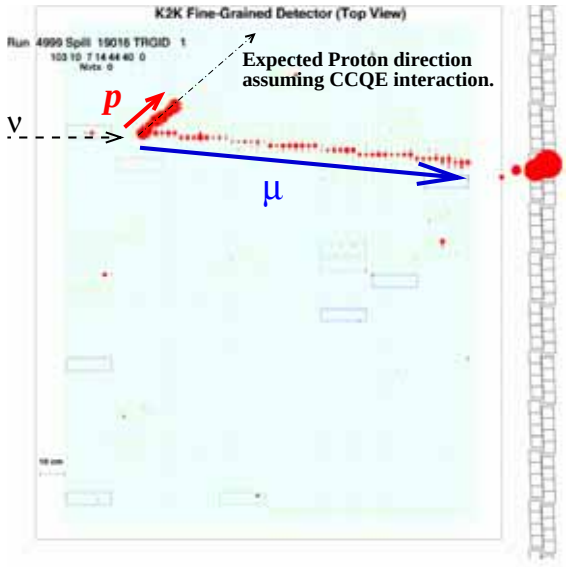

Figure 5.5: An event display of the typical CCQE event. In the display, each hit is shown as a closed circle, whose area is proportional to the deposited energy. One track extends to MRD is a muon and the other track with the larger energy deposition is a proton.

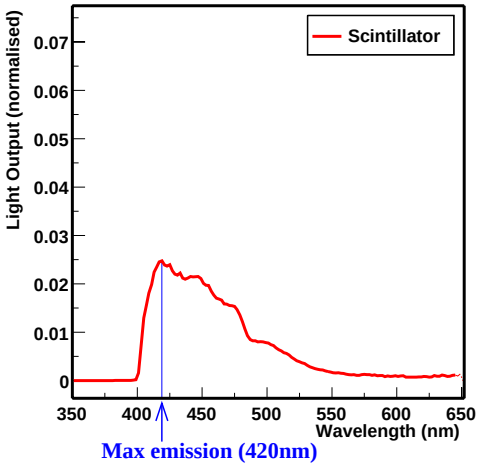

Figure 5.6: The emission light spectra from scintillator.

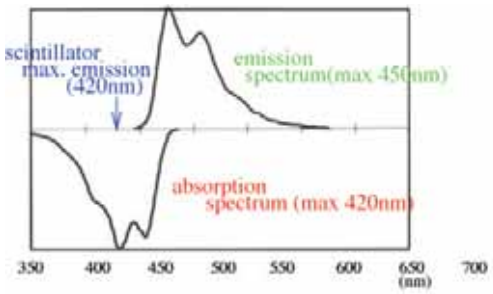

Figure 5.7: The absorption and emission spectra of the WLS fiber (Y11).

Table 5.2: The result of the scintillator-measurement. The dimension and weights of the 10% of all strips are measured.

	mean (mm)	RMS (mm)
width	25.01	0.21
thickness	12.87	0.26
length	3022	10
weight	994.6	8.4

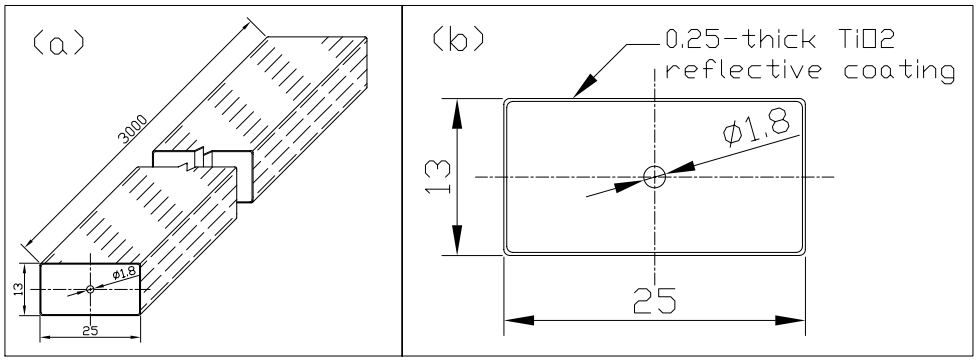

Figure 5.8: The drawing of scintillator strip.

5.2.2 Wave-length shifting fiber

The green wavelength-shifting (WLS) fiber (1.5 mm in diameter), Kuraray Y11 (200) MS type [84], is used to readout the scintillation light to avoid the effects of a short attenuation length of the scintillator, which is less than 10 cm [85]. The WLS fiber converts the blue scintillation light into green and transports it to a photo-detector with the longer attenuation length, typically 350 cm.

The WLS fiber has a polystyrene core containing the WLS flour (200 ppm), a thin acrylic inner clad and a thin polyfluor outer clad as shown in Fig. 5.9. They have refraction indices of 1.59, 1.49 and 1.42, respectively. Re-emitted light from the core can pass through the WLS fiber only when the reflection angle θ satisfies the relation:

$$\cos\theta \geq \frac{1.42}{1.59} \rightarrow \theta < 26.7 \text{ degree} \tag{5.1}$$

We measure the attenuation length and the relative light collection efficiency before installation [86]. Figure 5.10 and 5.11 show the result of the measurements for all the WLS fibers, respectively. The attenuation length depends on the production batch. Thus, the result distributes around 330 cm and 350 cm because our fibers were produced in two different periods. The mean value is 347.6 cm. For the light collection efficiency, all fibers show the same level performance (RMS is 6.2%). We check and monitor the attenuation length by using the cosmic-ray muons after installation. We confirm that all the fibers keep the same quality.

Sixty-four fibers are bundled with a custom-made alignment fixture shown in Fig. 5.12. In total, 224 fiber bundles are used in SciBar. Each bundle is connected to the photo-detector with custom-made system [87]. All fibers are aligned to pixels of MAPMT within 0.2 mm precision.

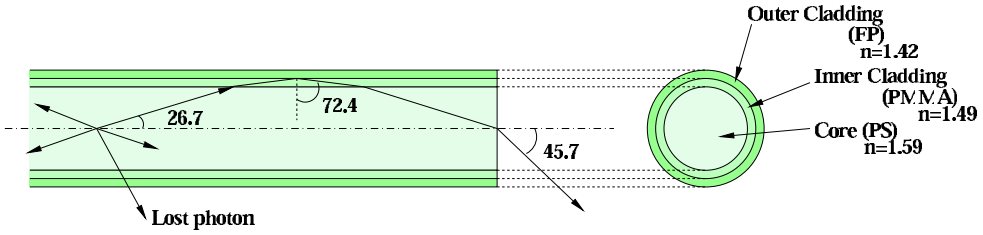

Figure 5.9: The wavelength-shifting fiber Kuraray Y11 (200)

Table 5.3: Basic characteristic of WLS fiber

Diameter	1.5 mm
Core	polystyrene (n = 1.59)
Inner clad	acrylie (n = 1.49)
Outer clad	polyfluor (n = 1.42)
Wavelength shifter	Y-11 fluor (200 ppm)
Absorption wavelength	430 nm (peak)
Emission wavelength	476 nm (peak)
Attenuation length	350 cm (typical)

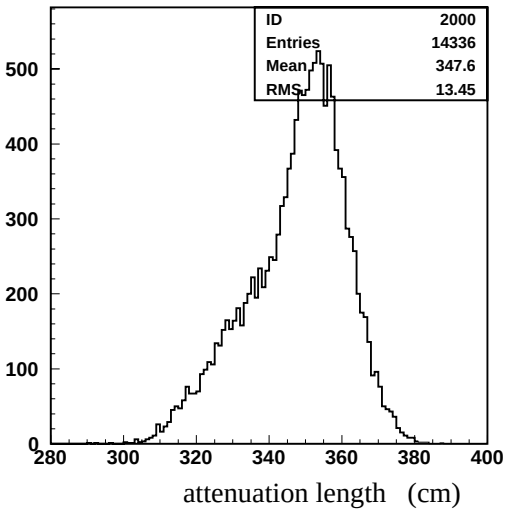

Figure 5.10: The attenuation length of all WLS fibers measured before installation.

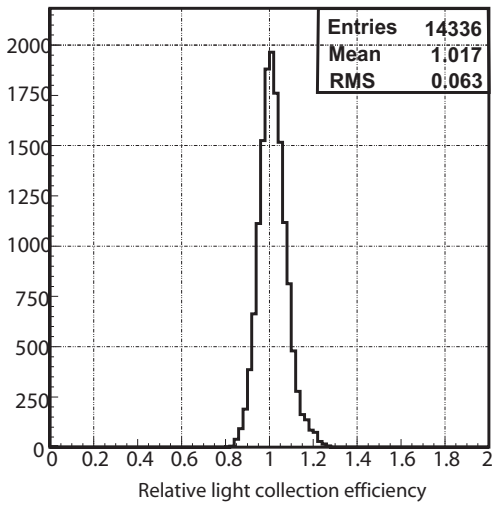

Figure 5.11: The relative light collection efficiency of all WLS fibers measured before installation.

Figure 5.12: The picture of the alignment fixture "cookie".

Table 5.4: Specifications of the MAPMT.

Model	Hamamatsu H8804
Manufacturer	Hamamatsu Photonics K.K.
Tube size	30×30 mm^2
Photo-cathod	Bialkali (Sb-K-Cs)
Anode	8×8 (2×2 mm^2/pixel)
Sensitive wave length	300-650 nm (Peak:420 nm)
Quantum Efficiency	12% at $\lambda = 500$ nm
Dynode	Metal channel structure, 12 stages
Typical gain	6×10^5 at $\sim$800 V
Pixel-to-pixel gain uniformity (max./min.)	$\leq\sim 2$
Response linearity	200 photo-electrons at gain 6×10^5
Cross talk	4 %

5.2.3 64-channel multi-anode PMT

The light from the WLS fiber is detected by a 64-channel multi-anode PMT (MAPMT), Hamamatsu H8804 [88], situated at the edge of the detector. Table 5.4 summarizes the specifications. MAPMT has 64 anodes, whose pixel size is 2×2mm^2, and they are arranged in an 8×8 array. The photocathode area is coated by a bialkali (Sb-K-Cs) material, whose quantum efficiency is about 12% at the wavelength of 500 nm.

Basic characteristics of MAPMT are measured before installation. The cross-talk effect[2] is measured to be 4% for adjacent pixels and 1% for orthogonally opposite pixels with the 1.5 mm diameter WLS fiber. The pixel-to-pixel gain uniformity is measured to be 21% in RMS. The ratio of the maximum to minimum gain is less than two for typical tubes as shown in Fig. 5.13. The operation high voltage is tuned so that the averaged gain of 64 channels is 6×10^5. The absolute gain is determined with the single photoelectron peak as shown in Fig. 5.14. The temperature coefficient of the gain is measured to be 0.3%/deg [85]. The response linearity is kept within 10% up to 200 photo-electrons (pe) with the gain of 6×10^5 as shown in Fig. 5.15

5.2.4 High Accuracy gain monitoring SystEm (HASE-moni)

The MAPMTs are very sensitive to the small changes of surrounding temperature and applied high voltage. In order to monitor and correct the short term gain variation, High Accuracy gain monitoring SystEm (HASE-moni) is developed with the following requirements.

1. All MAPMT channels (14336) are monitored simultaneously with a few light sources.
2. The channel-by-channel variation of injected light is less than a factor of 6 to avoid the saturation of MAPMT.
3. The monitor precision is better than 1 % to measure the gain drift at 1 % level.

System Overview

Figure 5.16 shows a schematic view of HASE-moni. This system is based on only 4 pulsed blue LEDs monitored by PIN photo-diodes. Each LED light is divided into 56 and carried to 56 MAPMTs by clear fibers. Each MAPMT has an optical fan-out, a light injection module, to illuminate 64 individual fibers. The light similar with that from a scintillator is emitted

[2]The cross-talk is mainly caused by the incident light spreading at the face-window.

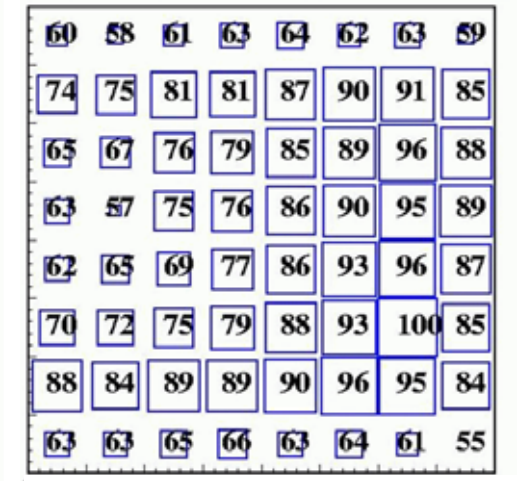

Figure 5.13: Pixel-to-pixel gain uniformity. Each number in the figure represents the relative gain of each pixel.

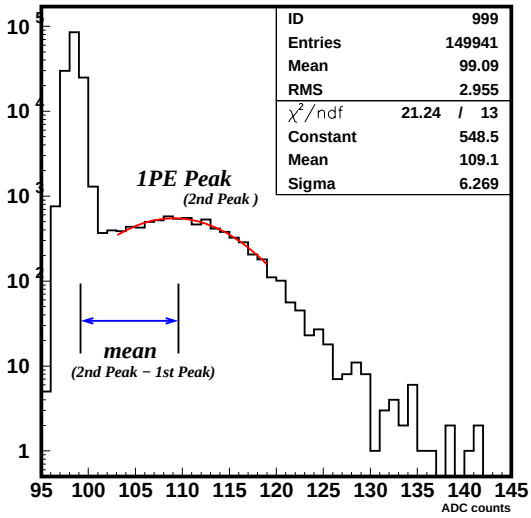

Figure 5.14: Single photoelectron ADC distribution.

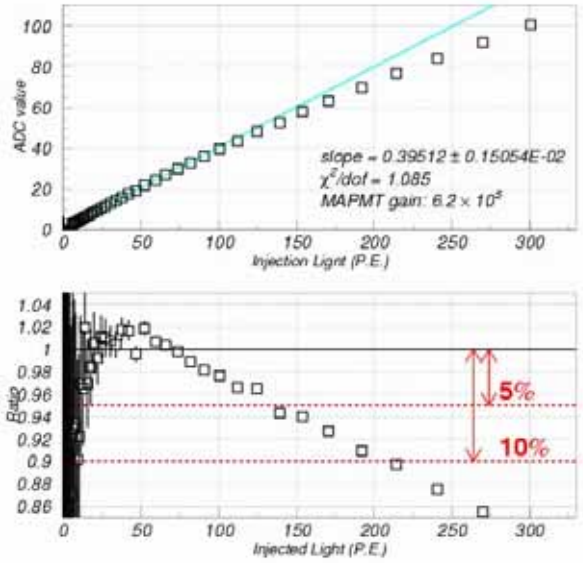

Figure 5.15: Linearity curve. The upper figure shows a response for various input charge from 0 to 300 photo-electrons and the lower figure shows the ratio of the measured to the expected response.

Table 5.5: PIN diode specifications.

Active area size	$10.0 \times 10.0\text{cm}^2$
Spectral response	190-1000 (nm)
Dark current	0.02 nA (@ 25 deg.)
Temperature coefficient	-
of dark current	12% /deg.
Photosensitivity @ 470 nm	0.24 A/W
Temperature coefficient	-
of photosensitivity	$\leq$ 0.01% /deg

in the WLS fiber and goes to each channel in MAPMT. A short term gain-drift is measured by comparing the response of MAPMT channel to the signal of the PIN photodiode. In the following, we explain them in order.

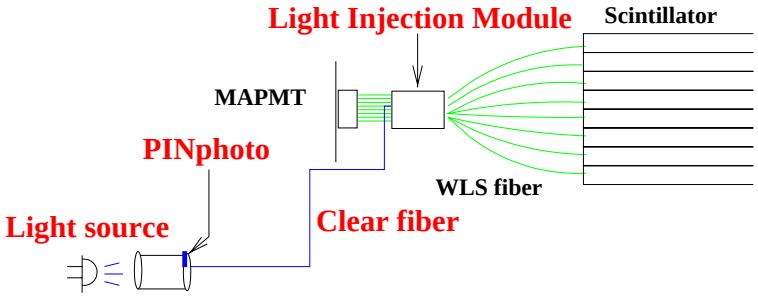

Figure 5.16: Schematic view of the gain monitoring system (HASE-moni)

Components

LED

The LED used as a light source are Nichia NSPB510 [89]. Its emission spectrum (max:460nm) matches with absorption spectrum of WLS fiber. The re-emitted spectrum is quite similar to that excited with scintillation light as shown in Fig. 5.17 [90].

Figure 5.18 shows the short term variation of the LED pulse intensity measured for 30 minutes. The variation is within 0.53%. This width is consistent with electronics noise. This good stability allows us to monitor the LED intensity without any loss of the accuracy.

The left figure in Fig. 5.19 shows a track of the LED intensity monitored by the PIN photo-diode for the whole operation period. The sudden change of intensity is observed when we re-set the monitor system for the hardware work such as a replacement of MAPMTs or the experimental shutdown. The light intensity is usually stable at 0.20% level as shown in the right figure of Fig. 5.19.

PIN photodiode

The PIN photo-diode, Hamamatsu S1227-1010BQ [88] is used to monitor the LED intensity. The basic specifications of the PIN photo-diode are summarized in Table 5.5. The linearity is shown in Fig. 5.20 [85]. The PIN photo-diode has a very good linearity up to 10^9 photons, corresponding to 10^3 pe for MAPMT.

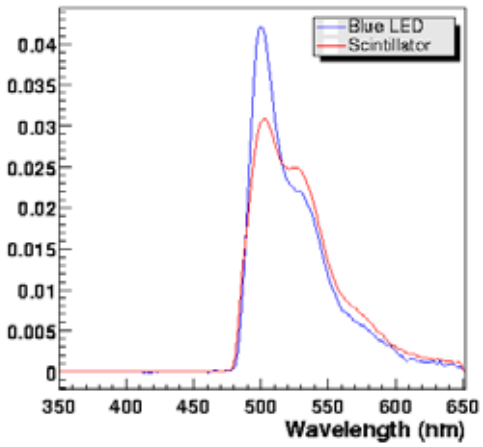

Figure 5.17: Spectrum of light emitted from WLS fiber excited with the LED light and scintillation light. [90]

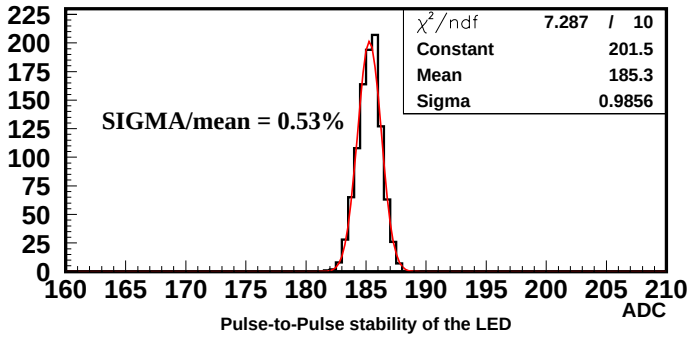

Figure 5.18: Pulse-to-Pulse stability of the LED intensity.

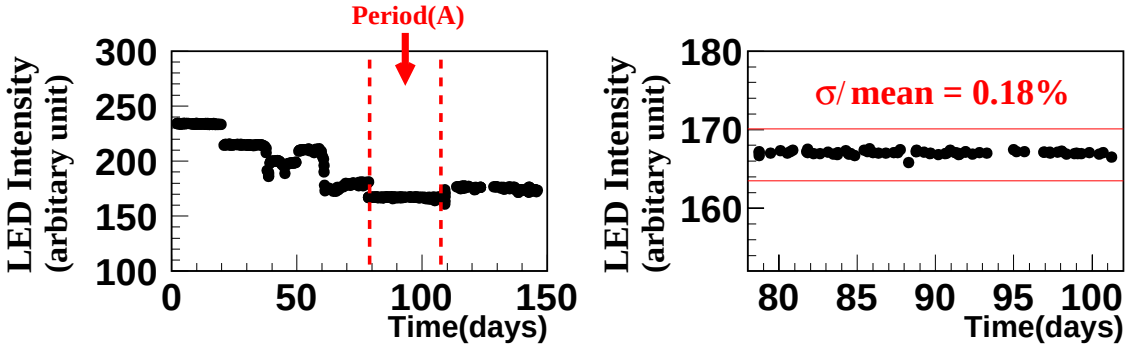

Figure 5.19: History of the LED light intensity for all SciBar operation period (left) and for short-term stability (right) in the period (A) defined in the left figure.

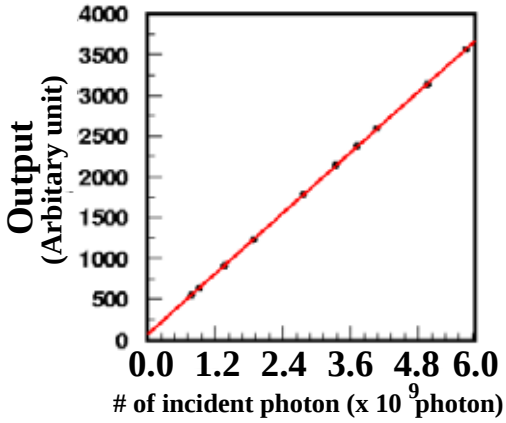

Figure 5.20: The linearity curve of the PIN photo-diode. PIN photo-diode has a very good linearity up to 10^9 photo level, which corresponds to 10^3 p.e. level for MAPMTs.

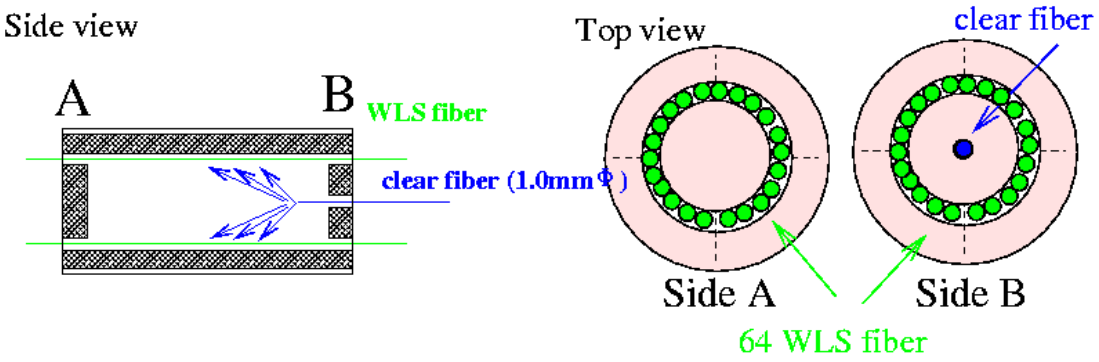

Figure 5.21: Schematic view of light injection module.

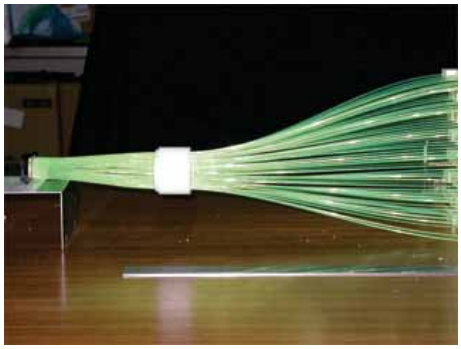

Figure 5.22: Light injection module. White cylinder in the center of picture is LIM.

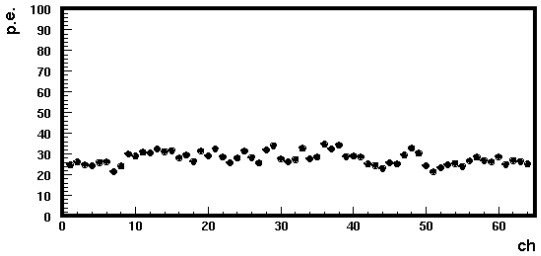

Figure 5.23: Injected light yield vs MAPMT channel.

Light injection module (LIM)

The light injection module (LIM) is a white cylinder assembled to a WLS fiber bundle in order to illuminate the uniform light to 64 WLS fibers. LIM is made of Delrin, which is softer than the clad of the WLS fiber. A schematic drawing and a picture of LIM are shown in Fig. 5.21 and 5.22, respectively. LED light carried by a clear fiber is distributed to 64 fibers inside the LIM connector and goes into each MAPMT channel. The light distributed to 64 channels are uniform within 12% (RMS) as shown in Fig. 5.23.

Monitor result

Figure 5.24 shows the relative gain drift of a typical channel monitored by HASE-moni for the whole SciBar operation period. The relative gain is monitored every 12 hours with a 0.1% level precision. The gain is stable within ± 5%. A gain drift between 30 and 60 days is due to a change of temperature by a trouble of the air conditioner.

The number of dead channels is also monitored by HASE-moni. The dead channels are detected with less than 15 ADC counts to the LED light (Fig. 5.25). Figure 5.26 shows the history of the number of dead channels. The number of dead channels is gradually increased until 110 days. This is due to the gain decrease of two MAPMTs at the rate of 10% per week. After replacement of two bad MAPMTs, the number of dead channel is only one out of 14336 (0.007%).

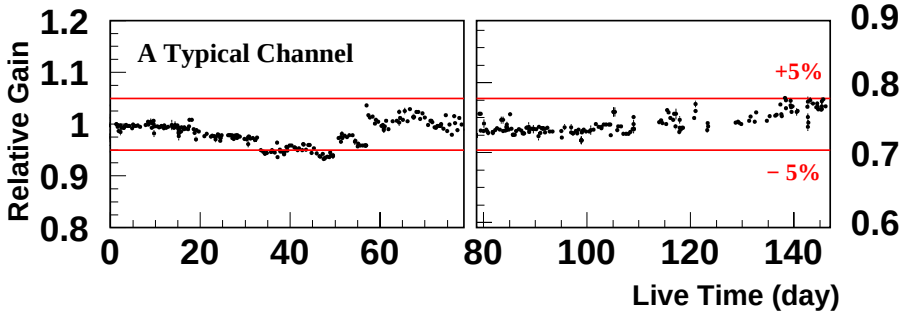

Figure 5.24: The relative gain drift for the typical channel measured by HASE-moni. In the figure, horizontal axis shows the operation time from the beginning of SciBar data taking.

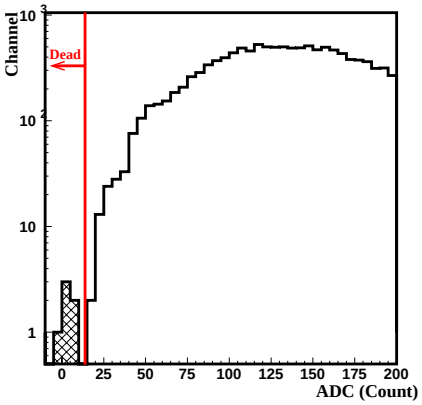

Figure 5.25: Response to the LED light for all channel. Channels with ADC less than 15 counts are defined as dead channel.

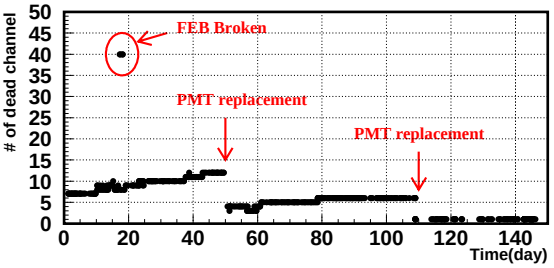

Figure 5.26: History of the number of dead channel monitored by HASE-moni. In this period, two MAPMTs, whose corner of the photo-cathode is cracked, are replaced.

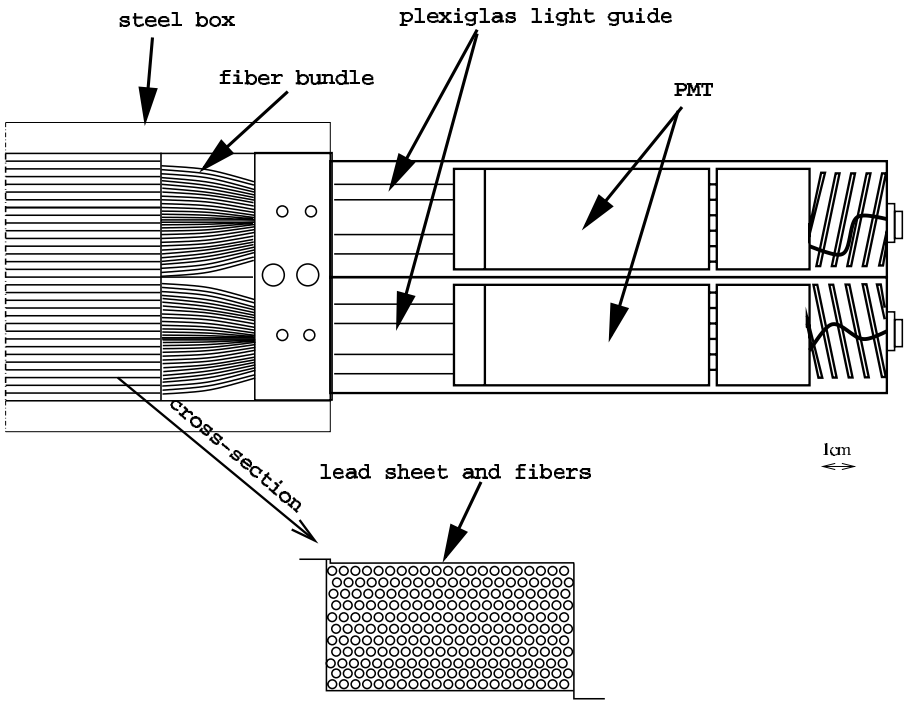

Figure 5.27: Schematic drawing of an electro-magnetic calorimeter module.

5.2.5 Electro-magnetic calorimeter

An electro-magnetic calorimeter (EC) is installed behind of the scintillator part. EC is comprised of 2 planes of 30 horizontal and 32 vertical modules reused from the CHORUS experiment [91]. The module is made of lead sheets and scintillating fibers. The dimension is $4 \times 8 \times 262$ cm^3, consisting of two $4 \times 4 \times 262$ cm^3 cells. The schematic drawing is shown in Fig. 5.27. EC has 11 radiation length along the beam axis and covers the 2.6×2.6 m^2 area. The energy resolution is $14/\sqrt{E\ (\mathrm{GeV})}$ % for electrons.

5.2.6 Readout system

The MAPMT signals are processed by custom built electronics. The electronics consists of front-end circuit boards (FEB) attached to MAPMTs and backend VME modules (DAQ Board) to control and readout the FEBs. On FEB, a combination of ASICs –VA and TA– are employed to multiplex pulse-height information and to make a fast-triggering signal. The VA has preamplifires for 32 input channels and shapes the output with a peaking time of 1.2 μs. The 32 signals from VA shapers are captured by the sample-and-hold circuits and passed to an analog multiplexer. The signal after preamplification in VA is sent to a fast shaper in TA, with a peaking time at 80 ns. Logical OR of distributed signal from 32 channels is sent out from a TA. The intrinsic time jitter of the discriminated output is shorter than 1 ns. Figure 5.28 shows a picture of FEB. Each FEB has two sets of VA and TA packages, thus processing 64 input channels in total for one MAPMT.

The DAQ Board is developed as a standard VME-9U board. A picture of the module is shown in Fig. 5.29. Each of the eight channels has line drivers to control a FEB and a 12-bit flash ADC to digitize multiplexed analog signal from a FEB. Timing information is sent to a multi-hit TDC. The timing resolution and full range are 0.78 nsec and 50 μ sec, respectively. The resolution allows us to distinguish multiple events occurred in one spill.

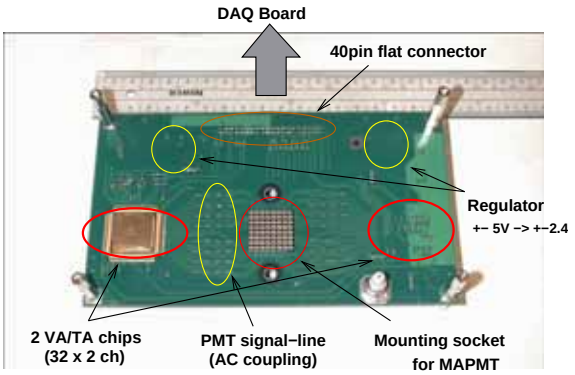

Figure 5.28: Picture of VA/TA front-end board (FEB).

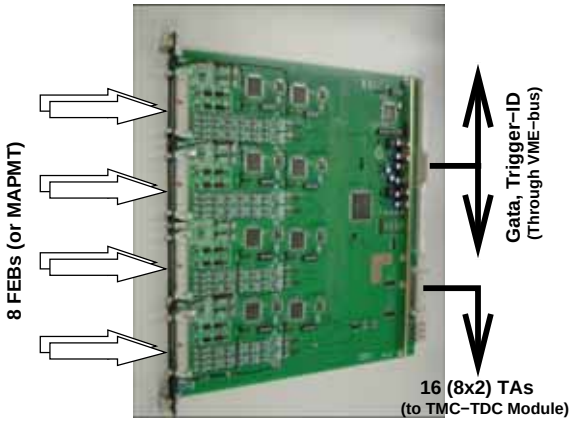

Figure 5.29: Picture of DAQ board.

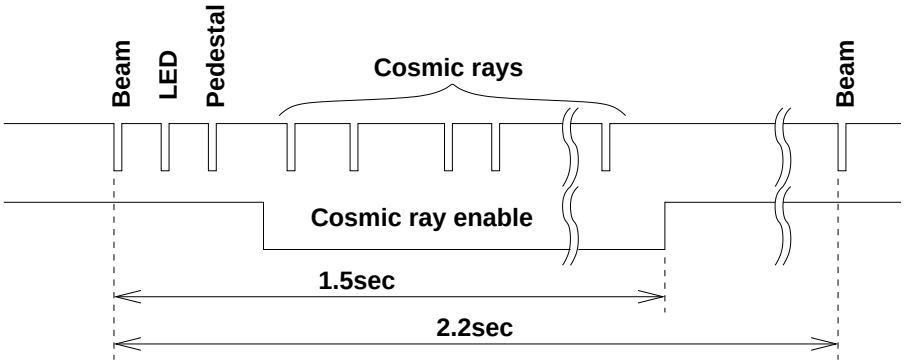

Figure 5.30: Timing diagram of the data acquisition.

5.2.7 Data acquisition

The timing diagram of the data acquisition is summarized in Fig. 5.30. The neutrino data is taken by using the beam trigger signal from the accelerator. After the beam trigger, pedestal and LED triggers are generated. The cosmic-ray data are continuously corrected until 1.5 sec after the beam.

5.3 Calibration

5.3.1 Energy scale calibration

The energy scale of each scintillator strip is calibrated with cosmic-ray muons. Figure 5.31 shows the light yield distribution of one strip for the cosmic-ray muons. The path length inside the strip and the attenuation effect in the WLS fiber are corrected in the figure. The mean light yield is measured to be 26 pe/1.3 cm. This value is used as the calibration constant between pe and the energy. Figure 5.32 shows the distribution of the calibration constant for all the strips. The mean value of 9.1 pe/MeV is consistent with the expectation of 9.3 pe/MeV from the laboratory measurement [85].

The stability of the calibration constant is also monitored with cosmic-ray muons. The upper figure in Fig. 5.33 shows the time variation of the light yield of one strip. As described in the

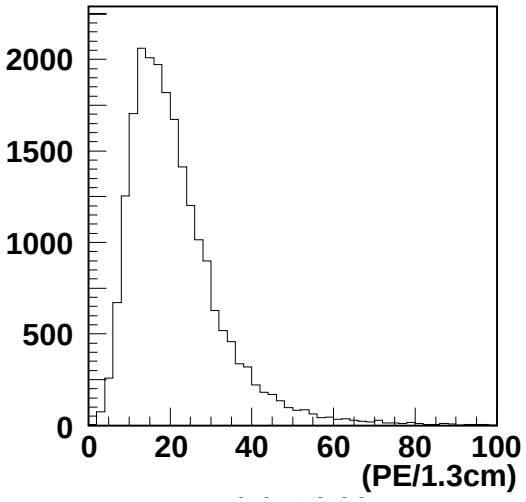

Figure 5.31: The light yield distribution of a typical scintillator strip for the cosmic-ray muons.

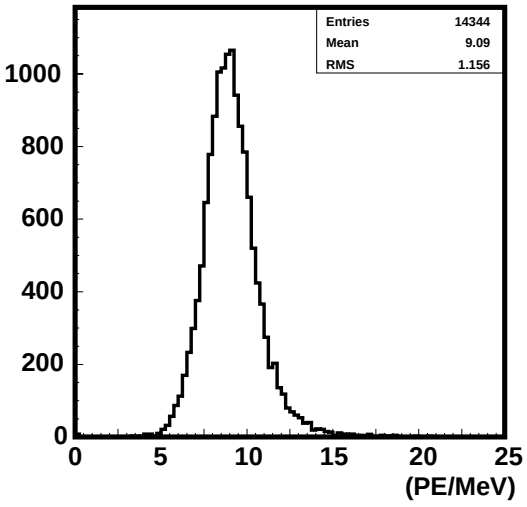

Figure 5.32: Energy calibration constant of all strips.

section of HASE-moni, the fluctuation around $30-60$ days is due to the change of the MAPMT gain. After applying the gain correction, the calibration constant is stable with 1.0 % precision as shown in the lower figure of Fig. 5.33.

5.3.2 Timing calibration

The timing resolution is measured by the time difference between two adjacent TAs along a cosmic-ray muon track in SciBar. The TOF of the muon, the light propagating time in the WLS fiber and the correlation between timing and charge shown in Figure 5.34 are corrected.

Figure 5.35 shows the timing difference after applying the corrections. The standard deviation of the distribution is 1.9 nsec. The timing resolution of one TA is evaluated to be $1.9/\sqrt{2} = 1.3$ nsec. This is good enough to select the beam timing window (1.1 μsec) and to distinguish the 9 bunch (125 nsec spacing) in the beam spill.

5.3.3 Calibration with test beam

We performed a test beam experiment T551 with a smaller proto-type detector of SciBar in the KEK T1 beam-line in March 2004. This beam-line provides the pions and protons up to 2 GeV/c. The purposes of T551 are to measure the scintillator quenching effect and the absolute energy scale.

Scintillator Quenching

Scintillation light yield does not respond linearly to the energy given by ionization processes, and results in reduction of light yield. The visible energy, $\Delta E_{\rm vis}$, obtained from observed light yield is not exactly equal to the deposited energy, ΔE, especially for proton with the non-linear quenching effect. The relation is expressed as a function of the expected energy deposition per unit length, dE/dx(expected), by the Birk's formula, as

$$\frac{\Delta E_{\rm vis}}{\Delta E} = \frac{c_1}{1 + c_2 \cdot dE/dx(\text{expected})}, \tag{5.2}$$

where c_2 is Birks constant to be determined by the measurement.

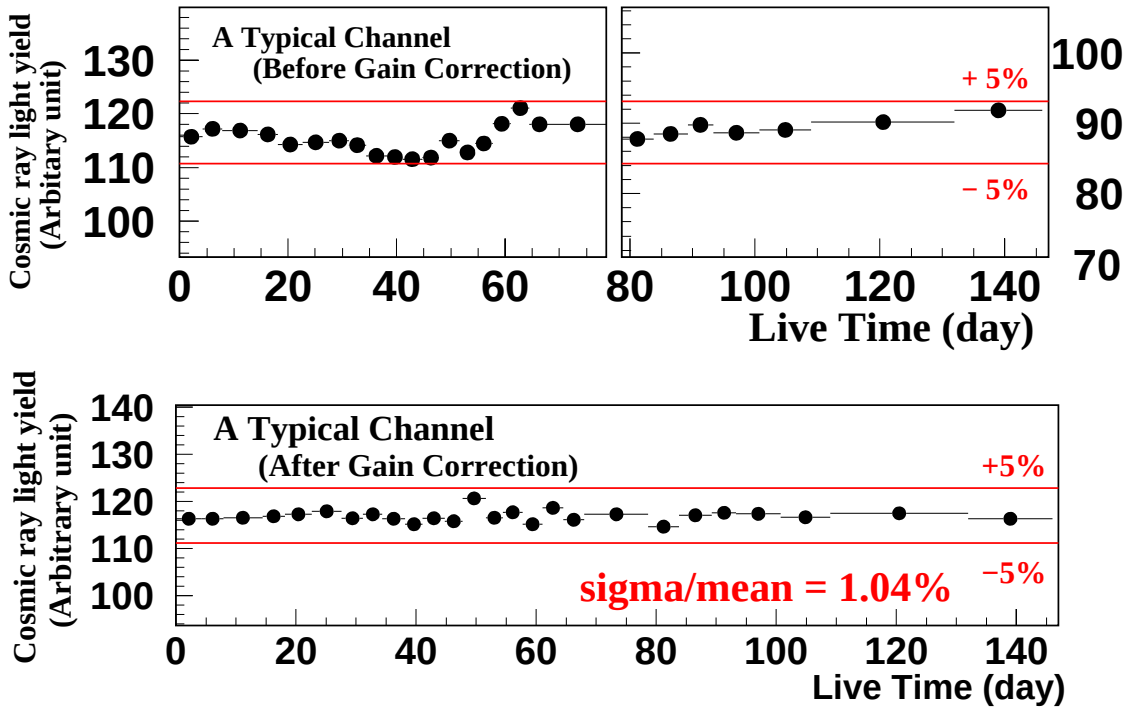

Figure 5.33: The stability of the energy scale calibration constant for a typical strip over the whole SciBar operation period, K2K-IIb and K2K-IIc, before (upper) and after (lower) applying the relative gain correction of MAPMT. The light yield of cosmic-ray muons are plotted.

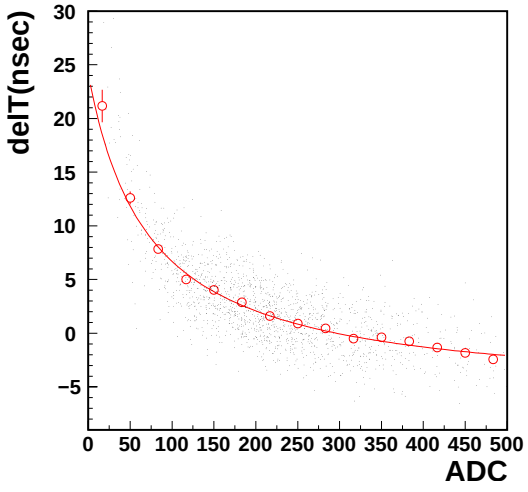

Figure 5.34: TQ-map, a two-dimensional plot of measured timing difference between a certain two adjacent TA pair along a cosmic-ray muon track and charge for one of the two TA blocks.

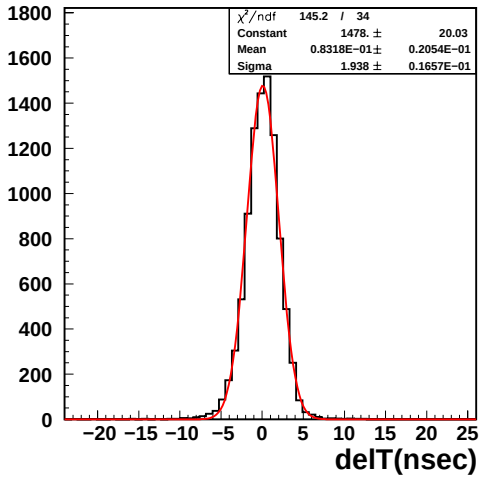

Figure 5.35: The timing difference between adjacent TA channels along a cosmic-ray muon track afterapplying the correction of the correlation between timing and charge.

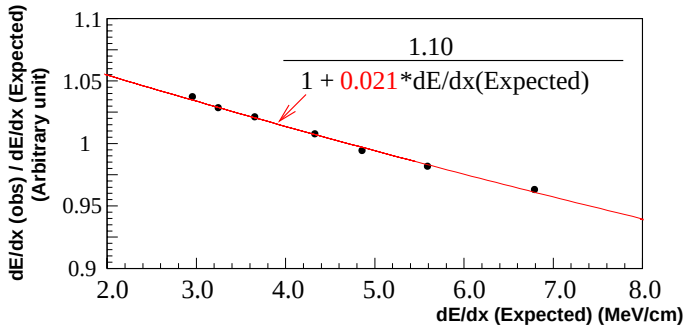

Figure 5.36: The ratio of the observed deposited energy per unit length (dE/dx) to the expected dE/dx by the MC simulation as a function of the expected dE/dx. A red line shows a birks relation with best fit constants.

Figure 5.36 shows the $\Delta E_{\rm vis}/\Delta E$ as a function of true dE/dx estimated by the MC simulation for various incident proton momentum. In Fig. 5.36, the quenching effect is clearly seen and this effect is well reproduced by Equation (5.2) with the best fit value as

$$\text{Birks constant } (c_2) = 0.0208 \pm 0.0003 \text{ (stat.)} \pm 0.0023 \text{ (syst) cm/MeV}$$

where the systematic error is evaluated by changing the fitting conditions, such as fitted region and the data set. This result is included in the MC simulation.

Chapter 6

Event Reconstruction in SciBar

Charged current (CC) neutrino interaction and the neutrino energy spectrum are measured with the SciBar detector. We describe the basic event reconstruction used to identify the CC events and the classification of the events in the analysis.

The outline of the reconstruction processes is:

1. Track finding.
2. Muon identification.
3. Counting the number of tracks originated from the interaction vertex.
4. The quasi-elastic (QE) and non quasi-elastic (nonQE) event classification.
5. Particle identification.

6.1 Track Finding

We select hits for the track finding. The noise hits are rejected by the threshold cut after applying the cross-talk correction. The cross-talk correction is described in Appendix-A in detail. After the hit selection, we reconstruct the track candidates in each x and y view individually (2D track search) by using a cellular automaton tracking algorithm [44, 92]. Then we perform the matching of tracks between x and y views (3D track reconstruction) by using the information of timing and the positions of track edges. In this section, we discuss the following items.

- Hit efficiency of the scintillator strips
- Track finding efficiency

6.1.1 Hit efficiency

Selection

Figure 6.1 shows the timing distribution of all hits in the beam gate. Here we select $-100 < t < 1200$ nsec as a beam time window. The hit is required to be 3 σ higher than the pedestal level, corresponding to 0.5 photo-electrons. There are many background hits after the beam time window. They are mainly due to cosmic-ray muons and beam-induced neutron backgrounds called sky-shine [93]. We select the hits inside the beam time window. Then we apply the cross-talk correction in order to remove the fake hits. Figure 6.2 shows the number

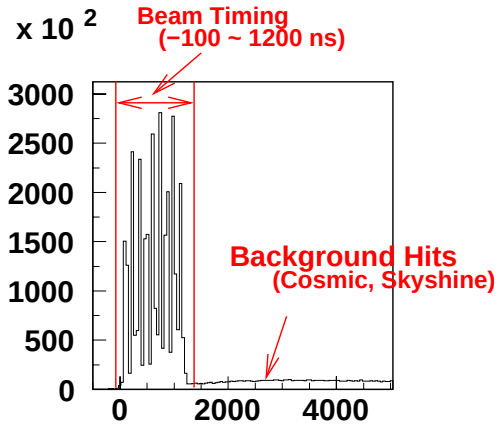

Figure 6.1: The timing distribution for all hits in the on-spill gate.

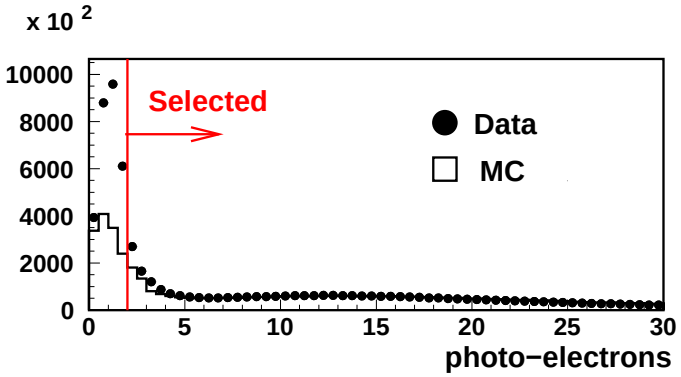

Figure 6.2: The number of photo-electron distribution for all hits survived after the cross-talk correction. In the figure, black circle shows data and the histogram shows the MC simulation, which is normalized by the entry in the region of more than 5 photo-electron.

of photoelectrons (pe) distribution after the cross-talk correction. A big discrepancy is found in the low photo-electron region. These hits only appeared in real data are not synchronized with the neutrino event according to eye scan. We select the hits with 2.0 pe threshold.

Hit Finding Efficiency

The hit finding efficiency of the n-th plane of each x and y view, $\epsilon^{\rm n}_{\rm hit}$, is defined as:

$$\epsilon^{\rm n}_{\rm hit} = \frac{\text{\# of events with hit on the n-th plane}}{\text{\# of events with hits on the (n-1)-th and (n+1)-th plane}} \tag{6.1}$$

for cosmic-ray muon events.

Figure 6.3 shows a schematic view of the cosmic-ray event. Both hits at the most upstream (1st) and most downstream (64th) plane are required in order to select the clean single tracks. The result of the hit finding efficiency of each plane in x and y views are shown in Fig. 6.4. Both data and the MC simulation show the good hit finding efficiency of more than 99 %. We also check the hit finding efficiency as a function of the light path-length in the WLS fiber since the light is attenuated in the fiber. Fig. 6.5 shows the averaged hit finding efficiency of all the planes in x and y views as a function of the light path-length in the WLS fiber shown in Figure 6.3. The efficiency is uniform for whole region because of the very low threshold.

6.1.2 Track finding efficiency

We estimate the track finding efficiency by using cosmic-ray muons and the muons from neutrino event occurred inside the SciFi detector.

Figure 6.6 illustrates the method with cosmic-ray muons. At first, we select the single track events. Then we mask some hits in the upstream and downstream region. After that, we re-apply the track finding algorithm to a partially masked hit sequence of the track. The efficiency is measured as follows.

$$\text{efficiency} = \frac{\text{\# of single track events after masking}}{\text{\# of single track events}} \tag{6.2}$$

Figure 6.7 shows the result of the track finding efficiency as a function of the number of planes used in the track finding. The track finding efficiency is more than 98% for a track length of

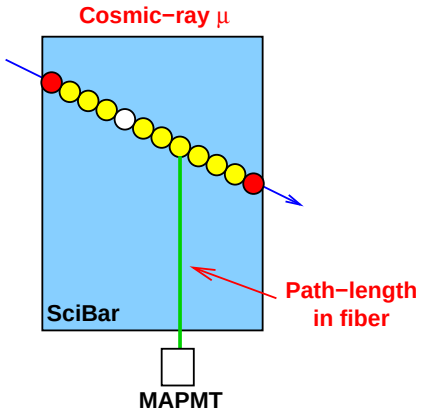

Figure 6.3: Schematic view of the cosmic-ray event. both hits on upstream (1st) and downstream (64th) plane are required in the analysis.

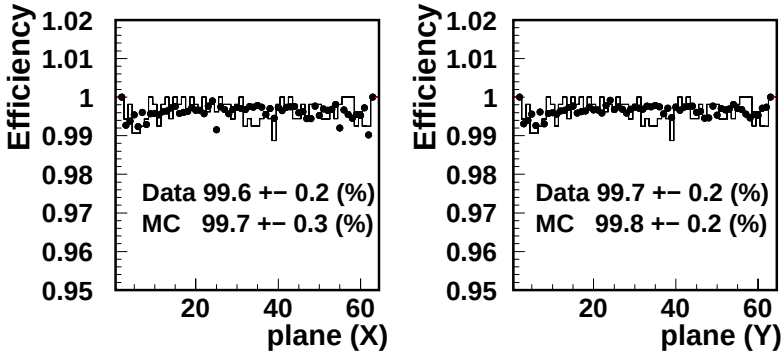

Figure 6.4: The hit finding efficiency for each plane using cosmic-ray muons. The closed circles are data and the histogram shows the MC data.

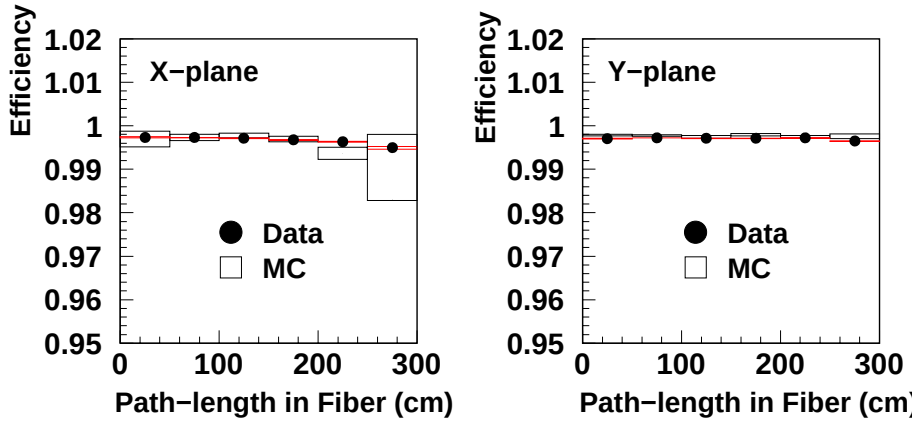

Figure 6.5: The hit finding efficiency as a function of the path-length in the WLS fiber. The closed circles and boxes are data and the MC expectation, respectively. The efficiency is uniform for whole region inside the detector.

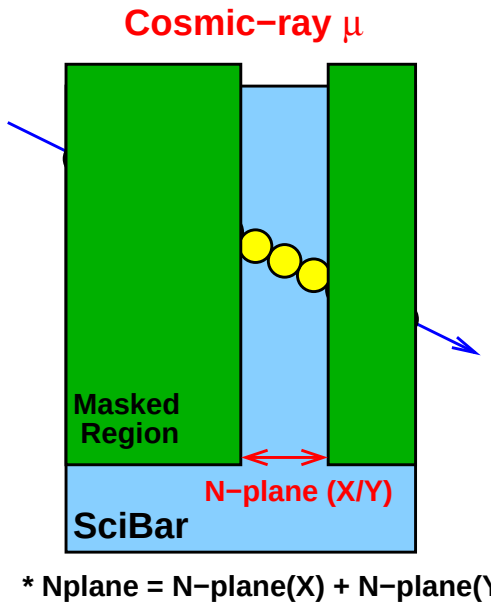

Figure 6.6: The schematic view of the method to estimate a track finding efficiency with cosmic-ray muons. The track finding algorithm is re-applied after some parts of hits are masked.

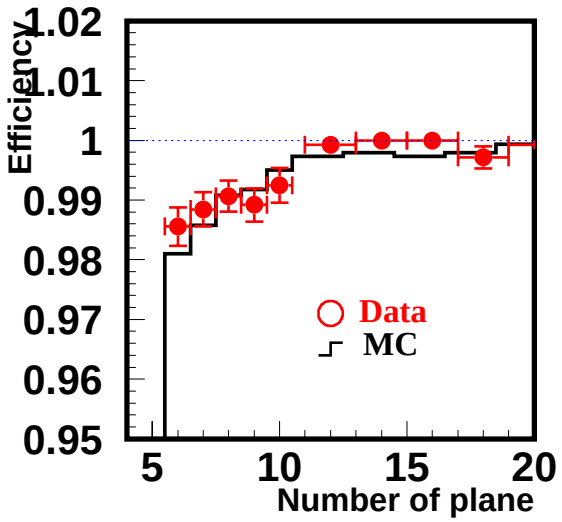

Figure 6.7: The track finding efficiency estimated with cosmic-ray muons. For both data and the MC simulation, more than 98% efficiency is achieved for all tracks with the track length more than 6 planes ($\sim$ 8 cm).

more than 6 planes ($\sim$ 8 cm) and reaches almost 100% at 12 planes ($\sim$ 16 cm) for both data and the MC simulation.

Figure 6.8 illustrates how to estimate the track finding efficiency with the SciFi track. We require the following condition to select the clean isolated track from SciFi with the expected length of more than 8 cm in SciBar;

- Track starts from the upstream half of SciFi to remove the mis-reconstructed tracks.
- The track goes out from the most downstream layer of SciFi
- The extrapolation of the track is matched to hits of the trigger counter. The matching condition is that the residual distance is less than 50 cm for both of x and y views.
- The extrapolation of the track is matched to the hits at both the first layer and the third layer of SciBar. The matching condition is same as that for the trigger counter.

The number of selected events is defined as $N_{\rm exp}^{\rm SB}$.

We apply the tracking algorithm to the selected events and count the number of tracks matched with the SciFi track. The matching condition is that the position residual between the extrapolation of SciFi track and the start point of the reconstructed SciBar track is less than 50 cm, and the angle between them is less than 0.4 radian for both projection. The number of selected events is defined as $N_{\rm obs}^{\rm SB}$.

The track finding efficiency defined as $N_{\rm obs}^{\rm SB}/N_{\rm exp}^{\rm SB}$ is measured to be 99.2$\pm$0.1% for data and 99.1$\pm$0.1% for MC, respectively. Therefore, the track finding efficiency of isolated single track is very high. The MC simulation reproduce data well.

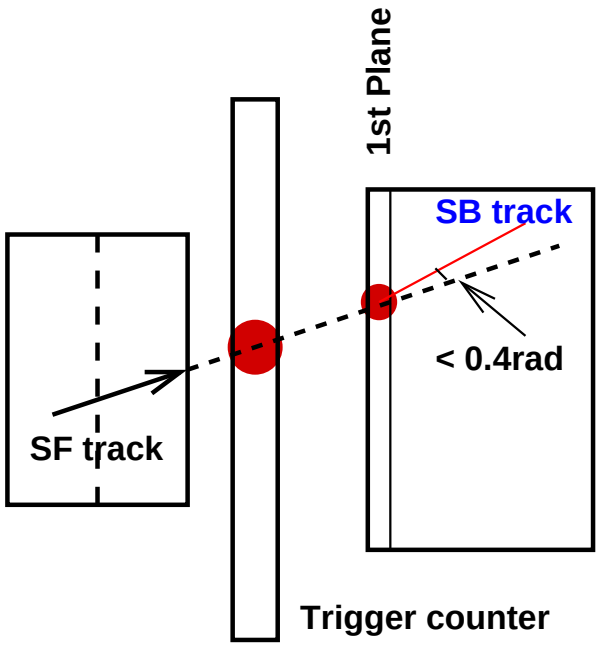

Figure 6.8: The schematic event display of SciFi events matching to SciBar. The matching condition between SciFi and SciBar tracks are also shown.

6.2 Muon Identification

CC events with a muon are used for the analysis. We identify the muon tracks by requiring that the reconstructed track starting in SciBar is matched with a track or hits in MRD as shown in Fig. 6.9. In this section, we describe the muon identification.

6.2.1 Selection

SciBar-MRD 3D matching track

The SciBar track which matches with the MRD track is defined as the SciBar-MRD 3D track. The matched MRD track is required to start from the first chamber plane in MRD and to stop inside MRD in order to reconstruct the muon energy using its range information correctly. The matching condition is that the residual distance between the extrapolation of the SciBar track and the start point of the MRD track is less than 20 cm, and the angle between them is less than 0.5 radian for both x and y projections. When more than two SciBar-MRD 3D tracks are found, the most energetic one is selected as the muon track.

SciBar-MRD 1L matching track

The SciBar track which matches with hits at the MRD first layer is defined as SciBar-MRD 1L track excluding MRD-3D track. The matching condition is the differences between the extrapolation of the SciBar track and the MRD first layer hits are less than 20 cm for both X and Y projections. When more than two SciBar-MRD 1L tracks are found, the most energetic one is selected as the muon track.

Performance

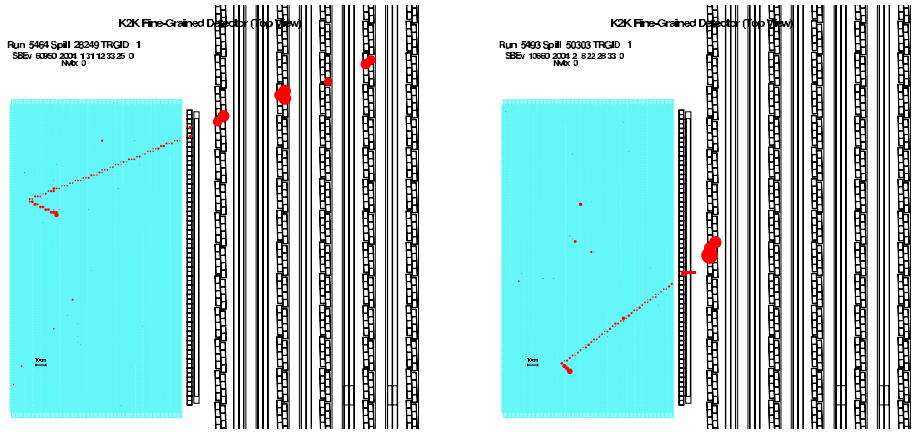

Figure 6.9: The event display of SciBar with a track matched to the MRD track (left) and the MRD hit (right).

Figure 6.10 shows the true muon momentum distribution and the selection efficiency as a function of the muon momentum estimated with the MC simulation. Here, the selection efficiency is defined as:

$$\text{efficiency} = \frac{\#\text{ muons selected as the SciBar-MRD track in the SciBar fiducial volume}}{\#\text{ muons generated in the SciBar fiducial volume}}$$

where we define the fiducial volume in the next subsection. As shown in the left figure in Figure 6.10, the SciBar-MRD track selection imposes a threshold for muon momentum, p_μ, of 0.40 GeV/c. The efficiency increases with the muon momentum and reaches 90% at the momentum of 1 GeV/c. However, the efficiency drops above 3 GeV/c because the muon is not contained in MRD.

6.2.2 Vertex finding and fiducial volume definition

Vertex definition

We define the upstream edge of the SciBar-MRD matching track as the interaction vertex as shown in Fig. 6.11. Figure 6.12 shows the vertex resolution estimated with the MC simulation. For the x and y directions, the resolution is 0.7 cm. As for the z direction, the resolution if 0.5 cm with the second peak due to the cross-talk.

Fiducial volume

We select the events whose vertex is in the SciBar fiducial volume of 260cm $\times$ 260cm $\times$ 135.2cm, which corresponds to 9.38t. Figure 6.13 shows the vertex distributions for all the SciBar-MRD events together with the MC expectation. The definition of the fiducial volume is also shown. In total, 11463 SciBar-MRD events are found in the SciBar fiducial volume. All the SciBar-MRD events are used for the neutrino energy spectrum measurement described in Chapter 8. The partial data of 10049 SciBar-MRD events obtained in K2K-IIb are used for the cross section measurement of CC coherent pion production described in Chapter 7.

Timing distribution and non neutrino-induced background

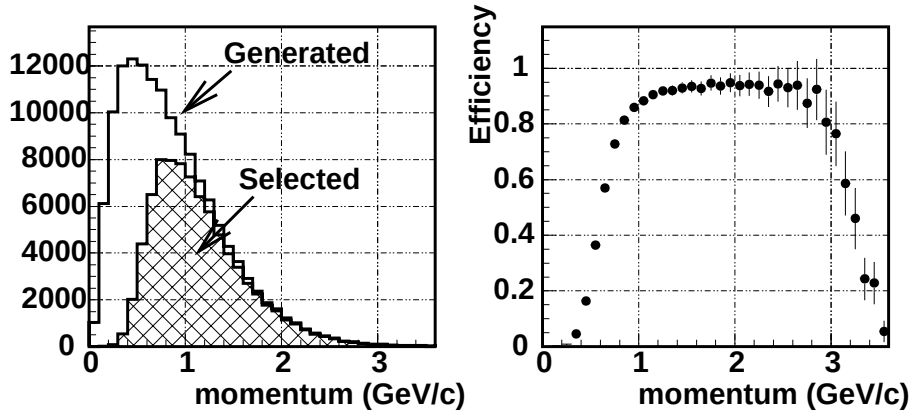

Figure 6.10: The solid line in the left figure shows all the generated muons in the fiducial volume in the MC simulation as a function of the muon momentum. The hatched region shows the muons selected as the SciBar-MRD track. The right figure shows the selection efficiency as a function of momentum. The efficiency is defined as the ratio of the hatched region to the solid line in the left figure.

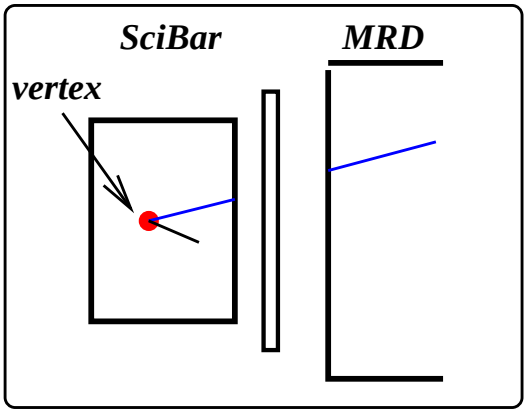

Figure 6.11: The definition of the interaction vertex. We define the upstream edge of the MRD matching track as the vertex.

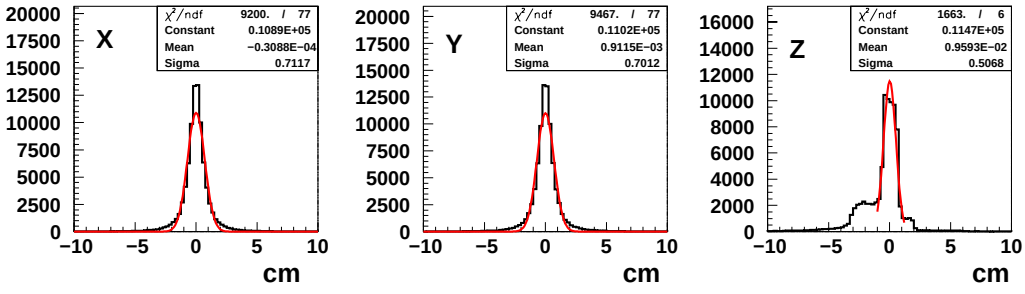

Figure 6.12: The vertex resolution estimated in the MC simulation. The second peak in the z direction is caused by the cross talk effect.

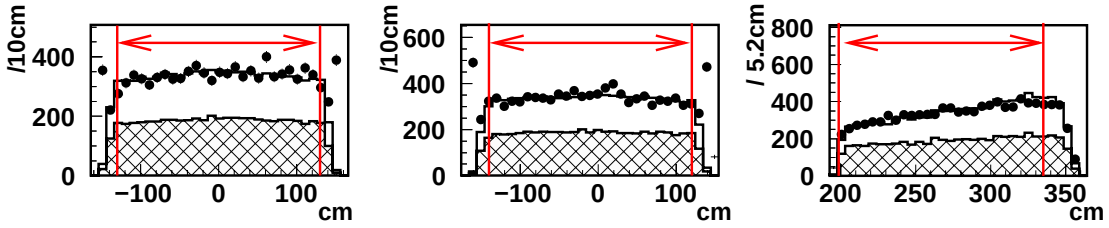

Figure 6.13: The vertex distribution of SciBar-MRD matching events. The black circles, open histogram and the hatched histogram are data, the MC events and the expected QE events, respectively. The definition of the fiducial volume is also shown.

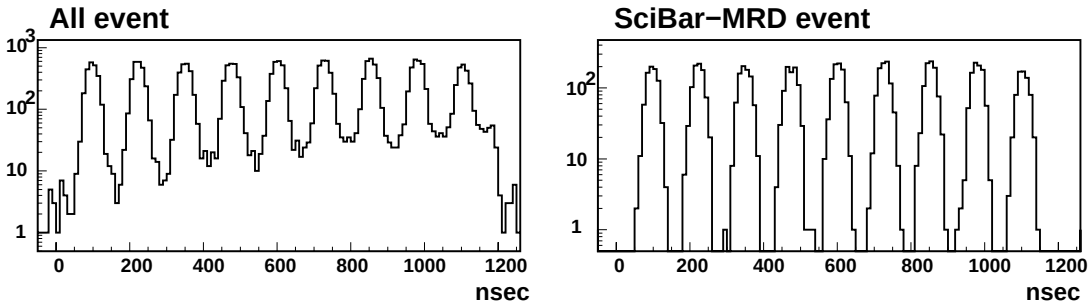

Figure 6.14: The timing distribution of all events, which have one or more reconstructed track inside SciBar (left), and all SciBar-MRD events (right).

Figure 6.14 shows the timing distribution of all events with one or more reconstructed tracks inside SciBar (left), and all events with the SciBar-MRD track (right), respectively. In the left figure in Fig. 6.14, non neutrino-induced events of sky-shine, which increase with time, are seen under the beam timing structure. Those background events are removed by applying the SciBar-MRD event selection. Thus, non neutrino-induced background is negligible after the selection.

Detection efficiency and CC fraction

Figure 6.15 shows the neutrino selection efficiency for all and CC interactions as a function of the neutrino energy, respectively. The efficiency is defined as:

$$\text{selection efficiency} = \frac{\#\text{ all (CC) events selected as SciBar-MRD evens}}{\#\text{ generated all (CC) events in the SciBar fiducial volume}}$$

The efficiencies are estimated to be 43.4 % (3D - 34.1, 1L - 9.3 %) and 58.7 % (3D - 46.8 %, 1L - 11.8 %) for all and CC interaction, respectively. The fraction of the CC events is estimated to be 97.8 % (3D - 99.5 %, 1L - 91.7 %). The rests are neutral current (NC) interactions accompanied by a charged pion or a proton which reaches MRD.

6.2.3 Muon selection efficiency

We estimate the selection efficiency of muons in neutrino interaction by using the following CC candidate events selected without the SciBar track information.

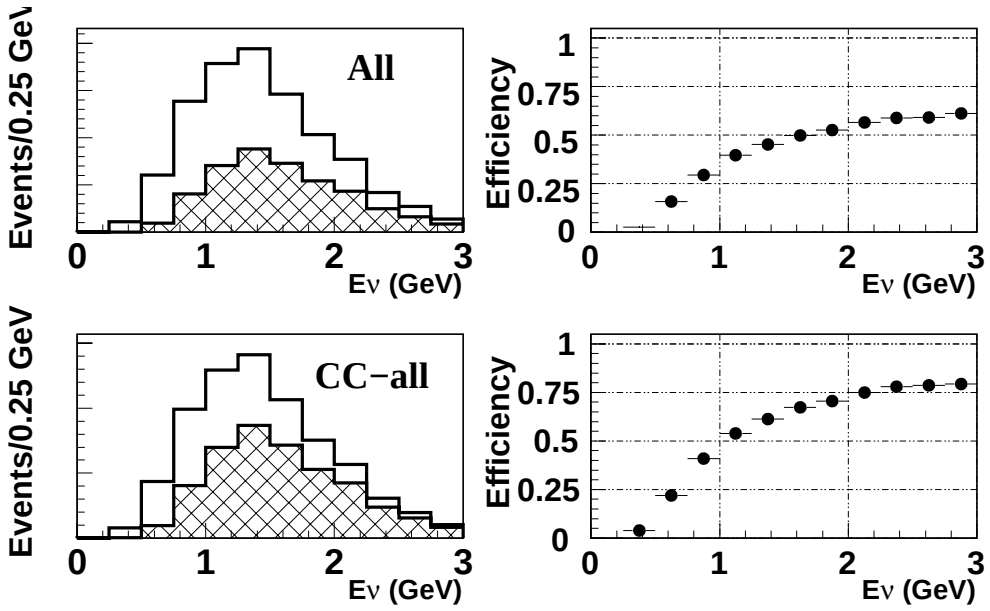

Figure 6.15: The solid line in the left side figures shows all the generated events (upper) and all CC events (lower) in the fiducial volume as a function of the neutrino energy. The hatched region shows the selected events as the SciBar-MRD event. The right side figures show the selection efficiency as a function of the neutrino energy. The efficiency is defined as the ratio of the hatched region to the solid line in the left figure.

1. We choose a MRD track starting from the first chamber layer and stopping inside MRD.
2. We select the events in which the extrapolation of the track to the upstream side is matched to hits of EC for both x and y projection. The matching condition is the residual distance of the expectation is less than 10 cm for each projection.
3. We collect the SciBar hits near the extrapolation of the track. The matching condition is the residual distance is less than 20 cm for each projection.
4. If the most upstream hit which matches with the extrapolation of the MRD track is out of the SciBar fiducial region, we reject the event.

The schematic drawing of the selection is shown in Fig. 6.16. The number of selected CC candidate events are defined as $N_{\rm CC}^{\rm exp}$.

Then we apply the SciBar-MRD matching selection to the CC candidate events. The number of events selected as SciBar-MRD events are defined as $N_{\rm CC}^{\rm select}$. The muon selection efficiency defined as $N_{\rm CC}^{\rm select}/N_{\rm CC}^{\rm exp}$ is measured to be 92.0±0.3% and 91.4±0.2% for data and the MC simulation, respectively. The mis-selection mainly occurs due to the following reasons.

- When the two or more particles go out from SciBar, the combination of 2D tracks is sometimes swapped with each other.
- If the events have many hits around the vertex, the 2D track finding process sometimes fails in connecting hits along the muon correctly. For the events, X-track and Y-track of muon are not paired because the edge position is not matched.

Figure 6.17 shows the muon selection efficiency as a function of the muon angle, where the muon angle is the angle of matched MRD track. Although the efficiency becomes worse with increasing the angle, the slope is not steep and it is well reproduced by the MC simulation.

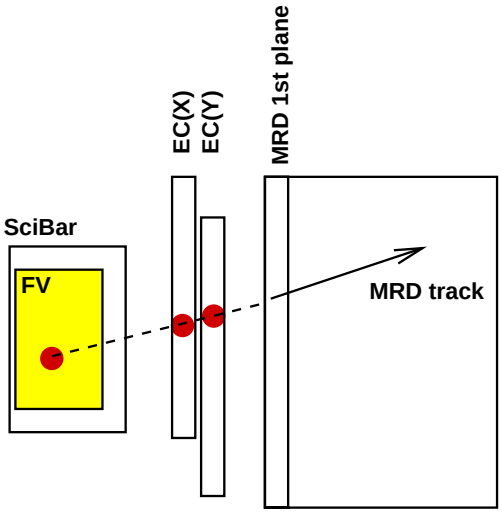

Figure 6.16: The schematic event picture of the selected CC candidate event for the study of muon selection without SciBar tracking information.

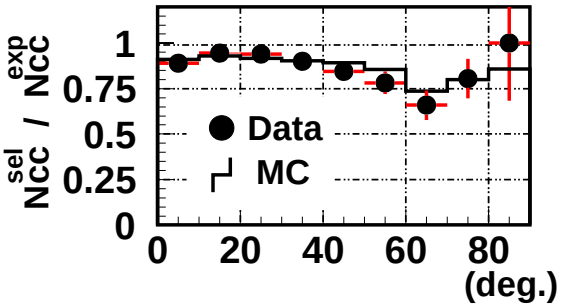

Figure 6.17: Muon selection efficiency vs Muon angle.

6.2.4 Muon energy reconstruction

The energy of the selected muon is reconstructed by using its range through SciBar, EC and MRD as;

$$E_\mu = E_\mu^{\rm SciBar} + E_\mu^{\rm EC} + E_\mu^{\rm MRD}, \tag{6.3}$$

$$E_\mu^{\rm X} = \left(\frac{dE}{dx}\right)^{\rm X} \cdot L^{\rm X}, \qquad {\rm X} = \ {\rm SciBar,\ EC} \tag{6.4}$$

where $E_\mu^{\rm X}$ (X=SciBar, EC, MRD), $L^{\rm X}$ (X=SciBar, EC) and $(dE/dx)^{\rm X}$ (X=SciBar, EC) are energy deposit, the track length and the energy deposit per unit length in each detector. The track length inside EC is calculated by using the SciBar track. The values of 2.10 MeV/cm and 11.25 MeV/cm are used for dE/dx in SciBar and EC, respectively. $E_\mu^{\rm MRD}$ is calculated from the range-to-energy look-up table based on the GEANT MC code, where $E_\mu^{\rm MRD}$ includes the muon mass.

Figure 6.18 shows the muon momentum distribution of the SciBar-MRD sample. The MC simulation well reproduce the observation. Figure 6.19 shows the resolution of E_μ estimated in the MC simulation. The resolution is about 80 MeV and dominated by the MRD resolution. The systematic uncertainty for E_μ is estimated to be 2.7 % in which the 1.0 % comes from the uncertainty of iron density and the 1.7 % comes from the dE/dx uncertainty of MRD [44].

6.2.5 Muon angle

Figure 6.20 shows the distribution of muon angle with respect to the beam direction of all the SciBar-MRD events. The MC simulation well reproduce the data. Figure 6.21 shows the angular resolution estimated by the MC simulation. The resolution for the 3D angle and the 2D angle in the projection to the X view and the Y view are evaluated to be 1.6, 1.0 and 1.0 degrees, respectively.

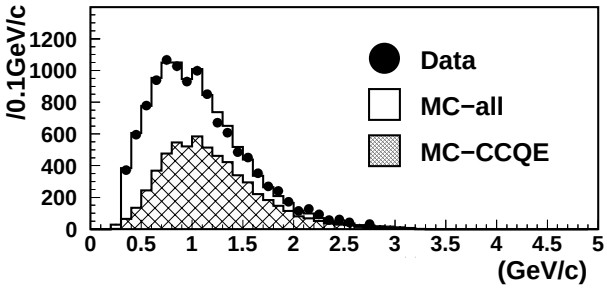

Figure 6.18: The muon momentum distribution for MRD sample. The black circles, open histogram and hatched histogram show data, the MC expectation and the expected CC-QE component, respectively. The MC expectation is normalized by entries.

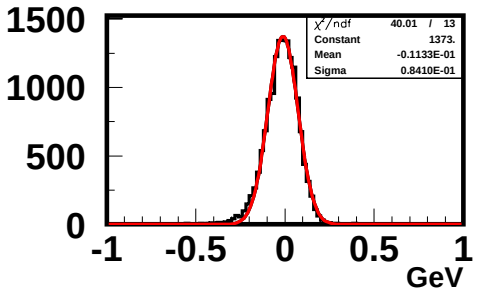

Figure 6.19: The muon energy resolution estimated by the MC simulation.

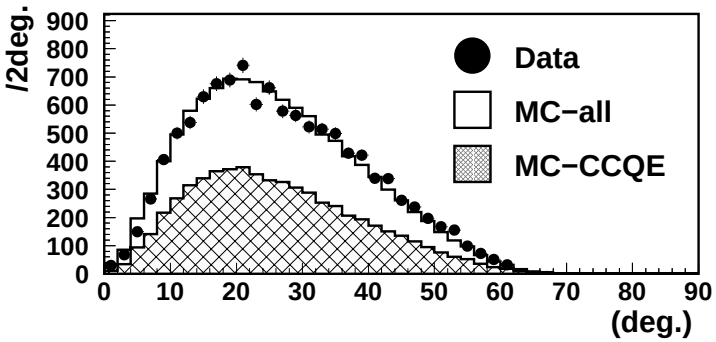

Figure 6.20: The distribution of muon angle with respect to the beam direction. Black circles, open histogram and hatched histogram show data, the MC expectation and the expected CC-QE component, respectively. The MC expectation is normalized by entries.

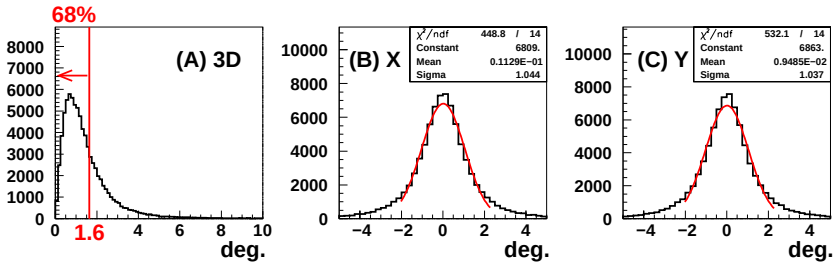

Figure 6.21: The angular resolutions estimated by the MC simulation. Figure (A) shows the 3D residual angle between the true and the reconstructed direction. Figure (B) and (C) show the angle in the projection to the X view and Y view, respectively.

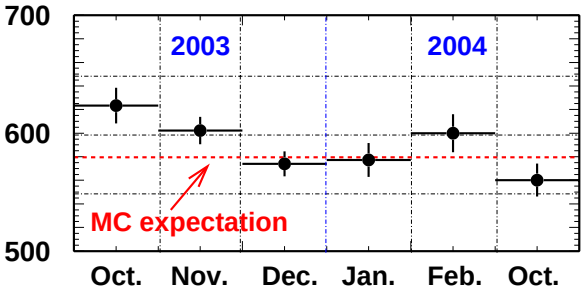

Figure 6.22: The number of MRD matching events (CC candidate events) per 10^{18} POT for each month. The dashed line shows the expected event rate.

6.2.6 Event rate

The number of SciBar-MRD events per 10^{18} POT for each month is shown in Fig. 6.22. The observed event rate is stable within the statistical fluctuation and consistent with the MC expectation. The expectation is derived by using the neutrino flux from Beam-MC, the cross section of neutrino-nucleus interaction from NEUT and the SciBar-MRD event selection efficiency from the GEANT simulation.

6.3 Track Counting and the Second Track Efficiency

6.3.1 Track counting

Once a muon track and the interaction vertex are reconstructed, we search other extra tracks originated from the interaction vertex as follows.

1. We calculate the distance between a track edge and the vertex.
2. If the distance is within 9.0 cm in the x and y directions and within 4.5 cm in the z direction, we count the track originated from the vertex. The 95% of QE events with two reconstructed tracks identified as a muon and a proton are selected as two track event after applying this cut in the MC simulation.

Figure 6.23 and 6.24 show the residual distance of each projection and the number of tracks originated from the vertex, respectively. The one or two track events are used for the analysis in this thesis. Hereafter, for two track events, the SciBar-MRD track is defined as the first track and the other track is defined as the second track.

6.3.2 Second track finding efficiency

We evaluate the second track finding efficiency by eye-scanning because we do not have any good control sample. Figure 6.25 shows the result of the second track finding efficiency and the ratio of data to the MC events, as a function of the number of hits along the second track from the vertex. As shown in the figure, the MC events reasonably agree with data. We take into account the difference between them as a systematic error.

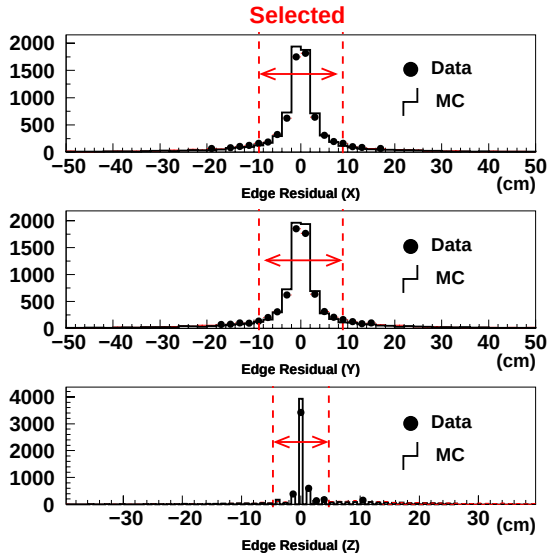

Figure 6.23: The start position difference between the muon track and a second track in each axis. In the figures, the black circles and the histogram show data and the MC events, respectively. The criteria for track counting is also shown.

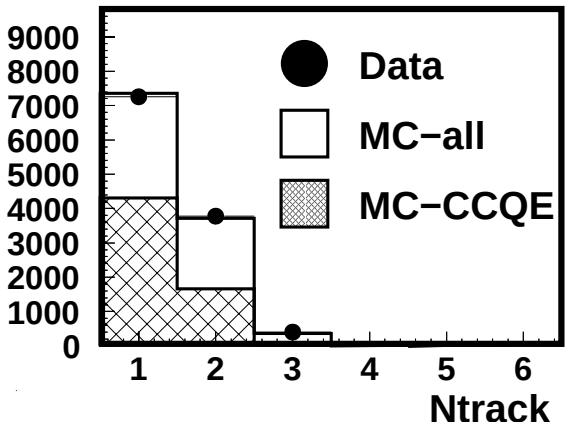

Figure 6.24: The number of tracks originated from the vertex. The points show data. The open and the hatched histogram show the MC simulation and the expected QE events, respectively. The MC events are normalized by entries.

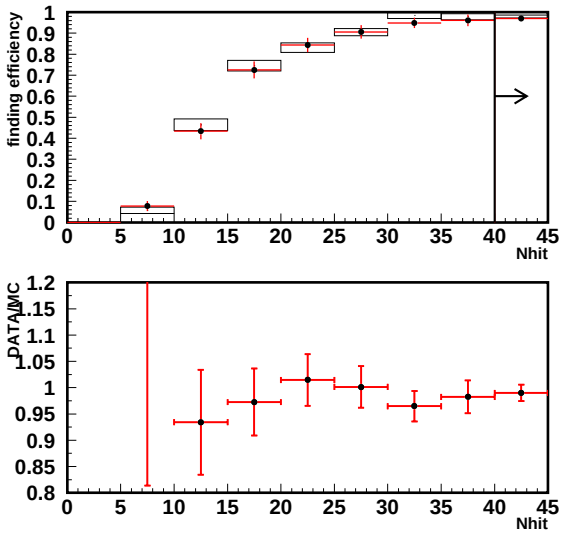

Figure 6.25: The upper figure shows the second track finding efficiency evaluated by the eye-scanning for data and the MC events as a function of the number of hits. The bottom figure shows the ratio of data to the MC events.

6.4 QE and nQE Event Selection

For two track events in the CC sample, we divide them into two categories — QE and non-QE samples — by using kinematic information. Assuming QE interaction, the proton direction is predicted from p_μ and θ_μ as

$$\vec{p_p} = (-p_{\mu x}, -p_{\mu y}, p_\nu^{rec} - p_\mu \cos\theta_\mu) \tag{6.5}$$

where,

$$p_\nu^{rec} = \frac{1}{2}\frac{(M_p^2 - m_\mu^2) + 2E_\mu(M_n - V) - (M_n - V)^2}{-E_\mu + (M_n - V) + p_\mu \cos\theta_\mu} \tag{6.6}$$

and $p_{\mu x}$, $p_{\mu y}$ and V are the projected muon momentum of the x and y view and nuclear potential set at 27 MeV.

Using this formula, we calculate the angular difference between the observed second track direction and the expected direction ($\Delta\theta_p$) as

$$\cos\Delta\theta_p = \frac{-p_{\mu x}\tan\theta_{xz} - p_{\mu_y}\tan\theta_{yz} + p_\nu^{rec} - p_\mu\cos\theta_\mu}{\sqrt{[(p_\nu^{rec})^2 + p_\mu^2 - 2p_\nu^{rec}p_\mu\cos\theta_\mu][\tan^2\theta_{xz} + \tan^2\theta_{yz} + 1]}} \tag{6.7}$$

where θ_{xz} and θ_{yz} are the second track angle of each view with respect to the beam direction.

Fig 6.26 shows the $\Delta\theta_p$ distribution. Events with $\Delta\theta_p$ less than 25 degrees are selected as the QE sample and events with $\Delta\theta_p$ more than 25 degrees are selected as the nonQE sample. With this selection, the QE fraction is 72% in the QE sample, and the nonQE fraction is 83% in the nonQE sample.

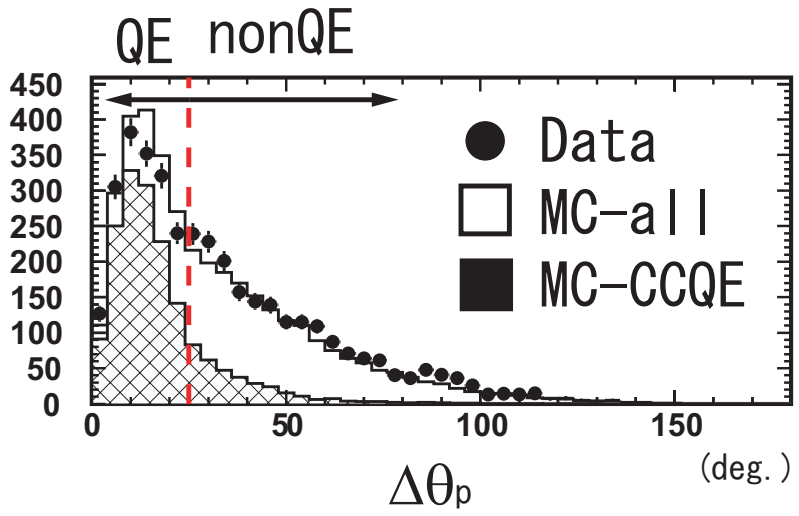

Figure 6.26: The $\Delta\theta_p$ distribution of the 2-track sample. Hatched area are QE components in the MC distribution.

6.5 Particle Identification (Proton/Pion separation)

Figure 6.27 shows the dE/dx distributions of the SciBar-MRD 3D matching track and the second track of the QE sample, in which the proton purity is estimated to be about 90%. The proton

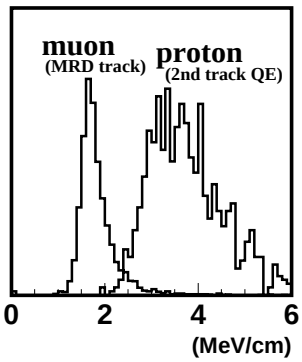

Figure 6.27: The distributions of the energy deposit per unit length for the muon candidate track matched with MRD and the proton candidate track in the QE sample.

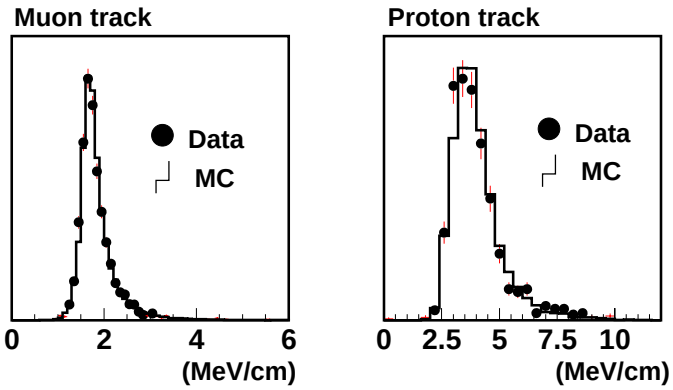

Figure 6.28: The dE/dx distributions of SciBar-MRD track (muon) and the second track in QE sample (proton) for data and the MC simulation.

track is clearly separated from the muon track. Since the pion track gives a similar dE/dx as the muon track, we perform the separation of proton from the pion by using the dE/dx information. As shown in Fig. 6.28, the MC simulation well reproduce the observed dE/dx distribution of a muon and a proton.

Definition of particle identification variable; MuCL

The first step of the particle identification is to estimate a confidence level that a particle is identified as a muon (pion) at plane-by-plane. The confidence level at each plane is defined as a fraction of events in the muon (pion) dE/dx distribution above the observed energy deposition per length, $(dE/dx)_{\rm obs}$. The dE/dx distribution of a muon is obtained from cosmic ray muons as shown in the top figure of Fig. 6.29. The bottom figure in Fig. 6.29 shows the result of the confidence level as a function of $(dE/dx)_{\rm obs}$. The confidence level at the i-th plane is referred to as CL_i.

The next step is to combine the CL_i obtained from all the planes penetrated by a track to form a likelihood. In the case of two planes, the procedure to combine the two confidence levels of CL_1 and CL_2 is as follows. If we assume the two confidence level to be independent of each other, the product $P = CL_1 \times CL_2$ is the combined probability. In the (CL_1, CL_2) plane, the hyperbola $P = CL_1 \times CL_2$ gives such a combined probability and the event which has a higher confidence level will be above the hyperbola. Therefore, the hatched area indicated in Fig. 6.30 can be considered as a unified confidence level CL_{12}, which is expressed as

$$CL_{12} = 1 - \int_P^1 d(CL_2) \int_{P/CL_2}^1 d(CL_1) \quad (6.8)$$

$$= P(1 - \ln P) \quad (6.9)$$

By analogy for the case of the two planes, the confidence level combined from n planes muon confidence level, MuCL, is expressed as

$$\mathrm{MuCL} = \Pi CL_i \times \Sigma_j \frac{(-\ln \Pi CL_i)^j}{j!}. \quad (6.10)$$

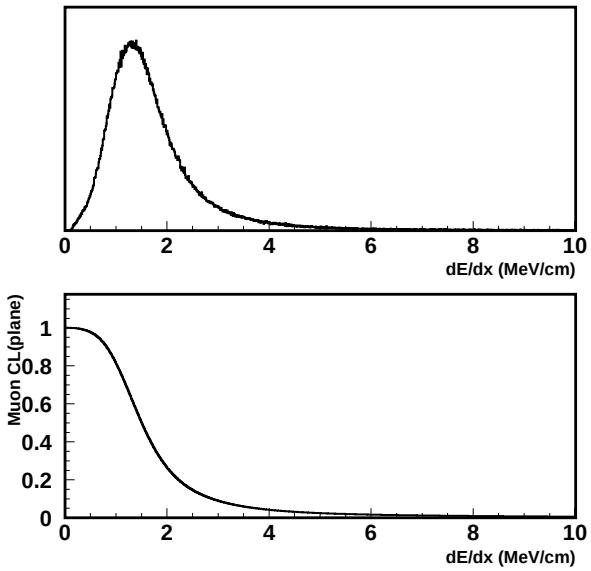

Figure 6.29: Upper figure shows dE/dx distribution of cosmic ray muon. Lower figure is muon confidence level as a function of dE/dx in each scintillator plane.

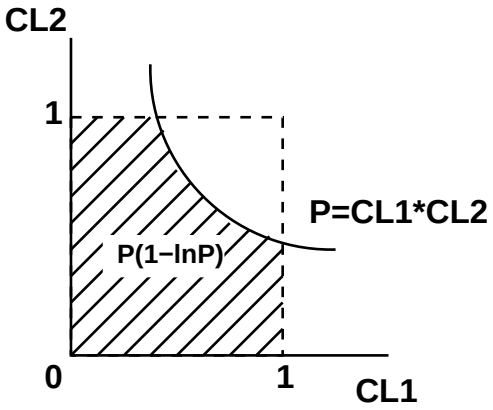

Figure 6.30: The hyperbola obtained from two independent confidence level, CL_1 and CL_2. This shaded area corresponds to the confidence level combined together from the two.

We sort CLs for each plane in a track sequentially from the bigger one and truncate CLs of 20% from the larger ones and 50% from the smaller ones for avoiding the effects of the inefficiency of scintillator (Fig. 6.31) and of track overlapping in one view.

Performance

Figure 6.32 shows the MuCL distribution of the muons and the protons. The muons and the protons are clearly separated. The probability to mis-identify a muon track as a proton is 1.92 ± 0.14 % and 1.76 ± 0.05 % for data and the MC events with the proton selection efficiency of 90 %.

nonQE-pion/nonQE-proton event selection

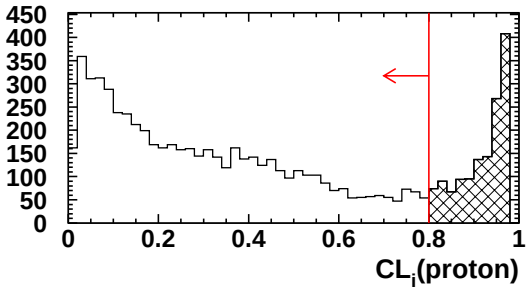

Figure 6.31: The CL_i distribution of proton track. A clear peak around 1 is caused by the inefficiency of scintillator. The 20% of CLs from larger ones shown by hatched histogram are not used for PID.

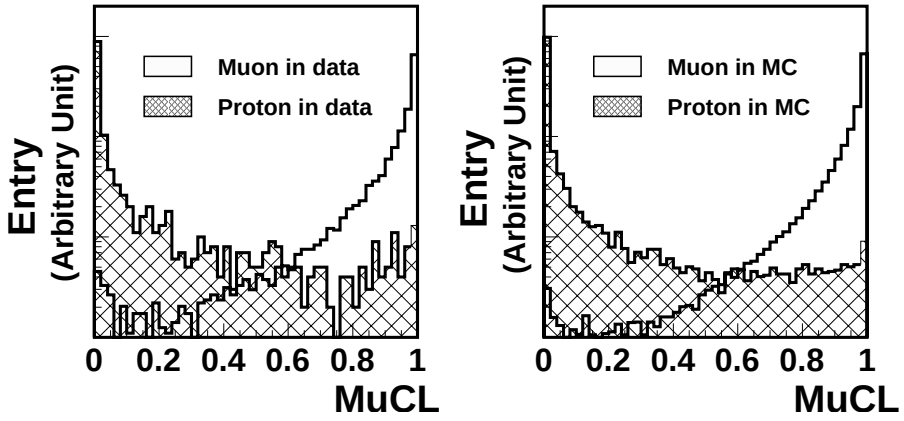

Figure 6.32: The MuCL distribution of the muon tracks and the proton tracks for data (left) and the MC events (right). The muons have a peak at 1, while the protons have a peak at 0.

The second track in the non-QE sample is then classified as a proton-like or a pion-like track by the PID algorithm. Figure 6.33 shows the MuCL distribution of the second track in the nonQE sample, which shows a good agreement between data and the MC simulation. Events with the MuCL more than 0.10 are categorized as a nonQE-pion sample and events with the MuCL less than 0.10 are categorized as a nonQE-proton sample. The efficiency and the fraction of the proton track in the nonQE-proton sample are 85 % and 80% estimated by the MC simulation, respectively.

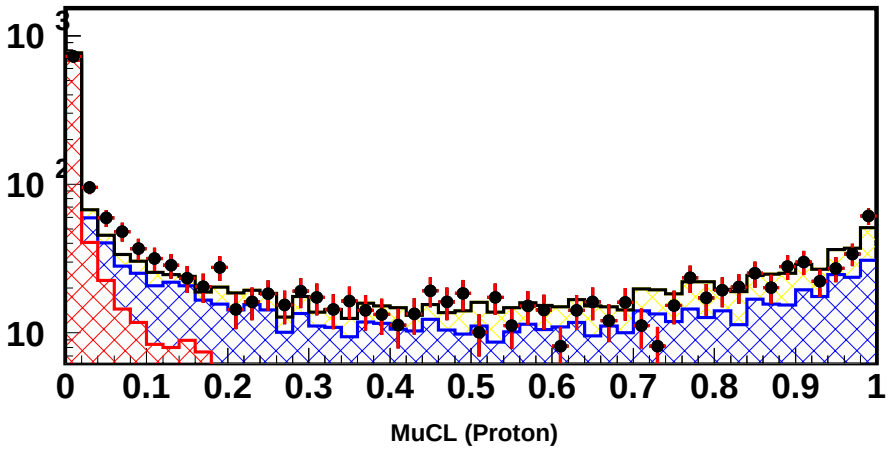

Figure 6.33: The MuCL distribution of the nonQE sample. The red hatched histogram is shown for protons, the blue is for pions, and the yellow is for other particles.

6.6 Selection and Data Summary

Figure 6.34 shows the summary of the event selections described in this chapter. After selecting the CC candidate events and applying the selections described in this chapter, the SciBar events are classified into the following four sub-samples;

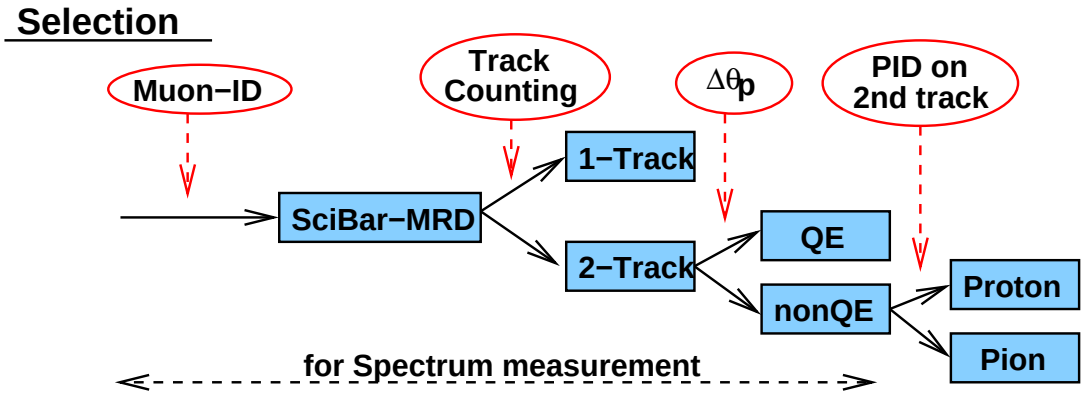

Figure 6.34: The analysis flow of the SciBar CC events.

Table 6.1: The summary table for the number of events in each subsample used in the CC coherent pion analysis and the spectrum measurement, respectively. The efficiency and fraction of the QE events are also shown.

Event category	Coherent analysis	Spectrum measurement	QE efficiency (%)	QE fraction (%)
1-track	6255	7256	50.0	57.8
QE	1623	1760	15.4	71.3
nQE	1773	2014	3.7	15.9
nQE-proton	930	-	2.9	26.3
nQE-pion	843	-	0.8	6.2

- 1-track sample
- 2-track QE enriched sample (QE sample)
- 2-track nonQE enriched sample in which second track is proton-like (nonQE-proton sample)
- 2-track nonQE enriched sample in which second track is pion-like (nonQE-pion sample)

The PID selection is not applied for the spectrum measurement as shown in the figure. The number of observed events in each subsample is summarized in Table 6.1 together with the efficiency and fraction of the QE event. The neutrino data of 20.3×10^{18} POT and 17.4×10^{18} POT are used for the neutrino spectrum measurement and the cross section measurement of CC coherent pion production, respectively.

Chapter 7

Study of Charged Current Coherent Pion Production

In this chapter, we describe the cross section measurement of CC coherent pion production with SciBar data. This is the first experimental result in the neutrino energy region of a few GeV. First, the motivation of this study and the theoretical models of the cross section are provided. Then, the analysis and result are presented in detail. The improvement on our MC simulation based on the result is also discussed in the last part of this chapter. The analysis and result in this chapter are also summarized in [94].

7.1 Motivation

Observation of a low-q^2 deficit

Figure 7.1 shows the reconstructed four momentum transfer squared ($q^2_{\rm rec}$) of all the CC candidate events. Here, q^2 is reconstructed with muon momentum (p_μ) and angle (θ_μ) with respect to the ν_μ beam direction by assuming QE interaction as,

$$q^2_{rec} = 2E_\nu(E_\mu - p_\mu \cos\theta_\mu) \tag{7.1}$$

$$E^{rec}_\nu = \frac{1}{2}\frac{(M_p^2 - m_\mu^2) + 2E_\mu(M_n - V) - (M_n - V)^2}{-E_\mu + (M_n - V) + p_\mu \cos\theta_\mu} \tag{7.2}$$

V : Nuclear Potential = 27MeV

In this figure, the MC expectations are shown separately for each interaction mode of QE, CC1π, coherent π, multi π and all neutral current interaction (NC). The coherent π components are estimated with the Rein and Sehgal model as will be discussed in Section 7.2.1. The other components are estimated with models described in Section 4.2. In this chapter, all figures are presented with the same manner unless otherwise specified.

As shown in Fig. 7.1, a small but significant discrepancy is seen for the events with $q^2_{\rm rec}$ less than 0.10 (GeV/c)^2. This discrepancy is also observed by other near detectors [44, 52, 55] and the MiniBooNE experiment [95]. This means that it is not due to the detector systematics. Furthermore, this discrepancy cannot be explained by the uncertainty of the neutrino energy spectrum. Therefore, the neutrino interaction model is considered as the source. However we do not figure out which interaction mode is the source. This is known as "low-q^2 problem" [96] and unsolved for over five years. Since this deficit may bias the neutrino energy spectrum measurement according to the toy MC study [44], to identify the cause of this problem is indispensable for the oscillation analysis.

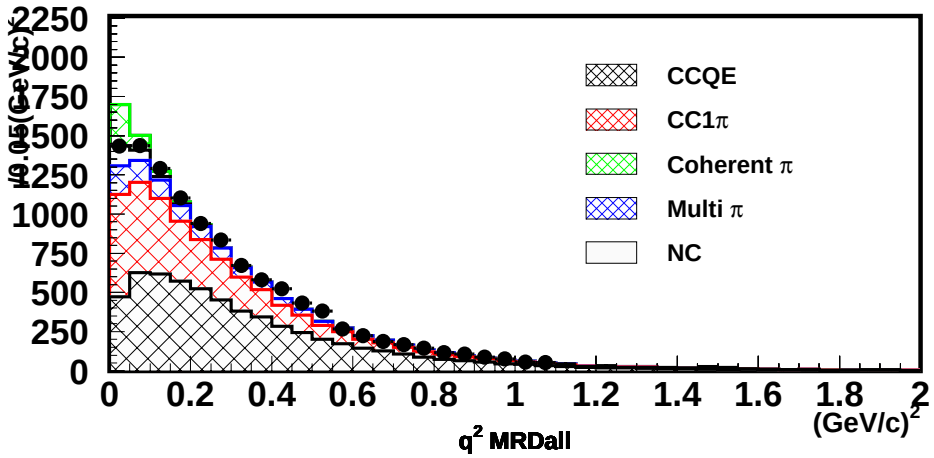

Figure 7.1: The $q^2_{\rm rec}$ distribution of all the CC candidate events. A small but significant discrepancy is seen for the events with $q^2_{\rm rec}$ less than 0.10 $(\mathrm{GeV/c})^2$.

A hint of the solution on the low-q^2 problem

Figure 7.2 shows the $q^2_{\rm rec}$ distribution of the 1-track, QE, nonQE-proton and nonQE-pion samples. A clear deficit is seen in the 1track and nonQE-pion sample. Because the QE component is very little in the nonQE-pion sample, QE is not the source of the low-q^2 deficit. Also the amount of the multi-π component is not sufficient to explain the deficit in the nonQE-pion sample. In addition, a deficit is not seen in the nonQE-proton sample. Thus, CC coherent pion production is the most suspicious mode as a cause of the low-q^2 deficit. This is the motivation on the analysis in this chapter. For the cross section measurement of CC coherent pion production, many past experimental data exist in the neutrino energy region from 7 to 100 GeV [97–101], while there is no measurement at lower energies. Therefore, this analysis gives the first experimental result of neutrino induced CC coherent pion production in the few GeV region.

7.2 Coherent Pion Production

Coherent pion production is the neutrino interaction with a whole nucleus instead of an individual nucleon. Because all of the nucleons respond in phase, i.e., the overall scattering amplitude is expressed to be a sum of amplitude of an individual nucleon, the process is referred to as "coherent". Because the nucleus must remain unaltered, the signature of coherent pion production is as follows,

1. The momentum transmitted to any nucleon must be small enough that it remains bound in the nucleus, i.e.,
$$|\mathbf{q}|c\ (\mathrm{MeV}) < \frac{\hbar c(\mathrm{MeV}\cdot\mathrm{fm})}{R(\mathrm{fm})}$$
where R is the nuclear radius.

2. The transfer of charge, spin, isospin, or any additive quantum number is forbidden.

3. For non-zero scattering angles, the process is suppressed by a factor $\sin^2 2\theta_\mu \leq (1/R\nu)^2$, since $K_T \sim \nu \sin\theta_\mu \leq 1/R$ [102], where K_T is the momentum transfer to a nucleus from

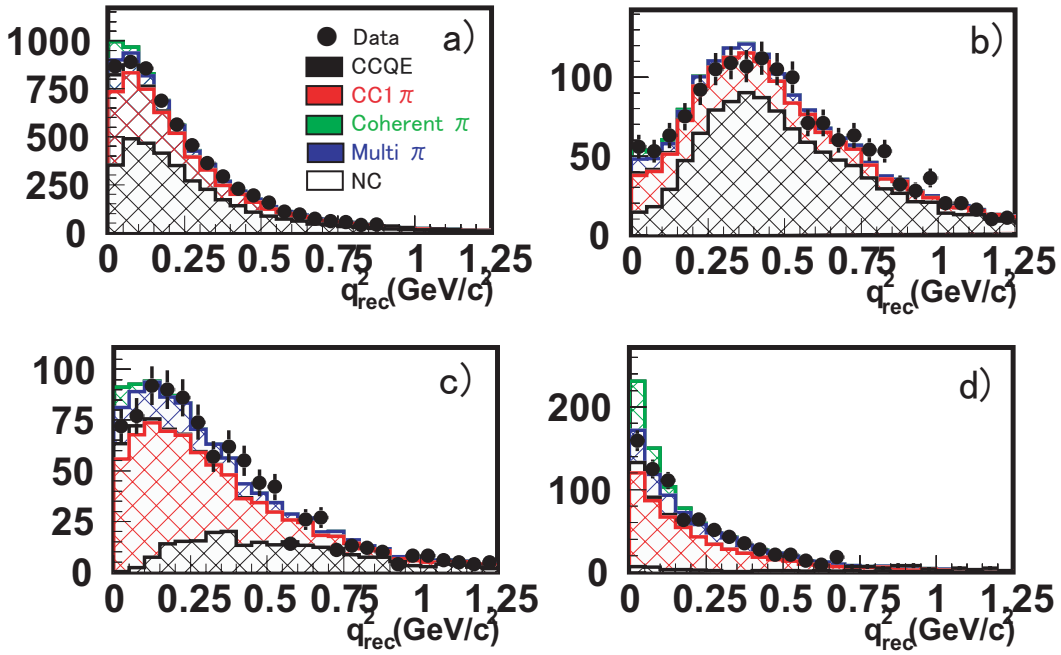

Figure 7.2: The $q^2_{\rm rec}$ distribution for the (a) 1-track, (b) QE, (c) nonQE-proton and (d) nonQE-pion samples.

pion, and ν is the energy transfer to a muon from neutrino. Thus the scattered muon angle is less than about 40 degrees for carbon or oxygen nucleus, while the scattered pion angle is generally not suppressed unlike muon.

There are many proposed theoretical predictions for the cross section [103–107]. They are built on the basis of Adler's theorem [108], relating the neutrino scattering cross section $\sigma(\nu_\mu \mathcal{N} \to \mu X)$ to the pion scattering cross section $\sigma(\pi \mathcal{N} \to X)$ at $q^2 = 0$. However, the predictions vary widely, especially around a energy region of the few GeV region as shown in Fig. 7.3. In the figure, the existing experimental results for NC coherent pion production are also shown, where they are scaled to the case of carbon target and CC production by assuming an $A^{1/3}$ dependence of the cross section (σ) and the relation of $\sigma(\mathrm{CC}) = 2\sigma(\mathrm{NC})$. The results are consistent with the prediction of the Rein and Sehgal and Marteau model.

7.2.1 Theoretical approach to the cross section

Cross section at $q^2 = 0$

Based on the validity of the partially conserved axial-vector current (PCAC) hypothesis, the Adler's theorem [108] provides a relation between the single pion production and the pion-nucleus elastic scattering cross section:

$$\frac{d^2\sigma(\nu \mathrm{A} \to \nu\pi \mathrm{A})}{dxdy} = \frac{G^2}{2\pi^2} f_\pi^2 m_N E_\nu (1-y) \sigma(\pi \mathrm{A} \to \pi \mathrm{A}) \tag{7.3}$$

where $G = 10^{-5} m_N^{-2}$ is the weak coupling constant, f_π is the pion decay constant, x and y are Bjorken dimension less variables. Because the axial parts of the neutral and charged currents form a triplet in isospace, we are led to $f_{\pi^0}^2 = (\sqrt{1/2} f_{\pi^+})^2 = \frac{1}{2} f_{\pi^+}^2$. Thus, the cross section of neutral current coherent pion is exactly half of the cross section of charged current in the framework.

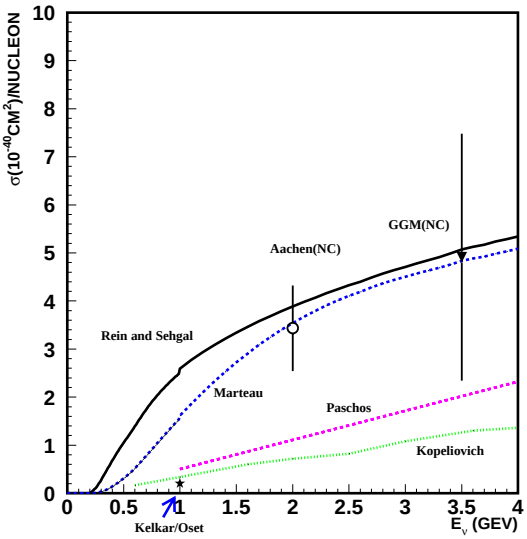

Figure 7.3: The prediction of coherent pion cross section by several models. Existing experimental results are also shown, where the results are scaled to the case of Carbon nucleus and CC production by assuming an $A^{1/3}$ dependence of the cross section (σ) and the relation of σ(CC) $= 2\sigma$(NC).

Cross section at $q^2 \neq 0$

The extrapolation of the cross section to non-zero q^2 is performed based on the method of hadron dominance, which treats interaction current as a superposition of hadrons. The model is an extension of the model used in electromagnetic interactions, the vector meson dominance (VMD) model. The VMD model treats the electromagnetic current as a superposition of the contribution from the lightest vector mesons as

$$\mathcal{A}(\gamma + \alpha \to \beta) = \sum_{V=\rho^0,\omega,\phi} \frac{e}{g_V} \frac{m_V^2}{q^2 + m_V^2} \mathcal{A}(V + \alpha \to \beta) \tag{7.4}$$

In case of weak interaction, the ρ meson is used for the vector current and the π and a_1 mesons are used for the axial current. For the coherent pion case, the a_1 meson contribution is considered to be dominant, and the vector current and the vector - (axial-vector) interference contribution are thought to be negligible [102, 109, 110]. Following the calculation of the VMD model, a cross section is then obtained in terms of the a_1 meson scattering component and extrapolated to non-zero q^2 with an a_1 propagator. The axial vector mass, m_A, is practically introduced in the propagator to consider the additional contributions from other mesons. The cross section for non-zero q^2 is expressed as

$$\frac{d^2\sigma(\nu\mathrm{A} \to \nu\pi\mathrm{A})}{dxdy} = \frac{G^2}{2\pi^2} f_\pi^2 m_N E_\nu (1-y) \left(\frac{m_A^2}{q^2 + m_A^2} \right)^2 \sigma(\pi\mathrm{A} \to \pi\mathrm{A}) \tag{7.5}$$

Basically, the proposed theories agree up to this point except for the Belkov and Kopeliovich model [105] as discussed later. The differences among them are seen only in the way of treating the pion-nucleus scattering cross section. In the following, the Rein and Sehgal model is firstly discussed in detail and then other models are briefly introduced.

Rein and Sehgal approach

By introducing the nuclear form factor, $F_{\mathcal{A}}(t)$, a cross section for pion scattering on nuclei is expressed with that on nucleons as

$$\frac{d\sigma(\pi \mathrm{A} \to \pi \mathrm{A})}{dt} = A^2 |F_{\mathrm{A}}(t)|^2 \frac{d\sigma(\pi \mathrm{N} \to \pi \mathrm{N})}{dt}|_{t=0} \tag{7.6}$$

where A is the atomic number of the nucleus. With the aid of the optical theorem, we find

$$\frac{d\sigma(\pi \mathrm{N} \to \pi \mathrm{N})}{dt}|_{t=0} = \frac{1}{16\pi} \left[\sigma_{\mathrm{tot}}^{\pi \mathrm{N}}\right]^2 (1+r^2), \qquad r = \frac{\mathrm{Re} f_{\pi \mathrm{N}}(0)}{\mathrm{Im} f_{\pi \mathrm{N}}(0)} \tag{7.7}$$

In the model, an average cross section from measurements of pion-deuteron scattering is incorporated as $\sigma_{\mathrm{tot}}^{\pi \mathrm{N}}$. For the nuclear form factor, a simple form of

$$|F_{\mathcal{A}}(t)|^2 = e^{-b|t|} F_{\mathrm{abs}} \tag{7.8}$$

is adopted, where b is related to the nuclear radius R by

$$b = \frac{1}{3} R^2, \qquad (R = R_0 A^{1/3}), \tag{7.9}$$

where $R_0 = 1.0$ fm is used in the model. The uncertainty of the radius is a dominant theoretical uncertainty, which is evaluated to be about 35% in the original paper. The F_{abs} is a t-independent attenuation factor representing the effects of pion absorption in the nucleus, and expressed as

$$F_{\mathrm{abs}} = e^{-<x>/\lambda} \tag{7.10}$$

where, λ^{-1} and $< x >$ are calculated as $A(4\pi R^3/3)^{-1}\sigma_{\mathrm{inel}}$ and 3/4R by assuming the nucleus is a homogeneous sphere with uniform density. This leads to the simple form as

$$F_{\mathrm{abs}} = \exp\left[-\frac{9A^{1/3}}{16\pi R_0^2}\sigma_{\mathrm{inel}}\right] \tag{7.11}$$

Therefore, the differential coherent pion cross section in the Rein and Sehgal model is expressed as

$$\frac{d^3\sigma(\nu \mathrm{A} \to \nu \pi \mathrm{A})}{dxdydt} = \frac{G^2}{2\pi^2} f_\pi^2 m_N E_\nu (1-y) \left(\frac{m_A^2}{q^2+m_A^2}\right)^2 A^2 \frac{(\sigma_{\mathrm{tot}}^{\pi \mathrm{N}})^2}{16\pi}(1+r^2) e^{-b|t|} F_{\mathrm{abs}} \tag{7.12}$$

Other models

The Belkov and Kopeliovich approach [105] is based on a dispersion relation formalism and uses the Glauber-Gribov model [102], in which the hadron-nucleus scattering amplitude is modified to be one minus the product of amplitudes for the hadron not to interact with any of the target nucleons. This cross section suppression is sometimes referred as "neutrino shadowing" [111]. Another difference is the assumption that non-resonant $\rho\pi$-systems dominate the axial current instead of a_1 meson. Thus, the form factor is changed as

$$\frac{m_A^2}{q^2+m_A^2} \to \frac{(m_\rho+m_\pi)^2}{q^2+m_\pi^2} \ln\left(1+\frac{q^2+m_\pi^2}{(m_\rho+m_\pi)^2}\right) \tag{7.13}$$

where the latter one is almost equal to the former one for small q^2 because the mass of $(\rho\pi)$-systems is similar to the a_1 mass.

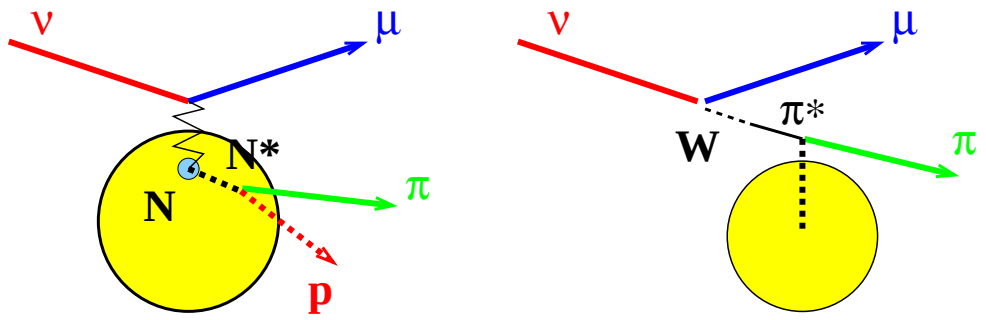

Figure 7.4: Schematic views of CC single pion production (left) and CC coherent pion production (right).

The Paschos and Kartavtset group [104] agrees with the Rein and Sehgal approach. However, they point that the cross section formula is very difficult to be calculated analytically. They perform the numerical calculation with consideration of the contribution from the various possible Feynman diagrams.

The last active group in this field is Kelkar *et al.* [106] who address coherent pion production mediated by Δ excitation in the nucleus. They employ a very detailed model of the nuclear physics that accounts for nuclear medium effects on the Δ. As a result, the cross section around 1 GeV region is strongly suppressed compared with that from other models.

Among the models, the Rein and Sehgal model [103] is commonly used in neutrino oscillation experiments because it is the only model that provides the kinematics of interaction. Therefore, we specifically compare our result with the Rein and Sehgal model in this thesis.

7.3 Analysis Overview

7.3.1 Experimental signatures of CC coherent pion production in SciBar

Figure 7.4 shows a schematic views of CC1π production (left) and CC coherent pion production (right). In SciBar, the experimental signatures of CC coherent pion production are the existence of two and only two tracks, both consistent with a minimum ionizing particle, and a small $q^2_{\rm rec}$. According to the MC simulation, the dominant background is the CC1π production, where the proton or the neutron is not detected.

7.3.2 Analysis flow in this chapter

Figure 7.5 shows a flow of the coherent pion analysis. The CC coherent pion candidates are extracted from the nonQE-pion sample. In order to suppress backgrounds, the following selections are further applied:

1. Events with a pion-like track going backward are rejected, according to momentum conservation in the beam direction.

2. Events with a vertex activity are rejected. Here, the vertex activity means a large deposited energy in the vertex strip or additional hits around the vertex.

3. Events are required to have a small $q^2_{\rm rec}$, $q^2_{\rm rec} < 0.10$ (GeV/c)^2.

The rejected events in the 1-track, QE, nonQE-proton and nonQE-pion samples are used to estimate the amount of the background events in the final sample. Then we extract the yield of

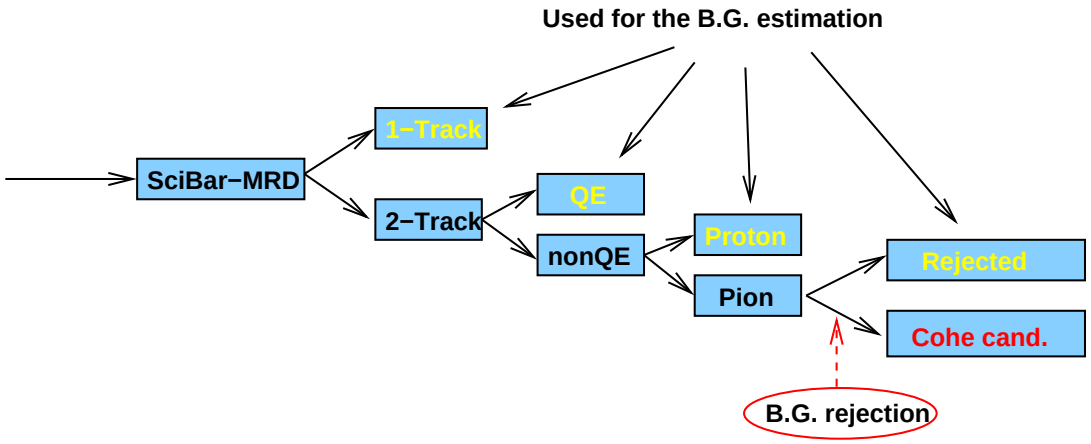

Figure 7.5: The analysis flow of the cross section measurement of CC coherent pion production.

the coherent pion events in the K2K neutrino beam and measure the cross section ratio to total CC interaction. In the following, we describe each analysis step.

7.4 Selection of the Coherent Pion Candidate Events

Second track direction

Figure 7.6 shows the angular distribution of the pion-like track in the nonQE-pion sample. In the CC coherent pion events, both the muon and pion tracks go forward. The events with the pion-like track angle more than 90 degrees are rejected.

Vertex activity cut 1 – 2D track cut –

As described in Section 6.1, tracks are reconstructed first in two-dimensional views projected in xz and yz planes. Then, xz and yz tracks are paired to reconstruct the 3D tracks. In the nonQE-pion sample, CC1π also results in a two track event when a recoil proton momentum is below the tracking threshold or a track is overlapped with the other track in one view. In the latter case, an additional '2D track' is found near the vertex in the other view. Figure 7.7 shows a typical event display of such an event. In the left figure of Fig. 7.7, the shortest track is the additional '2D track'. Figure 7.8 shows the distance between the vertex point and the edge of the additional 2D track when it exists. The hatched regions in Fig. 7.8 are the same area as used in track counting, $\pm$9.0 cm for x and y directions, $\pm$4.5 cm for z direction. We reject the events with an additional 2D track whose edge is inside this region.

Vertex activity cut 2 – Vertex strip activity cut –

The protons with momentum below the tracking threshold are detected as the large energy deposit in the vertex strip. We reject the CC1π events based on the activity in the vertex strip as shown in Fig 7.9. However, the vertex position for z direction is sometimes mis-reconstructed due to the cross-talk as shown in Fig. 6.12. To avoid the effect, we re-calculate the vertex position using information of the second track direction only for this selection. The point at the intersection of the first and the second tracks is re-defined as the vertex position as shown in Fig. 7.10. Figure 7.11 shows the vertex resolution after the re-calculation. The small peak in

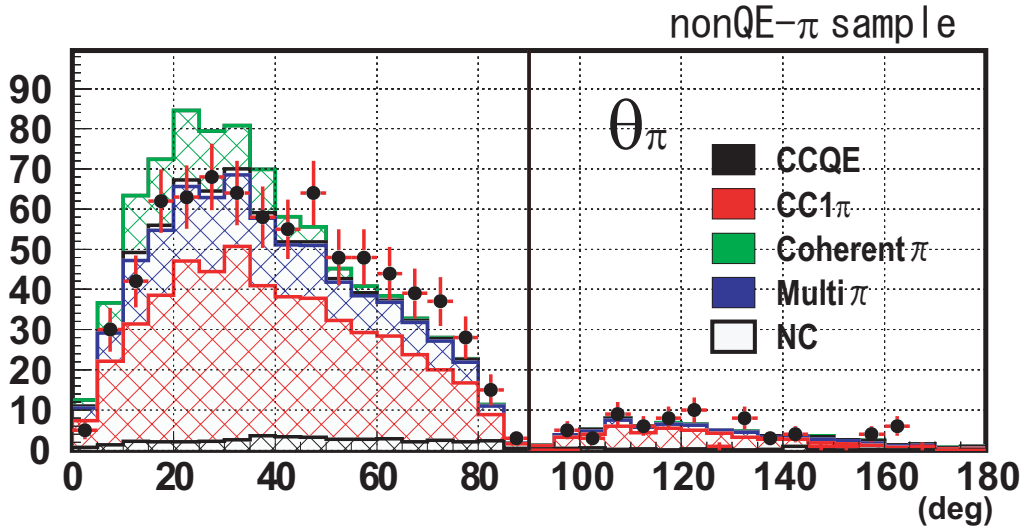

Figure 7.6: The angular distribution of the second track in the nonQE-pion sample. Black circles and histogram are data and the MC simulation, respectively. Events with the track angle more than 90 degrees are rejected.

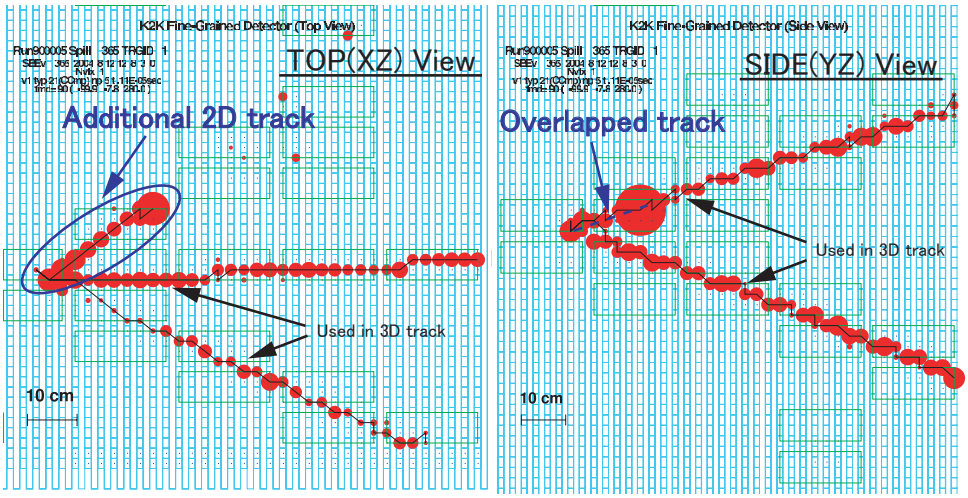

Figure 7.7: A display of an event rejected by the 2D track cut. The left figure is a xz-view and the right is a yz-view. In the xz-view, an additional 2D track is found.

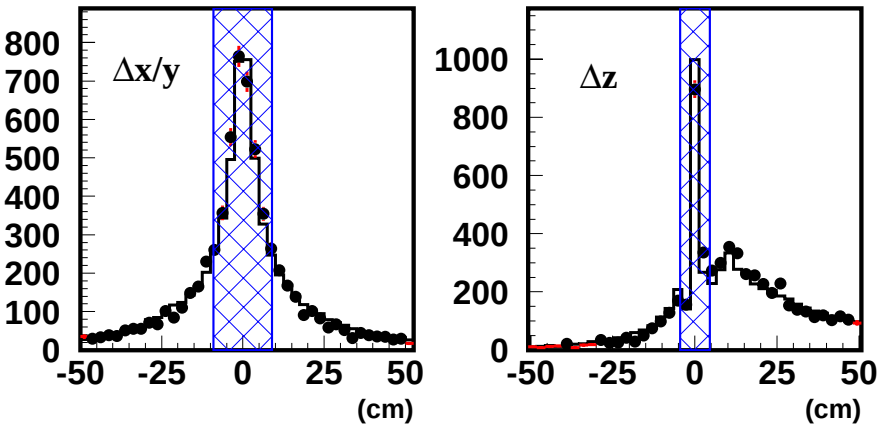

Figure 7.8: The distribution of the distance between the vertex and the edge of 2D track.

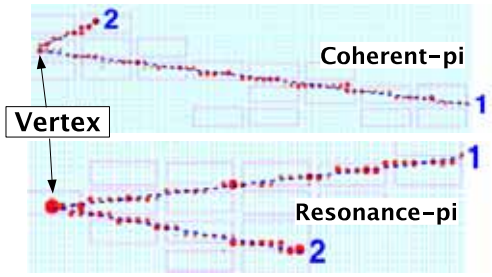

Figure 7.9: Event display for coherent pi (upper) and CC1π (lower) in the MC sample. Red marks indicate hits, and size of marks is proportionally related with energy deposition in the strip. Blue dashed lines denote the reconstructed 3D track.

the z direction due to the cross-talk effect disappears and the resolutions in all the directions are improved. The vertex resolutions after the re-calculation of vertex are 0.65 cm for the x and y and 0.88 cm for the z direction. The vertex shift is negligible.

Figure 7.12 shows a distribution of energy deposited in the vertex strip for the nonQE-pion and the QE sample. The expected contribution from each particle is calculated by assuming that the vertex position is the center of a strip and the angle with respect to the beam direction is a mean value of the angular distribution estimated by the MC simulation. The results are as follows.

$$\mu \ : \ 2.0\text{MeV/cm} \times (1.3/2)\text{cm}/\cos(30^\circ) \sim 1.5 \text{ (MeV)} \tag{7.14}$$

$$p \ : \ 3.6\text{MeV/cm} \times (1.3/2)\text{cm}/\cos(40^\circ) \sim 3.0 \text{ (MeV)} \tag{7.15}$$

$$\pi \ : \ 2.0\text{MeV/cm} \times (1.3/2)\text{cm}/\cos(40^\circ) \sim 1.7 \text{ (MeV)} \tag{7.16}$$

The activity is expected to be about 4.5 (=1.5+3.0) MeV for QE and 3.1 (=1.5+1.7) MeV for coherent pion production. The distributions in the figure are consistent with the expectations. The MC simulation well reproduce the data. We select events in which the vertex strip activity is less than 7.0 MeV.

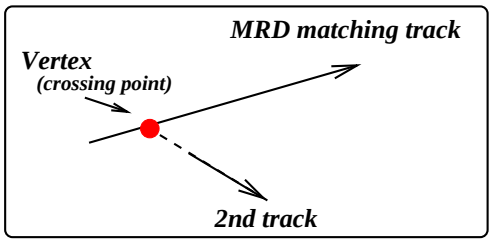

Figure 7.10: The re-definition of the vertex position. The vertex is constrained from both the primary and the second tracks for avoiding effects from the cross talk.

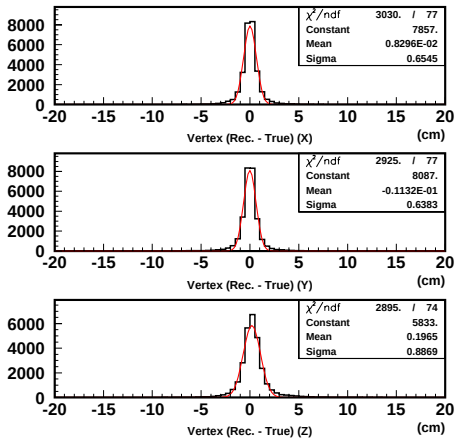

Figure 7.11: The vertex resolution after the recalculation of vertex. The small peak in the z direction due to the cross talk disappears. The resolution of each direction is improved.

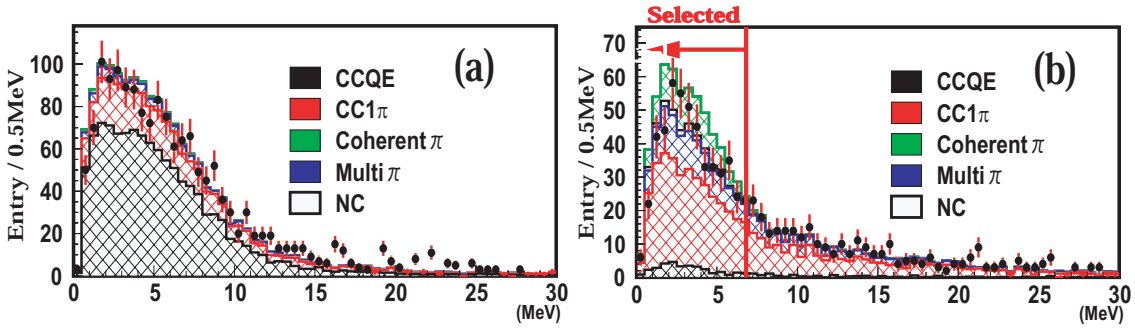

Figure 7.12: Energy deposit distribution in the vertex strip for the (a) QE sample and (b) nonQE-pion sample. Events with the activity less than 7 MeV are selected.

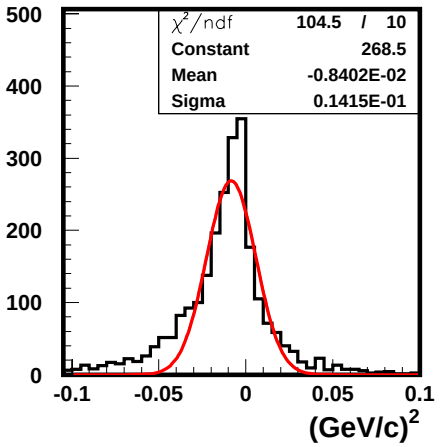

Figure 7.13: The distribution of the $q^2_{\rm true} - q^2_{\rm rec}$ for the simulated coherent pion events.

$q^2_{\rm rec}$ cut

The $q^2_{\rm rec}$ of coherent pion production event is expected to be very small due to the small scattering angle of a muon. Events are required to have a $q^2_{\rm rec}$ of less than 0.10 $({\rm GeV/c})^2$; this retains about 90% of the simulated coherent pion events. Although QE interaction is assumed, the q^2 of the CC coherent pion production is reconstructed with a resolution of 0.014 $({\rm GeV/c})^2$ and shift of 0.008 $({\rm GeV/c})^2$ as shown in Figure 7.13.

After applying all the cuts described above, 113 events out of 10049 SciBar-MRD events are found in the signal region. In the following section, we estimate the amount of the background events mainly from CC1π production, and measure the coherent pion yield.

7.5 Background Estimation

The background contamination in the signal region is estimated by the MC simulation. However, the background estimation is affected by systematic uncertainties such as neutrino interaction cross section and the magnitude of the nuclear effects. The $q^2_{\rm rec}$ distributions of all the samples are used to constrain the uncertainties. The $q^2_{\rm rec}$ distributions are compared between data and the MC simulation using a χ^2 fitting method. In the fit, the systematic uncertainties are treated as the fitting parameters.

7.5.1 Fitting overview

The 1-track, QE, nonQE-proton and nonQE-pion samples with $q^2_{\rm rec} > 0.10({\rm GeV/c})^2$ are fitted simultaneously. Free parameters of the fit are the nonQE to QE relative cross section ratio ($R_{\rm nqe}$), the magnitude of the nuclear effects and the momentum scale of muons. For the MC expectations, $q^2_{\rm rec}$ distribution is prepared separately for QE and nonQE interaction. Thus, 2×4 templates are used in total.

During the fit, the fitting parameters are re-weighted relative to the expected values in the MC simulation. Finally, the best fit parameters are determined by minimizing the χ^2 function defined below.

Fitting parameters

The fitting parameters are defined as follows,

$P^{\rm all}_{\rm norm}$	:	overall normalization factor
$R_{\rm nqe}$	:	nonQE to QE cross section ratio
$1+\delta_{\rm pscale}$	:	muon momentum scaling factor
$1+\delta_{\rm 2track/1track}$	:	the ratio of # 2-track events to # 1-track events
$1+\delta_{\rm nQE/QE}$	:	the ratio of # nonQE events to # QE events
$1+\delta_{\rm proton/pion}$	:	the ratio of # nonQE proton events to # nonQE pion events

where all contents are relative to the nominal value in the MC simulation.

The $\delta_{\rm pscale}$, $\delta_{\rm 2trk/1trk}$, $\delta_{\rm nonQE/QE}$, and $\delta_{\rm proton/pion}$ represent the possible systematic variations due to the nuclear effects and the detector systematic errors.

$q^2_{\rm rec}$ distribution

The $q^2_{\rm rec}$ distribution is divided into bins with 0.05 (GeV/c)^2 width. The expected number of events in the i-th $q^2_{\rm rec}$ bin in each sub-sample, $N^{\rm sample}_{i,\rm exp}$ (sample=1track, QE, nonQE-proton, nonQE-pion), is expressed with the fitting parameters as follows,

$$N^{\rm 1track}_{i,\rm exp} = P^{\rm all}_{\rm norm}\cdot\left[n^{\rm 1track}_{i,\rm QE} + R_{\rm nqe}\cdot n^{\rm 1track}_{i,\rm nQE}\right] \quad (7.17)$$

$$N^{\rm QE}_{i,\rm exp} = P^{\rm all}_{\rm norm}\cdot\left(1+\delta_{\rm 2trk/1trk}\right)\cdot\left[n^{\rm QE}_{i,\rm QE} + R_{\rm nqe}\cdot n^{\rm QE}_{i,\rm nQE}\right] \quad (7.18)$$

$$N^{\rm nQE-p}_{i,\rm exp} = P^{\rm all}_{\rm norm}\cdot\left(1+\delta_{\rm 2trk/1trk}\right)\cdot \left(1+\delta_{\rm nQE/QE}\right)\cdot\left(1+\delta_{\rm proton/pion}\right)\left[n^{\rm nQE-p}_{i,\rm QE} + R_{\rm nqe}\cdot n^{\rm nQE-p}_{i,\rm nQE}\right] \quad (7.19)$$

$$N^{\rm nQE-pi}_{i,\rm exp} = P^{\rm all}_{\rm norm}\cdot\left(1+\delta_{\rm 2trk/1trk}\right)\cdot \left(1+\delta_{\rm nQE/QE}\right)\cdot\left[n^{\rm nQE-pi}_{i,\rm QE} + R_{\rm nqe}\cdot n^{\rm nQE-pi}_{i,\rm nQE}\right] \quad (7.20)$$

where, $n^{\rm sample}_{i,\rm QE(nQE)}$ is the expected number of each bin with the baseline MC simulation for QE(nonQE) interaction.

Definition of χ^2

The χ^2 function to be minimized is defined as

$$\chi^2 = \chi^2_{\rm dist} + \chi^2_{\rm syst} \quad (7.21)$$

The $\chi^2_{\rm dist}$ is calculated using binned likelihood method with the assumption that the content of the observation in the i-th bin of each sample, $N^{\rm sample}_{i,\rm obs}$ follows the Poisson distribution with the mean of the expectation, $N^{\rm sample}_{i,\rm exp}$,

$$\chi^2_{dist} = -2\prod_{\rm sample,i}\ln\frac{P\left(N^{\rm sample}_{i,\rm obs}, N^{\rm sample}_{i,\rm exp}\right)}{P\left(N^{\rm sample}_{i,\rm obs}, N^{\rm sample}_{i,\rm obs}\right)} = 2\sum_{\rm sample,i}\left(N^{\rm sample}_{i,\rm exp} - N^{\rm sample}_{i,\rm obs} + N^{\rm sample}_{i,\rm obs}\cdot\ln\frac{N^{\rm sample}_{i,\rm obs}}{N^{\rm sample}_{i,\rm exp}}\right) \quad (7.22)$$

where, $P(A,B)$ is the Poisson probability of observing A events when a mean is B, expressed as:

$$P(A,B) = \frac{B^A}{A!}e^{-B} \tag{7.23}$$

The $\chi^2_{\rm syst}$ is calculated with systematic parameters by including the correlation among them.

$$\chi^2_{\rm syst} = \boldsymbol{P_{syst}}^t \boldsymbol{V^{-1}} \boldsymbol{P_{syst}} \tag{7.24}$$

where $\boldsymbol{P_{syst}}$ represents a set of systematic parameters and $\boldsymbol{V}$ is the non-diagonal covariance matrix.

$\boldsymbol{P_{syst}}$ consists of four systematic parameters defined as,

$$\boldsymbol{P_{syst}} \equiv \begin{pmatrix} \delta_{\rm pscale} \\ \delta_{\rm 2trk/1trk} \\ \delta_{\rm nQE/QE} \\ \delta_{\rm proton/pion} \end{pmatrix} \tag{7.25}$$

7.5.2 Systematic parameters and covariance matrix

In this subsection, we describe the systematic errors and the correlations.

(1) The systematic error of two track event selection, $\delta_{\rm 2trk/1trk}$

The systematic errors and the sources of the two track event selection are summarized in Table 7.1.

Table 7.1: The systematic error for $\delta_{\rm 2trk/1trk}$

Track counting	+2.7%	-1.0%
Threshold effect (±15%)	+0.7%	-0.0%
Cross talk (2%/4%/6%)	+1.1%	-1.1%
Second track finding efficiency	+0.9%	-4.3%
Sub-total (Detector originated)	+3.1%	-4.5%
Proton re-scattering (± 10%)	+2.9%	-2.6%
Pion absorption (± 30%)	+1.7%	-1.7%
Pion inelastic scattering (± 30%)	+2.3%	-2.9%
Sub-total (Nuclear effect)	+4.1%	-4.2%
Total	+5.1%	-6.2%

The size of detector originated systematic errors are comparable with the error from the nuclear effects. For the detector systematic errors, the dominant source is the error of the second track finding efficiency limited by the statistics of the event of eye-scanning.

Track counting

At the track counting, we require the second track to start within a certain region from the vertex as described in Section 6.3.1. When we change the requirement by ±50%, $\delta_{\rm 2trk/1trk}$ is changed by +2.7% and -1.0%. We assign the values to the systematic error of $\delta_{\rm 2trk/1trk}$.

Hit threshold

For the track finding, we set the hit threshold at 2.0 photo-electrons (pe). The energy deposition corresponding to 2.0 pe is varied by about ±15 % as shown in Fig.5.32. When we change the threshold by ±15%, $\delta_{\rm 2trk/1trk}$ is changed by +0.7%. We assign this value to the systematic error of $\delta_{\rm 2trk/1trk}$.

Cross-talk

The cross-talk of the MAPMT is set at 4% in the MC simulation. The absolute error of the cross-talk level is estimated to be 2% from the laboratory measurement [87]. When we change the cross-talk by ±2%, $\delta_{\rm 2trk/1trk}$ is changed by ±1.1 %. We assign this value to the systematic error of $\delta_{\rm 2trk/1trk}$.

Second track finding efficiency

As described in Section 6.3.2, we evaluate the systematic error of the second track finding efficiency by eye-scanning as a function of the number of hits associated with the track. We estimate the systematic error of $\delta_{\rm 2trk/1trk}$ by taking the difference between data and the MC simulation. The systematic shift of $\delta_{\rm 2trk/1trk}$ is found to be +0.9%, -4.3%.

Nuclear effects

In the MC simulation, nuclear effects on the produced hadrons are taken into account; for the pions originating from neutrino interactions, absorption, elastic scattering, and charge exchange inside the target nucleus are simulated based on the past experimental data. The cross section of charge exchange is negligible compared with the other two effects. The accuracy of the measurements is 30% level in the region of the pion momentum from the $\Delta(1232)$ decay [83]. The proton re-scattering inside the target nucleus changes the angle and the momentum of the proton. The uncertainty of the cross section is estimated to be 10% level [112]. We prepare several special MC event sets by changing the cross sections of the processes by 30% for the pion absorption and the pion inelastic scattering and by 10% for the proton re-scattering separetely. We check the variation of $\delta_{\rm 2trk/1trk}$ with the different MC event sets. The variation is +2.9%, -2.6% for the proton re-scattering, +1.7%, -1.7% for the pion absorption and +2.3%, -2.9% for the pion inelastic scattering. We assign the quadratic sum of the variations to the systematic error of $\delta_{\rm 2trk/1trk}$.

(2) The systematic error of QE and nonQE event selection, $\delta_{\rm nQE/QE}$

The systematic errors and the sources of the QE and nonQE event selection are summarized in Table 7.2. The dominant source is the uncertainties of the nuclear effect. Among the error sources, the systematic error from the cross-talk and nuclear effects are estimated with the same method as that of $\delta_{\rm 2trk/1trk}$.

Angular resolution

A difference of the angular resolution between the data and the MC simulation is evaluated by comparing the direction of the SciBar track with that of the MRD track in the SciBar-MRD sample.

We find that the RMS of the $(\theta_{\rm SB} - \theta_{\rm MRD})$ distribution is 3.5 degrees for the data and

Table 7.2: Systematic error for $\delta_{\mathrm{nonQE/QE}}$

Angle resolution	+1.0%	-0.0%
Cross Talk (2%/4%/6%)	+2.2%	-2.9%
Muon momentum scale (± 2.7%)	+1.5%	-4.3%
Sub-total (Detector Originated)	+2.8%	-5.2%
Proton Re-scattering (± 10%)	+2.9%	-2.8%
Pion absorption (± 30%)	+0.0%	-5.4%
Pion inelastic scattering (± 30%)	+0.3%	-4.7%
Sub-total (Nuclear effect)	+2.9%	-7.7%
Total	+4.0%	-9.3%

4.1 degrees for the MC simulation. When we intentionally change the angular resolution of the data by +2.1 ($=\sqrt{4.1^2 - 3.5^2}$) degrees, the $\delta_{\mathrm{nonQE/QE}}$ is changed by +1.0 %. We assign the number to the systematic error of $\delta_{\mathrm{nonQE/QE}}$.

Muon momentum scale

The systematic error of the muon momentum scale is 2.7% as stated in Section 6.2.4. When we change the scale by ± 2.7%, $\delta_{\mathrm{nQE/QE}}$ is changed by +1.5% and -4.3%. We assign this number to the systematic error of $\delta_{\mathrm{nQE/QE}}$.

(3) The uncertainty of nonQE-proton and nonQE-pion event separation, $\delta_{\mathrm{proton/pion}}$

The systematic errors and the sources of the nonQE-proton and nonQE-pion event separation are summarized in Table 7.3. The dominant source is the uncertainty of nuclear effects. Among the sources, the systematic error from hit threshold, cross-talk and nuclear effects are estimated with the same method as that of $\delta_{\mathrm{2trk/1trk}}$.

Table 7.3: Systematic error of $\delta_{\mathrm{proton/pion}}$

Threshold	+2.2%	-2.5%
Cross Talk (2%/4%/6%)	+1.1%	-1.3%
Particle ID	+0.0%	-1.8%
PMT resolution	+1.0%	-0.2%
Quenching factor	+2.2%	-2.3%
Sub-total (Detector Originated)	+3.4%	-4.1%
Proton Re-scattering (± 10%)	+0.0%	-6.3%
Pion absorption (± 30%)	+6.4%	-10.5%
Pion inelastic scattering (± 30%)	+0.0%	-4.2%
Sub-total (Nuclear effect)	+6.4%	-12.9%
Total	+7.2%	-13.5%

Stability of MuCL

The stability of PID performance is checked by using the muons. Figure 7.14 shows time

variation of the MuCL value to satisfy the 90% efficiency for muons. The MuCL value is stable within ± 0.008. We evaluate the systematic error of the MuCL cut value for the proton and pion identification. When we change the cut value by ± 0.008, the $\delta_{\mathrm{proton/pion}}$ is changed by $^{+0.0\%}_{-1.8\%}$. We assign the number to the systematic error of $\delta_{\mathrm{proton/pion}}$.

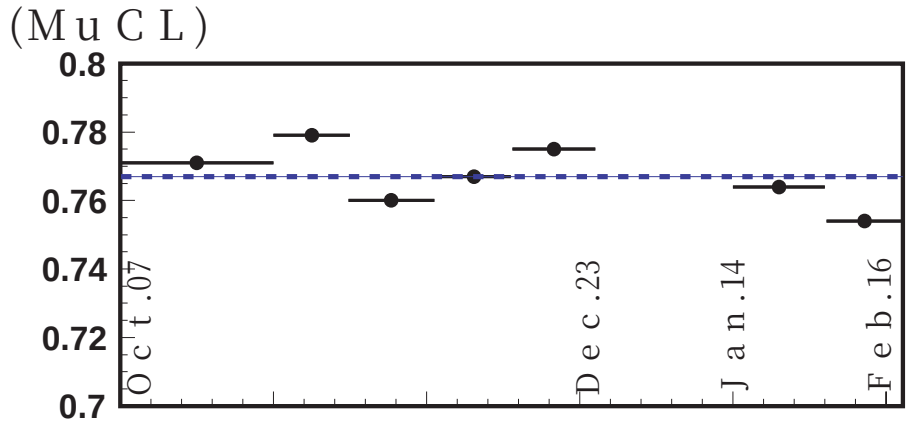

Figure 7.14: The stability of the threshold value of MuCL

PMT resolution

The PMT resolution of 40% is implemented in the MC simulation. The ensuing measurement in the laboratory reveal that the resolution is 70% – 100% at our operation voltage. We prepare another set of the MC events with 100% PMT resolution in order to cover the range. When we use the MC events with 100% PMT resolution, the $\delta_{\mathrm{proton/pion}}$ is changed by +1.0%. We assign the number to the systematic error of $\delta_{\mathrm{proton/pion}}$.

Scintillator quenching

We describe the details of the scintillator quenching in Section 5.3.3. We estimate the systematic error from the scintillator quenching by changing the Birk's constant within the measurement error and find the variation of $\delta_{\mathrm{proton/pion}}$ by $^{+2.2\%}_{-2.3\%}$. We assign the number to the systematic error of $\delta_{\mathrm{proton/pion}}$.

(4) Covariance matrix

As shown in Table 7.1, Table 7.2 and Table 7.3, the nuclear effects are common systematic error sources of the parameters; $\delta_{\mathrm{2trk/1trk}}$, $\delta_{\mathrm{nQE/QE}}$ and $\delta_{\mathrm{proton/pion}}$. Therefore, we take the correlation into consideration as,

$$cov(p_1, p_2) = \sum_{source} \frac{\sum_{condition}(\Delta(p_1)\Delta(p_2))}{\sum_{condition}}$$

where "source" means the following three kinds of nuclear effects: pion absorption, pion inelastic scattering and proton re-scattering, and "condition" means the sets of prepared MC simulation.

The covariance matrix is found to be,

Table 7.4: Best fit value of parameters in q^2 fitting.

parameter	value	error(total)	error(stat.)	estimated error (before fitting)
$R_{\mathrm{nQE/QE}}$	1.071	0.074	0.027	0.200
δ_{pscale}	-0.012	0.003	0.003	0.027
$\delta_{\mathrm{2trk/1trk}}$	0.014	0.026	0.020	0.062
$\delta_{\mathrm{nQE/QE}}$	0.043	0.054	0.030	0.093
$\delta_{\mathrm{proton/pion}}$	0.079	0.051	0.040	0.135

$$\mathbf{V} = \begin{array}{c} \\ \delta_{\mathrm{pscale}} \\ \delta_{\mathrm{2trk/1trk}} \\ \delta_{\mathrm{nQE/QE}} \\ \delta_{\mathrm{proton/pion}} \end{array} \begin{array}{c} \begin{array}{cccc} \delta_{\mathrm{pscale}} & \delta_{\mathrm{2trk/1trk}} & \delta_{\mathrm{nQE/QE}} & \delta_{\mathrm{proton/pion}} \end{array} \\ \begin{pmatrix} +(0.027)^2 & 0 & 0 & 0 \\ 0 & +(0.062)^2 & -(0.052)^2 & +(0.056)^2 \\ 0 & -(0.052)^2 & +(0.093)^2 & +(0.041)^2 \\ 0 & +(0.056)^2 & +(0.041)^2 & +(0.135)^2 \end{pmatrix} \end{array}$$

7.5.3 Fitting result

A minimum χ^2 point in multi-parameter space is found by changing the R_{nqe} and the systematic parameters. The χ^2 value in the region with q^2_{rec} greater than 0.10 $(\mathrm{GeV/c})^2$ at the best fit point is 73.2 for 82 degrees of freedom (DOF). The best fit values and the errors are summarized in Table 7.4. The statistical errors are also shown in the table. We estimate the statistical error by performing the fitting with all the other systematic parameters fixed to the best fit value. All the fitting parameters stay within their estimated errors.

Fig 7.15 shows the q^2_{rec} distributions of the data together with the MC simulation with the best fit parameters. The MC simulation well reproduces the observation in the region $> 0.10(\mathrm{GeV/c})^2$.

The number of background events in the signal region is estimated to be 111.4 by the MC simulation with the best fit parameters.

7.6 Coherent Pion Yield in the K2K Neutrino Beam

Figure 7.16 (a) shows the q^2_{rec} distribution after applying all the selections and Fig. 7.16 (b) shows the q^2_{rec} distribution of the rejected events in the nonQE-pion sample. As shown in the figure, a clear deficit is found in the region of $q^2_{\mathrm{rec}} < 0.10(\mathrm{GeV/c^2})$, while no deficit is found for the sample of rejected events as shown in Figure 7.16 (b). We use the events with q^2_{rec} less than 0.10 $(\mathrm{GeV/c})^2$ in the final sample for the cross section measurement.

The efficiency corrected number of coherent pion events is calculated as

$$N(\mathrm{coherent}\pi) = \frac{N_{\mathrm{obs}} - N^{\mathrm{exp}}_{\mathrm{BG}}}{\epsilon_{\mathrm{cohe}\pi}} \tag{7.26}$$

where N_{obs}, $N^{\mathrm{exp}}_{\mathrm{BG}}$ and $\epsilon_{\mathrm{cohe}\pi}$ are the number of observed events, the number of background events estimated by the MC simulation, and the detection efficiency of coherent pion calculated by the MC simulation defined as,

$$\epsilon_{\mathrm{cohe}\pi} = \frac{\text{the number of selected coherent pion events}}{\text{the number of generated coherent pion events in the fiducial volume}} \tag{7.27}$$

respectively.

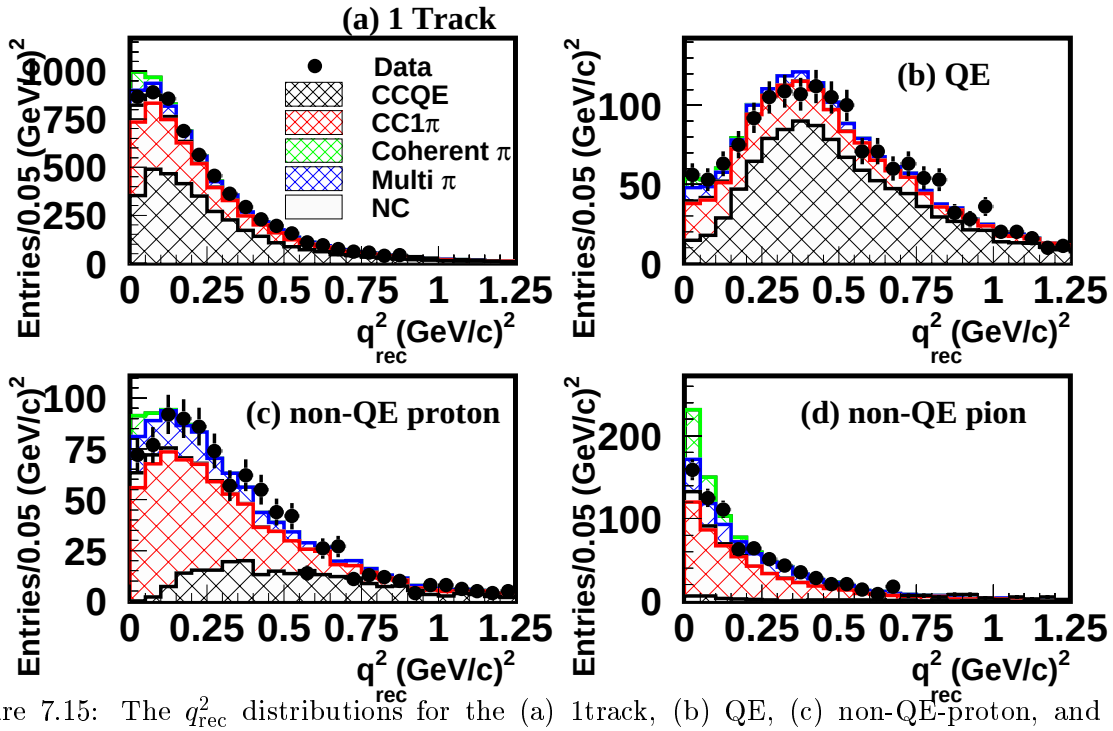

Figure 7.15: The $q^2_{\rm rec}$ distributions for the (a) 1track, (b) QE, (c) non-QE-proton, and (d) non-QE-pion samples.

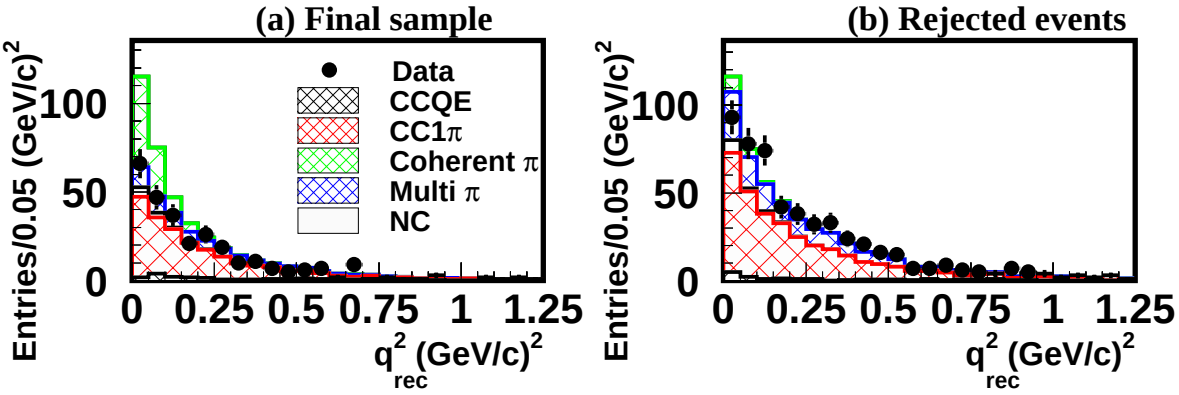

Figure 7.16: The $q^2_{\rm rec}$ distribution for (a) the final sample and (b) the sample of rejected events in the nonQE-pion sample.

These are found to be,

$$N_{\rm obs} = 113 \quad (7.28)$$
$$N_{\rm BG}^{\rm exp} = 111.389 \quad (7.29)$$
$$\epsilon_{{\rm cohe}\pi} = 0.211. \quad (7.30)$$

After subtracting the background and correcting the efficiency, the number of coherent pion events is measured to be,

$$N({\rm coherent}\pi) = 7.64 \pm 50.40({\rm stat.}) \quad (7.31)$$

in 9.38 ton fiducial volume with 17.4×10^{18} POT.

As a result, no evidence of CC coherent pion production is found in the data.

7.7 Cross Section Ratio to Total CC Interaction

7.7.1 Normalization; total CC interaction

In K2K, it is difficult to estimate the absolute neutrino flux due to difficulties in the estimation of the primary proton beam intensity, the proton targetting efficiency, and hadron production cross sections.

Therefore, total CC interaction is used for a normalization of the neutrino flux and the cross section ratio to total CC interaction is measured. The total number of CC interaction is estimated by using the SciBar-MRD sample. As described in Section 6.2.2, 10049 events are identified as the SciBar-MRD sample. The detection efficiency and purity in the sample are calculated by the MC simulation,

$$\epsilon_{CC} = \frac{\text{the number of selected CC events}}{\text{the number of CC events generated in the fiducial volume}} = 0.569 \quad (7.32)$$
$$\text{Purity}_{CC}^{exp} = \frac{\text{the number of selected CC events}}{\text{the number of events selected as a SciBar-MRD sample}} = 0.980 \quad (7.33)$$

By correcting the efficiency and purity, the total number of CC events is

$$N(\nu_\mu{\rm CC}) = \frac{N_{obs(MRD)} \cdot \text{Purity}_{CC}^{exp}}{\epsilon_{CC}} \quad (7.34)$$
$$= (17.30 \pm 0.16(stat.)) \times 10^3 \quad (7.35)$$

in 9.38 ton fiducial volume with 17.4×10^{18} POT.

7.7.2 Cross section ratio

We estimate the cross section ratio of CC coherent pion production to total CC interaction to be,

$$\sigma({\rm coherent}\ \pi)/\sigma(\nu_\mu CC) = N({\rm coherent}\ \pi)/N(\nu_\mu{\rm CC}) \quad (7.36)$$
$$= (0.04 \pm 0.29({\rm stat.})) \times 10^{-2}. \quad (7.37)$$

7.8 Systematic Error

In this section, we estimate the systematic error of the coherent π cross section ratio. The systematic errors and the sources are summarized in Table 7.5.

For convenience, the systematic error sources are divided into four categories; those related to (i) nuclear effect and the interaction model, (ii) background estimation, (iii) event selection, and (iv) detector response. As shown in Table 7.5, the systematic error is $+0.32 \times 10^{-2}$, -0.35×10^{-2} in total. The dominant sources are nuclear effect and the interaction model.

Table 7.5: The summary of systematic errors in the CC coherent pion cross section ratio.

Source of error	error($\times 10^{-2}$)	
Nuclear effect and the interaction model	**(+0.27, -0.25)**	
Pion absorption (± 30%)	+0.17	-0.08
Pion inelastic (± 30%)	+0.06	-0.19
Proton rescattering (± 10%)	+0.10	-0.09
Bodek correction (± 30%)	+0.05	-0.04
CC1π suppression	+0.14	-
M_A(CCQE,CC1π) (± 10%)	+0.05	-0.04
Background estimation	**(+0.12, -0.11)**	
$R_{nQE/QE}$ (± 2.7%)	+0.07	-0.07
Normalization($P_{nQE/QE}$) (± 3.0%)	+0.09	-0.08
Muon momentum scaling factor(P_{pscale}) (± 0.3%)	+0.02	-0.01
Spectrum shape (uncertainty of Spectrum fit04)	+0.03	-0.03
Event selection	**(+0.11, -0.17)**	
2Track event selection	+0.09	-0.05
$\Delta\theta_p$ cut	+0.00	-0.00
Particle Identification	+0.07	-0.03
2D track cut	+0.01	-0.16
Vertex strip activity cut	+0.00	-0.05
Detector response	**(+0.09, -0.16)**	
2nd track finding efficiency	+0.01	-0.00
Cross talk(2%,4%,6%)	+0.04	-0.03
Hit threshold(± 15%)	+0.05	-0.07
PMT resolution(80%/120%)	+0.00	-0.00
Scintillator quenching	+0.06	-0.14
Pion interaction (± 10%)	+0.00	-0.00

7.8.1 Nuclear effect and interaction model

Nuclear effect

The method how to estimate the systematic error from nuclear effect is already described in Section 7.5.2. The errors are shown in Table 7.3.

Bodek correction

We apply the Bodek and Yang correction to deep inelastic scattering. This correction is performed as a function of true q^2 as,

$$\text{Correction factor} \quad = \quad \frac{q^2_{true}}{q^2_{true} + 0.188} \tag{7.38}$$

This correction factor is extracted from the ep (μp) scattering data (SLAC,BCDMS and NMC). The uncertainty of the correction is about 30% [79]. We impose $\pm$30% error on the correction. When we change the correction factor by $\pm$ 30%, the cross section ratio is changed by $+0.05 \times 10^{-2}$ and -0.04×10^2. We assign the number to the systematic error of the cross section ratio.

q^2 distribution of CC1π interaction

In this analysis, we assume the q^2 distribution of CC1π interaction model. However the $q^2_{\rm rec}$ distribution of the nonQE-proton sample (Fig. 7.15 (c)) may indicate an additional deficit by the CC1π events in the region $q^2_{\rm rec} < 0.10({\rm GeV/c})^2$. We evaluate the possible amount of the additional CC1π deficit from the 1track, QE and nonQE-proton samples. Here CC coherent pion interaction is removed in the MC simulation. We use the suppression function to CC1π interaction used in the previous K2K oscillation analysis [43],

$$\frac{q^2_{\rm true} - 0.1}{\rm A} + 1 \quad \text{for } q^2_{\rm true} < 0.1$$

Fitting the $q^2_{\rm rec}$ distributions of three sub-samples in $q^2_{\rm rec} < 0.10$, we obtain $A = 0.255 \pm 0.102$. The $q^2_{\rm rec}$ distributions with additional CC1π suppression are shown in Fig. 7.17. When we use the CC1π suppression in the MC simulation, the coherent π cross section ratio is changed by $+0.1442 \times 10^{-2}$. We assign the change to the systematic error of the cross section ratio.

M_A(QE,CC1π)

In the MC simulation, we set M_A at 1.1 GeV/c^2 for both QE and CC1π. The uncertainty of M_A value is 0.1 GeV/c^2 [77]. When we change the M_A value by $\pm$0.1 GeV/c^2, the cross section ratio is changed as shown in Table 7.6. We assign the following number to the systematic error,

$$\text{Systematic Error}(M_A) \quad = \quad \sqrt{\text{syst.(QE)}^2 + \text{syst.}(1\pi)^2} = ^{+0.049}_{-0.038} \times 10^{-2} \tag{7.39}$$

Table 7.6: The cross section ratio with each condition for M_A. We quote the quadratic sum as the systematic error.

case	σ(coherent π)/$\sigma(\nu_\mu CC)$	variation from center value
M_A(QE) = 1.01	0.018×10^{-2}	-0.014×10^{-2}
M_A(QE) = 1.21	0.045×10^{-2}	$+0.013 \times 10^{-2}$
M_A(CC1π) = 1.01	-0.003×10^{-2}	-0.035×10^{-2}
M_A(CC1π) = 1.21	0.045×10^{-2}	$+0.047 \times 10^{-2}$

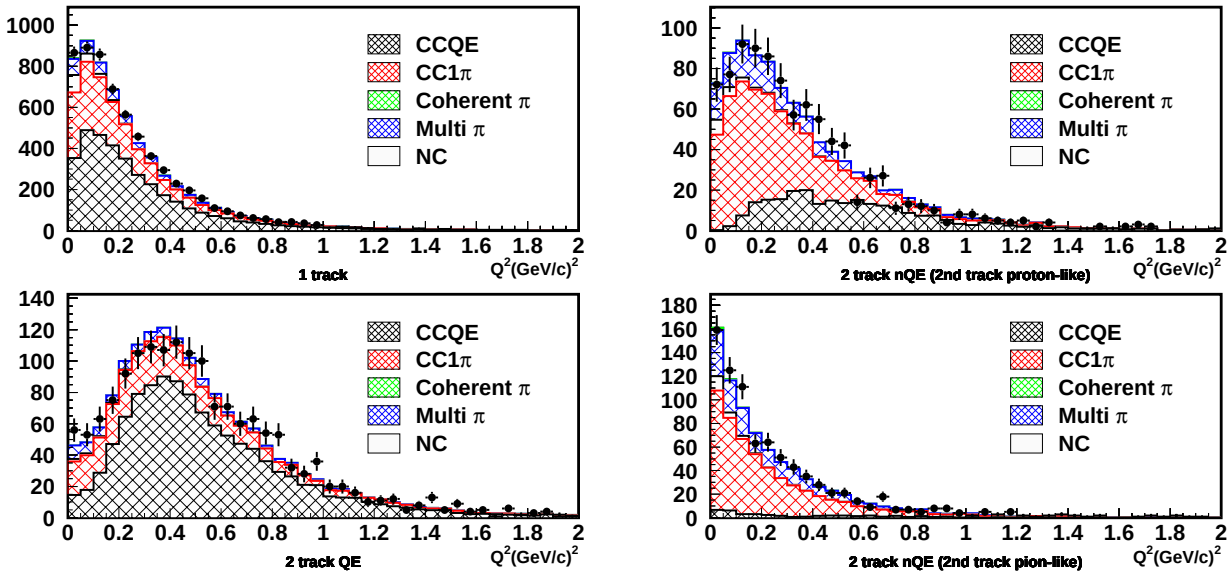

Figure 7.17: The $q^2_{\rm rec}$ distribution of all the sub-samples. The CC1π production is suppressed by $(q^2_{\rm true}-1)/{\rm A}+1$ for $q^2_{\rm true} < 0.1$ (GeV/c)^2 with A=0.255 in the MC simulation.

7.8.2 Background estimation

Fitting parameter $(R_{\rm nQE/QE}, \delta_{\rm nQE/QE}, \delta_{\rm pscale})$

We estimate the systematic error of the cross section ratio by the background estimation by varying the fitting parameter within the statistical error shown in Table 7.4. The systematic errors are summarized in Table 7.5.

Neutrino energy spectrum

We estimate the systematic error from the uncertainty of the neutrino energy spectrum. We vary the spectrum shape within the uncertainty of the previous K2K spectrum measurement [43, 44]. We consider the correlations among neutrino energy bins by using the error matrix shown below. The cross section ratio is affected by $\pm 0.03 \times 10^{-2}$ by the spectrum uncertainty.

$$\sqrt{\mathbf{M}} = \begin{array}{c} E_\nu \text{ bin} \\ \\ \\ \\ \\ \\ \\ \end{array} \begin{array}{c} \begin{array}{ccccccc} 0.0-0.5 & 0.5-0.75 & 0.75-1.0 & 1.5-2.0 & 2.0-2.5 & 2.5-3.0 & 3.0- \end{array} \\ \begin{pmatrix} 0.322 & -0.083 & 0.013 & -0.015 & -0.007 & -0.020 & 0.017 \\ -0.083 & 0.224 & -0.041 & 0.004 & -0.006 & 0.002 & -0.008 \\ 0.013 & -0.041 & 0.040 & -0.011 & 0.010 & 0.003 & -0.008 \\ -0.015 & 0.004 & -0.011 & 0.024 & -0.029 & 0.028 & -0.017 \\ -0.007 & -0.006 & 0.010 & -0.029 & 0.060 & -0.078 & 0.046 \\ -0.020 & 0.002 & 0.003 & 0.028 & -0.078 & 0.158 & -0.125 \\ 0.017 & -0.008 & -0.008 & -0.017 & 0.046 & -0.125 & 0.167 \end{pmatrix} \end{array}$$

7.8.3 Event selection

Track counting

We estimate the systematic error by the track counting with the same method described in Section 7.5.2. The error size is $+0.0914 \times 10^{-2}$ and -0.0476×10^{-2}.

$\Delta\theta_p$ cut

We estimate the systematic error from the $\Delta\theta_p$ cut by changing the cut value by ± 5 degrees. When we change the cut value by ± 5 degrees, the cross section ratio is changed by -0.046×10^{-2}. We assign this number to the systematic error.

Particle identification

We consider the following two systematic sources for the PID. One is the uncertainty of the MuCL cut described in Section 7.5.2. When we change the cut value of the data within the uncertainty, the cross section ratio is changed by $+0.0515 \times 10^{-2}$, -0.0258×10^{-2}.

Another source is the difference of MuCL distribution between the data and the MC simulation. We estimate the systematic error by changing the cut value of both the data and the MC simulation as shown in Fig. 7.18. When we change the cut value by ± 0.01, the cross section ratio is changed by $+0.0423 \times 10^{-2}$ and -0.0032×10^{-2}.

We assign the quadratic sum of $+0.0666 \times 10^{-2}$ and -0.0260×10^{-2} to the systematic error of the cross section ratio.

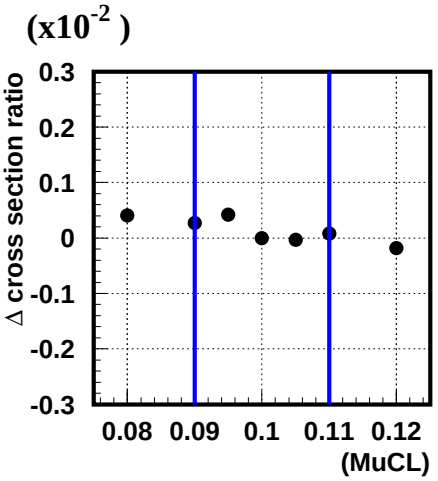

Figure 7.18: The variation of the cross section ratio by varying the cut value of PID.

2D track cut

At the additional 2D track search, we require the 2D track to start within a certain region from the vertex as described in Section 7.4. When we change the requirement by ± 50 %, the cross section ratio is changed by $+0.010 \times 10^{-2}$ and -0.157×10^{-2}. We assign the number to the systematic error of the cross section ratio.

Vertex strip activity cut

We estimate the systematic error from the vertex strip activity cut by changing the cut value by ± 1 MeV. When we change the cut value by ± 1 MeV, the cross section ratio is changed by -0.050×10^{-2}. We assign the number to the systematic error of the cross section ratio.

7.8.4 Detector response

We estimate the detector related systematic error with the same method as that described in Section 7.5.2 except for the pion-CH interaction described below. The error is shown in Table 7.5

Cross section of π interaction

We use the CALOR program library [113, 114] to simulate the pion-CH interaction in the detector simulation. Fig 7.19 shows the comparison of the cross section by CALOR with that by a custom-made code of SK. The SK code is based on the existing measurements. The uncertainty of the past measurements is estimated to be 10 %. The CALOR and the SK code agree well. When the cross section of π interaction is varied by ± 10 %, the coherent π cross section ratio changes by 0.004×10^{-2}. We assign the change to the systematic error of the cross section ratio.

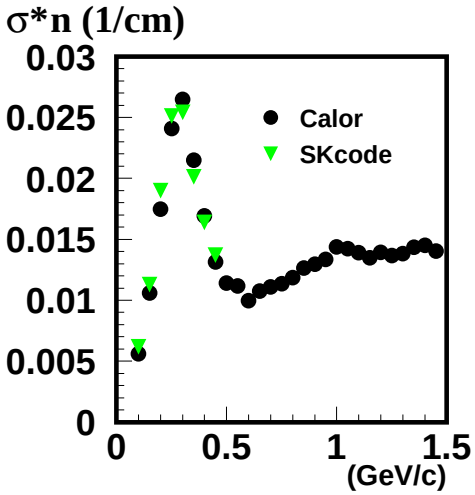

Figure 7.19: The pion-CH cross section in CALOR and SK code. The SK code is based on the past measurements.

7.9 Upper Limit

The cross section ratio of CC coherent pion production to total CC interaction is measured to be,

$$(0.04 \pm 0.29\ (\text{stat.})^{+0.32}_{-0.35}(\text{syst.})) \times 10^{-2}.$$

This result is consistent with the non-existence of CC coherent pion production in the K2K neutrino beam energy. An one-sided confidence interval of the cross section ratio at 90% CL is set as

$$\begin{aligned} \sigma(\text{CC coherent } \pi)/\sigma(\nu_\mu CC) &< 0.044 + 1.28 \times \sqrt{\text{stat.}^2 + \text{syst.}^2} \\ &= 0.60 \times 10^{-2}. \end{aligned}$$

This upper limit is 22.5 % of the prediction by the Rein and Sehgal model.

7.10 Summary and Discussion

In this chapter, we search for CC coherent pion production by muon neutrinos with a mean energy of 1.3 GeV. No evidence of CC coherent pion production is found. An upper limit on the cross section ratio of CC coherent pion production to total CC interaction is set to be 0.60×10^{-2} at 90% CL. This result is the first experimental limit for CC coherent pion production by neutrinos of the few GeV. The limit is inconsistent with the prediction of the model by Rein and Sehgal, 2.667×10^{-2}.

Figure 7.20 shows the comparison of our result with other existing experimental results for neutrino induced NC coherent pion production in the few GeV region. In the figure, the absolute cross section of our result is estimated based on the total charged current cross section calculated by averaging over the K2K neutrino energy spectrum in the MC simulation, $1.07 \times 10^{-38}\mathrm{cm}^2$/nucleon. In addition, the other results are scaled to the case of the charged current production with carbon target by assuming an $A^{1/3}$ dependence of the cross section and the relation of $\sigma(\mathrm{CC}) = 2\sigma(\mathrm{NC})$ from the isospin relation. The discrepancy between the extrapolation from the NC measurement and the present result is as large as three standard deviation; Rein and Sehgal model cannot explain both CC and NC interactions consistently. To build a consistent picture of this interaction, the theoretical models have to be modified for at least one of the following points:

- The energy dependence of the cross section below 2 GeV
- The atomic number dependence of the cross section
- The cross section relation between NC and CC

These points will be more precisely checked with additional data from planned high statistics experiments, namely SciBooNE [115] [1] and/or Minerνa [116], in the near future.

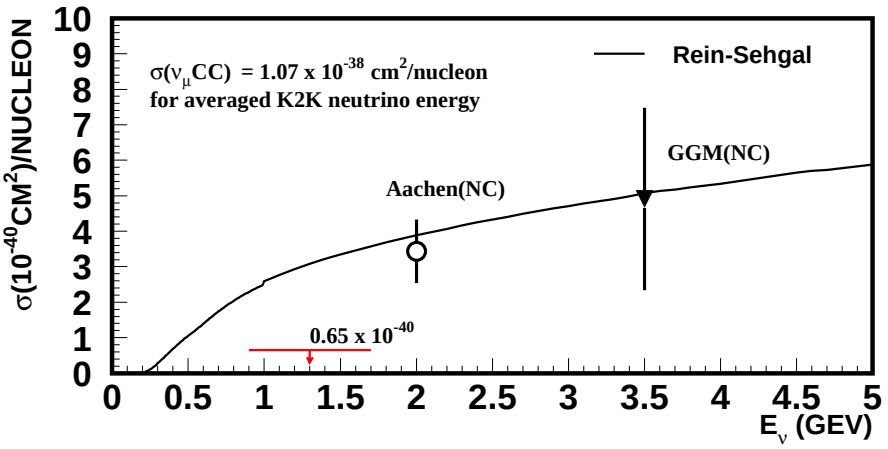

Figure 7.20: Comparison of our data with other existing experimental results in the few GeV neutrinos. Results of other experiments are scaled to the carbon target.

[1] In addition, SciBooNE also plans to study this channel with anti-neutrinos

7.10.1 Comparison between the observation and no CC coherent pion model

As discussed above, the $q^2_{\rm rec}$ distribution of SciBar-MRD sample strongly indicate no CC coherent pion production by the K2K neutrino beam. To validate this result we check several distributions, such as p_μ, θ_μ, the second track length in SciBar ($L_{\rm 2nd}$), and second track angle with respect to the beam direction ($\theta_{\rm 2nd}$). Some distributions of other near detectors are also shown.

Figure 7.21 shows the p_μ and θ_μ distributions of the 1 track sample together with the MC expectations with (upper) and without (lower) CC coherent pion production. The MC expectations without CC coherent pion well reproduce the observation including events with forward muons ($<$ 10deg.) unlike those with CC coherent pion. Figure 7.22–7.24 show the p_μ, θ_μ, $L_{\rm 2nd}$ and $\theta_{\rm 2nd}$ for the QE, nonQE-proton and nonQE-pion sample, respectively. For each sample, the MC expectations of upper figures include CC coherent pion production and the lower figures do not include it. For the QE and nonQE-proton sample, the MC expectations in both with and without CC coherent pion case reproduce the observation at the same level [2] because almost no coherent pion event is expected in these samples. This fact also indicates that QE and CC1π production are not a primary source of the 'low-q^2' problem. For the nonQE-pion sample, the MC expectations without CC coherent pion reproduce the observation, and the clear discrepancies are found in especially the angular distributions in the case with CC coherent pion production. Thus, SciBar data support no CC coherent pion model.

In addition, other near detector data also support no CC coherent pion result. Figure 7.25 and 7.26 shows θ_μ and $q^2_{\rm rec}$ distributions of 1KT CC sample and the SciFi nonQE sample together with the MC expectations with and without CC coherent pion production. For 1KT, data are reasonably reproduced by no CC coherent pion MC simulation. For SciFi, no CC coherent pion model show better agreement with the observation.

Therefore, a model without CC coherent pion well reproduces all the observations.

7.10.2 Neutrino interaction model for the oscillation analysis

As described above, the non-existence of CC coherent pion production gives a solution of the "low-q^2" problem described in the beginning of this Chapter. Consequently, we adopt the no CC coherent pion model in the MC simulation. By using the modified MC simulation, we can reliably predict the observations including low-q^2 events without any correction as was done in the previous analysis [43, 44]. The MC simulation is now ready for the oscillation analysis.

[2] The agreement of the second track angular distribution is not good. We already confirmed that it is not due to the reconstruction bias. However, we do not specify the cause yet.

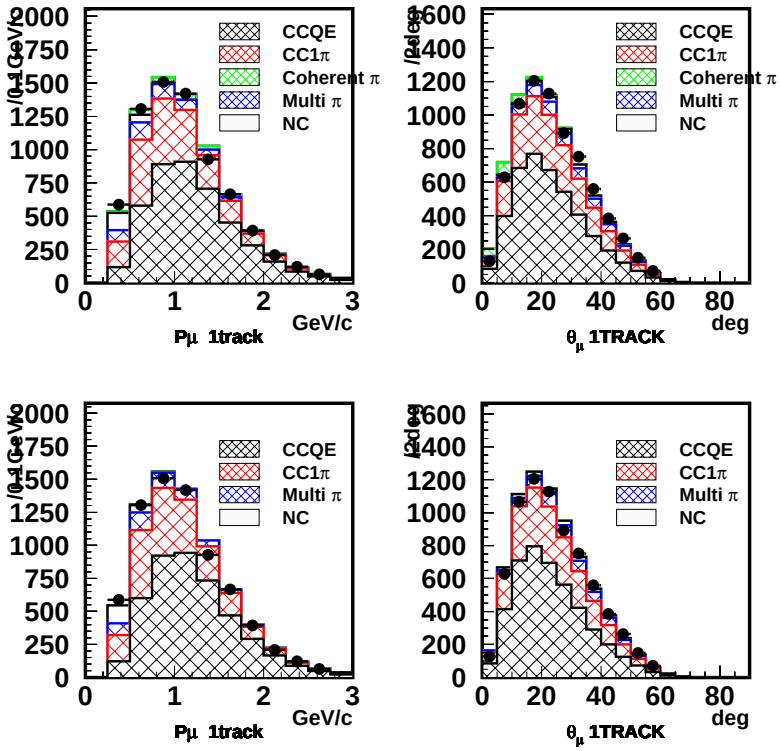

Figure 7.21: The p_μ and θ_μ distributions for the 1 track sample. The MC expectations of upper figures include CC coherent pion production and the lower ones do not include it.

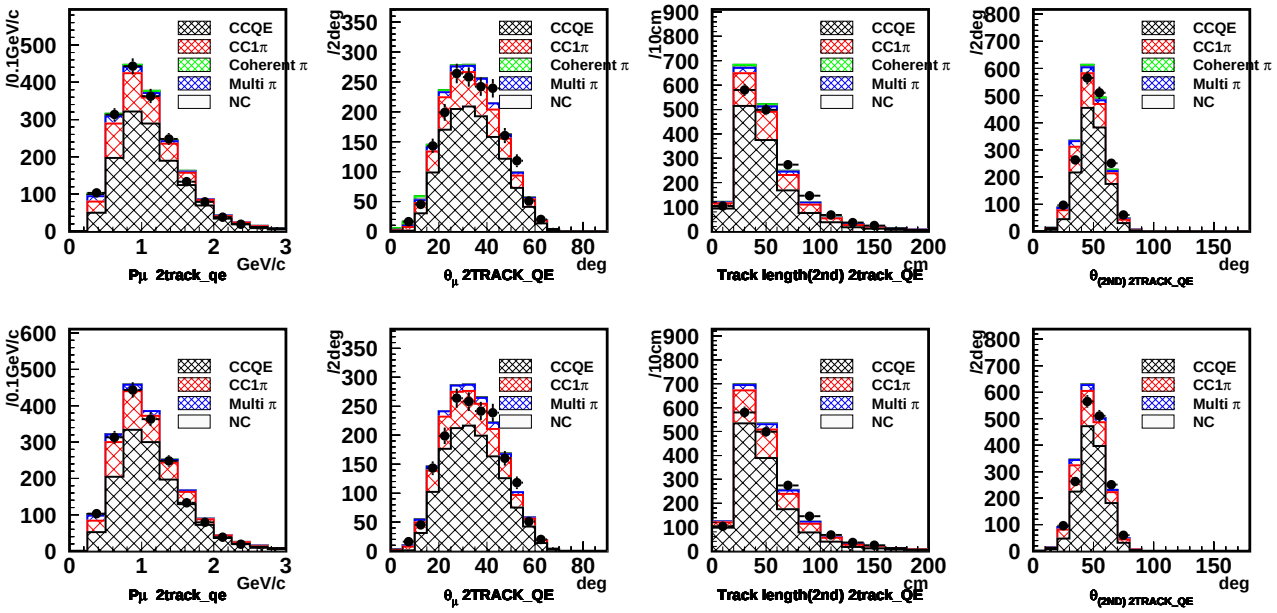

Figure 7.22: The distributions of p_μ, θ_μ, $L_{2\mathrm{nd}}$ and $\theta_{2\mathrm{nd}}$ for the QE sample. The MC expectations of upper figures include CC coherent pion production and the lower ones do not include it.

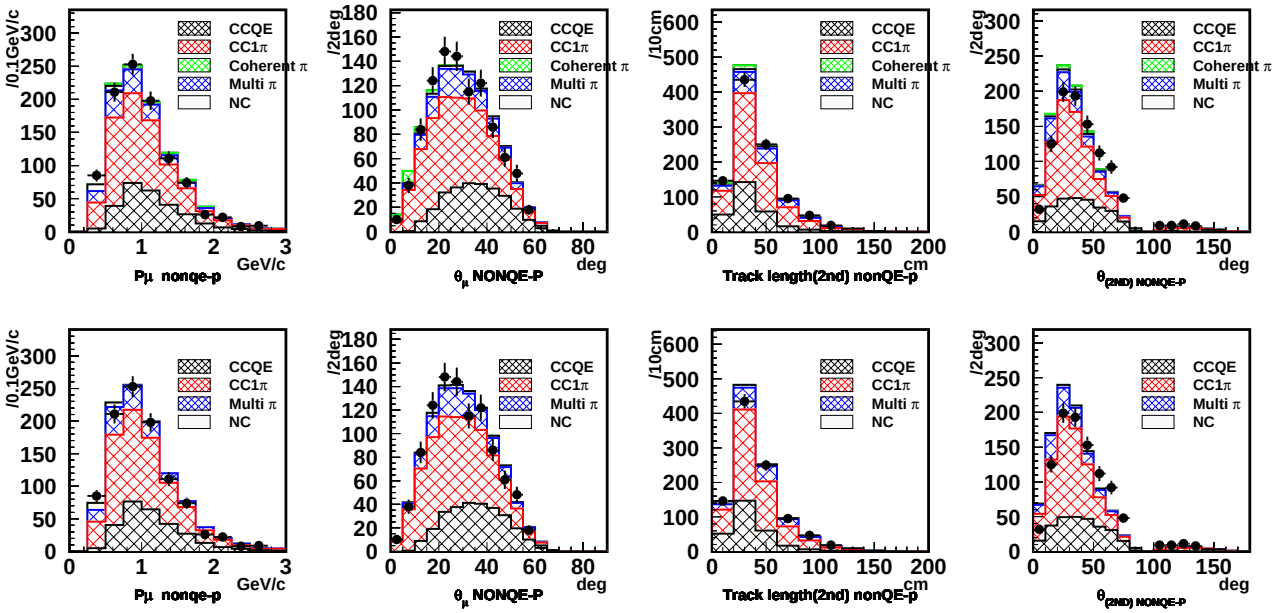

Figure 7.23: The distributions of p_μ, θ_μ, $L_{\rm 2nd}$ and $\theta_{\rm 2nd}$ for the nonQE-proton sample. The MC expectations of upper figures include CC coherent pion production and the lower ones do not include it.

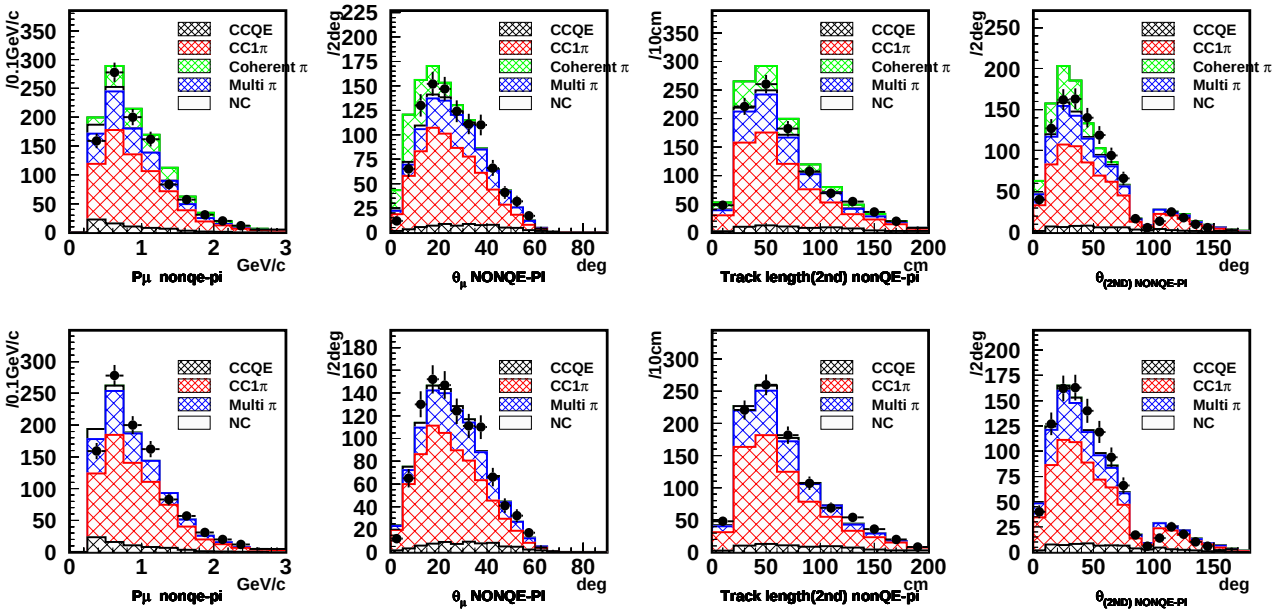

Figure 7.24: The distributions of p_μ, θ_μ, $L_{\rm 2nd}$ and $\theta_{\rm 2nd}$ for the nonQE-pion sample. The MC expectations of upper figures include CC coherent pion production and the lower ones do not include it.

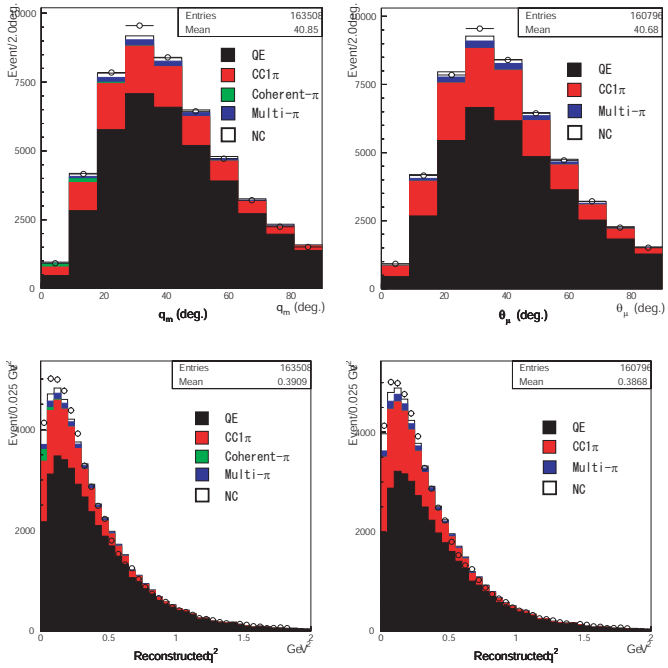

Figure 7.25: The θ_μ (top) and $q^2_{\rm rec}$ (bottom) distributions of the 1KT CC sample. The MC expectations of left side figures include CC coherent pion production and right side ones do not include it.

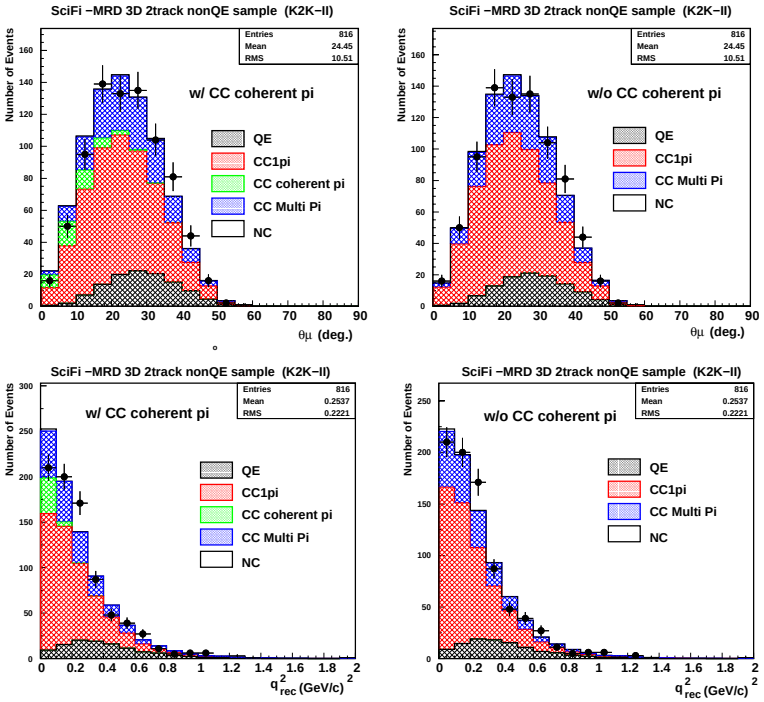

Figure 7.26: The θ_μ (top) and $q^2_{\rm rec}$ (bottom) distributions of the SciFi nonQE sample. The MC expectations of left side figures include CC coherent pion production and right side ones do not include it.

Chapter 8

Near Detector Analysis

The neutrino event rate and energy spectrum before neutrinos oscillate are measured with the near detector (ND) system to predict the rate and spectrum at SK. In this chapter, we describe the analysis procedures and present results of the measurements. At last, we briefly describe the far to near neutrino flux ratio that is used to extrapolate the near detector measurements to SK.

8.1 Number of Neutrino Events at the Near Site

The number of neutrino events is measured with 1KT to predict the number of neutrino events at SK. Since 1KT has the same detector technology and use the same interaction target as SK, most of the systematic errors on the prediction at SK, mainly from the uncertainties of the detection efficiency and the neutrino cross-sections are canceled out by extrapolating the 1KT measurement.

8.1.1 Analysis overview

We select the neutrino events by using the pulse height information of sum of all the PMTs signals (PMTSUM), recorded by Flash Analog-to-Digital Converter (FADC). If the FADC peak is greater than 1000 photo-electrons, we identify the event as a neutrino event. The threshold is high enough compared to the signals from the electron from a muon decay. A schematic view of the selection by FADC is shown in Fig. 8.1. In addition, we define the fiducial volume and select the events reconstructed inside the fiducial volume of the 1KT detector.

We often observe multiple neutrino events in one beam spill due to the high intensity of neutrino beam. Since it is hard to reconstruct the vertices of the multiple-event correctly, we select only the spills with one neutrino event (single-event) to guarantee the event reconstruction quality. Then, corrections for multiple events in a spill are applied to obtain the total number of neutrino events.

8.1.2 Event selection in the 1KT detector

The selection criteria for the measurement of the number of neutrino events are as follows:

- Timing cut
  The 1KT detector is triggered with more than 40 hits of inner PMTs within a 200 nsec time window. The events within a 1.1 μsec beam spill timing are selected.
- Pre-activity cut
  The events with an activity within 1.2 μsec before the beam timing are rejected.

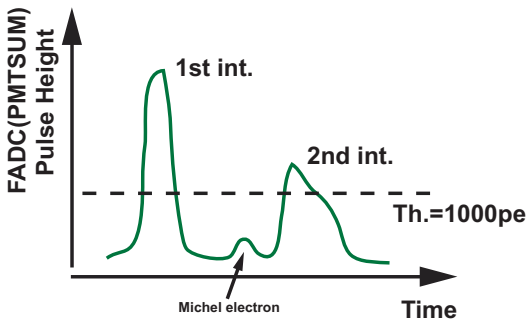

Figure 8.1: The schematic view of the pulse height distribution of PMTSUM in the case of two neutrino interactions occurring in one beam spill.

- Low energy event rejection
  The events with the total number of photo-electrons greater than 200 are selected. This threshold is equivalent to 30 MeV of electron deposited energy.

- Total photo-electron cut
  As described in the previous section, the events with a PMTSUM peak of at least 1,000 photo-electrons in FADC are selected. This threshold is equivalent to 100 MeV of electron deposited energy. We avoid counting the electron from the muon decay with this threshold. The total number of FADC peaks after this selection is defined as $N^{\rm total}_{\rm peak}$.

- Single event selection
  The events with more than one FADC peak in a spill are rejected to avoid mis-reconstruction of the vertices. The number of single events is defined as $N^{1}_{\rm peak}$. The ratio, $N^{\rm total}_{\rm peak}/N^{1}_{\rm peak}$, is used to correct the reduction rate by the single event selection.

- Fiducial volume cut
  The cylindrical volume with a radius of 2 m and a length of 2 m along the beam direction, is used as a fiducial volume. This selection imposes the fiducial mass of 25 ton. The 1KT fiducial volume is shown in Fig. 8.2.

The detailed description for the event selection and reconstruction are found in [52].

After applying all the selections, 163,784 single-events survive in total. The selection efficiency as a function of the neutrino energy is estimated with the MC simulation as shown in Figure 8.3. Here, the selection efficiency is defined as:

$$\text{selection efficiency} = \frac{\text{\# of detected neutrino events in 25 ton}}{\text{\# of generated neutrino events in 25 ton}} \tag{8.1}$$

The total efficiency is estimated to be 75 %.

8.1.3 Corrections on the number of selected event

We estimate the total number of neutrino events from the selected number of single events, $N^{\rm 1KT}_{\rm select}$, by considering the amount of possible background events and the effect of multiple events as follows.

$$N^{\rm 1KT}_{\rm obs} = N^{\rm 1KT}_{\rm select} \cdot \frac{1}{1+R_{\rm BG}} \cdot \frac{N^{\rm total}_{\rm peak}}{N^{1}_{\rm peak}} \cdot C_{\rm multi} \quad , \tag{8.2}$$

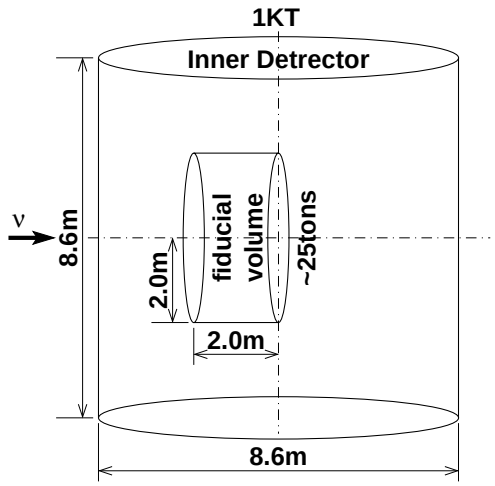

Figure 8.2: The definition of the fiducial volume of 1KT. It is a cylindrical region which has a radius of 2 m and a length of 2 m.

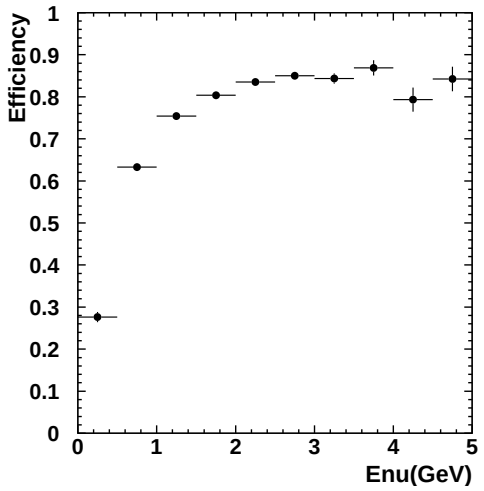

Figure 8.3: The selection efficiency as a function of E_ν.

where

$R_{\rm BG}$: a fraction of background contamination in the selected sample

$C_{\rm multi}$: a correction factor for multiple events in a spill which are not be identified as multiple events with the FADC selection.

In this subsection, we explain the corrections factors shown in Equation 8.2.

Background rate; $R_{\rm BG}$

The possible background sources are cosmic ray muon and an incoming muon produced by a neutrino. In addition, the fake events due to the reflection pulse in the signal cables occur only for the 1999 runs. The amount of the cosmic ray muon backgrounds is estimated with the random trigger data and found to be 1.0 %. For the neutrino-induced muon backgrounds, the amount of the background events is estimated to be 0.5 % by eye-scanning with information of outer PMTs. The fraction of fake events due to the reflection is estimated to be 2.6 % in the 1999 runs.

Reduction rate by the single-event selection; $N^{\rm total}_{\rm peak}/N^{1}_{\rm peak}$

The reduction rate by the single-event selection is shown in Table 8.1 for each K2K run period.

Multi event correction; $C_{\rm multi}$

Some multiple events are not identified by the FADC peak counting. The mis-identification rate is estimated with the MC simulation and found to be 2.3 %. The fraction of the multiple events in the total number of interaction is also estimated to be 0.34 with the MC simulation. Thus, the correction factor $C_{\rm multi}$ is calculated to be $1/(1-0.34*0.023) = 1.008$.

Table 8.1: The reduction rate of the neutrino events by the single-event selection for each K2K run period.

Period	$N_{\mathrm{peak}}^{\mathrm{total}}$	$N_{\mathrm{peak}}^{\mathrm{single}}$	reduction rate
K2K-Ia	109119	89782	1.215
K2K-Ib	1854781	1475799	1.257
K2K-II	2012446	1588669	1.267

Table 8.2: The systematic errors on the total number of events in 1KT.

Source	Error
Fiducial volume	3.0%
Energy scale	0.3%
FADC fluctuation	0.8%
FADC threshold	1.5%
Background rate	0.5%
Multi-event corr.	0.7%
Stability	1.6%
Beam profile	0.3%
Total	4.1%

8.1.4 Total number of neutrino events in 1KT

After applying all the selections and corrections, the total number of neutrino events in 1KT is measured to be 206,666. Table 8.2 shows the systematic error sources and the sizes on the total number of neutrino events. The total systematic error is 4.1%. The dominant systematic source is the uncertainty of the fiducial mass. The detailed description of the systematic error evaluation is found in [52].

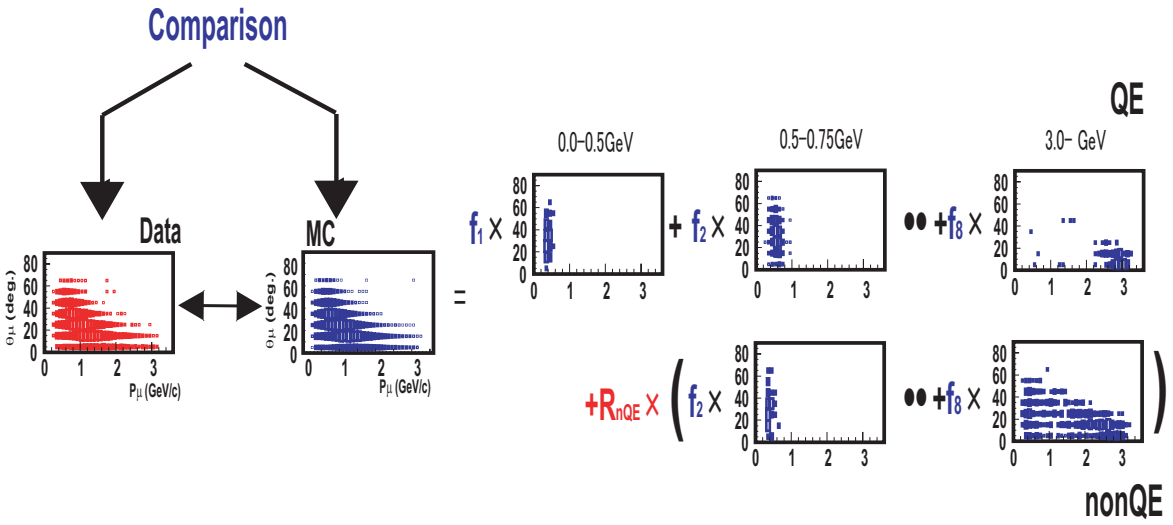

Figure 8.4: The (p_μ, θ_μ) two-dimensional distributions of the SciBar 1-track sample. The area of each box is proportional to the content. The observation and the MC expectation is compared in the fitting.

8.2 Neutrino Energy Spectrum at the Near Site

We measure the neutrino energy spectrum at the near site with 1KT, SciFi and SciBar. As described in Section 3.2, we cover the relevant neutrino energy region by using three detectors.

8.2.1 Analysis overview

We reconstruct the neutrino energy from the muon kinematics of p_μ and θ_μ by assuming QE interaction as shown in Equation 2.2. In the analysis, we use two-dimensional distributions of p_μ versus θ_μ to measure the neutrino energy spectrum. The observed (p_μ, θ_μ) distributions are compared with the MC expectations by using the χ^2 fitting, treating the neutrino energy spectrum in MC as fitting parameter.

The fitting method

In order to obtain the neutrino energy spectrum, we fit the (p_μ, θ_μ) distribution with the MC expectation as shown in Figure 8.4. The neutrino energy is divided into eight bins as shown in Table 8.4. For the MC expectation, the (p_μ, θ_μ) distribution is prepared separately for each E_ν bin and for each of QE and nonQE interactions. The 8×2 distributions are prepared in total for each event sample.

The free parameters in the fit are neutrino spectrum divided into eight energy bins $(f_1^\phi, ..., f_8^\phi)$ and the cross section ratio of CC-nonQE to CC-QE ($R_{\rm nQE}$). The systematic uncertainties, such as nuclear effects, the energy scale, the track finding efficiency, and other detector related systematics, are also incorporated as the fitting parameters ($\boldsymbol{f}$). In addition, the spectrum measurement by PIMON is used as a constraint of the spectrum for $E_\nu > 1.0$ GeV.

During the fit, the flux in each energy bin and $R_{\rm nQE}$ are re-weighted relative to the values in the MC simulation. The flux for $E_\nu = 1.0 - 1.5$ GeV bin is fixed to unity for the normalization, and another set of parameters are prepared to normalize the distributions in each detector.

The χ^2 functions are separately defined for each detector and then summed to build a

Table 8.3: The E_ν interval of each bin.

	f_1^ϕ	f_2^ϕ	f_3^ϕ	f_4^ϕ	f_5^ϕ	f_6^ϕ	f_7^ϕ	f_8^ϕ
E_ν [GeV]	0.0−0.5	0.5−0.75	0.75−1.0	1.0−1.5	1.5−2.0	2.0−2.5	2.5−3.0	3.0−

Table 8.4: The summary table for the number of events in each sample used in the analysis. The efficiency and fraction of the QE events are also shown.

Event category	Number of Events	QE efficiency (%)	QE fraction (%)
1-track	7256	50.0	57.8
QE	1760	15.4	71.3
nonQE	2014	3.7	15.9

combined χ^2 function as

$$\chi^2_{\rm ND} = \chi^2_{\rm 1KT} + \chi^2_{\rm SF} + \chi^2_{\rm SB} + \chi^2_{\rm PIMON} \tag{8.3}$$

Finally, a set of the fitting parameters $(f_i^\phi, R_{\rm nQE} : \boldsymbol{f})$ is found by minimizing the χ^2 function. The best fit values, their error size and the correlation among them are used as inputs of the oscillation analysis.

In the following, we describe the analysis of only the SciBar part because the analysis procedures of all the detector parts are same. The descriptions for the 1KT, SciFi and PIMON parts are found in Appendix-C and references [47, 52, 55].

8.2.2 Analysis of the SciBar part

Event selection

In the analysis, the 1 track, QE and nonQE samples selected in Chapter 6 are used. The number of events, fraction and efficiency of QE events for each category are summarized in Table 8.4. Here, the fraction and efficiency of QE are defined as:

$$\text{QE efficiency} \;:\; \frac{\#\text{ QE events selected in the fiducial volume}}{\#\text{ QE events generated in the fiducial volume}}$$

$$\text{QE fraction} \;:\; \frac{\#\text{ QE events selected in the fiducial volume}}{\#\text{ Events selected in the fiducial volume}}$$

The selection procedure and the performance of the reconstruction are described in Chapter 6.

(p_μ, θ_μ) distribution

The bin width of the (p_μ, θ_μ) distribution is 0.1 GeV/c for p_μ and 10 degrees for θ_μ. Figure 8.5 shows the two-dimensional templates of the 1-track sample as an example. As described, the MC templates for 1-track sample is prepared separately for each E_ν bin. In addition, separate template is prepared for QE and nonQE interactions. Thus, the contents in each (i,j)-th (p_μ, θ_μ) bin of 1track-sample, $N^{\rm Exp\ 1trk}(i,j)$, is expressed with the 16 templates and the fitting parameters as,

$$N^{\rm Exp\ 1trk}(i,j) = P^{\rm SB}_{\rm Norm} \cdot \sum_{k=1}^{8} f_k^\phi \cdot \left[n^{\rm Exp\ 1trk}_{k,\rm QE}(i,j) + R_{\rm nQE} \cdot n^{\rm Exp\ 1trk}_{k,\rm nonQE}(i,j) \right], \tag{8.4}$$

where

$P^{\rm SB}_{\rm Norm}$: a normalization parameter

$n^{\rm Exp\ 1trk}_{k,{\rm QE}}(i,j)$: the expected number of contents in (i,j)-th bin for QE interaction with the baseline MC simulation.

$n^{\rm Exp\ 1trk}_{k,{\rm nonQE}}(i,j)$: the expected number of contents in (i,j)-th bin for nonQE interaction with the baseline MC simulation.

The bin contents for QE and nonQE sample is expressed in a similar way.

$$N^{\rm Exp\ 2trk\text{-}QE}(i,j) = P^{\rm SB}_{\rm Norm}\cdot P^{\rm SB}_{\rm 2trk/1trk} \times\sum_{k=1}^{8} f^{\phi}_{k}\cdot\left[n^{\rm Exp\ 2trk\text{-}QE}_{k,{\rm QE}}(i,j)+R_{\rm nQE}\cdot n^{\rm Exp\ 2trk\text{-}QE}_{k,{\rm nonQE}}(i,j)\right], \tag{8.5}$$

$$N^{\rm Exp\ 2trk\text{-}nonQE}(i,j) = P^{\rm SB}_{\rm Norm}\cdot P^{\rm SB}_{\rm 2trk/1trk}\cdot P^{\rm SB}_{\rm nonQE/QE} \times\sum_{k=1}^{8} f^{\phi}_{k}\cdot\left[n^{\rm Exp\ 2trk\text{-}nonQE}_{k,{\rm QE}}(i,j)+R_{\rm nQE}\cdot n^{\rm Exp\ 2trk\text{-}nonQE}_{k,{\rm nonQE}}(i,j)\right], \tag{8.6}$$

where $P^{\rm SB}_{\rm 2trk/1trk}$ and $P^{\rm SB}_{\rm nonQE/QE}$ are free parameters already defined in the coherent pion analysis in Section 7.5.1. In addition, the MC distributions are scaled along the p_μ axis by

$$p'_\mu = \frac{p_\mu}{P^{\rm SCIBAR}_{\rm p-scale}} \tag{8.7}$$

where $P^{\rm SCIBAR}_{\rm p-scale}$ is a parameter to vary the p_μ scale within its systematic uncertainty as stated in the Section 6.2.4.

Definition of $\chi^2_{\rm SB}$

The χ^2 of the SciBar part consists of the following two components,

$$\chi^2_{\rm SciBar} = \chi^2_{\rm cont} + \chi^2_{\rm syst} \tag{8.8}$$

The $\chi^2_{\rm cont}$ is calculated based on the binned likelihood method as follows,

$$\chi^2_{\rm cont} = -2\sum_{\rm C}\ln\frac{\mathcal{L}\left(N^{\rm obs}_{\rm C};N^{\rm exp}_{\rm C};\sigma\right)}{\mathcal{L}\left(N^{\rm obs}_{\rm C};N^{\rm obs}_{\rm C};\sigma\right)} \tag{8.9}$$

$$\mathcal{L}\left(N^{\rm obs}_{\rm C};N^{\rm exp}_{\rm C};\sigma\right) \equiv \prod_{i,j}\int_0^\infty \frac{1}{\sqrt{2\pi}\sigma_{ij}}\exp\left[-\frac{(x-N^{\rm exp}(i,j))^2}{2\sigma^2_{ij}}\right]\cdot\frac{x^{N^{\rm obs}(i,j)}e^{-x}}{N^{\rm obs}(i,j)!}dx. \tag{8.10}$$

where, C runs through the 1track, QE and nonQE samples, and $N^{\rm obs}(i,j)$, $N^{\rm exp}(i,j)$ and σ_{ij} are the observed number of event, the expected number of event and the systematic error of the expectation in the (i,j)-th bin in each sample.

The $\chi^2_{\rm syst}$ is calculated with systematic parameters by including the correlation among them.

$$\chi^2_{\rm syst} = (\boldsymbol{P_{syst}}-\boldsymbol{P_0})^t\boldsymbol{V^{-1}}(\boldsymbol{P_{syst}}-\boldsymbol{P_0}) \tag{8.11}$$

where $\boldsymbol{P_{\rm syst}}$ represents a set of systematic parameters, $\boldsymbol{P_0}$ is the nominal value of the systematic parameters, and $\boldsymbol{V}$ is the non-diagonal covariance matrix. $P_{\rm syst}$ and P_0 consist of three

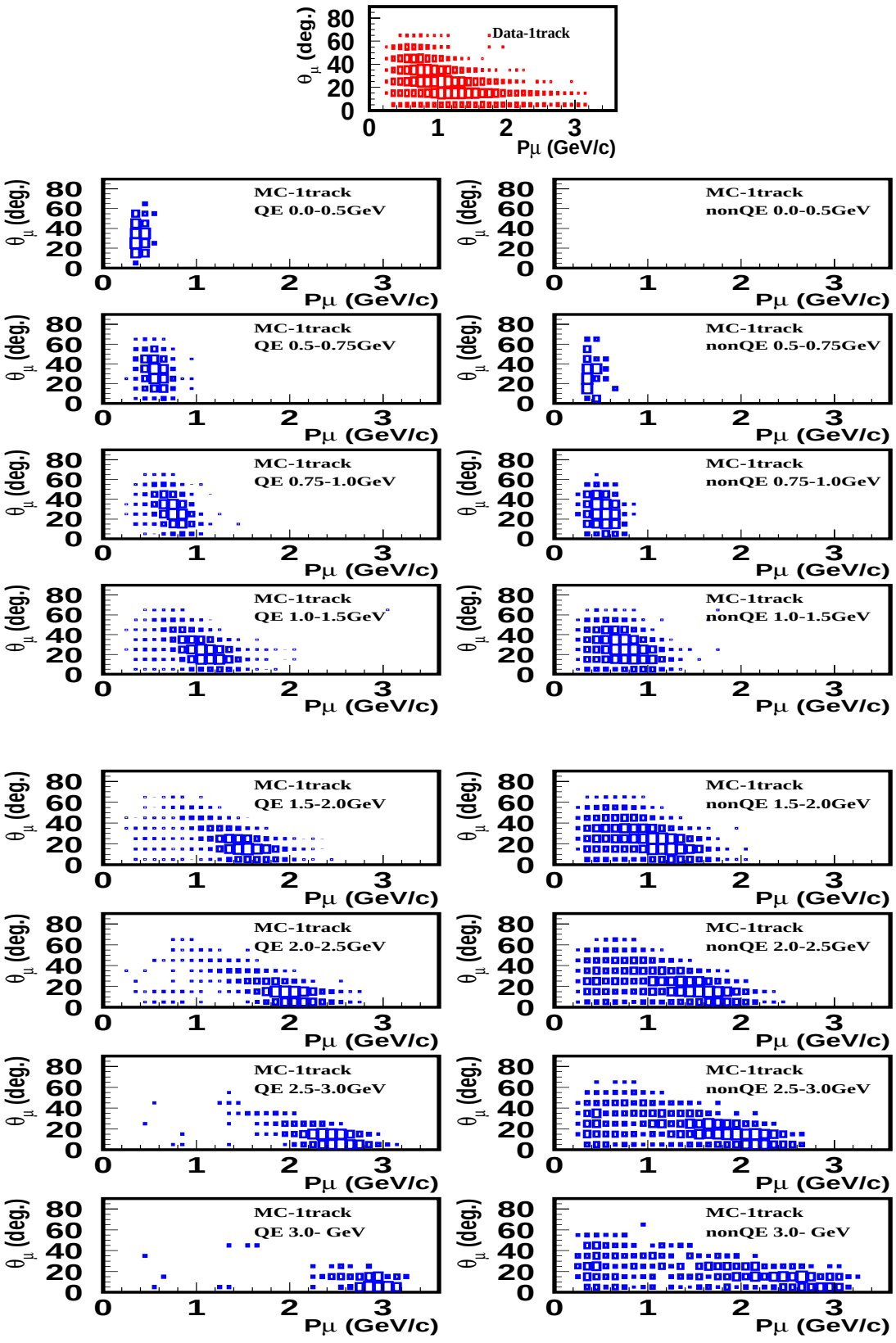

Figure 8.5: The (p_μ, θ_μ) distributions of the SciBar 1-track sample. The topmost figure shows the observed data, and the others are the MC simulation divided into each E_ν bin, each QE and nonQE interaction. The templates are arranged in order of increasing the corresponding neutrino energy from top to bottom, and those for QE (nonQE) interaction are put to the left (right) side. The area of each box is proportional to the content.

systematic errors and defined as,

$$\boldsymbol{P} \equiv \begin{pmatrix} P^{\rm SB}_{p\text{-scale}} \\ P^{\rm SB}_{\rm 2trk/1trk} \\ P^{\rm SB}_{\rm nonQE/QE} \end{pmatrix} \qquad \langle P_0 \rangle \equiv \begin{pmatrix} 1.0 \\ 1.0 \\ 1.0 \end{pmatrix}. \tag{8.12}$$

The error and correlation among the parameters are evaluated with the same manner as in the coherent pion analysis, and found to be,

$$V \equiv \begin{pmatrix} (0.027)^2 & 0 & 0 \\ 0 & +(0.058)^2 & +(0.017)^2 \\ 0 & +(0.017)^2 & +(0.059)^2 \end{pmatrix}. \tag{8.13}$$

8.2.3 Fit results

We find the minimum χ^2 point in the multi-parameter space by changing the spectrum shape, $R_{\rm nQE}$ and the systematic parameters. The central values and the errors of the fitting parameters are summarized in Table 8.5. The result of the spectrum measurement is shown in Fig. 8.6 with the prediction of the Beam-MC simulation. All the systematic parameters stay within their estimated errors.

Figure 8.7, 8.8, 8.9 show the p_μ, θ_μ, and $q^2_{\rm rec}$ distributions for each sample of 1KT, SciFi and SciBar. The event samples and selections for 1KT and SciFi are described in Appendix-C. The expected distributions of the MC simulation with the best fit parameters are also shown. The MC simulation reproduce all the distributions well.

The result of the measurement with only one detector data is also shown in Table 8.5. All the fitting parameters are in good agreement within their errors each other except for $R_{\rm nQE}$. We discuss the discrepancy on $R_{\rm nQE}$ among the three detectors below.

Additional $\mathbf{R_{nQE}}$ error

As described above, the fit result for $R_{\rm nQE}$ is inconsistent among the three detectors. The $R_{\rm nQE}$ is constrained by the shape of (p_μ, θ_μ) distribution for the 1KT measurement because only one sample is used for the measurement as shown in Appendix-C, while the $R_{\rm nQE}$ is constrained by the ratio of the number of events in nonQE sample to those in QE sample for the SciFi and SciBar measurement. The discrepancy originates from the lack of understanding of nuclear effect, energy dependence of nonQE to QE cross section ratio and the detector-specific systematics. Thus, the discrepancy should be treated as a systematic error.

However, the $R_{\rm nQE}$ value strongly depends on the E_ν spectrum or the systematic parameters, like correlation between $R_{\rm nQE}$ and $\rm P^{SB}_{nonQE}$ as shown in Table 8.5. We perform the second fit for each detector sample to check the inconsistency on $R_{\rm nQE}$ obtained under the same fitting condition. In the second fit, the E_ν spectrum and the systematic parameters, except for the overall normalization parameters, are fixed at the best fit values with three detectors. The best fit value of $R_{\rm nQE}$ in the second fit is (1KT, SciFi, SciBar) = (0.76, 0.99, 1.06), while the fit result with three detectors is 0.96. Therefore, we assign an additional error of 0.20 to $R_{\rm nQE}$ in order to account for the inconsistency.

Error matrix as an input of oscillation analysis

Finally, the errors of the measurement are obtained in the form of an error matrix. Correlations between the parameters in the fit are taken into account in the oscillation analysis with this error matrix. The elements in the error matrix are shown in Table 8.6. In the table, the square root of the error matrix (sign $[M_{ij}] \cdot \sqrt{|M_{ij}|}$) is shown in the unit of %.

Table 8.5: Results of the spectrum measurement. The best fit value of each parameter is listed for the fits with all the detectors data, with the 1KT data, with the SciFi data and with the SciBar data, respectively. The reduced χ^2 ($\chi^2_{\rm total}$/DOF) and the averaged χ^2 of each detector ($\chi^2/{\rm N_{bin}}$) are also shown.

parameter	**1KT+SciFi+SciBar**	1KT only	SciFi only	SciBar only
f_1 (0.00-0.50 GeV)	$\mathbf{1.657 \pm 0.437}$	2.310 ± 0.373	$\equiv 1$	$\equiv 1$
f_2 (0.50-0.75 GeV)	$\mathbf{1.108 \pm 0.075}$	1.178 ± 0.071	0.882 ± 0.317	1.166 ± 0.251
f_3 (0.75-1.00 GeV)	$\mathbf{1.155 \pm 0.060}$	1.066 ± 0.065	1.157 ± 0.201	1.145 ± 0.134
f_4 (1.00-1.50 GeV)	$\mathbf{\equiv 1}$	$\equiv 1$	$\equiv 1$	$\equiv 1$
f_5 (1.50-2.00 GeV)	$\mathbf{0.918 \pm 0.040}$	0.882 ± 0.087	0.980 ± 0.107	0.963 ± 0.070
f_6 (2.00-2.50 GeV)	$\mathbf{1.045 \pm 0.053}$	0.908 ± 0.176	1.188 ± 0.096	0.985 ± 0.086
f_7 (2.50-3.00 GeV)	$\mathbf{1.185 \pm 0.137}$	0.970 ± 0.668	1.062 ± 0.230	1.291 ± 0.283
f_8 (3.00- GeV)	$\mathbf{1.232 \pm 0.179}$	$\equiv 1$	1.323 ± 0.203	1.606 ± 0.749
$R_{\rm nQE}$	$\mathbf{0.964 \pm 0.035}$	0.556 ± 0.062	1.069 ± 0.060	1.194 ± 0.092
$\mathrm{P}^{\rm 1kt}_{\rm Norm}$	$\mathbf{0.948 \pm 0.024}$	1.168 ± 0.047	—	—
$\mathrm{P}^{\rm 1kt}_{\rm p-scale}$	$\mathbf{0.984 \pm 0.004}$	0.998 ± 0.006	—	—
$\mathrm{P}^{\rm SF}_{\rm Norm}$	$\mathbf{1.009 \pm 0.028}$	—	0.925 ± 0.058	—
$\mathrm{P}^{\rm SF}_{\rm Escale}$	$\mathbf{0.979 \pm 0.006}$	—	0.980 ± 0.007	—
$\mathrm{P}^{\rm SF}_{\rm LG-density}$	$\mathbf{0.929 \pm 0.011}$	—	0.928 ± 0.012	—
$\mathrm{P}^{\rm SF}_{\rm LG-cluster}$	$\mathbf{-1.389 \pm 2.488}$	—	-1.859 ± 2.567	—
$\mathrm{P}^{\rm SF}_{\rm 2nd-eff}$	$\mathbf{0.960 \pm 0.014}$	—	0.932 ± 0.017	—
$\mathrm{P}^{\rm SF}_{\rm rescat}$	$\mathbf{1.049 \pm 0.055}$	—	0.993 ± 0.062	—
$\mathrm{P}^{\rm SB}_{\rm Norm}$	$\mathbf{0.998 \pm 0.010}$	—	—	1.003 ± 0.011
$\mathrm{P}^{\rm SB}_{\rm Pscale}$	$\mathbf{0.976 \pm 0.004}$	—	—	0.972 ± 0.004
$\mathrm{P}^{\rm SB}_{\rm 2trk/1trk}$	$\mathbf{0.954 \pm 0.022}$	—	—	0.961 ± 0.023
$\mathrm{P}^{\rm SB}_{\rm nonQE/QE}$	$\mathbf{1.066 \pm 0.032}$	—	—	0.978 ± 0.040
$\chi^2_{\rm total}$/DOF	**688.2/588**	47.7 / 71	328.7 / 273	253.3 / 228
$\chi^2_{\rm 1kt}/{\rm N_{bin}}$	**85.6 / 80**	47.7 / 80	—	—
$\chi^2_{\rm SciFi}/{\rm N_{bin}}$	**336.3 / 286**	—	328.7 / 286	—
$\chi^2_{\rm SciBar}/{\rm N_{bin}}$	**265.5 / 239**	—	—	253.3 / 239
$\chi^2_{\rm PIMON}/{\rm N_{bin}}$	**0.8 / 3**	0.5 / 3	—	—

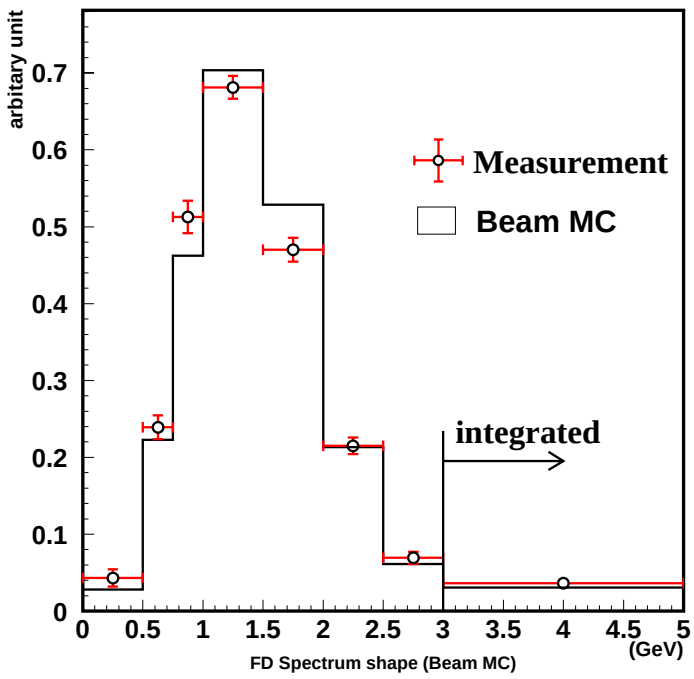

Figure 8.6: The neutrino energy spectrum measured at the near site. The expectation with the Beam-MC simulation is also shown.

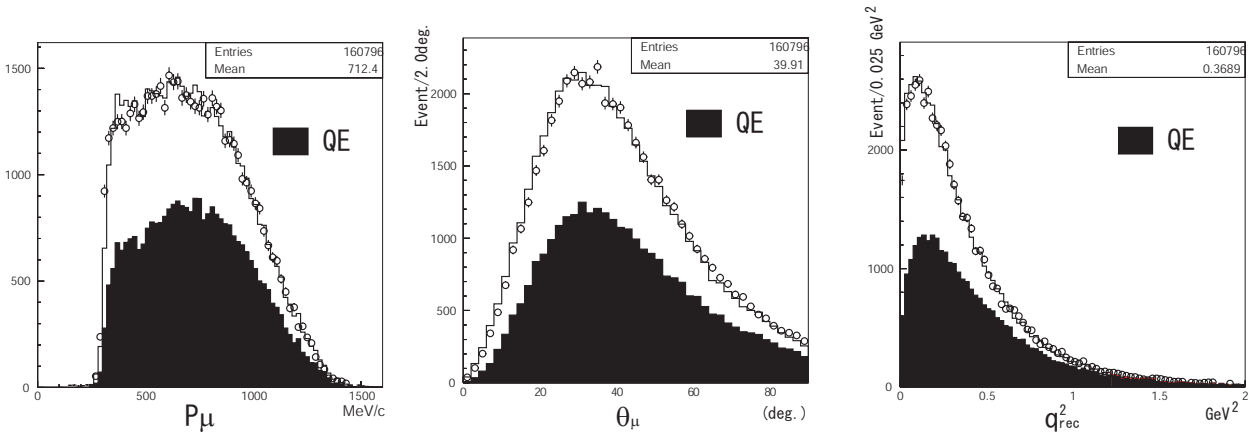

Figure 8.7: The 1KT p_μ, θ_μ, and $q^2_{\rm rec}$ distributions of the events with one reconstructed ring identified as muon. The expectations of MC simulation with the best fit parameters are shown by open histograms. The QE components in the MC simulations are also shown by filled histograms.

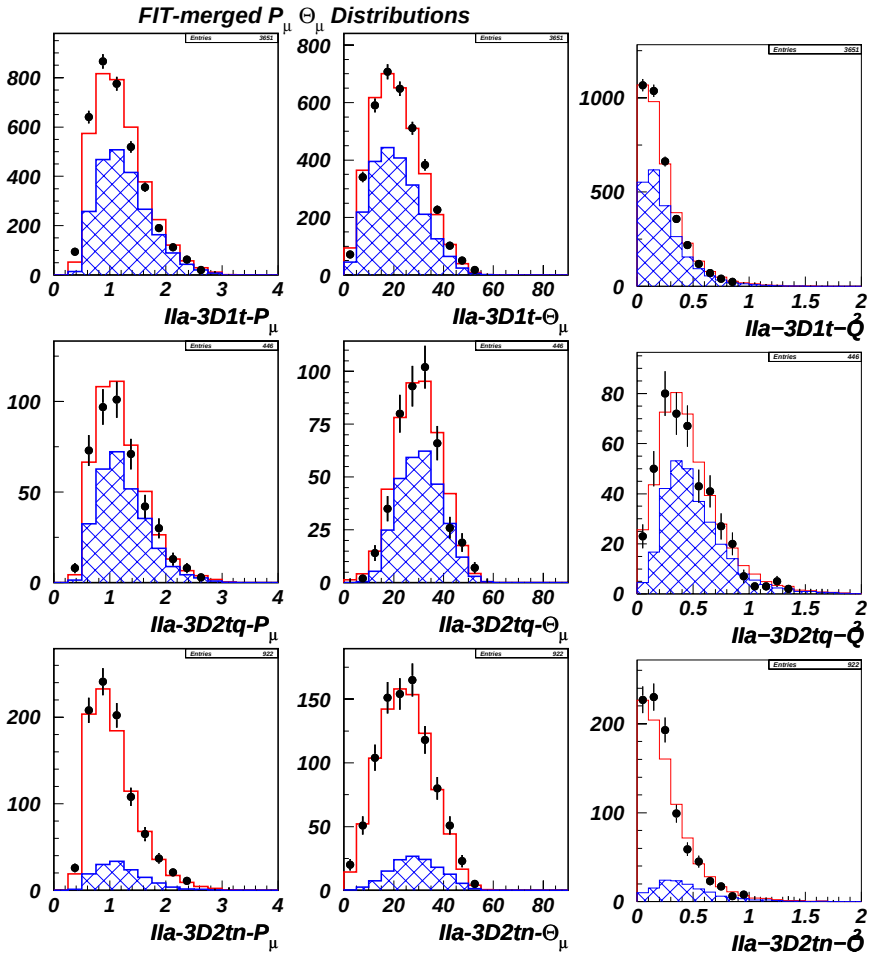

Figure 8.8: The SciFi p_μ, θ_μ, and $q^2_{\rm rec}$ distributions for 1-track (top), QE (middle) and nonQE (bottom) event. The event selection of SciFi is described in Appendix-C. The expectations of MC simulation with the best fit parameters are shown by open histograms. The QE components in the MC simulations are also shown by hatched histograms.

Table 8.6: The best fit values, errors, and error matrix for $f_{\rm i}$ and $R_{\rm nQE}$. The square root of error matrix (sign $[M_{ij}] \cdot \sqrt{|M_{ij}|}$) is shown in the unit of %.

	f_1	f_2	f_3	f_4	f_5	f_6	f_7	f_8	$R_{\rm nQE}$
Best fit	1.657	1.108	1.155	$\equiv 1$	0.918	1.045	1.185	1.232	0.964
Error (%)	0.437	0.075	0.060	fixed	0.040	0.053	0.137	0.179	0.035
f_1	43.86	-3.16	7.28	—	-2.21	-0.76	-3.48	0.81	-8.62
f_2	-3.16	7.51	1.97	—	1.90	0.62	1.29	2.43	-5.68
f_3	7.28	1.97	6.00	—	3.38	1.63	3.44	1.71	-2.99
f_4 (fixed)	—	—	—	—	—	—	—	—	—
f_5	-2.21	1.90	3.38	—	4.04	-1.86	4.53	2.20	1.65
f_6	-0.76	0.62	1.63	—	-1.86	5.28	-5.85	5.11	0.94
f_7	-3.48	1.29	3.44	—	4.53	-5.85	13.67	-10.14	4.09
f_8	0.81	2.43	1.71	—	2.20	5.11	-10.14	18.35	-11.77
$R_{\rm nQE}$	-8.62	-5.68	-2.99	—	1.65	0.94	4.09	-11.77	20.30

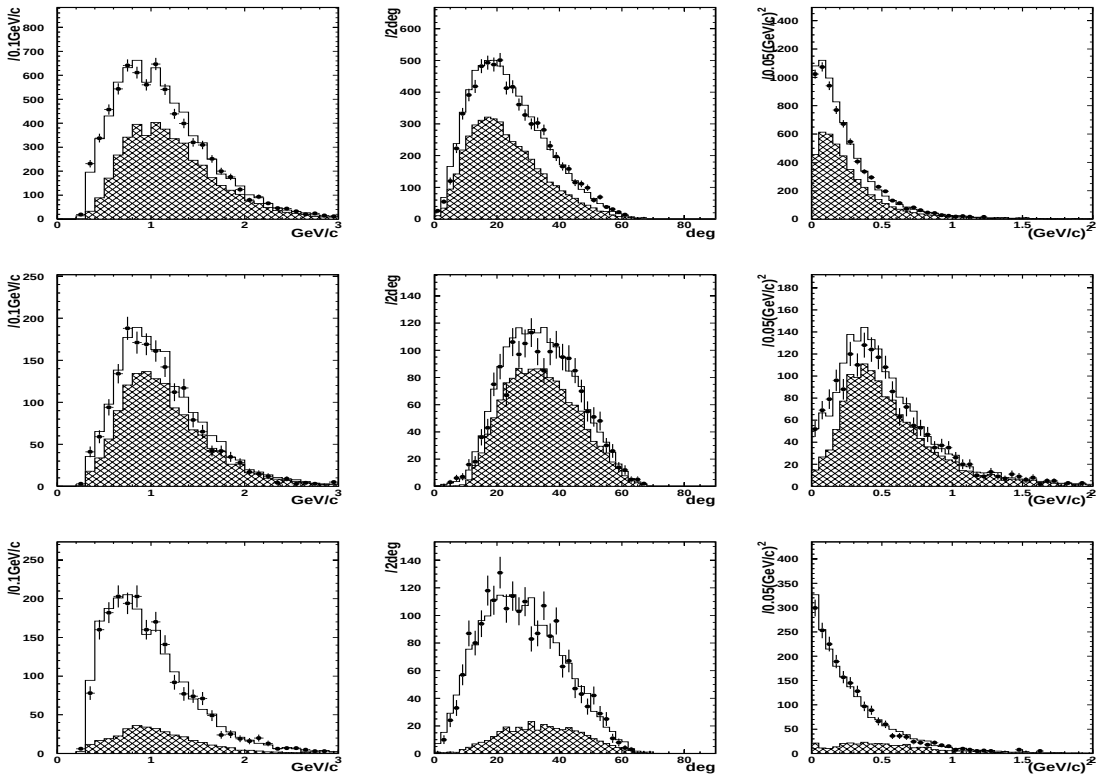

Figure 8.9: The SciBar p_μ, θ_μ, and $q^2_{\rm rec}$ distributions of 1-track (top), QE (middle) and nonQE (bottom) sample. The expectations of MC simulation with the best fit parameters are shown by open histograms. The QE components in the MC simulations are also shown by hatched histograms.

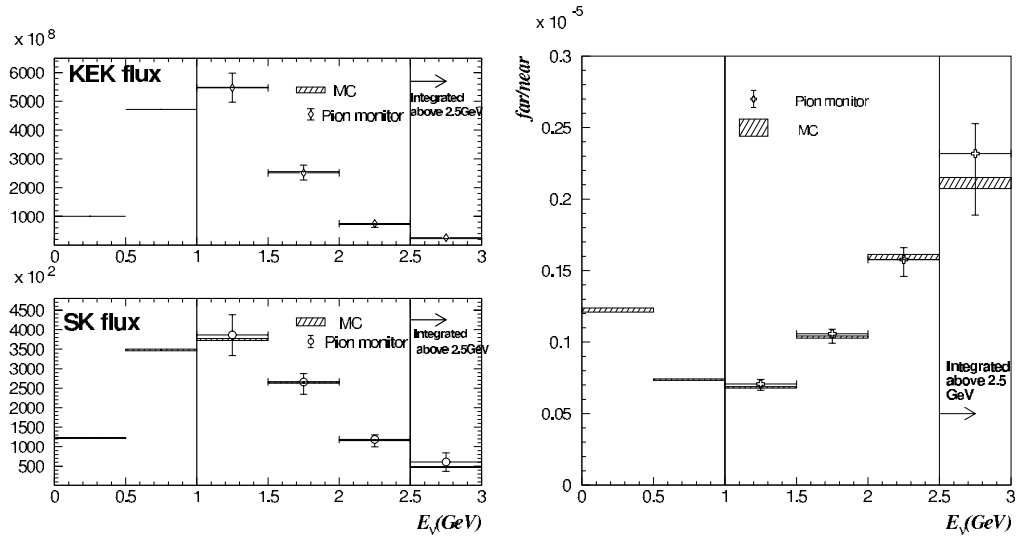

Figure 8.10: Energy spectra (left) and the far/near flux ratio (right) measured by PIMON for K2K-Ib. The cross points with error bars show the result of the PIMON measurement, and hatched boxes show the prediction of the Beam-MC simulation.

8.3 Far/Near Flux Ratio

We use the neutrino flux ratio of the near site to the far site as a function of E_ν, far/near flux ratio ($R_{F/N}(E_\nu)$), in order to estimate

- the number of events in SK from the number of neutrino events in 1KT.
- the neutrino energy spectrum at SK from the spectrum measurement at the near site

We evaluate $R_{F/N}(E_\nu)$ by the beam-MC simulation described in Section 4.1. The validity of the result is confirmed by the pion monitor (PIMON) measurement. Figure 8.10 shows the results of the neutrino spectra and the far/near flux ratio by PIMON. PIMON is sensitive to neutrinos with energy greater than 1 GeV because the momentum threshold for pions is set at 2 GeV/c in order to be insensitive to the primary 12 GeV protons. The prediction of the Beam-MC simulation is shown in Fig. 8.10. The PIMON result and the calculation by Beam-MC simulation are consistent with each other. We use the verified Beam-MC simulation shown by hatched boxes in the right figure of Fig. 8.10 as the central value of $R_{F/N}(E_\nu)$.

We also use the PIMON data to estimate the errors of the far/near flux ratio including correlation among each energy bin for the region above 1 GeV, while we use the Beam-MC simulation to estimate the errors on the region below 1 GeV. The central value and the error matrix of the far/near flux ratio is summarized in Table 8.7, where we assume no correlation between $E_\nu \geq 1$ GeV and $E_\nu \leq 1$ GeV. The detailed description of the PIMON measurement and the far/near ratio is found in Ref. [47, 52].

8.4 Summary and Discussion of Near Detector Analysis

In this chapter, we evaluate the number of neutrino event, the neutrino energy spectrum and the far/near flux ratio based on the measurement in ND.

The number of neutrino events is measured with 1KT. Based on this number and evaluated $R_{F/N}(E_\nu)$, we estimate the number of neutrino events in SK.

Table 8.7: The center values, errors, and error matrix of the far/near flux ratio since K2K-Ib. Errors are the square root of the diagonal element of the error matrix (%).

E_ν [GeV]	0.0–0.5	0.5–1.0	1.0–1.5	1.5–2.0	2.0–2.5	2.5–
$\bar{R}_{F/N}$ ($\times 10^{-6}$)	1.222	0.677	0.625	0.968	1.501	1.837
Error (%)	2.6	4.3	6.5	10.4	11.1	12.2
0.0–0.5	6.6×10^{-4}	-2.7×10^{-4}	0	0	0	0
0.5–1.0	-2.7×10^{-4}	1.8×10^{-3}	0	0	0	0
1.0–2.5	0	0	4.3×10^{-3}	5.7×10^{-4}	-3.2×10^{-4}	-1.6×10^{-3}
1.5–2.0	0	0	5.7×10^{-4}	1.1×10^{-2}	9.1×10^{-3}	2.5×10^{-3}
2.0–2.5	0	0	-3.2×10^{-4}	9.1×10^{-3}	1.2×10^{-2}	5.2×10^{-3}
2.5–	0	0	-1.6×10^{-3}	2.5×10^{-3}	5.2×10^{-3}	1.5×10^{-2}

The neutrino energy spectrum at the near site is measured using the (p_μ, θ_μ) two-dimensional distributions in 1KT, SciFi, and SciBar CC events. Since the MC prediction is now reliable even in the low-q^2 region thanks to the cross section measurement of CC coherent pion production described in Chapter 7, we can use all the events in the measurement with confidence unlike in the previous measurements [43, 44]. The nonQE to QE cross section ratio, $R_{\rm nQE}$, is also estimated in the measurement. Since the result for $R_{\rm nQE}$ is inconsistent between three detectors beyond their fitted errors, we assign the additional error on $R_{\rm nQE}$ to cover the discrepancy. The correlation between each energy bin and $R_{\rm nQE}$ is estimated in the form of an error matrix. Based on these results and $R_{F/N}(E_\nu)$, we estimate the neutrino energy spectrum at SK.

The results of ND measurements extrapolated to SK are used in the oscillation analysis described in Chapter 10, together with the observations in SK presented in the next chapter.

Chapter 9

Observation in the Far Detector

In this chapter, we describe the event selection of the accelerator-produced neutrinos at the far detector, SK.

9.1 Neutrino Event Selection

9.1.1 Timing selection

The far detector, SK, is continuously taking data of atmospheric neutrinos in addition to our accelerator-produced neutrinos. We use the timing information from the GPS system described in Chapter 3 to identify the accelerator produced neutrinos. The time window in our analysis is defined as:

$$\Delta T \equiv T_{\rm SK} - T_{\rm KEK} - {\rm TOF} \tag{9.1}$$

where, $T_{\rm SK}$ is the observed time at SK, $T_{\rm KEK}$ is the beam spill time at KEK and TOF is the time of flight of neutrinos between KEK and SK, approximately 833 μsec. In the analysis, we select the events with ΔT between -0.2 μsec and 1.3 μsec where we consider the spill length of 1.1 μsec and the resolution of GPS of 0.15 μsec. Thanks to the timing selection, the atmospheric neutrinos is suppressed by the order of 10^{-6}.

9.1.2 FCFV event selection

Other backgrounds, such as a cosmic-ray muon, low energy gamma produced inside the surrounding rock, are rejected with the following selections.

- **Decay electron cut**

  If a muon stops in the tank, it decays into an electron and neutrinos:

  $$\mu \rightarrow e + \nu_\mu + \nu_e \tag{9.2}$$

  To avoid the $e^{\pm}$s being mis-identified as a neutrino event, the SK events with an activity 30 μsec prior to the event time are rejected. A dead time by this cut is less than 0.1%.

- **HE (High Energy) trigger**

  The events with more than 31 (16) hits in the inner detector within 200 nsec time window are selected for SK-I (SK-II). This threshold corresponds to 50-100 (20-50) photo-electrons for SK-I (SK-II).

- **Total photo-electron cut**

  The events with the light yield more than 200 (94) photo-electrons in a 300 nsec time window are selected for SK-I (SK-II) to remove low energy backgrounds such as the gamma-ray from radon in water and from the surrounding rock. This threshold corresponds to about 20 MeV of electron deposited energy.

- **Flasher event cut**

  The events caused by a spark inside PMT are called 'flasher event' and fake neutrino events. The flasher events are rejected by imposing the following three selection criteria;

  Maximum photo-electron cut

  Since the flashing PMT has a large charge signal, the events with $\mathrm{PE_{max}/PE_{300}}$ greater than 0.2 (0.4) are rejected for SK-I (SK-II), where $\mathrm{PE_{max}}$ is the maximum number of photoelectrons in PMTs and $\mathrm{PE_{300}}$ is the total photo-electrons within 300 nsec time window.

  Hit timing distribution cut

  The flasher events typically have a broad hit-timing distribution because of continuous flashing. We search for the minimum number of PMT hits within 100 nsec by sliding the time window in the range from 300 to 800 nsec after the trigger time (N_{100}^{min}). If the total number of PMT hits is greater than 800, we require $N_{100}^{\mathrm{min}} < 14$ (19) for SK-I (SK-II) to reject the events with significant delayed hits. If the number of PMT hits is less than 800, we require $N_{100}^{\mathrm{min}} \leq 10$ (10) for SK-I (SK-II).

  Goodness of vertex fit cut

  The vertex position is not reconstructed correctly for the flasher events. We use the goodness of a vertex reconstruction to reject the flasher events. If the goodness is less than 0.4, we reject the events as a flasher event.

- **OD (outer detector) activity cut**

  In order to remove incoming particles, such as cosmic-ray muons, we reject the events with an activity in OD. We require the maximum number of hits in the OD cluster is less than 10. Furthermore, events with the number of OD hits more than 50 within a 800 nsec time window are also rejected. We select the fully contained (FC) events with this selection.

- **Visible energy cut**

  We select the events with the visible energy greater than 30 MeV in order to remove the remaining low energy backgrounds such as the gamma-ray from radon in water and from the surrounding rock. Here, the visible energy, E_{vis}, is the sum of electron-equivalent energy for each ring.

- **Eye scanning cut**

  To eliminate the flasher event completely, we perform eye-scanning for all the remaining events. We confirm that the selected events are neutrino events.

- **Fiducial volume cut**

  Figure 9.1 shows the (r,z) distribution of survived events in K2K-I and K2K-II after applying all the selections mentioned above. Finally, we select the events with the vertices more than 2 m away from the ID wall in order to select neutrino interactions occurring inside the SK detector. This selection imposes the 22.5 kt water fiducial volume (FV).

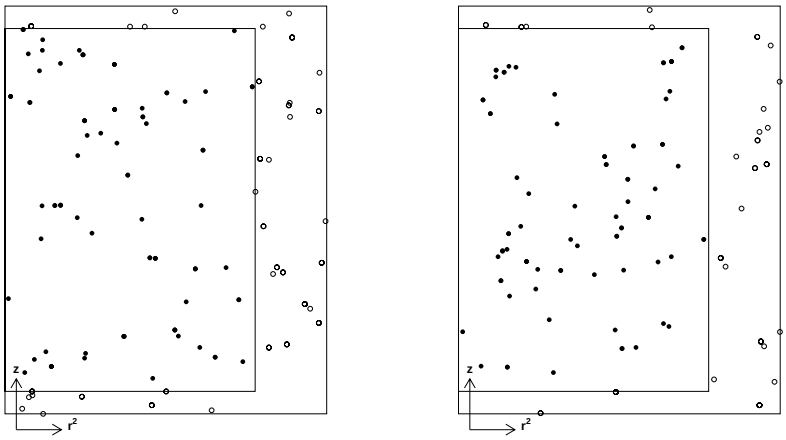

Figure 9.1: Vertex distribution in Super-K. The left (right) figure shows K2K-I (K2K-II). In the figure, the inner line shows the 22.5 kt fiducial volume and the events inside the fiducial volume are selected.

After applying all the selections mentioned above, 112 FCFV events are observed. The number of events at each selection stage is listed in Table 9.1. The selection efficiency estimated by the MC simulation is 77.2 % and 77.9 % for SK-I and SK-II, respectively. As shown in Fig. 9.2, the remaining 112 events are concentrated inside the 1.5 μsec time window synchronized with the beam spill timing. The number of events observed outside the 1.5 μsec time window is three, which is consistent with 2.3 expected background events by atmospheric neutrinos. The relation between the accumulated number of protons on target (POT) and the number of observed events in SK is shown in Fig. 9.3. The observed number of events is proportional to the accumulated POT as expected.

The observed 112 events are further classified into several categories with the number of rings and the particle type. The number of events in each event category with the MC expectation without oscillation are summarized in Table 9.2. In data, 58 single ring muon-like (1Rμ) events are observed, which are used for the spectrum analysis. A typical display of the 1Rμ event is shown in Fig. 9.4.

Table 9.1: Summary of the number of selected events at each reduction step in SK.

	Selection Criteria	K2K-I	K2K-II	Total
1	Analyzed number of spill	9177578	8214003	17391581
2	Rough timing cut ($\|\Delta T\| \leq 500$ μsec)	107892	470469	578361
3	HE trigger	36560	29878	66438
4	Total photo-electron cut	18902	16623	35525
5	Visible energy cut	103	88	191
6	Eye scanning cut	95	87	182
7	Fiducial volume cut	56	59	115
8	Fine timing cut ($-0.2 < \Delta T$ (μsec) < 1.3)	55	57	112

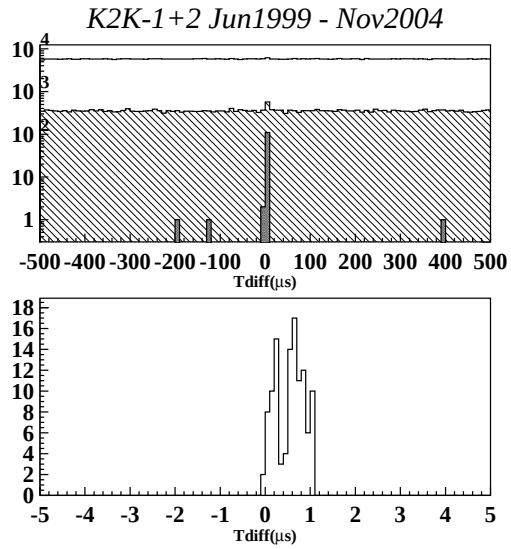

Figure 9.2: The time difference distribution. Upper figure shows the HE (High Energy) triggered events in ± 500 μsec time window after the decay electron cut (solid line), total photo-electron cut (light hatch), and fiducial volume cut (dark hatch). Lower figure shows the HE events in ± 5 μsec time window after the fiducial volume cut.

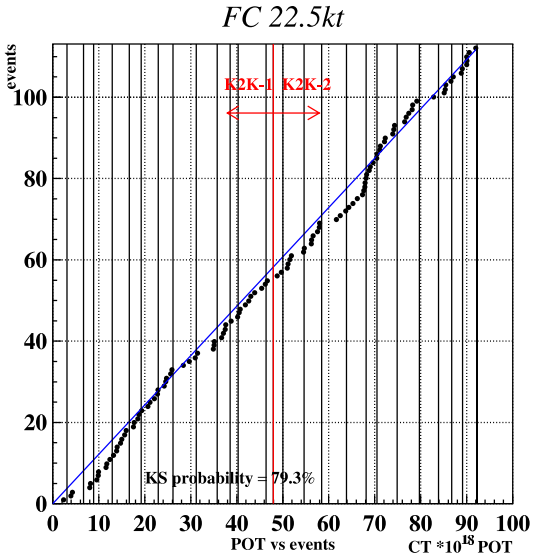

Figure 9.3: The number of observed FCFV events as a function of POT. Dots are data and the solid line is the linear fit to the average event rate.

Table 9.2: The observed number of neutrino events in each category in SK. The MC expectation for the null oscillation case is also shown. Each number in K2K-I and K2K-II is shown in the brackets.

		DATA (K2K-I,K2K-II)	MC (K2K-I,K2K-II)
FC 22.5Kt		112 (55, 57)	155.9 (79.7, 76.2)
1-ring		67 (33, 34)	99.0 (50.2, 48.8)
	mu-like	58 (30, 28)	90.8 (46.4, 44.4)
	e-like	9 (3, 6)	8.2 (3.8, 4,4)
Multi-ring		45 (22, 23)	56.8 (29.5, 27.3)

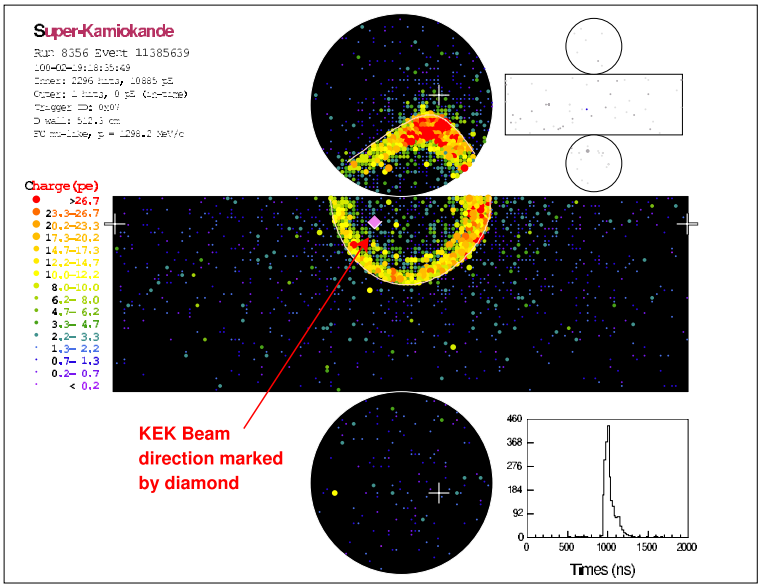

Figure 9.4: A typical event display of single-ring muon-like event at SK.

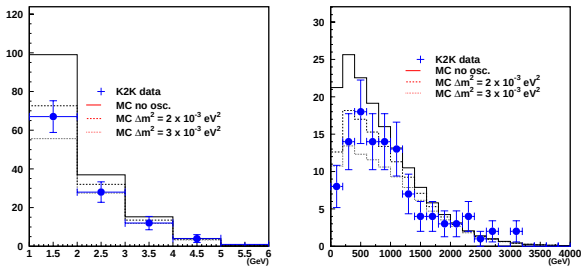

Figure 9.5: The number of rings (left) and the visible energy distributions of FCFV events. Closed circles with error bars are data, and solid lines show the MC expectation without neutrino oscillation. Dashed (dotted) lines show the expected distributions with neutrino oscillation with $\Delta m^2 = 3\times10^{-3}$ (2×10^{-3}) eV^2 and $\sin^2 2\theta = 1$.

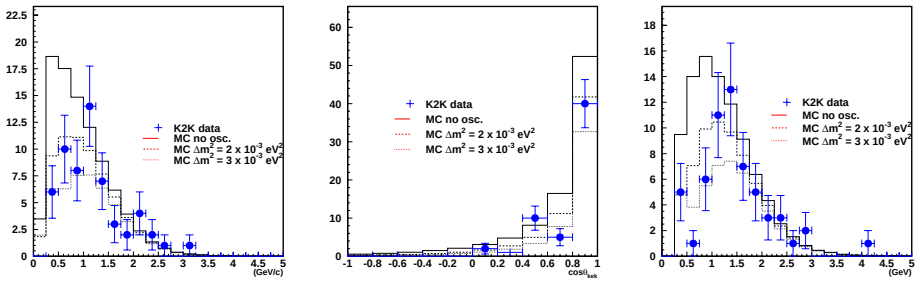

Figure 9.6: The p_μ (left), $\cos\theta_\mu$ (center) and $E_\nu^{\rm rec}$ (right) distributions of 1Rμ events. Closed circles with error bars are data, and solid lines show the MC expectation without neutrino oscillation. Dashed (dotted) lines show the expected distributions with neutrino oscillation with $\Delta m^2 = 3\times10^{-3}$ (2×10^{-3}) eV^2 and $\sin^2 2\theta = 1$.

9.2 Observed SK Event

Figure 9.5 shows the number of rings and the visible energy distributions of the FCFV events. Figure 9.6 shows the p_μ, $\cos\theta_\mu$ and $E_\nu^{\rm rec}$ distributions of 1Rμ events. The expected distributions without oscillation and with oscillation are also shown. One hundred twelve observed events is significantly lower than the expectation without oscillation of 155.9. Especially, the 1Rμ events in the lower reconstructed energy region show clear deficit as expected by the neutrino oscillation hypothesis. We test the oscillation hypothesis and obtain the oscillation parameters in the next chapter.

9.3 Systematic Error

9.3.1 Systematic error of the total number of events

The systematic errors and sources of the total number of events are listed in Table 9.3. The dominant error source is the uncertainty of the fiducial volume.

Energy scale

Table 9.3: Summary of the systematic uncertainty on the total number of observed event.

source	K2K-I (%)	K2K-II (%)
Energy scale	0.1	0.1
OD cut	0.2	0.1
Fiducial volume	2.0	2.0
Decay-e cut	0.1	0.1
MC stat.	0.6	0.4
Total	2.4	2.3

The energy scale error is evaluated to be 2.0% (2.1%) for SK-I (SK-II). When we change the visible energy cut by the amount of the error, the total number of events is changed by 0.1 % (0.1 %) for K2K-I (K2K-II). We assign the variation to the systematic error.

OD cut

The discrepancy of the number of hits in an OD cluster between data and the MC simulation is studied by using the atmospheric neutrino data. The difference of 15% (30%) is found for SK-I (SK-II). When we change the threshold of the OD cut by 15% (30%), the number of events in the MC simulation varies 0.2% (0.4%) for K2K-I (K2K-II). We assign the variations to the systematic error by the OD cut.

Fiducial volume

Two kinds of vertex reconstruction algorithms are employed [44, 52] to verify the fiducial volume. The difference of the ratios of data to the MC simulation between two vertex algorithms is found to be 2% by using the 1Rμ sample of the atmospheric neutrinos. We assign this difference to the systematic error.

Decay-e cut

The electron from a muon decay is detected as a neutrino events if the muon is not detected because of the energy lower than the Cherenkov threshold. The amount of this electron event in FCFV sample is estimated to be 0.1% by the MC simulation. Since the uncertainty of the MC prediction for this type of events is large, we assign the $\pm$100% of the predicted electron events to the systematic error by decay-e cut, conservatively.

MC statistics

The statistics error of the MC simulation is 0.6% and 0.4% for K2K-I and K2K-II, respectively.

Total

As a result, the quadratic sum of all the systematic errors is 2.4% (2.3%) for K2K-I (K2K-II). We assign 3% to the systematic error of the total number of events for each period conservatively.

Table 9.4: The summary of the systematic errors on 1Rμ events of SK.

E_ν [GeV]		0.0–0.5	0.5–1.0	1.0–1.5	1.5–2.0	2.0–2.5	2.5–
K2K-I	Fiducial volume [%]	2.0	2.0	2.0	2.0	2.0	2.0
	Ring counting [%]	3.4	2.7	3.0	4.5	4.5	4.5
	Particle ID [%]	0.7	0.3	0.5	0.4	0.4	0.4
	$\pi^\pm$ contamination [%]	0.5	0.0	0.0	0.0	0.0	0.0
	Total [%]	4.1	3.4	3.6	4.9	4.9	4.9
K2K-II	Fiducial volume [%]	2.0	2.0	2.0	2.0	2.0	2.0
	Ring counting [%]	5.3	4.1	3.7	3.8	3.8	3.8
	Particle ID [%]	1.7	0.4	0.3	0.6	0.6	0.6
	$\pi^\pm$ contamination [%]	2.0	0.0	0.0	0.0	0.0	0.0
	Total [%]	6.2	4.6	4.2	4.3	4.3	4.3

9.3.2 Energy dependent error of the 1Rμ sample

The 1Rμ events are used in the energy spectrum analysis. We estimate the energy dependent error of the 1Rμ events. The systematic errors and the sources of the 1Rμ event selection are listed in Table 9.4. The error from the energy scale error is included in the fitting parameters of oscillation analysis, and is not shown in Table 9.4. The dominant error source is the uncertainty of the ring counting.

Fiducial volume

The systematic error of the number of events by the fiducial volume cut is 2.0% for both K2K-I and K2K-II. We assign this error to the systematic error on all the energy bins.

Ring counting

The number of Cherenkov rings in an event is counted by using the charge pattern [66]. The systematic uncertainty of the ring counting is estimated by using the atmospheric neutrino data as a control sample. Since we find a difference in the performance between data and MC simulation, we tune the MC simulation to match the performance of the data by changing the criteria. We assign the change as the systematic error for the selection criteria of ring counting.

The systematic error of the number of 1Rμ events by the ring counting is estimated by changing the criteria in the K2K MC simulation by the error estimated above. The deviation is calculated in each E_ν bin and assigned as the systematic error.

Particle identification

The particle identification (PID) of each reconstructed ring is performed by using the ring pattern and the opening angle [66]. The systematic error of the particle identification is evaluated with a similar way to that on the ring counting. We adjust the criteria for PID in the MC simulation to the data with atmospheric neutrino data, and assign the adjustment to the systematic error for the selection criteria of PID.

The systematic error of the number of 1Rμ events by PID is estimated by changing the selection criteria of μ-like ring in the K2K MC simulation by the error estimated above. The deviation is calculated in each E_ν bin and assigned as the systematic error.

Pion contamination

Cherenkov rings induced by a charged pion is often mis-identified as a muon. Events with the pion ring result in a 1Rμ event when a muon is not detected or the event is originated from NC interaction. Those events are reconstructed in the low energy bin ($E_\nu < 0.5$ GeV). The uncertainty of the amount of pion contamination in 1Rμ sample is evaluated with the lower energy ring of events with two mu-like rings in the atmospheric neutrino data, which contains a muon and a pion from the CC resonance π production. We adjust the criteria of PID for the second ring in the MC simulation to the data, and assign the adjustment to the systematic error for the selection criteria of PID.

When we change the selection criteria of PID in K2K MC simulation by the estimated error, the number of 1Rμ events in K2K-I (K2K-II) varies by 0.5% (2.0%). We assign the differences to the systematic error on the 1Rμ contents of $0.0 < E_\nu < 0.5$ GeV bin from pion contamination.

Chapter 10

Neutrino Oscillation Analysis

10.1 Analysis Method

Two flavor neutrino oscillation analysis is performed with the maximum likelihood method. The signatures of neutrino oscillation appear as a reduction in the number of neutrino events and a distortion of the neutrino energy spectrum. The likelihood function is defined as the product of the likelihoods for the number of observed events in SK ($\mathcal{L}_{\rm norm}$), for the shape of the $E_\nu^{\rm rec}$ spectrum ($\mathcal{L}_{\rm shape}$) and for the systematic uncertainty ($\mathcal{L}_{\rm syst}$). The best fit value of oscillation parameters, $(\sin^2 2\theta, \Delta m^2)$, is obtained by maximizing the likelihood function. One-hundred twelve FC events and 58 FC 1Rμ events are used in $\mathcal{L}_{\rm norm}$ and $\mathcal{L}_{\rm shape}$, respectively.

10.2 Definition of Likelihood

The likelihood function to be maximized is defined as

$$\mathcal{L}(\sin^2 2\theta, \Delta m^2, \boldsymbol{f}) = \mathcal{L}_{\rm norm}(\sin^2 2\theta, \Delta m^2, \boldsymbol{f}) \times \mathcal{L}_{\rm shape}(\sin^2 2\theta, \Delta m^2, \boldsymbol{f}) \times \mathcal{L}_{\rm syst}(\boldsymbol{f}), \quad (10.1)$$

where $\boldsymbol{f}$ represents the systematic parameters as defined below, and θ and Δm^2 are the mixing angle and mass-squared difference in the two flavor scenario.

Systematic parameters

The contents of $\boldsymbol{f}$ are

$$\boldsymbol{f} \equiv (\boldsymbol{f}^{\phi}, f^{\rm nonQE}, f^{\rm NC}, \boldsymbol{f}^{F/N}, \boldsymbol{f}^{\epsilon_{\rm SK\text{-}I}}, f^{E\text{-scale}}_{\rm SK\text{-}I}, \boldsymbol{f}^{\epsilon_{\rm SK\text{-}II}}, f^{E\text{-scale}}_{\rm SK\text{-}II}, f^{\rm norm}_{\rm K2K\text{-}Ia}, f^{\rm norm}_{\rm K2K\text{-}Ib}, f^{\rm norm}_{\rm K2K\text{-}II}), \quad (10.2)$$

- $\boldsymbol{f}^{\phi}$: The E_ν spectrum measured by ND.
- $f^{\rm nonQE}, f^{\rm NC}$: The CC-nonQE/CC-QE and NC/CC-QE cross-section ratios.
- $\boldsymbol{f}^{F/N}$: The Far/Near flux ratio.
- $\boldsymbol{f}^{\epsilon_{\rm SK\text{-}X}}$: The detection efficiency of single-ring μ-like events in SK for each E_ν bin. X takes I and II, representing SK runs.
- $f^{E\text{-scale}}_{\rm SK\text{-}X}$: The energy scale of SK.
- $f^{\rm norm}_{\rm K2K\text{-}X}$: The overall normalization of the MC simulation to the prediction by 1KT. X takes Ia, Ib and II, representing experimental periods.

Each systematic parameter is defined as the relative value to the MC prediction. The systematic parameters are restricted by $\mathcal{L}_{\rm syst}$ within the errors.

10.2.1 Expectation at SK

In this section, we predict the neutrino energy spectrum and the number of neutrino events in SK by using the ND measurement. We also describe the neutrino interaction cross section with consideration of ND measurement. These are used to construct the likelihood function later.

Neutrino energy spectrum

The neutrino energy spectrum at the near site denoted $\Phi_{\rm ND}^{\text{K2K-}X}$ is measured in ND detector as described in Section 9.2, and they are expressed as

$$\Phi_{\rm ND}^{\text{K2K-}X}(E_\nu^{\rm true};\boldsymbol{f}) \equiv f_i^\phi \cdot \Phi_{\rm ND}^{\rm MC} \tag{10.3}$$

where $\Phi_{\rm ND}^{\rm MC}$ is the neutrino energy spectrum estimated with the MC simulation and f_i^ϕ is the weighting factor for the i-th energy bin measured in ND. The f_i^ϕ vary the energy spectrum within its estimated error (Table 8.5).

The energy spectrum at SK without oscillation is extrapolated from $\Phi_{\rm ND}^{\text{K2K-}X}$ by multiplying the far/near flux ratio, $R_{F/N}(E_\nu)$;

$$\begin{aligned}\Phi_{\rm SK}^{\text{K2K-}X}(E_\nu^{\rm true};\boldsymbol{f}) &\equiv f_j^{F/N}\cdot R_{F/N}(E_\nu)\cdot\Phi_{\rm ND}^{\text{K2K-}X}(E_\nu^{\rm true};\boldsymbol{f})\\ &= f_i^\phi\cdot f_j^{F/N}\cdot R_{F/N}(E_\nu)\cdot\Phi_{\rm ND}^{\rm MC}(E_\nu^{\rm true})\end{aligned} \tag{10.4}$$

where $f_j^{F/N}$ is a factor relative to $R_{F/N}(E_\nu)$. The $f_j^{F/N}$ vary the far/near ratio within its estimated error (Table 8.7). When we take into account neutrino oscillation, $\Phi_{\rm SK}^{\text{K2K-}X}$ is expressed as;

$$\Phi_{\rm SK}^{\text{K2K-}X}(E_\nu^{\rm true};\Delta m^2,\sin^2 2\theta,\boldsymbol{f}) = P(E_\nu^{\rm true};\Delta m^2,\sin^2 2\theta)\cdot\Phi_{\rm SK}^{\text{K2K-}X}(E_\nu^{\rm true};\boldsymbol{f}) \tag{10.5}$$

where P is the neutrino oscillation probability written as

$$P(E_\nu^{\rm true};\Delta m^2,\sin^2 2\theta,\boldsymbol{f}) = \begin{cases} 1-\sin^2 2\theta\cdot\sin^2\dfrac{1.27\cdot\Delta m^2\cdot L}{E_\nu^{\rm true}} & \text{CC}\\ 1 & \text{NC,}\end{cases} \tag{10.6}$$

The cross section of neutrino interaction

The cross section of neutrino interaction is defined as

$$\sigma^{\mathcal{I}}(E_\nu^{\rm true}) = f^{\mathcal{I}}\cdot\sigma^{\rm MC}(E_\nu^{\rm true}) \tag{10.7}$$

where $f^{\mathcal{I}}$ is a fit parameter to vary the cross section for each interaction mode, and $\sigma^{\rm MC}$ is the cross section evaluated with the MC simulation. In the present analysis, the interaction mode are classified into the following three modes, QE, CC-nonQE and NC interaction. The total cross section is written as

$$\sum_{\mathcal{I}}\sigma^{\mathcal{I}} = f^{\rm QE}\cdot\sigma_{\rm QE}^{\rm MC} + f^{\rm CC-nonQE}\cdot\sigma_{\rm CC-nonQE}^{\rm MC} + f^{\rm NC}\cdot\sigma_{\rm NC}^{\rm MC}, \tag{10.8}$$

where the error on $f^{\rm CC-nonQE}$ is approximately 20% as evaluated in ND measurement (Table 8.5) and the error on $f^{\rm NC}$ is estimated to be 15.3% based on the past experiment [117, 118]. In the present analysis, $f^{\rm QE}$ is fixed 1 and only the relative size of CC-nonQE and NC, i.e., $f^{\rm CC-nonQE}$ and $f^{\rm NC}$, are treated as adjustable parameters.

The number of neutrino events

The number of neutrino events for each period is expected by using the observed number of events in 1KT, $(N_{\rm ND}^{\rm obs})_{\rm K2K\text{-}\mathit{X}}$, as follows,

$$N_{\rm K2K\text{-}\mathit{X}}^{\rm exp}(\Delta m^2, \sin^2 2\theta; \boldsymbol{f}) \equiv f_{\rm K2K\text{-}\mathit{X}}^{\rm norm} \cdot (N_{\rm ND}^{\rm obs})_{\rm K2K\text{-}\mathit{X}} \cdot \frac{{\rm N}_{\rm SK}^{\rm K2K\text{-}\mathit{X}}(\Delta m^2, \sin^2 2\theta, \boldsymbol{f})}{{\rm N}_{\rm ND}^{\rm K2K\text{-}\mathit{X}}(\boldsymbol{f})} \cdot \frac{M_{\rm SK}}{M_{\rm ND}} \cdot \frac{{\rm POT}_{\rm SK}^{\rm K2K\text{-}\mathit{X}}}{{\rm POT}_{\rm KT}^{\rm K2K\text{-}\mathit{X}}} \cdot C_{\nu_e}, \quad (10.9)$$

where

$${\rm N}_{\rm SK}^{\rm K2K\text{-}\mathit{X}} \equiv \int dE_\nu^{\rm true} \cdot \Phi_{\rm SK}^{\rm K2K\text{-}\mathit{X}}(E_\nu^{\rm true}; \Delta m^2, \sin^2 2\theta, \boldsymbol{f}) \cdot \sum_{\mathcal{I}} \sigma^{\mathcal{I}}(E_\nu^{\rm true}, \boldsymbol{f}) \cdot \epsilon_{\rm SK\text{-}\mathit{X}}^{\mathcal{I}}(E_\nu^{\rm true})$$

$${\rm N}_{\rm ND}^{\rm K2K\text{-}\mathit{X}} \equiv \int dE_\nu^{\rm true} \cdot \Phi_{\rm ND}^{\rm K2K\text{-}\mathit{X}}(E_\nu^{\rm true}; \boldsymbol{f}) \cdot \sum_{\mathcal{I}} \sigma^{\mathcal{I}}(E_\nu^{\rm true}, \boldsymbol{f}) \cdot \epsilon_{\rm 1KT}^{\mathcal{I}}(E_\nu^{\rm true})$$

- $f_{\rm K2K\text{-}\mathit{X}}^{\rm norm}$: The overall normalization defined by Equation 10.2.
- $(N_{\rm ND}^{\rm obs})_{\rm K2K\text{-}\mathit{X}}$: The number of observed event in 1KT.
- ${\rm N}_{\rm SK(ND)}^{\rm K2K\text{-}\mathit{X}}$: the expected number of events in SK (1KT).
- $M_{\rm SK\,(ND)}$: The fiducial mass of SK (1KT), which is 22.5 ktons (25 tons).
- ${\rm POT}_{\rm SK\,(ND)}^{\rm K2K\text{-}\mathit{X}}$: The number of protons on target for SK (1KT). This accounts for the different live time of the detector.
- C_{ν_e} : The correction for the electron neutrino component in the neutrino beam. When the ν_e component is taken into account in the MC simulation, the number of events in SK increase by 0.6% and that in 1KT by 1.3%. Therefore, C_{ν_e} is set at 0.996 (=1.006/1.013).
- $\epsilon_{\rm SK\text{-}\mathit{X}(ND)}^{\mathcal{I}}$: The detection efficiency for SK (1KT) estimated with the MC simulation.

Since the $\Phi_{\rm SK}^{\rm K2K\text{-}\mathit{X}}$ is extrapolated from $\Phi_{\rm ND}^{\rm K2K\text{-}\mathit{X}}$ as described in Section 10.2.1, $\Phi_{\rm ND}^{\rm K2K\text{-}\mathit{X}}$ are included in both the numerator and denominator in Equation (10.9). Even if $\Phi_{\rm ND}^{\rm K2K\text{-}\mathit{X}}$ have ambiguities, their deviation from the true values are identical. As a result, their influence on $N_{\rm K2K\text{-}\mathit{X}}^{\rm exp}$ are reduced to be almost negligible. The effects from the uncertainty of the neutrino interaction cross section and the detection efficiency are reduced for the same reason. The error cancellation between ND and SK is one of the advantage of this analysis.

10.2.2 Normalization term

The $\mathcal{L}_{\rm norm}$ is calculated with the assumption that the observed number of SK fully contained (FC) events ($N^{\rm obs}$) follows the poisson distribution with the mean of the expected number of events ($N^{\rm exp}$) as

$$\mathcal{L}_{\rm norm} = \frac{(N^{\rm exp})^{N^{\rm obs}}}{N^{\rm obs!}} e^{-N^{\rm exp}} \quad (10.10)$$

where the expected number is separately estimated for each experimental period because the experimental setup are different, and summed up as

$$N^{\rm exp} = N_{\rm Ia}^{\rm exp} + N_{\rm Ib}^{\rm exp} + N_{\rm II}^{\rm exp} \quad (10.11)$$

The expectation for each period is already described in Section 10.2.1.

10.2.3 Spectrum shape term

The shape term,

$$\mathcal{L}_{\rm shape} = \prod_{i=1}^{N^{1{\rm R}\mu}_{\rm K2K\text{-}Ib}} PDF_{\rm I}(E_i^{\rm rec};\Delta m^2,\sin^2 2\theta,\boldsymbol{f}) \times \prod_{i=1}^{N^{1{\rm R}\mu}_{\rm K2K\text{-}II}} PDF_{\rm II}(E_i^{\rm rec};\Delta m^2,\sin^2 2\theta,\boldsymbol{f}) \quad (10.12)$$

is a product of the probability for each event to be observed at reconstructed neutrino energy $E_\nu^{\rm rec}$, where the $N^{1{\rm R}\mu}_{\rm K2K\text{-}Ib}$ $(=30)$ and $N^{1{\rm R}\mu}_{\rm K2K\text{-}II}$ $(=28)$ are the number of observed 1Rμ events for K2K-Ib and K2K-II, respectively. The probability density function of $\rm PDF_{Ib}$ and $\rm PDF_{II}$ are expressed as

$$\begin{aligned} &PDF_X(E_\nu^{\rm rec};\sin^2 2\theta,\Delta m^2,\boldsymbol{f}) \\ &\equiv \int dE_\nu^{\rm true}\cdot\Phi_{\rm SK}^{\rm K2K\text{-}X}(E_\nu^{\rm true};\Delta m^2,\sin^2 2\theta,\boldsymbol{f})\sum_{\mathcal{I}}\cdot\sigma^{\mathcal{I}}(E_\nu^{\rm true},\boldsymbol{f})\epsilon^{1R\mu\mathcal{I}}_{\rm SK\text{-}X}(E_\nu^{\rm true})\cdot f(E_\nu^{\rm true}\rightarrow E_\nu^{\rm rec},\boldsymbol{f}), \end{aligned} \quad (10.13)$$

where $\epsilon^{1R\mu\mathcal{I}}_{\rm SK\text{-}X}(E_\nu^{\rm true})$ and $f(E_\nu^{\rm true}\rightarrow E_\nu^{\rm rec},\boldsymbol{f})$ are the detection efficiency of 1Rμ events and the detector response function representing the probability density to observe the 1Rμ event with a true energy of $E_\nu^{\rm true}$ as $E_\nu^{\rm rec}$. In the actual analysis, the neutrino energy is binned with 50 MeV and the integral in Equation 10.13 is replaced by summation. In addition, the reconstructed neutrino energy, $E_\nu^{\rm rec}$, is scaled by $f^{E\text{-scale}}_{\rm SK\text{-}X}$ with the constraint of the energy scale error in SK. Also the energy dependent error in the SK reconstruction efficiency of 1Rμ events is taken into account by replacing the efficiency $\epsilon^{1R\mu\mathcal{I}}_{\rm SK\text{-}X}(E_\nu^{\rm true})$ by $\boldsymbol{f}^{\epsilon_{\rm SK\text{-}X}}\cdot\epsilon^{1R\mu\mathcal{I}}_{\rm SK\text{-}X}(E_\nu^{\rm true})$ with the parameter $\boldsymbol{f}^{\epsilon_{\rm SK\text{-}X}}$ shown in Table 9.4.

10.2.4 Systematic term

In the present analysis, some systematic parameters are treated as the fitting parameters assumed to follow the Gaussian distribution with the constraint of the error as

$$\begin{aligned} \mathcal{L}_{\rm syst} \equiv& \exp\left[-{}^t\Delta\boldsymbol{f}^{\phi,\rm nonQE}\cdot(M^{\phi,\rm nonQE})^{-1}\cdot\Delta\boldsymbol{f}^{\phi,\rm nonQE}-\frac{(\Delta f^{\rm NC})^2}{2(\sigma^{\rm NC})^2}\right] \\ &\times\exp\left[-{}^t\Delta\boldsymbol{f}^{F/N}\cdot(M^{F/N})^{-1}\cdot\Delta\boldsymbol{f}^{F/N}\right] \\ &\times\exp\left[-\sum\frac{(\Delta f_i^{\epsilon_{\rm SK\text{-}X}})^2}{2(\sigma_i^{\epsilon_{\rm SK\text{-}X}})^2}-\sum\frac{(\Delta f^{E\text{-scale}}_{\rm SK\text{-}X})^2}{2(\sigma^{E\text{-scale}}_{\rm SK\text{-}X})^2}-\sum\frac{(\Delta f^{\rm norm}_{\rm K2K\text{-}X})^2}{2(\sigma^{\rm norm}_{\rm K2K\text{-}X})^2}\right], \end{aligned} \quad (10.14)$$

where $\Delta f = f-\langle f\rangle$ is the difference of the parameters from their nominal values, and $M^{\phi,\rm nonQE}$, $M^{F/N}$ are error matrices for the corresponding parameters as shown in Table 8.6 and 8.7, respectively. The central values and the errors of the systematic parameters are summarized in Table 10.1.

10.3 Comparison of the Observation with the Expectation without Oscillation

10.3.1 Expectation for the null oscillation case

The total number of events and the spectrum shape of the 1Rμ events are estimated without oscillation. For the number of events, many sets of parameters $\boldsymbol{f}$ are randomly generated assuming Gaussian distribution with consideration of the correlations. The $N^{\rm exp}$ is calculated for each systematic parameter set by using Equation 10.11 and 10.9. Figure 10.1 is the result

Table 10.1: Summary of the central values and the errors of the systematic parameters. If a parameter is correlated with another, the square root of the diagonal element is written as the error.

	Center	Error
f_1^{ϕ} (0.0–0.5 GeV)	1.657	± 0.437
f_2^{ϕ} (0.5–0.75 GeV)	1.108	± 0.075
f_3^{ϕ} (0.75–1.0 GeV)	1.155	± 0.060
f_4^{ϕ} (1.0–1.5 GeV)	1.000	± 0.000
f_5^{ϕ} (1.5–2.0 GeV)	0.918	± 0.040
f_6^{ϕ} (2.0–2.5 GeV)	1.045	± 0.053
f_7^{ϕ} (2.5–3.0 GeV)	1.185	± 0.137
f_8^{ϕ} (3.0 GeV –)	1.232	± 0.179
f^{nonQE}	0.964	± 0.203
f^{NC}	1.000	± 0.153
$f_1^{F/N}$ (0.0–0.5 GeV)	1.000	± 0.026
$f_2^{F/N}$ (0.5–1.0 GeV)	1.000	± 0.043
$f_3^{F/N}$ (1.0–1.5 GeV)	1.000	± 0.065
$f_4^{F/N}$ (1.5–2.0 GeV)	1.000	± 0.104
$f_5^{F/N}$ (2.0–2.5 GeV)	1.000	± 0.111
$f_6^{F/N}$ (2.5 GeV –)	1.000	± 0.122
$f^{\mathrm{norm}}_{\mathrm{K2K\text{-}Ia}}$	1.000	$^{+0.80}_{-0.68} \cdot \left(\frac{1}{N^{\mathrm{exp}}_{\mathrm{K2K\text{-}Ia}}}\right)$
$f^{\mathrm{norm}}_{\mathrm{K2K\text{-}Ib}}$	1.000	± 0.051
$f^{\mathrm{norm}}_{\mathrm{K2K\text{-}II}}$	1.000	± 0.051

	Center	Error
$f_1^{\mathrm{SK\text{-}I}}$ (0.0–0.5 GeV)	1.000	± 0.041
$f_2^{\mathrm{SK\text{-}I}}$ (0.5–1.0 GeV)	1.000	± 0.034
$f_3^{\mathrm{SK\text{-}I}}$ (1.0–1.5 GeV)	1.000	± 0.036
$f_4^{\mathrm{SK\text{-}I}}$ (1.5–2.0 GeV)	1.000	± 0.049
$f_5^{\mathrm{SK\text{-}I}}$ (2.0–2.5 GeV)	1.000	± 0.049
$f_6^{\mathrm{SK\text{-}I}}$ (2.5 GeV –)	1.000	± 0.049
$f^{E\text{-scale}}_{\mathrm{SK\text{-}I}}$	1.000	± 0.020
$f_1^{\mathrm{SK\text{-}II}}$ (0.0–0.5 GeV)	1.000	± 0.062
$f_2^{\mathrm{SK\text{-}II}}$ (0.5–1.0 GeV)	1.000	± 0.046
$f_3^{\mathrm{SK\text{-}II}}$ (1.0–1.5 GeV)	1.000	± 0.042
$f_4^{\mathrm{SK\text{-}II}}$ (1.5–2.0 GeV)	1.000	± 0.043
$f_5^{\mathrm{SK\text{-}II}}$ (2.0–2.5 GeV)	1.000	± 0.043
$f_6^{\mathrm{SK\text{-}II}}$ (2.5 GeV –)	1.000	± 0.043
$f^{E\text{-scale}}_{\mathrm{SK\text{-}II}}$	1.000	± 0.021

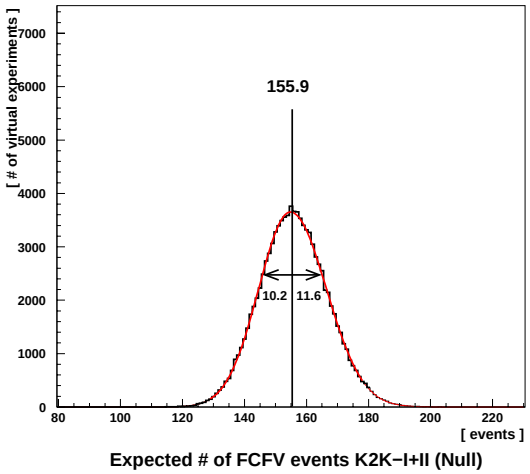

Figure 10.1: Distribution of $N^{\rm exp}$ for the null oscillation, when the systematic parameters are randomly generated within their errors. The distribution is fitted with an asymmetric Gaussian.

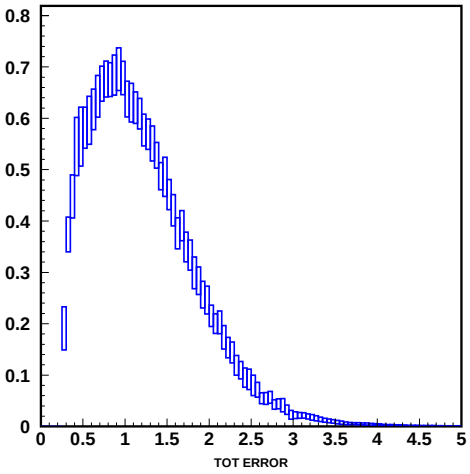

Figure 10.2: Expected $E_\nu^{\rm rec}$ shape for the null oscillation. Vertical axis is arbitrary unit. The height of boxes indicates the size of error.

of the $N^{\rm exp}$ distribution. The number of FCFV events without oscillation is estimated to be $155.9^{+11.6}_{-10.2}$ by fitting the distribution with an asymmetric Gaussian. The dominant error sources are the far/near flux ratio $\binom{+5.0\%}{-4.9\%}$ and the overall normalization $f^{\rm norm}_{\rm K2K\text{-}X}$ $\binom{+4.7\%}{-4.8\%}$.

The spectrum shape without oscillation is estimated in a similar way. The result is shown in Fig. 10.2. The contribution of each systematic error is estimated by turning only one systematic error on. The contribution of each systematic error is shown in Fig. 10.3. The dominant error source is the SK energy scale.

10.3.2 Comparison with the observation

Figure 10.4 shows the expected number of events and the expected $E_\nu^{\rm rec}$ shape without oscillations together with the observation. For the number of events, the distribution is estimated by convolving the Poisson distribution and the systematic fluctuation of $N^{\rm exp}$. The probability that less than 112 events is observed due to the statistical fluctuation is estimated to be 0.23%. For the $E_\nu^{\rm rec}$ shape, a clear distortion is seen in the low energy region as expected by neutrino oscillation. The Kolgomorov-Smirnov (KS) probability is calculated to be 0.11%. Therefore both the observed number of events and $E_\nu^{\rm rec}$ shape are inconsistent with the expectation without oscillation. Because the expectations are changed with the oscillation parameters, we search the best combination of parameters to match the observations with the expectations of neutrino oscillation by the maximum likelihood method.

10.4 Fitting Result

We search for the point to maximize the likelihood in the Δm^2 and $\sin^2 2\theta$ space by changing the systematic parameters within the uncertainties. The MINUIT program library [119] is employed to perform the fit. The best fit point in the physical region of oscillation parameter space defined as $\sin^2 2\theta \leq 1.0$ is found at

$$(\sin^2 2\theta, \Delta m^2) = (1.00, 2.76 \times 10^{-3}{\rm eV}^2). \tag{10.15}$$

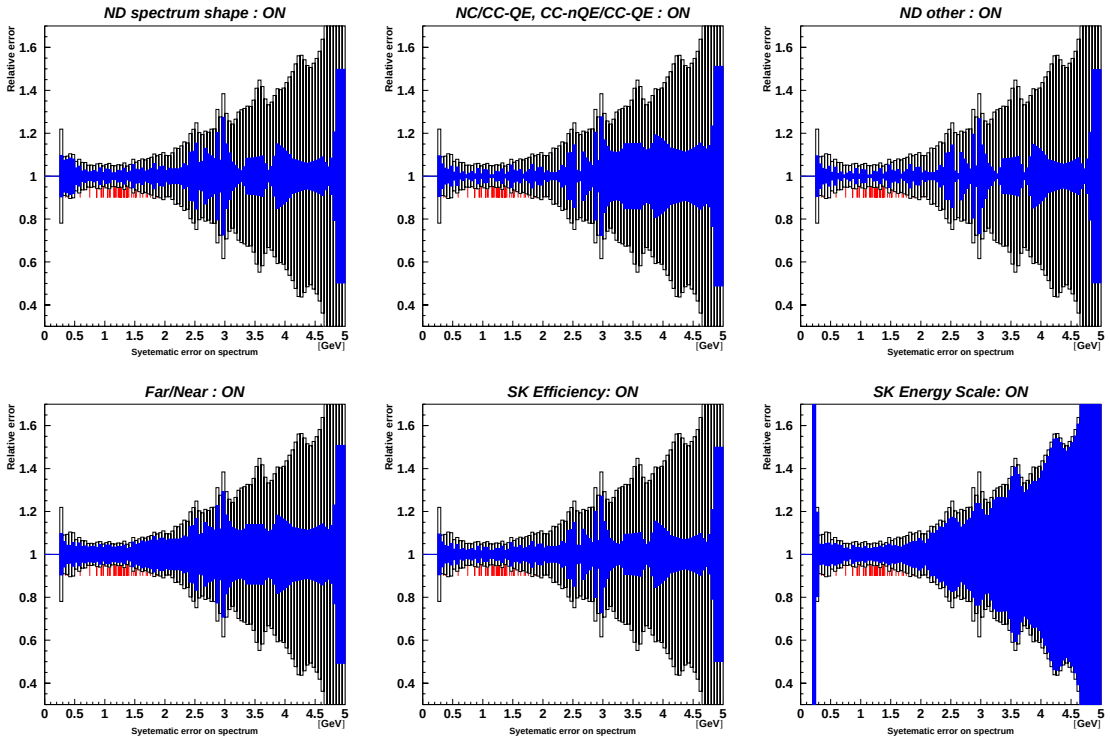

Figure 10.3: Contributions of various systematic errors to the reconstructed neutrino energy spectrum. The vertical axis is the relative error of the spectrum shape. The source of error is indicated in each plot. The blank histograms show the total error and the filled histograms show the contribution from each source.

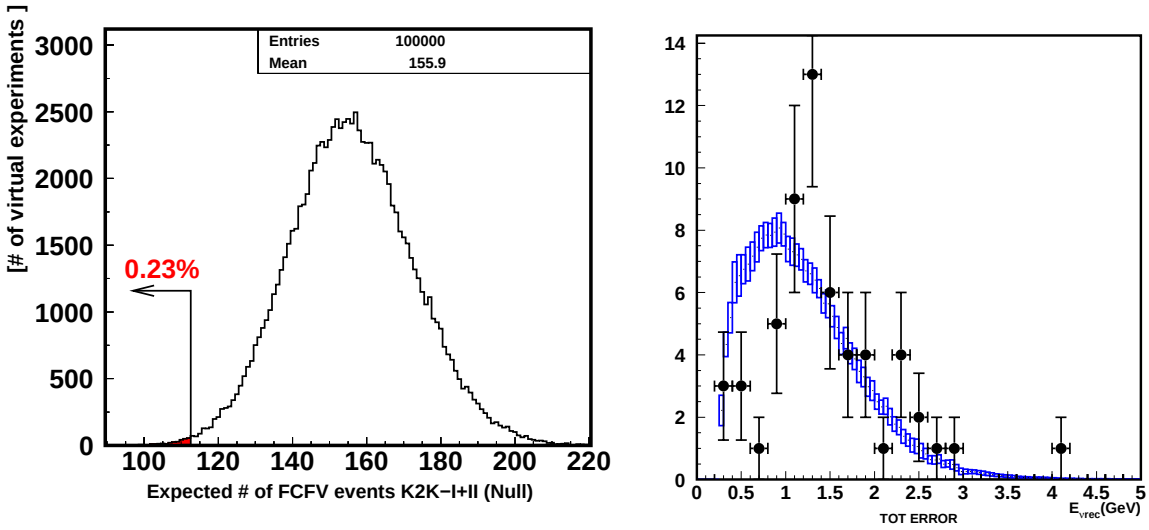

Figure 10.4: The expected number of observed FCFV events (left) and the expected $E_\nu^{\rm rec}$ distribution (right) together with the observation.

Table 10.2: Summary of the oscillation parameters at the best fit point for each fitting condition. If the best fit point is unphysical, the best point within the physical region is also listed.

		all region		physical region	
		$\sin^2 2\theta$	Δm^2 [eV^2]	$\sin^2 2\theta$	Δm^2 [eV^2]
K2K-I+II	shape + norm.	1.19	2.55×10^{-3}	**1.00**	$\mathbf{2.76\times10^{-3}}$
	shape only	1.25	2.77×10^{-3}	1.00	2.94×10^{-3}
K2K-I only	shape + norm.	1.08	2.77×10^{-3}	1.00	2.88×10^{-3}
K2K-II only	shape + norm.	1.35	2.37×10^{-3}	1.00	2.64×10^{-3}

Table 10.3: Summary of the expected number of events with the best fit parameters. For the reference, the number of observed events and the expected number in the null oscillation case are also listed.

	Best fit in physical region	Observation	Null oscillation
$(\Delta m^2$ [eV^2], $\sin^2 2\theta)$	$(2.76\times10^{-3}, 1.0)$	—	$(0, 0)$
K2K-I+II	**107.7**	112	$155.9^{+11.5}_{-10.2}$
K2K-I only	55.1	55	$79.7^{+6.2}_{-5.4}$
K2K-II only	52.6	57	$76.2^{+5.9}_{-5.1}$

The best fit values extending to the unphysical region of oscillation parameter space is

$$(\sin^2 2\theta, \Delta m^2) = (1.19, 2.55 \times 10^{-3}\text{eV}^2). \tag{10.16}$$

The best fit values are summarized in Table 10.2 together with the result with only shape likelihood. In addition, the best fit values with only K2K-I data and with only K2K-II data are summarized in Table 10.2. We cannot find the best fit point with only normalization term since the degree of freedom of the normalization likelihood is one, and two parameters cannot be determined.

Comparison with the observation

Table 10.3 summarizes the expected number of events at the best fit point in physical region for each data set together with the observation. The expectations without oscillation are also shown for the reference. The expected number of events is 107.7, which agrees with the observation of 112 within the statistical error.

Figure 10.5 shows the E_ν^{rec} distribution together with the MC expectation with the best fit parameters. The K2K-I and K2K-II only data are also shown. The KS probability between the observation and the expectation is 39 %. The observed E_ν^{rec} agrees with the expectation.

The observations are consistent with the neutrino oscillation hypothesis.

Systematic parameters

The best-fit values of the systematic parameters are summarized in Table 10.5. Since the SK energy scale strongly affect on the spectrum shape as shown in Fig. 10.3, only the SK energy scale parameters are more fluctuated than other parameters. All the parameters stay within the estimated 1σ errors.

The validation of the best fit parameters

Table 10.4: Summary of the KS-probability for each $E_\nu^{\rm rec}$ distribution. This test is performed both at the best fit point in the physical region and at the null oscillation point.

	Best fit in physical region	Null oscillation
$(\Delta m^2\ [\mathrm{eV}^2], \sin^2 2\theta)$	$(2.76\times10^{-3}, 1.0)$	$(0, 0)$
K2K-I+II	**39%**	0.049%
K2K-I only	69%	1.6%
K2K-II only	42%	1.4%

Table 10.5: Summary of the systematic errors in the oscillation analysis. The best-fit value, deviation between the best-fit value and the nominal value (Δf), estimated error (σ) and the ratio of the deviation to the estimated error ($\Delta f/\sigma$) are listed for each error.

Systematic Parameter	best-fit value	Δf (best$-$nominal)	estimated error (σ)	$\Delta f/\sigma$
f_1^ϕ (0.0–0.5 GeV)	1.660	+0.003	±0.437	+0.0
f_2^ϕ (0.5–0.75 GeV)	1.107	−0.001	±0.075	−0.0
f_3^ϕ (0.75–1.0 GeV)	1.151	−0.004	±0.060	−0.1
f_4^ϕ (1.0–1.5 GeV)	1.000	—	—	—
f_5^ϕ (1.5–2.0 GeV)	0.917	−0.001	±0.040	−0.0
f_6^ϕ (2.0–2.5 GeV)	1.042	−0.003	±0.053	−0.1
f_7^ϕ (2.5–3.0 GeV)	1.189	+0.004	±0.137	+0.0
f_8^ϕ (3.0 GeV –)	1.238	+0.006	±0.179	+0.0
$f^{\rm nonQE}$	0.946	−0.018	±0.203	−0.1
$f^{\rm NC}$	0.988	−0.012	±0.153	−0.1
$f^{\rm norm}_{\rm K2K\text{-}Ia}$	1.027	+0.027	+0.176,-0.149	+0.2
$f^{\rm norm}_{\rm K2K\text{-}Ib}$	1.006	+0.006	±0.051	+0.1
$f^{\rm norm}_{\rm K2K\text{-}II}$	1.006	+0.006	±0.051	+0.1
$f_1^{F/N}$ (0.0–0.5 GeV)	1.000	+0.000	±0.026	+0.0
$f_2^{F/N}$ (0.5–1.0 GeV)	0.998	−0.002	±0.043	−0.1
$f_3^{F/N}$ (1.0–1.5 GeV)	1.014	+0.014	±0.065	+0.2
$f_4^{F/N}$ (1.5–2.0 GeV)	1.012	+0.012	±0.104	+0.1
$f_5^{F/N}$ (2.0–2.5 GeV)	1.010	+0.010	±0.111	+0.1
$f_6^{F/N}$ (2.5 GeV –)	1.010	+0.010	±0.122	+0.1
$f_1^{\rm SK\text{-}I}$ (0.0–0.5 GeV)	1.000	+0.000	±0.041	+0.0
$f_2^{\rm SK\text{-}I}$ (0.5–1.0 GeV)	0.999	−0.001	±0.034	−0.0
$f_3^{\rm SK\text{-}I}$ (1.0–1.5 GeV)	1.002	+0.002	±0.036	+0.1
$f_4^{\rm SK\text{-}I}$ (1.5–2.0 GeV)	1.000	+0.000	±0.049	+0.0
$f_5^{\rm SK\text{-}I}$ (2.0–2.5 GeV)	0.998	−0.002	±0.049	−0.0
$f_6^{\rm SK\text{-}I}$ (2.5 GeV –)	1.001	+0.001	±0.049	+0.0
$f^{E\text{-scale}}_{\rm SK\text{-}I}$	0.991	−0.009	±0.020	−0.5
$f_1^{\rm SK\text{-}II}$ (0.0–0.5 GeV)	1.000	+0.000	±0.062	+0.0
$f_2^{\rm SK\text{-}II}$ (0.5–1.0 GeV)	0.999	−0.001	±0.046	−0.0
$f_3^{\rm SK\text{-}II}$ (1.0–1.5 GeV)	1.002	+0.002	±0.042	+0.1
$f_4^{\rm SK\text{-}II}$ (1.5–2.0 GeV)	0.999	−0.001	±0.043	−0.0
$f_5^{\rm SK\text{-}II}$ (2.0–2.5 GeV)	1.000	+0.000	±0.043	+0.0
$f_6^{\rm SK\text{-}II}$ (2.5 GeV –)	1.000	+0.000	±0.043	+0.0
$f^{E\text{-scale}}_{\rm SK\text{-}II}$	0.984	−0.016	±0.021	−0.8

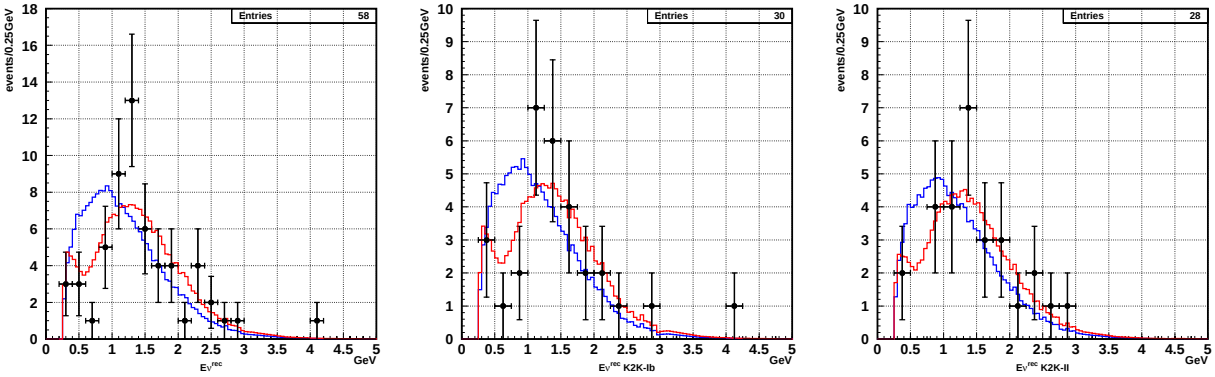

Figure 10.5: The $E_\nu^{\rm rec}$ distribution with the MC expectation with the best fit parameters (red) and the null oscillation case (blue) for K2K-I+II (left), K2K-I (center) and K2K-II (right).

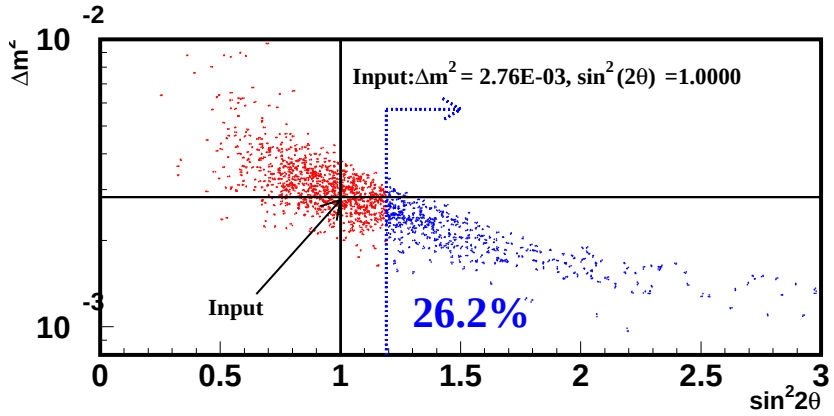

Figure 10.6: Fit result for the many virtual experimental data generated at $(\Delta m^2, \sin^2 2\theta) = (2.76 \times 10^{-3}\ [\mathrm{eV}^2],\ 1.0)$. Each point shows the global best fit value for each data. The probability of getting $\sin^2 2\theta \geq 1.19$ although the true parameter is at our best fit value in physical region is 26.2 %.

As described above, the best fit point including the unphysical region is found at

$$(\sin^2 2\theta, \Delta m^2) = (1.19, 2.55 \times 10^{-3}\mathrm{eV}^2). \tag{10.17}$$

Although this point is in the unphysical region, the log-likelihood ratio of the best fit point in the physical region to the best fit point in the unphysical region is 0.36 (0.39σ equivalent). Thus, the statistical significance between two points is small. As a check, we generate many virtual experiments with our best fit value in the physical region of, $(\Delta m^2, \sin^2 2\theta) = (2.76 \times 10^{-3}[\mathrm{eV}^2],\ 1.0)$ and perform the analysis. The distribution of the results of oscillation parameters is shown in Fig. 10.6. The probability that we would get $\sin^2 2\theta \geq 1.19$ with the true parameters of our best fit value in the physical region is 26.2 %. Therefore, we conclude that the unphysical best fit value is consistent with a statistical fluctuation.

Table 10.6: Summary of the null oscillation probability. Each row is classified by the likelihood, and each column represents the data set.

	K2K-I+II	K2K-I only	K2K-II only
Shape + Norm.	**0.0039% (4.19σ)**	0.20% (3.0σ)	0.68% (2.7σ)
Shape only	0.52% (2.8σ)	8.3%	5.6%
Norm. only	0.19% (3.1σ)	0.9%	3.8%

10.5 Null Oscillation Probability

The probability that the observations are due to a statistical fluctuation instead of neutrino oscillation is estimated by computing the log-likelihood ratio of the null oscillation point to the best fit point as

$$\Delta \ln \mathcal{L}_{\rm null} \equiv \ln \left(\frac{\mathcal{L}^{\rm phys}_{\rm max}}{\mathcal{L}_{\rm null}} \right). \tag{10.18}$$

The null oscillation probability is calculated to be 0.0039 %, which is equivalent to 4.19σ. When only normalization (spectrum) information is used, the probability is 0.19% (0.52%), which is equivalent to 3.1σ (2.8σ). The probabilities for the partial information and partial dataset are summarized in Table 10.6.

The null oscillation hypothesis is strongly disfavored and we confirm neutrino oscillation.

10.5.1 Effect of systematic uncertainties

Table 10.7 shows the effect of each systematic error on the null oscillation probability. The effect is tested by turning on only one error source shown in the first column in Table 10.7. The dominant contributions to the probability with the normalization information are the uncertainties of the far/near flux ratio and the normalization error, while the dominant contributions to the probability with the information of neutrino energy spectrum is the energy scale error of SK.

10.6 Constraint on the Oscillation Parameters

Allowed region of oscillation parameters are evaluated based on the log-likelihood ratio of each point to the best fit point as

$$\Delta \ln \mathcal{L}(\Delta m^2, \sin^2 2\theta) \equiv \ln \left(\frac{\mathcal{L}^{\rm phys}_{\rm max}}{\mathcal{L}(\Delta m^2, \sin^2 2\theta)} \right) = \ln \mathcal{L}^{\rm phys}_{\rm max} - \ln \mathcal{L}(\Delta m^2, \sin^2 2\theta), \tag{10.19}$$

where $\mathcal{L}(\Delta m^2, \sin^2 2\theta)$ is the likelihood at $(\Delta m^2, \sin^2 2\theta)$. The results are shown in Figure 10.7. Three contours correspond to the 68%, 90% and 99% CL allowed regions which are defined as $\ln \mathcal{L} = \ln \mathcal{L}^{\rm phys}_{\rm max} - 1.31, -2.50$ and -4.82, respectively. These intervals are derived by using the two-dimensional Gaussian approximation from the maximum in the unphysical region [48]. The 90% CL contour crosses the $\sin^2 2\theta = 1$ axis at $\Delta m^2 = 1.88 \times 10^{-3}$ and 3.48×10^{-3} eV^2. This result is consistent with the result from Super-Kamiokande atmospheric neutrino measurements, as discussed later. Figure 10.8 shows the function of $\ln \mathcal{L}^{\rm phys}_{\rm max} - \ln \mathcal{L}(\Delta m^2, \sin^2 2\theta)$ at $\Delta m^2 = 2.76 \times 10^{-3}$eV^2 as a function of $\sin^2 2\theta$ and at $\sin^2 2\theta = 1.00$ as a function of Δm^2. The oscillation parameters preferred by the normalization and the $E^{\rm rec}_\nu$ shape alone agree well as shown in Fig. 10.9. Therefore, both information are consistent with each other and support neutrino oscillation with the best fit point. In addition, the allowed regions calculated with the K2K-I data or the K2K-II data are shown in Fig. 10.10. Both results are consistent with each other.

Table 10.7: Effect of each systematic uncertainty on the null oscillation probability. The numbers in the table are null oscillation probabilities when only the error in the first column is taken into account.

	Norm-only	Shape-only	Combine
No sys. error (stat. only)	0.01%	0.26%	0.0002% (4.74σ)
FD spectrum	0.01%	0.27%	0.0002% (4.72σ)
nQE/QE,NC/CC	0.01%	0.26%	0.0002% (4.74σ)
Far/Near (F/N)	0.10%	0.30%	0.0007% (4.48σ)
$\epsilon^{1R\mu}$	—	0.26%	0.0002% (4.74σ)
Energy scale	—	0.42%	0.0003% (4.65σ)
Normalization	0.04%	—	0.0007% (4.51σ)
F/N + Norm	0.18%	0.30%	0.0015% (4.33σ)
F/N + Escale	0.10%	0.48%	0.0012% (4.37σ)
Norm + Escale	0.04%	0.43%	0.0010% (4.41σ)
F/N + Norm + Escale	0.18%	0.48%	0.0025% (4.22σ)
All errors	0.19%	0.52%	0.0028% (4.19σ)

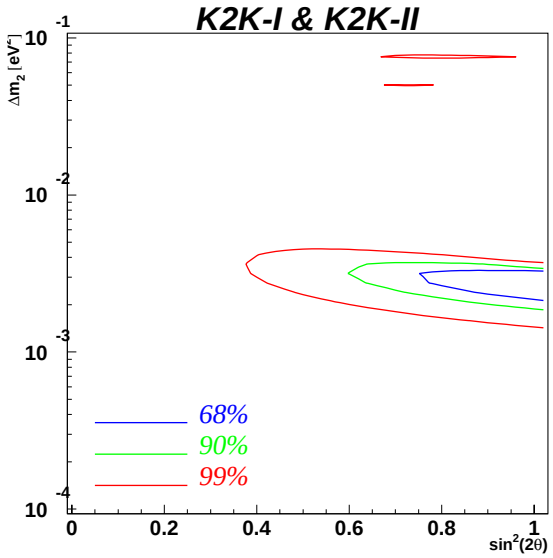

Figure 10.7: Allowed regions of oscillation parameters. The horizontal axis is $\sin^2 2\theta$ and the vertical axis is Δm^2.

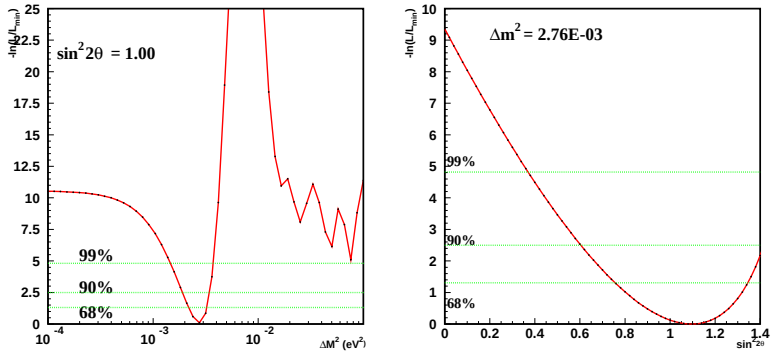

Figure 10.8: The function of $\ln \mathcal{L}_{\max}^{\mathrm{phys}} - \ln \mathcal{L}(\Delta m^2, \sin^2 2\theta)$ as a function of Δm^2 (left) and $\sin^2 2\theta$ (right), in which $\ln \mathcal{L}_{\max}^{\mathrm{phys}}$ is the maximum value of $\mathcal{L}$ in the physical parameter region. The $\sin^2 2\theta$ is set to be 1.00 in the left figure and Δm^2 is set at $2.76 \times 10^{-3}\mathrm{eV}^2$ in the right figure. Three horizontal lines correspond to the 68%, 90% and 99% CL intervals from the bottom.

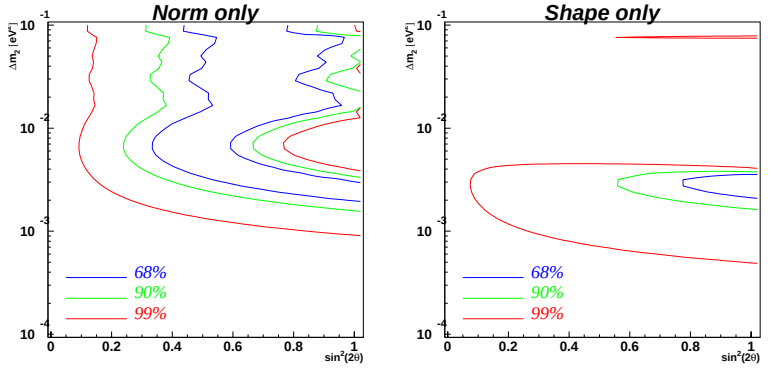

Figure 10.9: Allowed region of oscillation parameters evaluated with the normalization-only (left) and the E_ν^{rec} shape-only (right). Both results allow the consistent region on the parameters space.

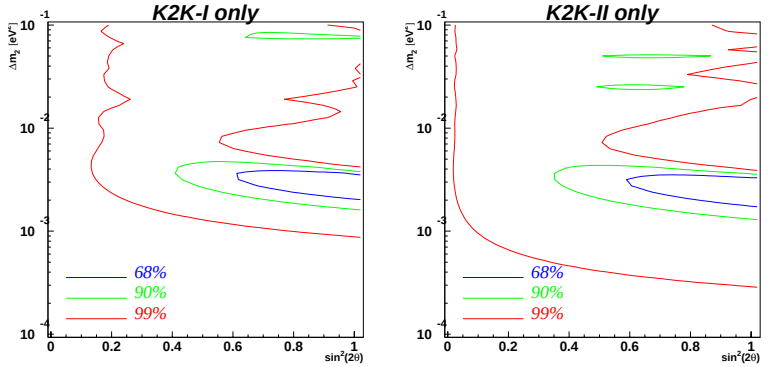

Figure 10.10: Allowed region of oscillation parameters evaluated with the partial data of K2K-I-only (left) and K2K-II-only (right). Both data allow the consistent region on the parameter space.

10.7 Test for Non-Standard Models

In this section, we compare neutrino oscillation with other hypothetical models which predict a different disappearance signature.

10.7.1 Neutrino decay

A neutrino decay model predicts a similar survival probability as predicted by neutrino oscillation. It explains the zenith angle dependence of muon neutrino oscillation reported by SK [45].

We compare the decay model with the oscillation hypothesis based on the log-likelihood difference like the test of null oscillation hypothesis.

Phenomenologically, neutrino decays and neutrino oscillation due to the mass difference can co-exist. The effect of neutrino decay is described by adding the term $-i\frac{1}{2\tau_\nu}$ to the hamiltonian, where τ_ν is a neutrino lifetime in the neutrino rest frame. Assuming that ν_μ is a mixture of mass eigenstates ν_2 and ν_3, and only ν_2 decays, the survival probability of ν_μ is expressed as

$$\begin{aligned} P(\nu_\mu \to \nu_\mu) &= \sin^4\theta + \cos^4\theta \exp\left(-\frac{m_2}{\tau_2}\frac{L_\nu}{E_\nu}\right) \\ &+ 2\sin^2\theta\cos^2\theta \exp\left(-\frac{m_2}{2\tau_2}\frac{L_\nu}{E_\nu}\right)\cos\left(\frac{\Delta m^2 L_\nu}{2E_\nu}\right), \end{aligned} \tag{10.20}$$

where m_2 is the mass of ν_2. In the case of $\tau_2 \to \infty$, Equation (10.20) is the exactly same formula as neutrino oscillation.

Here, we consider the case of no oscillation ($\Delta m^2 \to 0$). The survival probability is reduced to

$$P(\nu_\mu \to \nu_\mu) = \left[\sin^2\theta + \cos^2\theta \exp\left(-\frac{m^2}{2\tau_2}\frac{L_\nu}{E_\nu}\right)\right]^2. \tag{10.21}$$

The best fit point with the decay model is found to be at

$$(\cos^2\theta, m^2/\tau_2) = (1.00, 2.66 \times 10^{-3}\mathrm{GeV/km}). \tag{10.22}$$

Figure 10.11 shows the E_ν^{rec} distribution with the best fit expectation in the decay model. The KS probability is 3.4%. The E_ν^{rec} shape with the decay model with the best fit parameters does not agree with the observation well, while the expected number of events with the decay model is 107.6, which agrees with the observation. The log-likelihood difference from this result to oscillation hypothesis is 2.51. The decay model is less favored than oscillation hypothesis at 89.1% CL (1.7σ). For reference, the SK atmospheric neutrino result with L/E analysis disfavored this hypothesis at approximately 99.9% CL (3.4σ).

10.7.2 Neutrino decoherence

Neutrino decoherence model induced by new physics, such as quantum gravity, can also explain the deficit of ν_μ in atmospheric neutrinos [46]. Within the framework of the decoherence model, the survival probability of ν_μ is written as

$$P(\nu_\mu \to \nu_\mu) = 1 - \frac{1}{2}\sin^2 2\theta\left[1 - \exp(-\gamma L_\nu)\cos\left(\frac{\Delta m^2 L_\nu}{2E_\nu}\right)\right], \tag{10.23}$$

where γ is the parameter which characterize the decoherence effect, and expressed as $\gamma = \gamma_0(E_\nu)^n$. The equation (10.23) is equivalent to that of neutrino oscillation in the limit of $\gamma \to 0$. Here, we consider the pure decoherence case ($\Delta m^2 \to 0$) and assume that the index $n =$

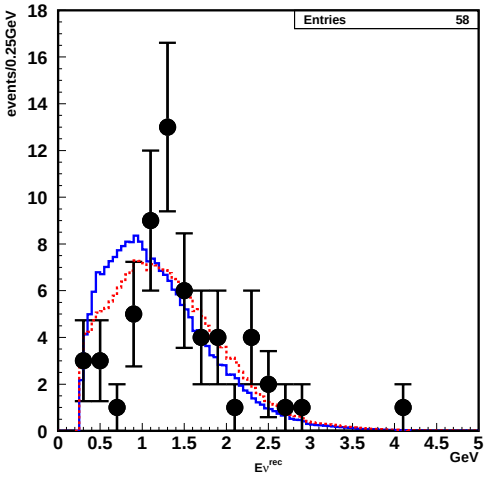

Figure 10.11: The $E_\nu^{\rm rec}$ distribution with the expectation of the decay model (dashed line) and the null decay expectation (line).

1 because the index gives a most probable solution to explain the zenith angle dependence observed in SK [46]. The survival probability is expressed as

$$P(\nu_\mu \to \nu_\mu) = 1 - \frac{1}{2}\sin^2 2\theta \left[1 - \exp\left(-\gamma_0 \frac{L_\nu}{E_\nu}\right)\right]. \tag{10.24}$$

The best fit point with the decoherence model is found at

$$(\sin^2 2\theta, \gamma_0) = (1.00, 6.05 \times 10^{-3}\,\text{GeV/km}). \tag{10.25}$$

Figure 10.12 shows the $E_\nu^{\rm rec}$ distribution with the decoherence model with the best fit parameters. The KS probability is 0.49%. The $E_\nu^{\rm rec}$ shape with the decoherence model with the best fit parameters does not agree with the observation well, while the expected number of events with the decoherence model is 114.0, which agrees with the observation. The log-likelihood difference from the result to the oscillation hypothesis is 3.82. The decoherence model is disfavored than the oscillation hypothesis at 96.3% CL (2.3σ). For reference, the SK atmospheric neutrino result with L/E analysis disfavored this hypothesis at approximately 99.99% CL (3.8σ).

10.7.3 Other models predicting L/E^n dependence

The finite masses of neutrinos is not only the source of neutrino oscillation. Any differences between two eigenvalues of the Hamiltonian is also the source of neutrino oscillation. Neutrino oscillation due to the mass difference predicts the L_ν/E_ν dependence for the survival probability of ν_μ. Several other models predict neutrino oscillations with other types of E_ν dependence as

$$P(\nu_\mu \to \nu_\mu) = 1 - \sin^2 2\theta \sin^2\left(\beta \frac{L_\nu}{E_\nu^n}\right) \tag{10.26}$$

where β and n are the frequency of neutrino oscillation and the power index introduced by the theory, respectively. Examples of the relevant theory are: the violation of Lorentz invariance [120] which predicts $n = -1$, the violation of the equivalence principle [121] ($n = -1$), CPT violation [122] ($n = 0$) and coupling to space-time torsion fields [123] ($n = 0$).

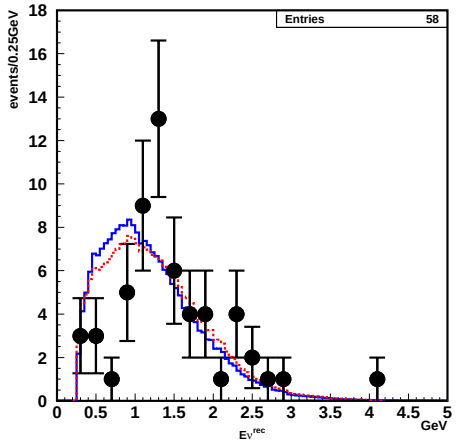

Figure 10.12: The $E_\nu^{\rm rec}$ distribution with the expectation with the decoherence model with the best fit parameters (dashed line) and without the decoherence model (line).

Possible theories with different energy indices are tested based on the log-likelihood ratio from that at the best fit index point as

$$\Delta\ln\mathcal{L}(n) \equiv \ln\left(\frac{\mathcal{L}_{\rm max}}{\mathcal{L}(n)}\right) = \ln\mathcal{L}_{\rm max} - \ln\mathcal{L}(n), \tag{10.27}$$

where n is scanned from -1 ($L\cdot E$) to 2 (L/E^2) with a step size of 0.01 although the predicted energy index n is integer.

Figure 10.13 shows the result of $\Delta\ln\mathcal{L}(n)$ distribution. The energy index n is estimated to be $n = 1.29^{+0.36}_{-0.32}$. Therefore, the result favors the standard (mass differences induced) neutrino oscillation hypothesis, while the non-standard neutrino oscillation hypotheses which predict $n \neq 1$ are disfavored.

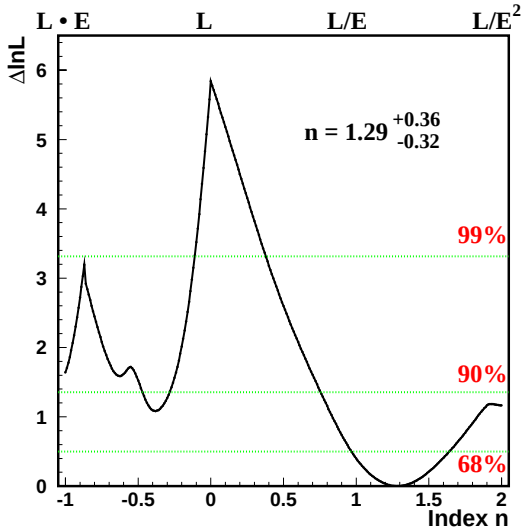

Figure 10.13: The function of log-likelihood difference from that at the maximum point as a function of the energy index n. The maximum log-likelihood point is at $n = 1.29$.

Chapter 11

Discussion

11.1 Discussion on Possible Improvements

In this section, we discuss some ideas for future improvements of sensitivity for neutrino oscillation. We study whether they are effective or not for our current data.

11.1.1 Far/Near Flux ratio

The far/near flux ratio is estimated with the beam-MC simulation. The uncertainty is evaluated based on the PIMON measurement for $E_\nu > 1$ GeV and the ambiguities in the hadron production models for $E_\nu < 1$ GeV. As a result, about 5-10% errors on the far/near flux ratio are quoted. This error is the leading one for the estimation of the number of events at SK. In order to reduce the error, we joined the HARP experiment, and took data with the same target material used in K2K. Figure 11.1 shows the HARP preliminary result. The far/near flux ratio predicted by the beam-MC simulation and that by HARP are very similar. The error of the HARP measurement is smaller than the current one. In the very near future, it is expected that the uncertainty of the far/near flux ratio goes down to the 3% level, and the significance of the null oscillation sensitivity may increase by about 0.10 - 0.15 σ.

11.1.2 Multi-ring events for spectrum analysis

In the oscillation analysis, we used only 1-ring μ-like events for the spectrum analysis. In fact, the multi-ring events are also available to the spectrum analysis. The multi-ring events mainly come from resonance single π production, $\nu_\mu + N \rightarrow \mu + \Delta(\rightarrow N + \pi)$. For resonance production, the neutrino energy can be reconstructed with the same manner as QE by replacing the proton mass with the delta mass in Equation 2.2. The energy resolution is about 13% compared with that of 8% for QE.

However, tha parent neutrino energy of the multi-ring events are fairly higher than that of 1-ring μ-like events as shown in Fig. 11.2. Since there are few multi-ring events around the energy region of oscillation maximum, $E_\nu < 1.0$ GeV, the multi-ring events are not sensitive to neutrino oscillation. A difference between $E_\nu^{\rm rec}$ distributions of multi-ring events with and without oscillation is very small as shown in Fig. 11.3. That is why we do not use multi-ring events in the spectrum analysis.

11.1.3 The number of 1-ring μ-like events for normalization analysis

The number of 1-ring μ-like events and the number of other events, consisting of 1-ring e-like and multi-ring events, are independent information. Thus, the likelihood ratio for the normalization

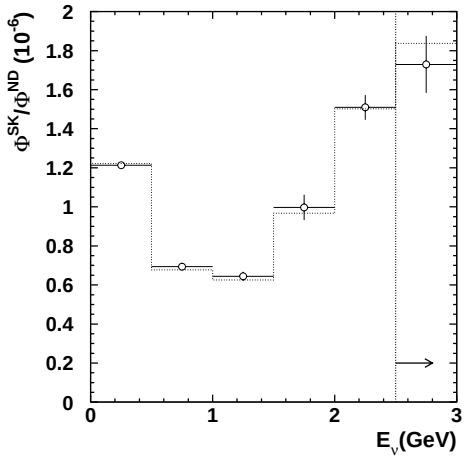

Figure 11.1: Ratio of muon neutrino fluxes predicted at the far (SK) and near (ND) detectors in the absence of neutrino oscillations, as a function of neutrino energy E_ν. The prediction based on the Cho-CERN hadronic model is shown by the dotted histogram, the one based on the HARP π^+ production measurement and systematic error evaluation is shown by empty circles with error bars. The arrow indicates that the contents in last bin are integrated over all neutrino energies above 2.5 GeV.

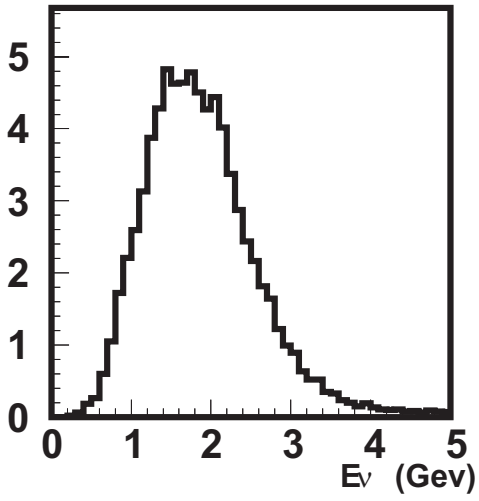

Figure 11.2: The $E_\nu^{\rm true}$ distribution for multi-ring events. The histogram is normalized by the number of multi-ring events with at least one muon-like ring (31).

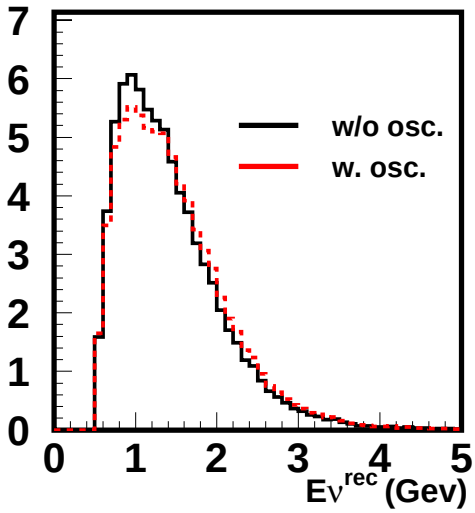

Figure 11.3: The expected $E_\nu^{\rm rec}$ distribution for multi-ring events for the null oscillation case (line) and for the oscillation case with our best fit parameters (dashed line). Both histograms are normalized with the same manner as Figure 11.2.

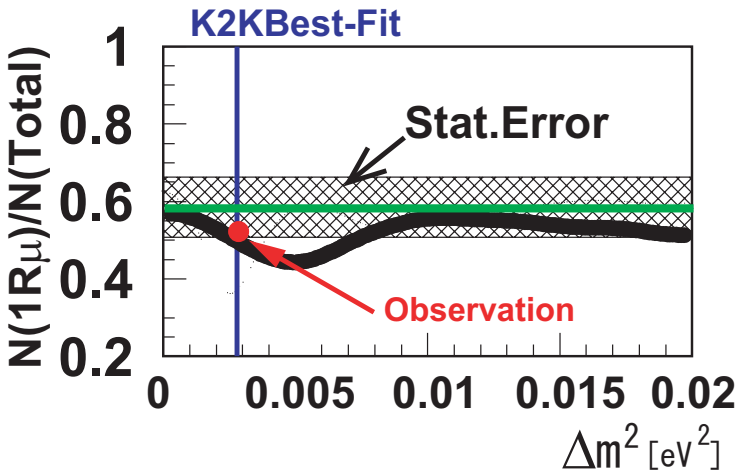

Figure 11.4: The expected fraction of 1-ring μ events as a function of Δm^2. The black line shows the expectation and the hatched band shows the statistical error for the null oscillation case. The green line shows the expectation without oscillation. The led point shows the observation.

term is written as follows;

$$\begin{aligned}\mathcal{L}(\text{norm}) &= \mathcal{L}(\#1\text{ring}-\mu)\times\mathcal{L}(\#\text{Other}) \\ &= \frac{\exp\left(-N^{\text{exp}}_{1R\mu}\right)\cdot\left(N^{\text{exp}}_{1R\mu}\right)^{N^{\text{obs}}_{1R\mu}}}{\left(N^{\text{obs}}_{1R\mu}\right)!}\cdot\frac{\exp\left(-N^{\text{exp}}_{\text{Other}}\right)\cdot\left(N^{\text{exp}}_{\text{Other}}\right)^{N^{\text{obs}}_{\text{Other}}}}{\left(N^{\text{obs}}_{\text{Other}}\right)!} \qquad (11.1)\end{aligned}$$

After some trivial algebra, this reduces to

$$\begin{aligned}\mathcal{L}(\text{norm}) &= \left[\frac{\exp\left(-N^{\text{exp}}_{\text{Total}}\right)\cdot\left(N^{\text{exp}}_{\text{Total}}\right)^{N^{\text{obs}}_{\text{Total}}}}{\left(N^{\text{obs}}_{\text{Total}}\right)!}\right]\cdot\left[{}_{N_{\text{Total}}}C_{N_{1R\mu}}\left(\frac{N^{\text{exp}}_{1R\mu}}{N^{\text{exp}}_{\text{Total}}}\right)^{N^{\text{obs}}_{1R\mu}}\left(\frac{N^{\text{exp}}_{\text{Other}}}{N^{\text{exp}}_{\text{Total}}}\right)^{N^{\text{obs}}_{\text{Other}}}\right] \\ &= \mathcal{L}(\#\text{Total})\times\mathcal{L}(\#1\text{R}\mu/\#\text{Total}) \qquad (11.2)\end{aligned}$$

Therefore, we can add the likelihood function for the fraction of the 1-ring μ-like event as an additional information.

Figure 11.4 shows the expected fraction of 1-ring μ-like events as a function of oscillation parameter, Δm^2 at $\sin^2 2\theta = 1$. The expected fraction shown by the black line is consistent with the null oscillation case within the statistical error around our best fit parameter region. That is why we do not use this information in the oscillation analysis.

11.2 Comparison with the Atmospheric Neutrino Results

11.2.1 Comparison with the SK atmospheric neutrino results

Figure 11.5 and Table 11.1 compare this K2K results with the SK L/E analysis [25]. Both results consistently favor the same parameter region. Therefore, we achieve the confirmation of SK atmospheric neutrino results using other neutrino sources, accelerator-produced neutrinos with different systematic uncertainties.

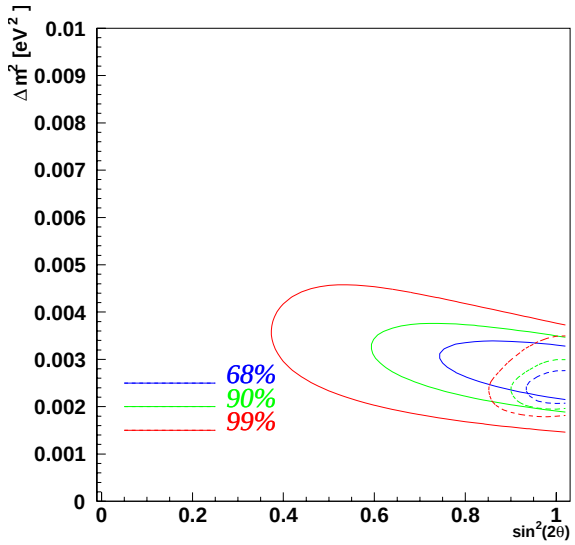

Figure 11.5: Allowed region from the K2K result (line) and the SK L/E result (dashed line).

Table 11.1: Summary of the combined analysis as will be discussed in Section 11.2.2. The best fit oscillation parameters and the 90% CL interval for Δm^2 at $\sin^2 2\theta = 1.0$. are shown.

		$\sin^2 2\theta$	Δm^2[eV^2]	90% CL for Δm^2
K2K	Best	1.19	2.55×10^{-3}	
	Best in phys	1.00	2.76×10^{-3}	$(1.88 - 3.48) \times 10^{-3}$eV^2 $(\sin^2 2\theta = 1)$
SK-I L/E	Best	1.03	2.37×10^{-3}	
	Best in phys	1.00	2.38×10^{-3}	$(1.92 - 2.97) \times 10^{-3}$eV^2 $(\sin^2 2\theta = 1)$
Combined	Best	1.03	2.48×10^{-3}	
	Best in phys	1.00	2.49×10^{-3}	$(2.05 - 3.01) \times 10^{-3}$eV^2 $(\sin^2 2\theta = 1)$

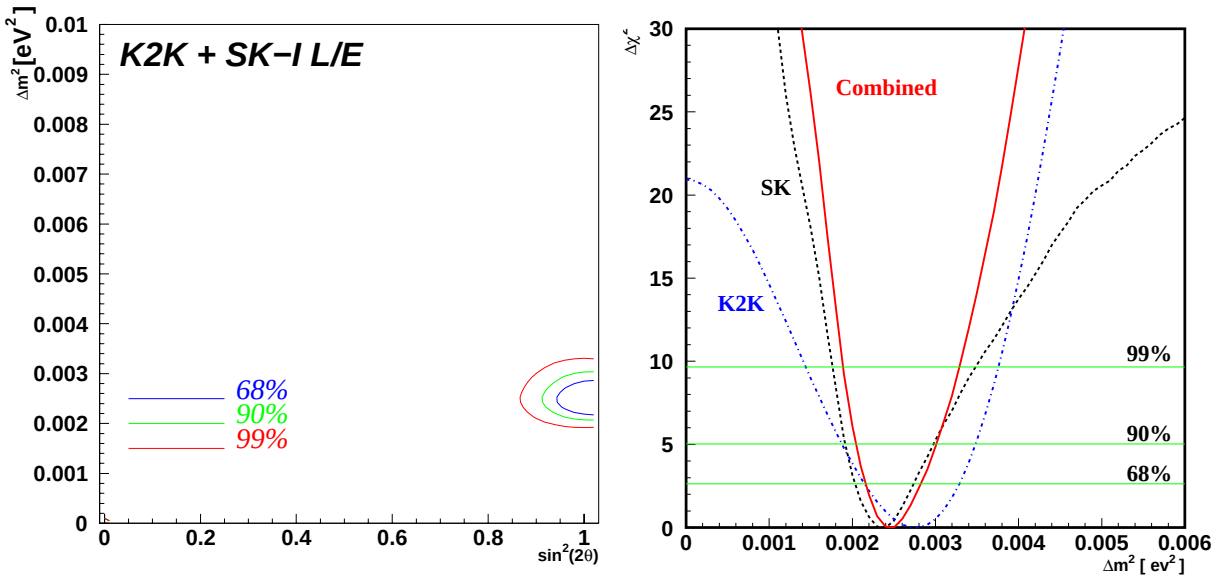

Figure 11.6: The allowed region estimated by the combined analysis of the K2K and SK L/E results (left). The $\Delta\chi^2 = \chi^2 - \chi^2_{\rm min}$ function as a function of Δm^2 (right), where the line, dashed line and dotted line show the combined result, the SK L/E result and the K2K result, respectively.

11.2.2 Combined analysis

Here, we obtain the combined allowed region of neutrino oscillation parameters by using the SK L/E data and the K2K data. The K2K data and the SK-I L/E data restrict the allowed Δm^2-$\sin^2 2\theta$ parameters as shown in Fig. 11.6 (left). A fit to Δm^2 and $\sin^2 2\theta$ is performed by adding the χ^2 for each analysis as

$$\chi^2 \quad = \quad \chi^2_{\rm K2K} + \chi^2_{\rm SK}. \tag{11.3}$$

The Δm^2 and $\sin^2 2\theta$ are scanned from 0.0 to 10^{-2} and 0.00 to 1.50 with a step size of 10^{-4} and 0.02, respectively.

In the combined analysis, the best fit point is found at

$$\begin{aligned} \text{Allregion} \quad &: \quad (\sin^2 2\theta, \Delta m^2) = (1.03, 2.48 \times 10^{-3}) \\ \text{Physical region} \quad &: \quad (\sin^2 2\theta, \Delta m^2) = (1.00, 2.49 \times 10^{-3}). \end{aligned}$$

As shown in Fig. 11.6 (right), the 90% CL contour crossed the $\sin^2 2\theta = 1$ axis at $\Delta m^2 = 2.05 \times 10^{-3}$ and 3.01×10^{-3}eV^2, which is the most stringent constraint for Δm^2 to date.

Chapter 12

Conclusion

The K2K long baseline neutrino oscillation experiment is performed to confirm ν_μ oscillation with the accelerator produced neutrinos. The data were taken from June 1999 to November 2004, corresponding to 9.2×10^{19} protons on target.

In K2K, the signatures of neutrino oscillation appear as a deficit in the number of neutrino events and a distortion of the neutrino energy spectrum at SK. The event distributions without oscillation in SK are predicted based on the measurements in the near neutrino detectors by using the neutrino interaction models and the detector simulation.

In order to improve the reliability of the prediction, the cross section of charged current (CC) coherent pion production ($\nu_\mu + A \to \mu^- + \pi^+ + A$) is measured for the first time in the energy region of a few GeV. This measurement is performed with SciBar. No evidence for coherent pion production is observed, and the following upper limit is set at 90% CL.

$$\sigma(\text{coherent pion})/\sigma(\nu_\mu CC) < 0.60 \times 10^{-2}$$

The neutrino interaction models including this result well reproduce all the measurements in the near detectors. By using the refined interaction models, the event distributions in SK are predicted.

One hundred twelve beam neutrino events are observed in the fiducial volume of SK, while the expectation without oscillation is $155.9^{+11.6}_{-10.2}$. This deficit confirms ν_μ disappearance at 99.8% CL. Among the observed events, fifty eight one-ring muon-like events are used to measure the neutrino energy spectrum. The observed energy spectrum shows a distortion compared with the expectation without oscillation at 99.5% CL. The probability that the observations are explained by a statistical fluctuation without oscillation is 0.003% (4.2σ).

A two-neutrino oscillation analysis results in the oscillation parameter set of $(\sin^2 2\theta, \Delta m^2) = (1.00, 2.8{\times}10^{-3}\text{eV}^2)$. The expectations assuming oscillation with the best fit parameters reasonably reproduce the observations. The expected number of events is 107.7, which is consistent with the observation within the statistical uncertainty. The KS probability of E_ν^{rec} is 36%. Therefore, our observations are consistent with the oscillation hypothesis.

Allowed region of the oscillation parameters are also evaluated. The 90% confidence interval of Δm^2 on the axis of $\sin^2 2\theta = 1$ is

$$1.9 \times 10^{-3} \leq \Delta m^2 \leq 3.5 \times 10^{-3}[\text{eV}^2]$$

This parameter region is consistent with the atmospheric neutrino results.

In addition, the neutrino oscillation hypothesis is compared with the alternative models such as neutrino decay and decoherence. As a result, neutrino oscillation due to massive neutrinos is the most favored as a primary mechanism of ν_μ disappearance although the statistical significance is not sufficient to exclude other models.

In conclusion, we establish neutrino oscillation and the existence of finite neutrino masses by using the accelerator produced neutrinos.

Appendix A

Neutrino Beam stability

Figure A.1 shows the stability of the sum of SPD signals normalized by POT, which is proportional to the muon yield. The yield has been stable at the standard deviation of 2.5%. This is quite small compared with the statistical uncertainty in the number of events at far site of $\sim$ 10%. Figure A.2 shows the stability of the center of the muon profile measured by ICH in MUMON. The beam have been pointed to the direction of SK within ± 1 mrad during whole run period. This result guarantees that the flux change during whole run period is less than 1%. Figure A.3 and A.4 show the vertex profile measured by MRD and the stabilities of their center, respectively The neutrino beam itself has been stable within ± 1 mrad except for the statistical fluctuation. The stability of the neutrino event rate for every 5×10^{12} POT measured with MRD data is shown in Fig. A.5. The event rate is also stable at the standard deviation of 2.6%. Figure A.6 shows the comparison of muon energy and angle distribution for each month. All the histograms are completely consistent with each other. It guarantees the E_ν spectrum is stable during whole run period within the statistical sensitivity. Therefore, we can perform the oscillation analysis on the assumption that the neutrino beam is stable. Although SciBar is installed in the middle of experimental period, we can combine the SciBar data with other ND data without any care.

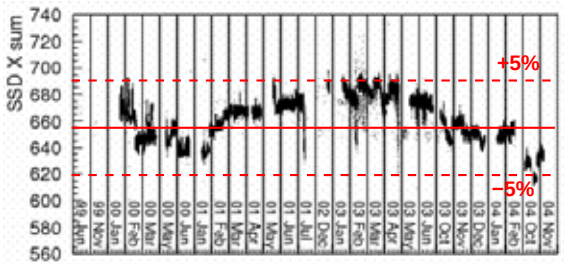

Figure A.1: Stability of secondary muon yield from pion decay measured by MUMON-SPD. The vertical axis shows the sum of ADC outputs from SPD normalized by the target CT (POT).

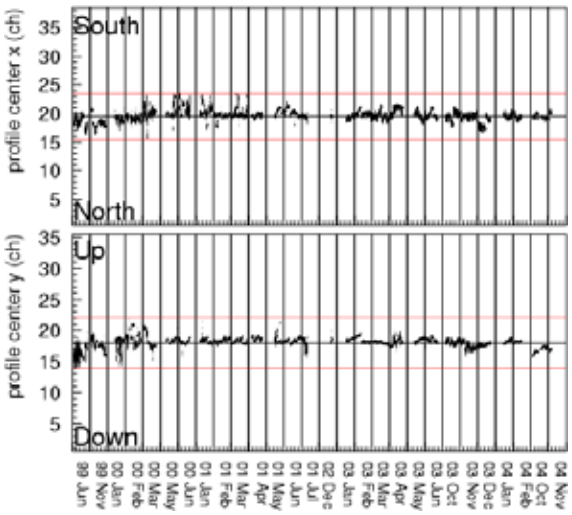

Figure A.2: Stability of beam center measured by MUMON-ICH. Horizontal black lines show the SK direction, and red lines show the ±1mrad off the center.

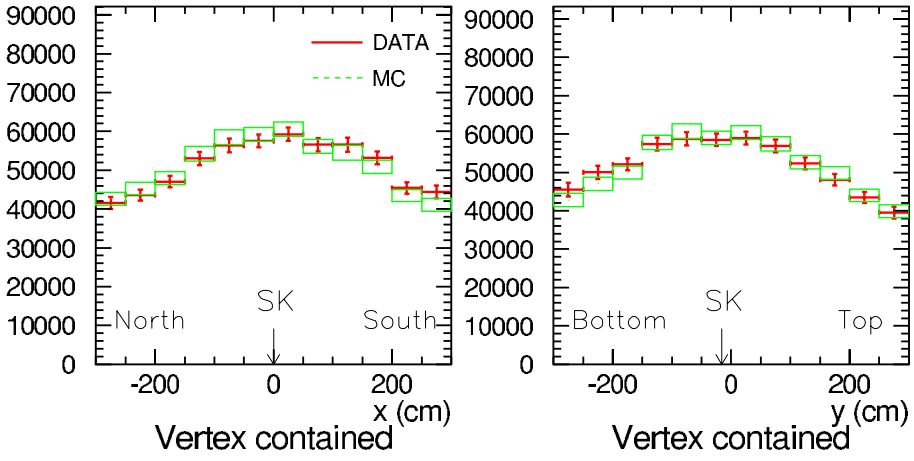

Figure A.3: Neutrino beam profile measured by MRD. The left figure shows the horizontal profile, and the right one shows the vertical profile. Crosses are data, and boxes are the MC simulation. The SK direction is specified by arrows. If the beam is 1 mrad off the SK direction, the profile is shifted by 30 cm.

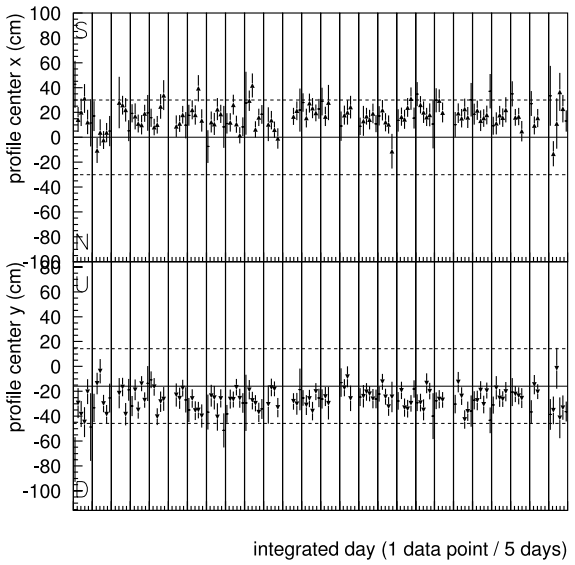

Figure A.4: Stability of the beam center measured by MRD. The upper figure shows the vertical position, and lower figure shows the horizontal position. Horizontal solid lines show the SK direction, and dashed lines indicate the 1mrad off the SK direction.

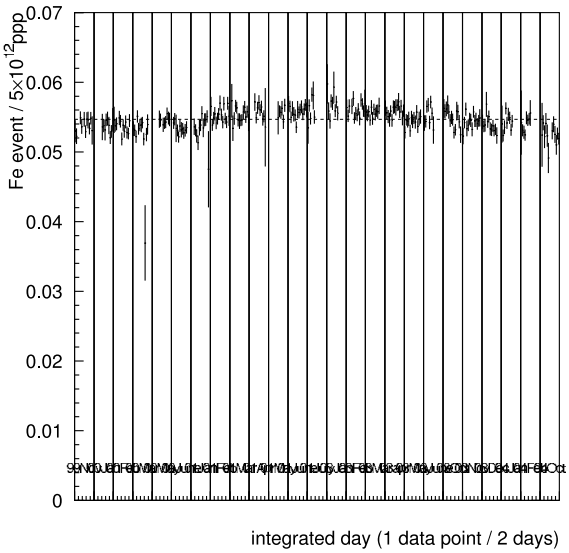

Figure A.5: Stability of the neutrino event rate measured by MRD. The vertical axis shows the number of events per 5×10^{12} POT.

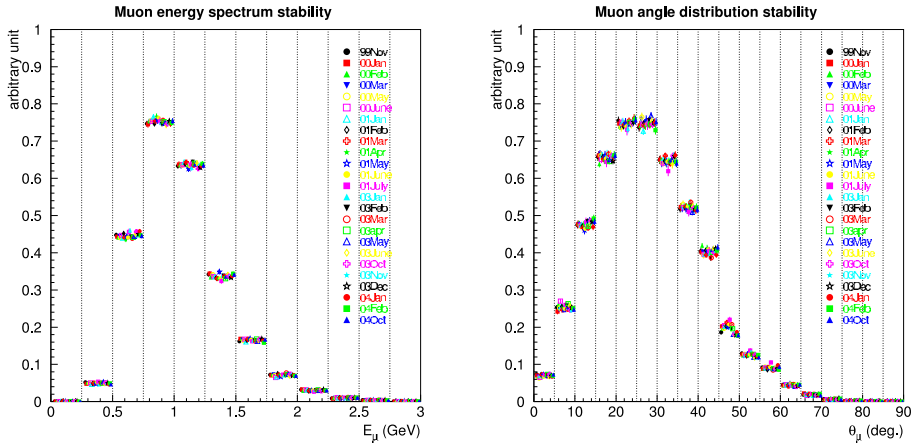

Figure A.6: Stability of the energy (left) and angle (right) distribution of muons generated by neutrino interaction in MRD.

Appendix B

Monte Carlo Simulation

In this chapter, we describe the Monte Carlo (MC) Simulation at K2K. The MC simulation is made of three constituents;

1. **Neutirino beam simulation.**
   This simulates from the proton injection on the production target, produces pions, focused and tracks them until they decay to neutrino or dumped, and provides neutrino flux and energy spectrum shape at near and far side.

2. **Neutrino interaction.**
   This simulates neutrino interaction on target nuclei and secondary interaction inside the targed nuclei. It provides kinematic information of produced particles.

3. **Detector simulation**
   This simulates the passage of particles and the detector responces.

In following sections, they are described in this order.

B.1 Neutrino Beam Generation

B.1.1 Proton injection to the target

Proton profile, as a input of the simulation, is measured using V39-SPIC and TGT-SPIC described in the chapter 3. The former is located just after the last magnet and the latter is located just before the target. As shown in Figure B.1, fitted profile width on both SPIC is extrapolated to the width and the divergence on the target front-face by assuming that the protons do not cross over and the proton density distribution is 2-dimensional Gaussian. For out standard simulation, proton beam center is set at the center of the target rod. Table B.1 summarizes the input proton beam parameters for June 1999 (K2K-Ia) and in the rest of the periods (K2K-Ib-).

B.1.2 Secondary particles production in the target rod

There are some hadron interaction models to simulate pion production in the target material. This is one of the largest ambiguities of the MC simulation. There have been various pion production experiments in the energy region of K2K beam. However results of these experiments are inconsistent with each other.

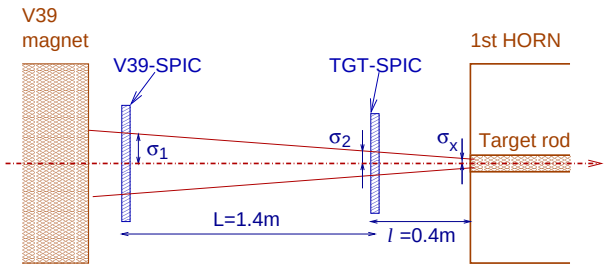

Figure B.1: Schematic view of the proton beam emittance calculation.

Table B.1: Proton beam parameters for the simulation.

Parameters	K2K-Ia (June 1999)	K2K-Ib - K2K-IIc (Nov. 1999 - Nov. 2004)
Target rod	Al	Al
Rod diameter	2 cmϕ	3 cmϕ
Horn current	200 kA	250 kA
Beam spread σ_x	1 mm	3.4 mm
Beam spread σ_y	6 mm	7.2 mm
Beam divergence k_x	-8 mrad/mm	-2.5 mrad/mm
Beam divergence k_y	-0.4 mrad/mm	-0.14 mrad/mm

1. **GCALOR/FLUKA Model [113, 114, 124].**
   GCALOR/FLUKA is one of the hadron simulation package prepared for GEANT simulation, which has a larger p-Al cross section than other models. It tends to produce higher energy secondary pions.

2. **Fit to Measurements (I), Sanford-Wang [72].**
   This model is an experimental parameterization using compilation of three measurements: Lundy *et al.* (13.4 GeV/c) [125], Dekkers *et al.* (11.8, 18.8 and 23.1 GeV/c) [126] and Baker *et al.* (10.9, 20.9 and 30.9 GeV/c) [127]. This result is comfirmed by measurement performed by Yamamoto [128].

3. **Fit to Measurements (II), Cho-ANL amd Cho-CERN [71, 129].**
   Other results of the compilations to fit several measurements to the Sanford-Wang formula. The measurements done by Marmer *et al.* (12.3 GeV/c) [130, 131], Cho *et al.* (12.4 GeV/c) [**?**], Asbury *et al.* (12.5 GeV/c) [132], and Allaby *et al.* (19.2 GeV/c) [133] are used in the Cho-ANL compilation [129]. There is another result of compilation called Cho-CERN [71], which uses the data set of mainly from Cho *et al.* (12.4 GeV/c). These two compilations give almost the same differential cross-sections.

The Sanford-Wang formula is an experimental parameterization, which gives the differencial yield of the secondary particle per interacting proton ($d^2n/d\theta dp$) as:

$$\frac{d^2n}{d\Omega dp} = C_1 p^{C_2} \left(1 - \frac{p}{p_B - 1}\right) \exp\left(-\frac{C_3 p^{C_4}}{p_B^{C_5}} - C_6\theta(p - C_7 p_B \cos^{C_8}\theta)\right), \tag{B.1}$$

where p_B and p are the momentum of the primary and secondary particle, respectively, θ is the angle between the secondary particle and the beam axis. C_i's are constants to be determined by fitting. The fit results of the positive pion production for Sanford-Wang, Cho-ANL, and

Table B.2: Fitted parameters of Sanford-Wang formula for the positive pions in Sanford-Wang, Cho-ANL, and Cho-CERN compilations.

	C_1	C_2	C_3	C_4	C_5	C_6	C_7	C_8
Sanford-Wang	1.09	0.65	4.05	1.63	1.66	5.03	0.17	82.7
Cho-ANL	0.96	1.08	2.15	2.31	1.98	5.73	0.13	24.1
Cho-CERN	1.05	1.01	2.26	2.45	2.12	5.66	0.14	27.3

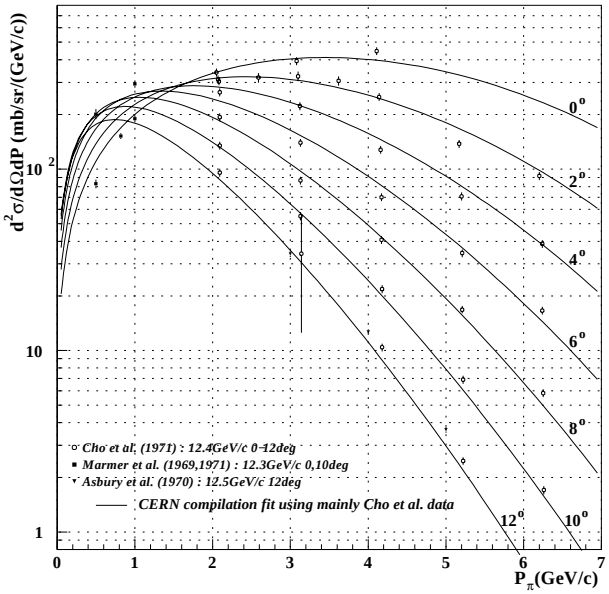

Figure B.2: Differential cross-section of positive pion production in past experiments and fitted curves of the Cho-CERN model. Data points are shown by symbols with error bars, and the fitted curves are shown by solid lines.

Cho-CERN compilations are summarized in Table B.2. Figure B.2 is the comparison of the experimental measurements with the fitted curves of Cho-CERN.

In GCALOR/FLUKA model, GEANT simulates everything using the GCALOR/FLUKA automatically. In the other models, only the interaction of energetic protons more than 10 GeV with the target aluminum is simulated according to the Equation B.1. The less energetic interactions are simulated according to GCALOR model. For secondary interaction of hadrons, GCALOR/FLUKA is always used. For Kaon production, the parameter set described in [72] is employed.

The Cho-CERN model is employed as the standard pion production model in our simulation because the momentum and angle distribution of the pion obtained by PIMON measurement strongly favored the simulation, while the other models are used for systematic evaluation.

B.1.3 Magnetic horn focusing

The scattered protons and generated secondary particles are traced by the MC simulation GEANT with GGALOR hadron interaction package through the magnetic field generated by the horn system described in Chapter 3 to the decay section.

The magnetic field in the simulation is given by calculation with Formula **??**,where we ignore the skin effect inside the target rod and assume the static approximation for all the area. The

uncertainty of the aymmetric field is considered in the systematic evaluation.

B.1.4 Particle decay

We employ a custum made program based on the V-A theory to simulate the energy and angular distribution of the decay products from the focused Kaons and muons because GEANT made decay particles only isotoropically. The following types of decays are considered in the simulation.

Pion

$\pi^{\pm} \to \mu^{\pm} + \nu_{\mu}$, whose branching fraction is almost 100%, is only taken into account.

Kaons

The main contribution to the neutrino beam are as follows;

- $\mathrm{K}^{\pm} \to \nu_{\mu} + \mu^{\pm}$ (63.51 %)
- $\mathrm{K}^{\pm} \to \pi^{0} + \mathrm{e}^{\pm} + \nu_{e}$ (4.82 %)
- $\mathrm{K}^{0}_{L} \to \pi^{\pm} + e^{\mp} + \nu_{e}$ (38.78 %)
- $\mathrm{K}^{\pm} \to \pi^{0} + \mu^{\pm} + \nu_{\mu}$ (3.18 %)
- $\mathrm{K}^{0}_{L} \to \pi^{\pm} + \mu^{\mp} + \nu_{\mu}$ (27.17 %)

Other decay modes are ignored because their branching fractions are quite small.

Muons

$\mu^{\pm} \to e^{\pm} + \nu_{\mu} + \bar{\nu}_{e}$, whose branching fraction is almost 100%, is only taken into account. The effect from μ polarization to the angular distribution of decay products is also taken into account. This mode is a dominant source of ν_e in out neutrino beam.

B.1.5 Neutrino flux and energy spectrum

The resulting neutrino flux at near and far site after Nobember 1999 configuration are shown in Figure B.3. From the beam simulation, the neutrino beam spread over 25 cm in radius at near site and over 200 m in radius at far site in average. The ν_e/ν_{μ} ratio is estimated to be 1.3%. $\bar{\nu_{\mu}}/\nu_{\mu}$ to be 0.5%, and $\bar{\nu_e}/\nu_{\mu}$ to be $\sim 2 \times 10^{-4}$, respectively.

The ν_{μ} energy spectrum difference between in the June 1999 configuration and in the November 1999 configuretion are shown in Figure B.4. The average neutrino beam energy is higher in the November 1999 configuration (1.30 GeV at far site) than in the June 1999 configuration (1.23 GeV at far site) because the horn current was higher in the November 1999 configuration, while the absolute flux is 2.7% smaller in November 1999 configuration due to the higher pion absorption inside the target rod.

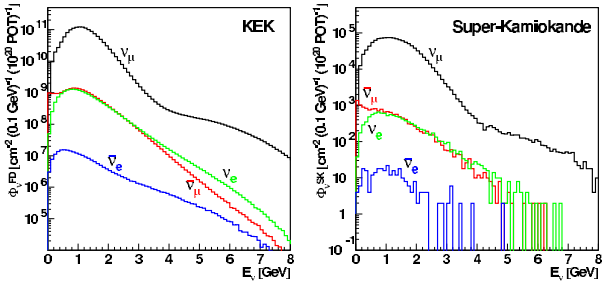

Figure B.3: Neutrino flux calculation by beam simulation. Left figure: Neutrino flux at near site. Right figure: Neutrino flux at far site.

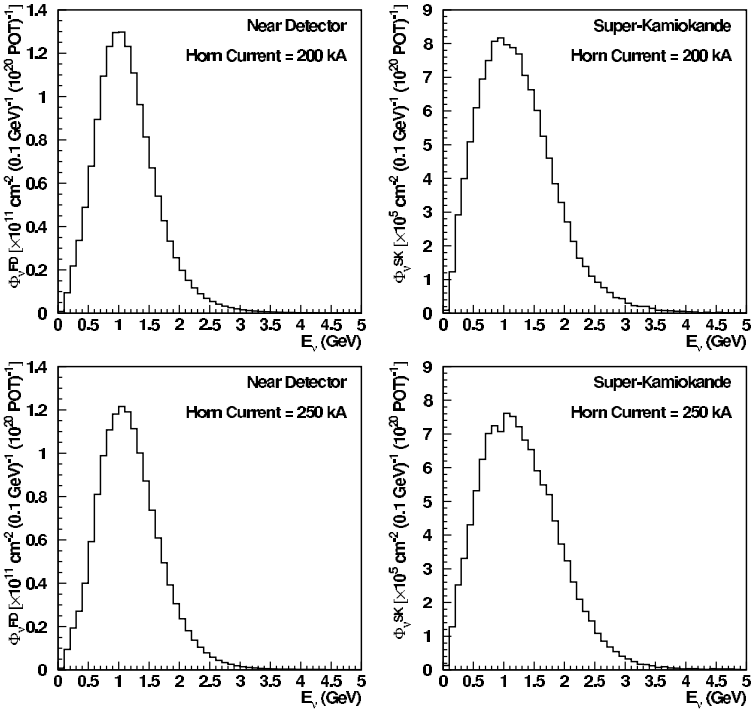

Figure B.4: Neutrino energy spectrum at near (left) and far (right) site. The upper (lower) two figures show the spectrum with horn current of 200 kA (250 kA).

B.2 Neutrino interaction simulation

The NEUT program library [69] is used to simulate the neutrino interactions with the nucleus in our Monte Carlo simulation. This library was first developed to study atmospheric neutrinos as a background of nucleon decay analysis in the Kamiokande experiment, and then it was inherited to the K2K experiment together with Super-Kamiokande experiment with various modifications [51, 63, 64, 74]. In the NEUT code, the following interactions are considered:

CC/NC (quasi-) elastic scattering	$\nu + N \to l + N'$
CC/NC single meson production	$\nu + N \to l + N' + \text{meson}$
CC/NC deep inelastic interaction	$\nu + N \to l + N' + \text{hadrons}$
CC/NC coherent pion production	$\nu + {}^{16}O\ ({}^{12}C) \to l + {}^{16}O\ ({}^{12}C) + \pi$

where N and N' are nucleons (proton or neutron) and l is a lepton, respectively.

The cross section of neutrino-electron elastic scattering is approximately three orders of magnitude smaller than that of the neutrino-nucleon interactions at $\sim$1 GeV neutrino energy and therefore it is simply omitted from the simulation.

B.2.1 Elastic and Quasi-Elastic Scattering

The reaction is the dominant mode in the K2K neutrino beam energy region. Our simulation of the interaction is based on the Llewellyn Smith's theory [75]. The amplitude of this process is described by the product of the hadron and lepton weak currents:

$$T = \frac{G_F}{\sqrt{2}}\,\bar{u}(k_2)\gamma^\mu(1-\gamma^5)u(k_1)\,\langle N'(p_2)|J_\mu^{\rm had}|N(p_1)\rangle, \tag{B.2}$$

where G_F is the Fermi coupling constant, p_1 (p_2) is the initial (final) nucleon four-momentum, and k_1 (k_2) is the initial (final) lepton four-momentum. The hadronic current, $\langle N'|J^{\rm had}|N\rangle$, can be expressed as a function of four-momentum transfer, $Q^2 \equiv -q^2 = -(p_1 - p_2)^2$:

$$\langle N'|J^{\rm had}|N\rangle = \cos\theta_c\,\bar{u}(N')\left[\gamma_\lambda F_V^1(Q^2) + \frac{i\sigma_{\lambda\nu}q^\nu\xi F_V^2(Q^2)}{2m_N} + \gamma_\lambda\gamma_5 F_A(Q^2)\right]u(N), \tag{B.3}$$

where θ_c is the Cabbibo angle, and m_N is the nucleon mass. The vector form factors, F_V^1 and F_V^2, are represented as follows:

$$F_V^1(Q^2) = \left(1 + \frac{Q^2}{4m_N^2}\right)^{-1}\left[G_E^V(Q^2) + \frac{Q^2}{4m_N^2}G_M^V(Q^2)\right], \tag{B.4}$$

$$\xi F_V^2(Q^2) = \left(1 + \frac{Q^2}{4m_N^2}\right)^{-1}\left[G_M^V(Q^2) - G_E^V(Q^2)\right], \tag{B.5}$$

$$G_E^V(Q^2) = \frac{1}{\left(1 + \frac{Q^2}{M_V^2}\right)^2}, \qquad G_M^V(Q^2) = \frac{1+\xi}{\left(1 + \frac{Q^2}{M_V^2}\right)^2}, \tag{B.6}$$

where $\xi \equiv \mu_p - \mu_n = 3.71$ is the difference of anomalous magnetic dipole moments between a proton and a neutron, and the vector mass in the dipole parametrization, M_V, is set to be 0.84 GeV/c. The axial form factor, F_A, is given by

$$F_A(Q^2) = \frac{-1.23}{\left(1 + \frac{Q^2}{M_A^2}\right)^2}, \tag{B.7}$$

where M_A is the axial vector mass. Past electron-nucleon and neutrino-nucleon scattering experiments give that M_A for (quasi-)elastic scattering is 1.0–1.1 GeV/c [77]. Since our previous analysis [52, 134] favors $M_A = 1.11$ GeV/c, we employ this value in our simulation.

Finally, the differential cross-section is expressed by

$$\frac{d\sigma}{dQ^2} = \frac{m_N^2 G_F^2 \cos^2\theta_c}{8\pi E_\nu^2}\left[A(Q^2) \mp B(Q^2)\frac{(s-u)}{m_N^2} + C(Q^2)\frac{(s-u)^2}{m_N^4}\right] \tag{B.8}$$

where E_ν is the incident neutrino energy, $(s-u) \equiv 4m_N E_\nu - Q^2 - m_l^2$, m_l is the lepton mass, and;

$$\begin{aligned} A(Q^2) = \frac{(m_l^2+Q^2)}{4m_N^2}\Bigg[&\left(4+\frac{Q^2}{m_N^2}\right)|F_A|^2 - \left(4-\frac{Q^2}{m_N^2}\right)|F_V^1|^2 + \frac{Q^2}{m_N^2}|\xi F_V^2|^2\left(1-\frac{Q^2}{4m_N^2}\right) \\ &+\frac{4Q^2 F_V^1 \xi F_V^2}{m_N^2} - \frac{m_l^2}{m_N^2}\left(|F_V^1+\xi F_V^2|^2 + |F_A|^2\right)\Bigg], \end{aligned} \tag{B.9}$$

$$B(Q^2) = -\frac{Q^2}{m_N^2}F_A\left(F_V^1 + \xi F_V^2\right), \tag{B.10}$$

$$C(Q^2) = \frac{1}{4}\left(|F_A|^2 + |F_V^1|^2 + \frac{Q^2}{m_N^2}\left|\frac{\xi F_V^2}{2}\right|^2\right). \tag{B.11}$$

The sign of $B(Q^2)$ in Equation (B.8) is $-$ for neutrinos and $+$ for anti-neutrinos.

Figure B.5 shows the quasi-elastic cross section as a function of E_ν with $M_A = 0.91, 1.01, 1.11$ GeV/c^2. They are consistent with various bubble chamber measurements around 1 GeV [135–138].

The cross-section of the NC elastic scattering is derived from following relations [139]:

$$\sigma(\nu p \to \nu p) = 0.153 \times \sigma(\nu n \to e^- p), \tag{B.12}$$

$$\sigma(\nu n \to \nu n) = 1.5 \times \sigma(\nu p \to \nu p). \tag{B.13}$$

The Fermi motion and the Pauli blocking effect are considered for the target nucleons bound in ^{16}O or ^{12}C. The Fermi gas model is adopted to reproduce the Pauli blocking effect. The final nucleon momentum is required to be larger than the Fermi surface momentum (225 MeV/c in ^{16}O and 217 MeV/c in ^{12}C). The Fermi surface momentum is estimated from an electron-^{12}C scattering experiment [140]. The cross-section depends on the target nucleus because of the Pauli blocking effect, and the difference of the cross-section between ^{16}O and ^{12}C is less than 1.5% in the neutrino energy region of $E_\nu > 0.5$ GeV.

B.2.2 Resonance production channel

The resonance production interaction produces one lepton and one pion intermediating a baryon resonance state N^*:

$$\begin{aligned} \nu + N &\to l^- + N^* \\ N^* &\to N' + \pi\ (\eta, K), \end{aligned} \tag{B.14}$$

which is the dominant process if the invariant mass of the hadron system is less than 2 GeV/c^2. The simulation of this mode is based on the Rein-Sehgal model [76].

The differential cross-section of the resonance production with the mass M is written by

$$\frac{d^2\sigma}{dQ^2 dE_\nu} = \frac{1}{32\pi m_N E_\nu^2}\cdot\frac{1}{2}\cdot\sum_{\text{spins}}|T(\nu N \to l N^*)|^2 \cdot \delta(W^2 - M^2), \tag{B.15}$$

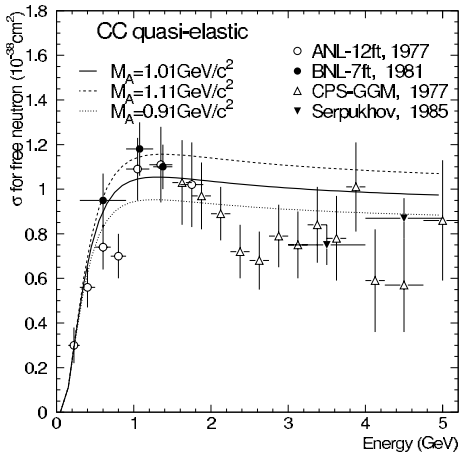

Figure B.5: Cross-section of CC-QE interaction on a free neutron in NEUT, together with the results of measurements by bubble chamber experiments. Horizontal axis is the incident neutrino energy. Solid, dashed, and dotted lines show the calculations of the cross-section in NEUT with M_A = 1.01, 1.11, and 0.91 GeV/c, respectively. Data points are from ANL [135], BNL [136], GGM [137], and Serpukhov [138].

where W is the invariant mass of the hadron system, and the width of the resonance decay is neglected. The amplitude of the resonance production, $T(\nu N \to lN^*)$, is calculated according to the FKR (Feynman-Kislinger-Ravndal) baryon model [141]. This model includes vector and axial-vector form factors using dipole parametrization with the same M_V and M_A values as CC-QE. The differential cross-section for the resonance with a finite decay width, Γ, is derived by replacing the δ-function in Equation (**??**) with a Breit-Wigner formula:

$$\delta(W^2 - M^2) \to \frac{1}{2\pi} \frac{\Gamma}{(W-M)^2 + \Gamma^2/4}. \tag{B.16}$$

In NEUT, $\Delta(1232)$ and other 17 resonance states with $W < 2.0$ GeV/c^2 are considered. Figure B.6 shows our calculation of the cross-section for each final state with $M_A = 1.01$ GeV/c^2 and experimental data [142–144]. In case of our choice, $M_A = 1.11$ GeV/c^2, and the cross-section is approximately 10% higher than that with $M_A = 1.01$ GeV/c^2. The cross-section is consistent with past experiments, no matter which M_A value we employ.

The decay kinematics of $\Delta(1232)$ is calculated by the Rein-Sehgal method. For the other resonance states, the meson direction is assumed to be isotropic in the rest frame of the resonance state.

B.2.3 Coherent pion production

The coherent pion production is the neutrino interaction with a whole nucleus instead of an individual nucleon, and it does not change the charge or the isospin of the nucleus. This reaction produces one pion with the same charge as the intermediating weak boson. The angular distribution of the recoil lepton is sharply peaked in the forward direction, and the nucleus does not break up due to the small momentum transfer.

The calculation of the cross-section and the kinematics is based on the Rein-Sehgal model [103] whose cross-section is modified to produce the model by J. Marteau *et al.* [145]. The differential cross-section of the Rein-Sehgal model is expressed by

$$\frac{d^3\sigma}{dQ^2 dy dt} = \frac{G_F^2 m_N E_\nu}{2\pi^2} f_\pi^2 A^2 (1-y) \cdot \left.\frac{d\sigma(\pi N \to \pi N)}{dq^2}\right|_{q^2=0} \cdot \left(\frac{1}{1+Q^2/M_A^2}\right)^2 e^{-bt} F_{\rm abs}, \tag{B.17}$$

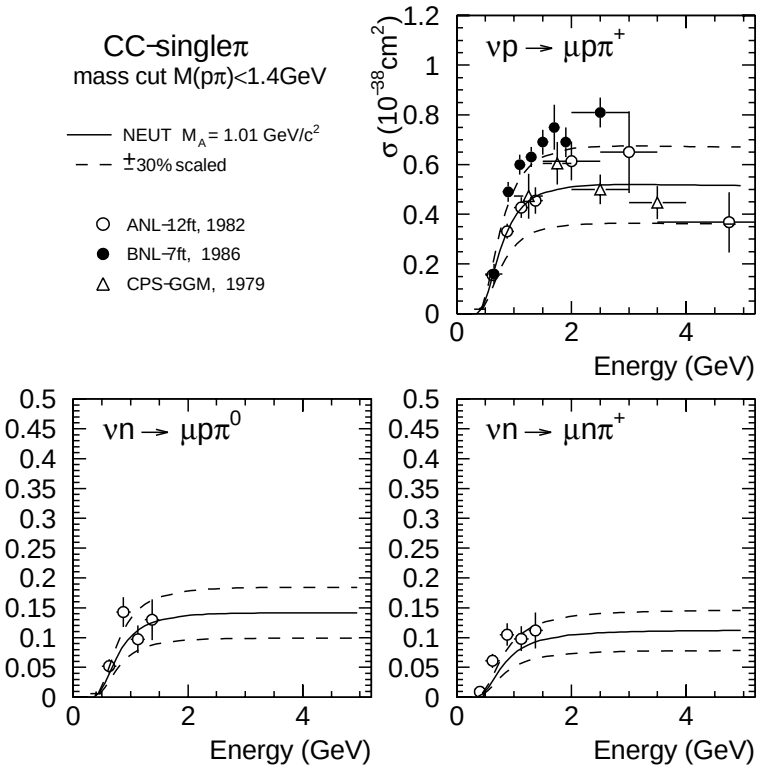

Figure B.6: Cross-sections of CC resonance production channels in NEUT, together with experimental results. Solid lines show our calculation, and dashed lines show the the cross-section scaled by $\pm 30\%$, where $M_A = 1.01$ GeV/c^2. The experimental results are from ANL [142], BNL [143], and GGM [144].

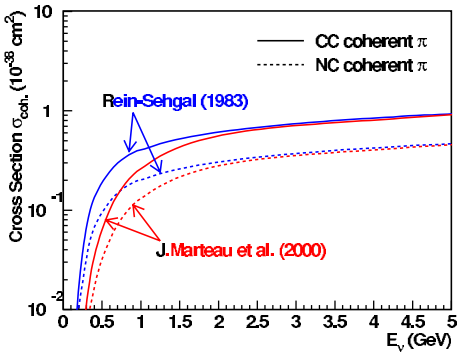

Figure B.7: Cross-section of the coherent pion production calculated by NEUT. Solid lines show the cross-section of CC, and dashed lines show that of NC. The cross-section modeled by Rein-Sehgal [103] and Marteau *et al.* [145] are drawn with blue and red lines, respectively.

where f_π is the pion decay constant of $0.93 m_\pi$, A is the atomic number, $b = (R_0 A^{1/3})^2/3$ is of the order of the transverse dimension of the nucleus taken to be 80 GeV^{-2} for oxygen, and t is the square of the four-momentum transfer to the nucleus. $F_{\rm abs}$ is a factor coming from the pion absorption in the nucleus. In this model, vector contribution is ignored. Therefore, coherent pion production occurs with equal cross section for neutrino and anti-neutrino. The axial parts of the neutral and charged currents form a triplet in isospace we are led to $f_{\pi^0}^2 = (\sqrt{1/2} f_{\pi^+})^2 = \frac{1}{2} f_{\pi^+}^2$, which appears in cross section formula. Therefore, the cross section of neutral current coherent pion is half of charged current in this model.

Figure B.7 shows the comparison of the cross-sections between the Rein-Sehgal model and its modification by Marteau *et al.* The cross-section of the former is slightly higher around 1 GeV.

B.2.4 Deep inelastic interactions

The differential cross-section of CC deep inelastic scattering is calculated by integrating the following equation in the range of the invariant mass of the hadronic system, $W > 1.3$ GeV/c^2 [146]:

$$\frac{d^2\sigma}{dxdy} = \frac{G_F^2 m_N E_\nu}{\pi} \cdot \left[(1 - y + \frac{1}{2}y^2 + C_1) F_2(x) + y(1 - \frac{1}{2}y + C_2)[xF_3(x)] \right] \tag{B.18}$$

$$C_1 = \frac{m_l^2 (y-2)}{4 m_N E_\nu x} - \frac{m_N x y}{2E_\nu} - \frac{m_l^2}{4E_\nu^2}$$

$$C_2 = -\frac{m_l^2}{4 m_N E_\nu x}$$

where $x = Q^2/(2m_N(E_\nu - E_l) + m_N^2)$ and $y = (E_\nu - E_l)/E_\nu$ are the Bjorken scaling parameters, and E_l is the energy of the final state lepton. The nucleon structure functions, F_2 and xF_3, are given by GRV94 [78] which is modified by Bodek and Yang [79]. The Bodek-Yang modification effectively changes the cross-section by a Q^2-dependent factor:

$$\frac{d^2\sigma}{dxdy} \rightarrow \frac{Q^2}{Q^2 + 0.188} \cdot \frac{d^2\sigma}{dxdy}. \tag{B.19}$$

It reduces the cross-section in low Q^2 region, which is favored by our previous analysis [52, 134].

The kinematics of the hadronic system is simulated by two methods according to the invariant mass, W. Only pions are considered in the region of $1.3 < W < 2.0$ GeV/c^2. The mean

multiplicity of pions is estimated from the result of Fermilab 15-foot hydrogen bubble chamber experiment [147]:

$$\langle n_\pi \rangle = 0.09 + 1.83 \ln W^2. \tag{B.20}$$

The number of pions for each event is determined using KNO(Koba-Nielsen-Olesen) scaling [148]. Since the range of W overlaps with that in the resonance production mode, $n_\pi \geq 2$ is required in this W region. The forward-backward asymmetry of pion multiplicity is also taken into account to be [149]:

$$\frac{\langle n_\pi^F \rangle}{\langle n_\pi^B \rangle} = \frac{0.35 + 0.41 \ln W^2}{0.50 + 0.09 \ln W^2}. \tag{B.21}$$

In the region of $W > 2.0$ GeV/c^2, the kinematics of the hadronic system is calculated by JETSET/PYTHIA package [81].

For the NC deep inelastic scattering, the ratio of NC to CC is assumed to be

$$\frac{\sigma(\mathrm{NC})}{\sigma(\mathrm{CC})} = \begin{cases} 0.26 & (E_\nu < 3 \text{ GeV}) \\ 0.26 + 0.04(E_\nu/3 - 1) & (3 < E_\nu < 6 \text{ GeV}) \\ 0.30 & (E_\nu > 6 \text{ GeV}) \end{cases}, \tag{B.22}$$

which is based on the experimental results [150].

B.2.5 Nuclear effects

Hadrons produced in an ^{16}O or ^{12}C nucleus often interact with nuclear medium inside the nucleus, called "nuclear effect". The nuclear effects of pions, nucleons, and Δ resonances are considered in NEUT. The neutrino interaction position in a nucleus is calculated using the Wood-Saxon type density distribution:

$$\rho(r) = \frac{Z}{A}\rho_0 \left\{ 1 + \exp\left(\frac{r - c}{a} \right) \right\}^{-1}, \tag{B.23}$$

where we choose $\rho = 0.48 m_\pi^3$, $a = 0.41$ fm, and $c = 2.69$ fm.

Pion

The nuclear effects for pions are classified into inelastic scattering, charge exchange, and absorption. The cross-section is calculated by the model of L. L. Salcedo *et al.* [82]. The Fermi motion and the Pauli blocking effect of nucleons are taken into account in the similar way as the CC-QE interaction. Figure **??** shows the calculated π^+-^{16}O interaction cross-section together with experimental data from C. H. Q. Ingram *et al.* [83], which agree well with each other. Since uncertainties in the past measurements are approximately 30%, we use this value as a systematic error on the nuclear effect for pions.

Nucleon

The nucleon-nucleon elastic scattering cross-section implemented in NEUT is based on the measurement by H. W. Bertini [151], which is used by GCALOR. The pion production interaction is also taken into account, according to the isobar production model of S. J. Lindenbaum *et al.* [152]. The effect of these models are compared with a past experiment by K. V. Alanakian *et al.* [153], which measured the yield of scattered protons in electron scattering on a ^{12}C target:

$$e + {}^{12}\mathrm{C} \to e' + p + X, \tag{B.24}$$

where the electron beam energy is 1.94 GeV, and the scattering angle of the electron is required to be 15 ± 2 degrees. The proton yield was measured at the scattering angles of 66 ± 8 degrees and 120 ± 8 degrees: the former corresponds to protons from pure QE process without nucleon-nucleon scattering, and the latter corresponds to those with scattering. This experiment is reproduced with NEUT by replacing the incident electron with an electron neutrino. Figure **??** shows the scattering angle of the proton using NEUT. We find that NEUT generates scattered protons 10% larger than the measurement. Therefore, we rescale the nuclear effect for nucleons by multiplying 0.9 to the cross-section, and we assign the error of 0.1 to this factor.

Δ resonance

The absorption of a Δ resonance [154] is taken into account. Approximately 20% of the Δ resonances are lost by this effect.

B.3 Detector Responce

Once the neutrino-induced event was generated as described above, the detector responce to the generated particles must be simulated as next step. In addition, the responce for each detector had to be correctly digitized so that analysis code would work for both real data and the MC data with same cut. In K2K, GEANT-3.21 package [70] is utilized for this perpose. This section describes the simulation of responces in all K2K detector elements, especially SciBar.

B.3.1 Simulation of Water Cerencov Detectors (1kt, SK)

The same technique is used for the detector simulation of 1kt and SK water cerencov detectors [66]. For the propagation of generated photons in water, Rayleigh scattering, Mie scattering and the absorptions of the photon are considered based on the cosmic-ray muon and the laser calibration data. Light reflection and absorption on detector material, such as the surface of PMTs and black sheets, are also simulated based on the data from direct measurements. The number of observed photo-electrons in each PMT is derived by summing up individual p.e. with a weight of a single p.e. distribution. The hit timing of each PMT is smeared according to the PMT timing resolution. Properties of the electronics system, such as the time width of ADC gate and the signal threshold, are also taken into account.

B.3.2 Simulation of SciFi

The light yield, attenuation in the SciFi and reflection from the aluminum coating at the edges are implemented based on the cosmic-ray muons and ^{90}Sr calibrations [56]. The responces of the IIT-CCD part is also considered based on the LED data in the MC simulation.

B.3.3 Simulation of SciBar

Light Yield

When charged particles traveled through the scintillator strip, true total energy deposition (MeV) in each strip is converted to the photo-electrons (PEs) with the conversion factor (MeV2PE) described in the previous chapter, where the scintillator quenching effect is also implemented. After the attenuation of the PEs according to the path-length in the WLS fiber, the PEs is smeared individually with photon-statistics and by Gaussian whose width is defined

as

$$\sigma = \frac{\sigma(1\mathrm{PE})}{\sqrt{\mathrm{PEs}}} \tag{B.25}$$

where $\sigma(1\mathrm{PE})$ is 1PE resolution, which is typically 80% from laboratory measurement.

In addition, the crosstalk effect described in the previous chapter is also implemented. We use a simple model for the crosstalk generation in the MC simulation as,

$$\begin{aligned} \mathrm{PEs}^{\mathrm{after}} &= (1-5\alpha)\cdot \mathrm{PEs}^{\mathrm{before}} \\ &\quad + \alpha \cdot \sum_{\mathrm{neighboring}} \mathrm{PEs}^{\mathrm{before}}(\mathrm{neighboring}) + \frac{1}{4}\alpha \cdot \sum_{\mathrm{diagnal}} \mathrm{PEs}^{\mathrm{before}}(\mathrm{diagonal}) \end{aligned}$$

where α is the crosstalk parameter set to be 4% from laboratory measurement, before/after means before/after applying the crosstalk effect and neighboring/diagonal means the neighoring/diagonal pixcel. In the analysis, we use a inverse process for the crosstalk correction in the data and the MC events.

Timing responce

The light velocity in the fiber of 0.059 (nsec/cm) from laboratory measurement [85, 155] is taken into account. In the analysis, we correct this propagation time for hits associated reconstructed tracks.

Digitization

After deciding the PEs and timing for each strip, the MC simulated digitization prosess. At first, the PEs is converted to ADC counts based on the conversion factor (PE2ADC) described in the previous chapter, where the electronics noise and the responce of VA slow shaper are also implemented. Then the timing information is converted to TDC counts with consideration of the input charge based on the T-Q correlation described in the previous chapter.

π interaction outside the target nucleus

We use CALOR program library to simulate the pion-CH interaction in the MC simulation. This package is known to reproduce the pion interactions well including more than 0.5 GeV/c region. For still lower energy region ($p_\pi \leq 0.5$ GeV/c), a custum made program library [80], which is originally developed for Super-K based on experimental data from $\pi - {}^{16}O$ scattering [156] and $\pi - p$ scattering [157], is used.

B.3.4 Simulation of MRD

Full structures including drift-tube modules and gas in MRD are taken into account [50]. For each hit, hit efficiency, noise hit estimated from the real data and timing information are correctly implemented.

Appendix C

Near detector analysis in the spectrum measurement

This chapter describes the details of the analysis of each near detector part on the neutrino spectrum measurement.

C.1 1KT part

Event sample

We select the fully-contained (FC) single-ring muon-like (1Rμ) events for the spectrum measurement because the proton momentum from CCQE event is usually below the cherenkov threshold. In addition, we require the muon is stopped inside the detector to measure the momentum. A typical event display is shown in Fig. C.1. According to the MC simulation, 97% of the events selected by the requirement are CC interaction, and the rest are mostly composed of NC interaction with an outgoing charged pion above its Cherenkov threshold. The efficiency for QE interaction is estimated to be 53 % and the QE fraction is 58 % in the sample. The detailed description for the event selection is found in [52].

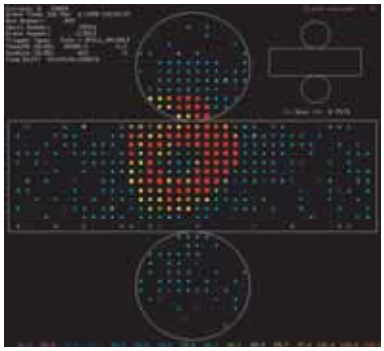

Figure C.1: A typical event display of a single muon event in 1KT.

definition of χ^2_{1KT}

The χ^2 for the 1KT term is defined as,

$$\chi^2_{\rm 1KT} \equiv \sum_{i,j} \frac{\left[N^{\rm data}(i,j) - N^{\rm MC}(i,j)\right]^2}{[\sigma^{\rm data}_{\rm stat}(i,j)]^2 + [\sigma^{\rm MC}_{\rm stat}(i,j)]^2 + [\sigma_{\rm syst}(i,j)]^2} + \frac{(P^{\rm 1KT}_{p\text{-scale}} - 1)^2}{(\sigma^{\rm 1KT}_{p\text{-scale}})^2}, \tag{C.1}$$

where $\sigma^{\rm data}_{\rm stat}(i,j)$ and $\sigma^{\rm MC}_{\rm stat}(i,j)$ are the statistical errors of data and the MC simulation in (i,j)-th bin, respectively. The second term is the constraint term for $P^{\rm 1KT}_{p\text{-scale}}$, which varies the momentum scale as

$$p'_\mu = \frac{p_\mu}{P^{\rm 1KT}_{p\text{-scale}}}, \tag{C.2}$$

The $\sigma^{\rm 1KT}_{p\text{-scale}}$ is evaluated to be $^{+2}_{-3}$% as described in Section 3.2.1.

The bin width of the (p_μ, θ_μ) distribution of 1KT is 0.1 GeV/c for p_μ and 10 degrees for θ_μ and the events above 90 degrees are integrated into one angular bin. The bin-by-bin systematic error, $\sigma_{\rm syst}(i,j)$, is also put into $\chi^2_{\rm 1KT}$. The sources and sizes of $\sigma_{\rm syst}(i,j)$ are summarized in [52] in detail.

C.2 SciFi part

Event sample

The SciFi data used in the analysis is taken under the two different detector configuration namely K2K-Ib and K2K-IIa as described before. For K2K-Ib data, CC candidate events are selected by requiring that at least one reconstructed track starting in the fiducial volume of SciFi is matched with a track or hits in the LG (SciFi-LG event) or MRD (SciFi-MRD event). On the other hand, only the SciFi-MRD-3D events are used for K2K-IIa data because LG is removed in this period. The significant hadron contamination is found in the SciFi-MRD-1L events due to a small amount of material between SciFi and MRD. A typical CC event display is shown in Fig. C.2. A schematic view of each event type is also shown in Fig. C.3 and C.4 for K2K-Ib and K2K-IIa, respectively. Each CC candidate sample is sub-divided into three categories of 1 track, QE and nonQE sample in the same way as SciBar. The number of event, the fraction and the efficiency for each category are summarized in Table C.1 and Table C.2, respectively. The detailed description for the event selection and classification is found in [55, 56].

Energy reconstruction

The muon energy in the CC candidate sample is reconstructed from its range through SciFi, LG and MRD for SciFi-MRD sample. The pulse height information of the cluster in LG is used for the SciFi-LG sample. The uncertainty for the energy reconstruction in LG part is evaluated to be 5 % and 30 MeV for SciFi-MRD sample and SciFi-LG sample, respectively, from the test beam experiment data (KEK-PS T501) [55]. The systematic uncertainty for the MRD part is 2.7 % as stated before.

definition of $\chi^2_{\rm SF}$

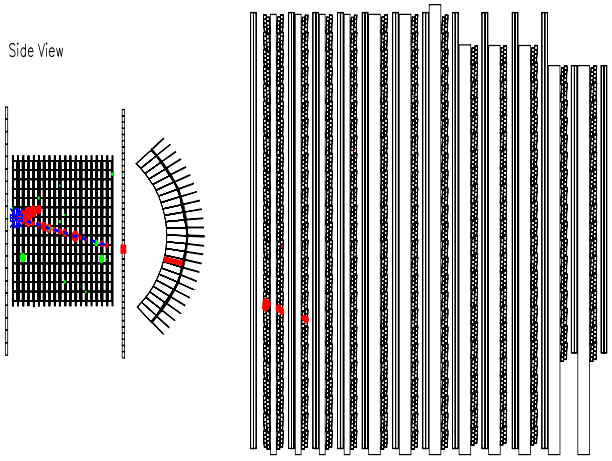

Figure C.2: The event display of a typical CC event in SciFi.

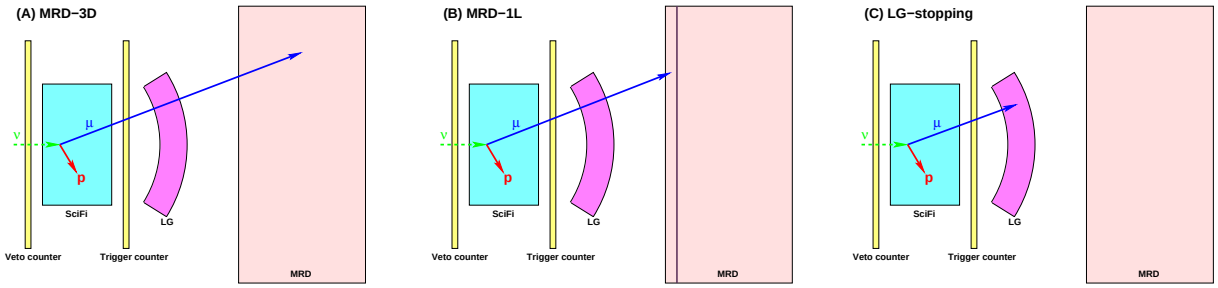

Figure C.3: Schematic view for each event type of SciFi in K2K-Ib. Figures (A), (B), and (C) show MRD 3D matching, MRD first layer matching, and LG stopping events, respectively.

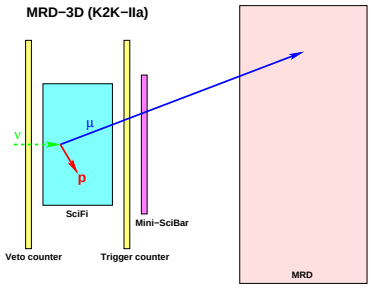

Figure C.4: The schematic view of the SciFi MRD-3D event in K2K-IIa.

Table C.1: SciFi event summary used in the analysis.

	K2K-Ib SciFi-MRD	K2K-Ib LG	K2K-IIa SciFi-MRD
1 track	5900	1450	3637
QE	758	108	455
nonQE	1218	737	816

The χ^2 for the SciFi is defined as,

$$\chi^2_{\rm SciFi} = 2\sum_{\mathcal{T}}\sum_{\mathcal{C}}\sum_{i,j}\left[N'^{{\rm MC},\mathcal{T},\mathcal{C}}(i,j) - N'^{{\rm data},\mathcal{T},\mathcal{C}}(i,j) + N'^{{\rm data},\mathcal{T},\mathcal{C}}(i,j)\ln\frac{N'^{{\rm data},\mathcal{T},\mathcal{C}}(i,j)}{N'^{{\rm MC},\mathcal{T},\mathcal{C}}(i,j)}\right] + \sum_{\mathcal{S}}\frac{(P^{\rm SciFi}_{\mathcal{S}} - \langle P^{\rm SciFi}_{\mathcal{S}}\rangle)^2}{(\sigma^{\rm SciFi}_{\mathcal{S}})^2}, \quad \text{(C.3)}$$

$$\mathcal{T} = \{\text{K2K-Ib-MRD, K2K-Ib-LG, K2K-IIa-MRD}\}, \quad \text{(C.4)}$$

$$\mathcal{C} = \{\text{1trk, 2trk-QE, 2trk-nonQE}\}, \quad \text{(C.5)}$$

$$\mathcal{S} = \{E\text{-scale, LG-density, LG-cluster, rescat, 2nd-eff}\}. \quad \text{(C.6)}$$

where the bin width of (p_μ, θ_μ) is the same intervals as E_ν for p_μ and 10 degrees for θ_μ, and each MC bin content are calculated by

$$N^{\rm MC,1trk}(i,j) = P^{\rm SciFi}_{\rm Norm}\cdot\sum_{k=1}^{8} f^\phi_k\cdot\left[N^{\rm MC,1trk}_{k,\rm QE}(i,j) + R_{\rm nQE}\cdot N^{\rm MC,1trk}_{k,\rm nonQE}(i,j)\right], \quad \text{(C.7)}$$

$$N^{\rm MC,2trk\text{-}QE}(i,j) = P^{\rm SciFi}_{\rm Norm}\cdot\sum_{k=1}^{8} f^\phi_k\cdot\Bigg[N^{\rm MC,2trk\text{-}QE}_{k,\rm QE}(i,j) + \frac{R^{\rm SciFi}_{\rm rescat}}{1-R^{\rm SciFi}_{\rm rescat}}(1-P^{\rm SciFi}_{\rm rescat})\cdot N^{\rm MC,2trk\text{-}QE}_{k,\rm QE}(i,j) + R_{\rm nQE}\cdot N^{\rm MC,2trk\text{-}QE}_{k,\rm nonQE}(i,j)\Bigg], \quad \text{(C.8)}$$

$$N^{\rm MC,2trk\text{-}nonQE}(i,j) = P^{\rm SciFi}_{\rm Norm}\cdot\sum_{k=1}^{8} f^\phi_k\cdot\Bigg[N^{\rm MC,2trk\text{-}nonQE}_{k,\rm QE}(i,j) - \frac{R^{\rm SciFi}_{\rm rescat}}{1-R^{\rm SciFi}_{\rm rescat}}(1-P^{\rm SciFi}_{\rm rescat})\cdot N^{\rm MC,2trk\text{-}QE}_{k,\rm QE}(i,j) + R_{\rm nQE}\cdot N^{\rm MC,2trk\text{-}nonQE}_{k,\rm nonQE}(i,j)\Bigg], \quad \text{(C.9)}$$

where $P^{\rm SciFi}_{\rm Norm}$ and $P^{\rm SciFi}_{\rm rescat}$ are overall normalization and the scaling factor of the proton rescattering cross-section. The second terms in the summations of Equation (C.8) and (C.9) represent the migration between 2-track-QE and 2-track-nonQE samples due to the proton rescattering. The uncertainty for the second track finding efficiency is also taken into account as,

$$N'^{\rm MC,1trk}(i,j) = (1-P^{\rm SciFi}_{\text{2nd-eff}})\cdot[N^{\rm MC,2trk\text{-}QE}(i,j) + N^{\rm MC,2trk\text{-}nonQE}(i,j)], \quad \text{(C.10)}$$

$$N'^{\rm MC,2trk\text{-}QE}(i,j) = P^{\rm SciFi}_{\text{2nd-eff}}\cdot N^{\rm MC,2trk\text{-}QE}(i,j), \quad \text{(C.11)}$$

$$N'^{\rm MC,2trk\text{-}nonQE}(i,j) = P^{\rm SciFi}_{\text{2nd-eff}}\cdot N^{\rm MC,2trk\text{-}nonQE}(i,j), \quad \text{(C.12)}$$

where $P^{\rm SciFi}_{\text{2nd-eff}}$ is the fitting parameter to vary the second track finding efficiency.

In addition, the systematic errors on $E^{\rm MRD}_\mu$, $E^{\rm LG}_\mu$, and $E^{\rm LGcluster}_\mu$ are separately taken into account by three fitting parameters, $P^{\rm SciFi}_{E\text{-scale}}$, $P^{\rm SciFi}_{\text{LG-density}}$, and $P^{\rm SciFi}_{\text{LG-cluster}}$, respectively. Using these parameter, the muon energy for each sample is expressed as follows,

K2K-Ib MRD-3D,1L: $$E'_\mu = E^{\rm SciFi}_\mu + E^{\rm TG}_\mu + E^{\rm LG}_\mu\cdot P^{\rm SciFi}_{\text{LG-density}} + E^{\rm MRD}_\mu\cdot P^{\rm SciFi}_{E\text{-scale}}, \quad \text{(C.13)}$$

K2K-Ib LG-Stopping: $$E'_\mu = E^{\rm SciFi}_\mu + E^{\rm TG}_\mu + E^{\rm LGcluster}_\mu + P^{\rm SciFi}_{\text{LG-cluster}}, \quad \text{(C.14)}$$

K2K-IIa MRD-3D: $$E'_\mu = E^{\rm SciFi}_\mu + E^{\rm TG}_\mu + E^{\text{Mini-SciBar}}_\mu + E^{\rm MRD}_\mu\cdot P^{\rm SciFi}_{E\text{-scale}}. \quad \text{(C.15)}$$

The center values and their error sizes are summarized in Table C.3.

C.3 PIMON part

definition of $\chi^2_{\rm PIMON}$

The PIMON data is used to constrain the E_ν spectrum shape above 1 GeV. The χ^2 for the PIMON term is defined as

$$\chi^2_{\rm PIMON} = \sum_{i=5}^{7} \frac{\left(f_i - f_i^{\rm PIMON}\right)^2}{(\sigma_i^{\rm PIMON})^2} \tag{C.16}$$

$$f_i^{\rm PIMON} \equiv \frac{\Phi_i^{\rm PIMON}/\Phi_i^{\rm MC}}{\Phi_4^{\rm PIMON}/\Phi_4^{\rm MC}} \qquad (i = 5, 6, 7) \tag{C.17}$$

where, $\Phi^{\rm PIMON}$ and $\Phi^{\rm MC}$ are the neutrino flux measured by PIMON and estimated with Beam-MC simulation, respectively. As described, we fixed the neutrino flux at 1.0-1.5 GeV at unity for a normalization in the fitting, and there is only one bin above 2.5 GeV in the PIMON measurement. Thus, the summention is performed from 5th-7th bin. The numbers used here are summarized in Table C.4.

Table C.2: The fraction and efficiency of CC-QE events for each event category of SciFi. The unit is %.

Event category		1-track	2-track QE	2-track nonQE	Total
Fraction	K2K-Ib	50	53	11	—
	K2K-IIa	57	58	12	—
Efficiency	K2K-Ib	39	5	2	46
	K2K-IIa	36	5	2	42

Table C.3: The central values and error sizes of the constraint terms in $\chi^2_{\rm SciFi}$.

Parameter	Central value	Error
$P^{\rm SciFi}_{E\text{-scale}}$	1.00	0.027
$P^{\rm SciFi}_{\rm LG\text{-}density}$	1.00	0.10
$P^{\rm SciFi}_{\rm LG\text{-}cluster}$ [GeV]	0.00	0.03
$P^{\rm SciFi}_{\rm rescat}$	0.87	0.10
$P^{\rm SciFi}_{\rm 2nd\text{-}eff}$	1.00	0.05

Table C.4: Summary of the numbers used in the $\chi^2_{\rm PIMON}$.

E_ν (GeV) (Bin number)	1.0-1.5 i=4	1.5-2.0 i=5	2.0-2.5 i=6	2.5 - i=7
$\Phi_i^{\rm PIMON}$	6.30×10^{11}	3.21×10^{11}	1.01×10^{11}	4.27×10^{10}
$\Phi_i^{\rm Beam-MC}$	6.19×10^{11}	3.35×10^{11}	1.05×10^{11}	3.96×10^{10}
$f_i^{\rm PIMON} \equiv \frac{\Phi_i^{\rm PIMON}}{\Phi_i^{\rm MC}} / \frac{\Phi_4^{\rm PIMON}}{\Phi_4^{\rm MC}}$	–	0.941	0.945	1.059
$\sigma_i^{\rm PIMON}$	–	$^{+10.7\%}_{-9.9\%}$	$^{+12.1\%}_{-17.7\%}$	$^{+47.7\%}_{-34.0\%}$

List of Tables

List of Figures

Bibliography

[1] W. Pauli, *Letter to the Physical Society of Tubingen* (1930), unpublished, the letter is reproduced in Brown, L.M. (1978), *Physics Today*, **31**, No. 9, 23.

[2] F. Reines and C. L. Cowan, Jr., Phys. Rev. **92**, 830 (1953).

[3] G. Danby *et al.*, Phys. Rev. Lett. **9**, 36 (1962).

[4] K. Kodama *et al.* (DONUT Collaboration), Phys. Lett. **B504**, 218 (2001), hep-ex/0012035.

[5] J. Drees (LEP Collaborations and LEP Electroweak Working Group), *the XX International Symposium on Lepton and Photon Interactions at High Energy*, Rome, Itary (2001).

[6] T. J. Loredo and D. Q. Lamb, Phys. Rev. **D65**, 063002 (2002), astro-ph/0107260.

[7] C. Kraus *et al.*, Eur. Phys. J. **C40**, 447 (2005), hep-ex/0412056.

[8] K. Assamagan *et al.*, Phys. Rev. **D53**, 6065 (1996).

[9] R. Barate *et al.* (ALEPH Collaboration), Eur. Phys. J. **C2**, 395 (1998).

[10] E. Majorana, Nuovo Cim. **14**, 171 (1937).

[11] H. V. Klapdor-Kleingrothaus, A. Dietz, H. L. Harney, and I. V. Krivosheina, Mod. Phys. Lett. **A16**, 2409 (2001), hep-ph/0201231.

[12] L. Baudis *et al.*, Phys. Rev. Lett. **83**, 41 (1999), hep-ex/9902014.

[13] D. N. Spergel *et al.*, Astrophys. J. Suppl. **148**, 175 (2003), astro-ph/0302209.

[14] U. Seljak *et al.* (2004), astro-ph/0407372.

[15] S. L. Glashow, Nucl. Phys. **22**, 579 (1961).

[16] S. Weinberg, Phys. Rev. Lett. **19**, 1267 (1967).

[17] A. Salam, In *Novel Symposium*, **No. 8** (1968).

[18] T. Yanagida, *Proc. of Workshop Unified theory and Baryon Number is the Universe (KEK, Tsukuba, Japan)* (1970).

[19] Y. Fukuda *et al.* (Kamiokande Collaboration), Phys. Lett. **B335**, 237 (1994).

[20] W. W. M. Allison *et al.* (Soudan-2 Collaboration), Phys. Lett. **B449**, 137 (1999), hep-ex/9901024.

[21] M. Ambrosio *et al.* (MACRO Collaboration), Phys. Lett. **B434**, 451 (1998), hep-ex/9807005.

[22] R. Becker-Szendy *et al.*, Phys. Rev. **D46**, 3720 (1992a).

[23] R. Clark *et al.*, Phys. Rev. Lett. **79**, 345 (1997).

[24] Y. Fukuda *et al.* (Super-Kamiokande Collaboration), Phys. Rev. Lett. **81**, 1562 (1998a), hep-ex/9807003.

[25] Y. Ashie *et al.* (Super-Kamiokande), Phys. Rev. Lett. **93**, 101801 (2004), hep-ex/0404034.

[26] B. T. Cleveland *et al.*, Astrophys. J. **496**, 505 (1998).

[27] W. Hampel *et al.* (GALLEX Collaboration), Phys. Lett. **B447**, 127 (1999).

[28] M. Altmann *et al.* (GNO Collaboration), Phys. Lett. **B490**, 16 (2000), hep-ex/0006034.

[29] J. N. Abdurashitov *et al.* (SAGE Collaboration), Phys. Rev. **C60**, 055801 (1999), astro-ph/9907113.

[30] Y. Fukuda *et al.* (Kamiokande Collaboration), Phys. Rev. Lett. **77**, 1683 (1996).

[31] S. Fukuda *et al.* (Super-Kamiokande Collaboration), Phys. Rev. Lett. **86**, 5651 (2001), hep-ex/0103032.

[32] Q. R. Ahmad *et al.* (SNO Collaboration), Phys. Rev. Lett. **89**, 011301 (2002), nucl-ex/0204008.

[33] K. Eguchi *et al.* (KamLAND Collaboration), Phys. Rev. Lett. **90**, 021802 (2003), hep-ex/0212021.

[34] M. Apollonio *et al.* (CHOOZ Collaboration), Phys. Lett. **B466**, 415 (1999), hep-ex/9907037.

[35] F. Boehm *et al.*, Phys. Rev. **D64**, 112001 (2001), hep-ex/0107009.

[36] Y. Declais *et al.*, Nucl. Phys. **B434**, 503 (1995).

[37] C. Athanassopoulos *et al.* (LSND Collaboration), Phys. Rev. Lett. **81**, 1774 (1998), nucl-ex/9709006.

[38] A. Aguilar *et al.* (LSND Collaboration), Phys. Rev. **D64**, 112007 (2001), hep-ex/0104049.

[39] B. Armbruster *et al.* (KARMEN Collaboration), Phys. Rev. **D65**, 112001 (2002), hep-ex/0203021.

[40] B. Armbruster *et al.*, Phys. Rev. **C57**, 3414 (1998), hep-ex/9801007.

[41] A. O. Bazarko (BooNe Collaboration) (1999), hep-ex/9906003.

[42] M. H. Ahn *et al.* (K2K), Phys. Rev. Lett. **93**, 051801 (2004), hep-ex/0402017.

[43] E. Aliu *et al.* (K2K), Phys. Rev. Lett. **94**, 081802 (2005), hep-ex/0411038.

[44] H. Maesaka, Ph.D. thesis, Kyoto University (2005).

[45] V. D. Barger, J. G. Learned, S. Pakvasa, and T. J. Weiler, Phys. Rev. Lett. **82**, 2640 (1999), astro-ph/9810121.

[46] E. Lisi, A. Marrone, and D. Montanino, Phys. Rev. Lett. **85**, 1166 (2000), hep-ph/0002053.

[47] T. Maruyama, Ph.D. thesis, Tohoku University (2000).

[48] S. Eidelman *et al.* (Particle Data Group), Phys. Lett. **B592**, 1 (2004).

[49] K. Nishikawa *et al.*, *Proposal for a Long Baseline Neutrino Oscillation experiment using KEK-PS and Super-Kamiokande* (1995), as KEK-PS proposal (E362).

[50] T. Inagaki, Ph.D. thesis, Kyoto University (2001).

[51] S. Yamada, Ph.D. thesis, University of Tokyo (2003).

[52] I. Kato, Ph.D. thesis, Kyoto University (2004).

[53] J. L. B. IV, Ph.D. thesis, UC/Irvine University (1997).

[54] S. Nakayama, Ph.D. thesis, Tokyo University (2003).

[55] H. Yokoyama, Ph.D. thesis, Tokyo University of Science (2004).

[56] T. Iwashita, Ph.D. thesis, Kobe University (2003).

[57] A. Suzuki *et al.* (K2K Collaboration), Nucl. Instrum. Meth. **A453**, 165 (2000), hep-ex/0004024.

[58] B. J. Kim *et al.*, Nucl. Instrum. Meth. **A497**, 450 (2003), hep-ex/0206041.

[59] T. Ishii *et al.* (K2K MRD Group), Nucl. Instrum. Meth. **A482**, 244 (2002), hep-ex/0107041.

[60] S. Fukuda *et al.*, Nucl. Instrum. Meth. **A501**, 418 (2003).

[61] Y. Fukuda *et al.* (Super-Kamiokande Collaboration), Phys. Lett. **B433**, 9 (1998b), hep-ex/9803006.

[62] H. Ishino, Master's thesis, Tokyo Institute of Technology (1996), in Japanese.

[63] K. Okumura, Ph.D. thesis, University of Tokyo (1999).

[64] M. Shiozawa, Ph.D. thesis, University of Tokyo (1999).

[65] J. Kameda, Ph.D. thesis, University of Tokyo (2002).

[66] M. Ishitsuka, Ph.D. thesis, University of Tokyo (2004).

[67] R. Becker-Szendy *et al.*, Phys. Rev. Lett. **69**, 1010 (1992b).

[68] S. Yamada, Master's thesis, University of Tokyo (1999), in Japanese.

[69] Y. Hayato, Nucl. Phys. Proc. Suppl. **112**, 171 (2002).

[70] *GEANT – Detector Description and Simulation Tool*, Application Software Group, Computing and Networks Division, CERN (1993), CERN Program Library Long Writeup W5013.

[71] Private communication with W. Gajewski, a K2K collaborator. I heard that there is a document in CERN reports which gives the information on Cho-CERN, but I could not find it. See also K2K internal note BEAM/BMMC/00-001.

[72] J. R. Sanford and C. L. Wang, AGS internal report BNL-11299 and BNL-11479, Brookhaven National Laboratory (1967), unpublished.

[73] C. L. Wang, Phys. Rev. Lett. **25**, 1068 (1970).

[74] K. Ishihara, Ph.D. thesis, University of Tokyo (1999).

[75] C. H. Llewellyn Smith, Phys. Rept. **3**, 261 (1972).

[76] D. Rein and L. M. Sehgal, Ann. Phys. **133**, 79 (1981).

[77] V. Bernard, L. Elouadrhiri, and U. G. Meissner, J. Phys. **G28**, R1 (2002), hep-ph/0107088.

[78] M. Glück, E. Reya, and A. Vogt, Z. Phys. **C67**, 433 (1995).

[79] A. Bodek and U. K. Yang, Nucl. Phys. Proc. Suppl. **112**, 70 (2002), hep-ex/0203009.

[80] M. Nakahata *et al.* (Kamiokande Collaboration), J. Phys. Soc. Jap. **55**, 3786 (1986).

[81] T. Sjostrand, CERN Report No. CERN-TH-7112-93 (1994), hep-ph/9508391.

[82] L. L. Salcedo, E. Oset, M. J. Vicente-Vacas, and C. Garcia-Recio, Nucl. Phys. **A484**, 557 (1988).

[83] C. H. Q. Ingram *et al.*, Phys. Rev. **C27**, 1578 (1983).

[84] *Kuraray Ltd., Tokyo, Japan.*

[85] M. Hasegawa, Master's thesis, Kyoto University (2002).

[86] T. Morita, Master's thesis, Kyoto University (2003).

[87] T. Sasaki, Master's thesis, Kyoto University (2003).

[88] *Hamamatsu Corporation, 325-6, Sunayama-Cho, Hamamatsu, Shizuoka, 430-8587, Japan; www.hamamatsu.com.*

[89] *Nichia Corporation. 491 OkaKamioka-Cho, Anan, Tokushima, 774-8601, Japan; www.nichia.co.jp.*

[90] P. Adamson *et al.*, Nucl. Instrum. Meth. **A492**, 325 (2002), hep-ex/0204021.

[91] S. Buontempo, A. Ereditato, F. Marchetti-Stasi, F. Riccardi, and P. Strolin, Nucl. Instrum. Meth. **A348**, 131 (1994).

[92] I. Abt, D. Emelyanov, I. Gorbunov, and I. Kisel, Nucl. Instrum. Meth. **A490**, 546 (2002).

[93] H. Maesaka, Master's thesis, Kyoto University (2001).

[94] M. Hasegawa *et al.* (K2K), Phys. Rev. Lett. **95**, 252301 (2005), hep-ex/0506008.

[95] M. O. Wascko (2004), hep-ex/0412008.

[96] F. Cavanna, Nucl. Phys. Proc. Suppl. **139**, 9 (2005).

[97] P. Vilain *et al.* (CHARM-II), Phys. Lett. **B313**, 267 (1993).

[98] P. P. Allport *et al.* (BEBC WA59), Z. Phys. **C43**, 523 (1989).

[99] P. Marage *et al.* (BEBC WA59), Z. Phys. **C31**, 191 (1986).

[100] H. J. Grabosch *et al.* (SKAT), Zeit. Phys. **C31**, 203 (1986).

[101] S. Willocq *et al.* (E632), Phys. Rev. **D47**, 2661 (1993).

[102] B. Z. Kopeliovich and P. Marage, Int. J. Mod. Phys. **A8**, 1513 (1993).

[103] D. Rein and L. M. Sehgal, Nucl. Phys. **B223**, 29 (1983).

[104] E. A. Paschos and A. V. Kartavtsev (2003), hep-ph/0309148.

[105] A. A. Belkov and B. Z. Kopeliovich, Sov. J. Nucl. Phys. **46**, 499 (1987).

[106] N. G. Kelkar, E. Oset, and P. Fernandez de Cordoba, Phys. Rev. **C55**, 1964 (1997), nucl-th/9609005.

[107] J. Marteau, J. Delorme, and M. Ericson, Nucl. Instrum. Meth. **A451**, 76 (2000).

[108] S. L. Adler, Phys. Rev. **135**, B963 (1964).

[109] P. Marage *et al.* (BEBC WA59), Z. Phys. **C49**, 385 (1991).

[110] C. A. Piketty and L. Stodolsky, Nucl. Phys. **B15**, 571 (1970).

[111] B. Z. Kopeliovich, Nucl. Phys. Proc. Suppl. **139**, 219 (2005), hep-ph/0409079.

[112] E. J. Jeon, Ph.D. thesis, The graduate university for advanced studies (2003).

[113] T. A. Gabriel, J. D. Amburgey, and B. L. Bishop (1977), ORNL/TM-5619.

[114] C. Zeitnitz and T. A. Gabriel, Nucl. Instrum. Meth. **A349**, 106 (1994).

[115] J. Alcaraz *et al.* (SciBooNE) (2005).

[116] D. Drakoulakos *et al.* (Minerva) (2004), hep-ex/0405002.

[117] E. H. Monsay, Phys. Rev. Lett. **41**, 728 (1978).

[118] S. Nakayama *et al.* (K2K), Phys. Lett. **B619**, 255 (2005), hep-ex/0408134.

[119] F. James, *MINUIT — Function Minimization and Error Analysis — Reference Manual*, Computing and Networks Division, CERN (1994), CERN Program Library Long Writeup D506.

[120] S. R. Coleman and S. L. Glashow, Phys. Lett. **B405**, 249 (1997), hep-ph/9703240.

[121] M. Gasperini, Phys. Rev. **D38**, 2635 (1988).

[122] S. R. Coleman and S. L. Glashow, Phys. Rev. **D59**, 116008 (1999), hep-ph/9812418.

[123] V. De Sabbata and M. Gasperini, Nuovo Cim. **A65**, 479 (1981).

[124] A. Fasso, A. Ferrari, J. Ranft, and P. R. Sala, *FLUKA: Present status and future developments* (1993), given at 4th International Conference on Calorimetry in High-energy Physics, La Biodola, Italy, 19-25 Sep 1993.

[125] R. A. Lundy *et al.*, Phys. Rev. Lett. **14**, 504 (1965).

[126] D. Dekkers *et al.*, Phys. Rev. **137**, B962 (1965).

[127] W. F. Baker *et al.*, Phys. Rev. Lett. **7**, 101 (1961).

[128] A. Yamamoto, KEK Report 81-13 (1981).

[129] Y. Cho *et al.*, Phys. Rev. **D4**, 1967 (1971).

[130] G. J. Marmer *et al.*, Phys. Rev. **179**, 1294 (1969).

[131] G. J. Marmer and D. E. Lundquist, Phys. Rev. **D3**, 1089 (1971).

[132] J. G. Asbury *et al.*, Phys. Rev. **178**, 2086 (1969).

[133] J. V. Allaby *et al.*, CERN Report No. CERN-TH-70-12 (1970), unpublished.

[134] M. H. Ahn *et al.* (K2K), Phys. Rev. Lett. **90**, 041801 (2003), hep-ex/0212007.

[135] S. J. Barish *et al.*, Phys. Rev. **D16**, 3103 (1977).

[136] N. J. Baker *et al.*, Phys. Rev. **D23**, 2499 (1981).

[137] S. Bonetti *et al.*, Nuovo Cim. **A38**, 260 (1977).

[138] S. V. Belikov *et al.*, Z. Phys. **A320**, 625 (1985).

[139] L. A. Ahrens *et al.*, Phys. Rev. Lett. **56**, 1107 (1986).

[140] F. A. Brieva and A. Dellafiore, Nucl. Phys. **A292**, 445 (1977).

[141] R. P. Feynman, M. Kislinger, and F. Ravndal, Phys. Rev. **D3**, 2706 (1971).

[142] G. M. Radecky *et al.*, Phys. Rev. **D25**, 1161 (1982).

[143] T. Kitagaki *et al.*, Phys. Rev. **D34**, 2554 (1986).

[144] M. Pohl *et al.*, Lett. Nuovo Cim. **24**, 540 (1979).

[145] J. Marteau, Eur. Phys. J. **A5**, 183 (1999), hep-ph/9902210.

[146] C. H. Albright and C. Jarlskog, Nucl. Phys. **B84**, 467 (1975).

[147] M. Derrick *et al.*, Phys. Rev. **D17**, 1 (1978).

[148] H. Sarikko, Proc. of the NEUTRINO'79 p. 507 (1979).

[149] S. Barlag *et al.* (Amsterdam-Bologna-Padua-Pisa-Saclay-Turin), Zeit. Phys. **C11**, 283 (1982).

[150] P. Musset and J. P. Vialle, Phys. Rept. **39**, 1 (1978).

[151] H. W. Bertini, Phys. Rev. **C6**, 631 (1972).

[152] S. J. Lindenbaum *et al.*, Phys. Rev. **105**, 1874 (1957).

[153] K. V. Alanakian *et al.*, Phys. Atom. Nucl. **61**, 207 (1998).

[154] T. S. Kosmas and E. Oset, Phys. Rev. **C53**, 1409 (1996).

[155] I. Kato, Master's thesis, Kyoto University (2000).

[156] E. Bracci *et al.*, CERN Report No. CERN-HERA-72-1 (1972).

[157] A. S. Carroll *et al.*, Phys. Rev. **C14**, 635 (1976).